Exploration of Late-Stage Methodologies for Precision-Engineered CPP Nanomaterials

by

Veronica R. Spaulding

A dissertation accepted and approved in partial fulfillment of the
requirements for the degree of
Doctor of Philosophy
in Chemistry

Dissertation Committee:
Dr. Michael Pluth, Chair
Dr. Ramesh Jasti, Advisor
Dr. Amanda Cook, Core Member
Dr. Paul Dalton, Institutional Representative

Spring 2026

© 2026

Veronica R. Spaulding

DISSERTATION ABSTRACT

Veronica R. Spaulding

Doctor of Philosophy in Chemistry

Title: Exploration of Late-Stage Methodologies for Precision-Engineered CPP Nanomaterials

Cycloparaphenylenes (CPPs) are strained, radially conjugated macrocycles whose curvature and modular synthesis enable precise control over electronic structure, yet methods to diversify their functionality remain limited. This work establishes late-stage functionalization strategies to access structurally diverse, π-rich CPPs with tunable properties. High-yielding S_NAr transformations of fluorinated CPPs enable incorporation of redox-active thianthrene units, affording multi-substituted macrocycles with enhanced host–guest interactions with C_{60} and decreased oxidation potentials. Mechanistic studies further reveal how strain and radial conjugation influence S_NAr reactivity, providing insight into the role of CPP properties in governing substitution pathways. In parallel, we demonstrate the first Diels–Alder cycloadditions on alkyne-embedded CPPs, where strain-promoted reactivity enables efficient access to π-extended architectures with increased effective Stokes shifts while preserving high absorptivity and quantum yield.

To translate these tunable CPP scaffolds into functional systems, we extend CPP modification toward biological applications through thiol–ene conjugation using norbornene-substituted CPPs. This approach enables efficient attachment to small molecules, peptides, and proteins, establishing CPPs as versatile fluorescent probes for multiplexed imaging. Collectively, this work positions late-stage functionalization as a unifying strategy to expand the structural, electronic, and functional scope of CPP-based nanocarbons, linking fundamental reactivity with supramolecular and bioimaging applications.

This dissertation includes both published and unpublished coauthored work describing these methodologies in detail.

ACKNOWLEDGMENTS

I wish to express my sincere gratitude to Dr. Ramesh Jasti for his support and mentorship, as well as to my committee members for their guidance throughout my PhD program. I am also grateful to my labmates, past and present, for their collaboration, camaraderie, and willingness to answer my many questions.

I am especially indebted to my undergraduate mentors, Dr. John Hoberg and Dr. Bruce Parkinson, who helped me develop as a researcher and encouraged me to pursue graduate studies. I would also like to thank the many family, friends, and mentors who followed my journey with continued interest and support — all have shaped me over the years and given me so much to carry forward.

Finally, I acknowledge the funding sources that made this work possible, as detailed in concluding remarks.

DEDICATION

To Lorraine Stoltzner, my mum. For showing me how to be resilient in the face of adversity, encouraging my dreams, and always supporting me.

To Travis Keune, my partner. For being there with me through all the tears and celebrations.

To all the animals in my life. For all the cuddles and the reminder that life is more than work.

— Be like an electron and quantum tunnel

Table of Contents

Table of Contents 6

Chapter I: Background 13

1.1 The Inception of Cycloparaphenylenes (CPPs) 13

1.2 S_NAr Chemistry for Modular CPP Diversification and Host–Guest Tuning . . 15

1.3 Diels-Alder Strategies for Late-Stage Property Tuning of CPPs 17

1.4 Developing CPPs as a Bioconjugation Handle 19

1.5 Bridge to Chapter II 21

1.6 Citations 21

Chapter II: S_NAr Chemistry for Modular CPP Diversification and Host–Guest Tuning . 26

2.1 Redox-Active Multi-Thianthrene-Containing Cycloparaphenylenes 26

2.1.1 Contributions 26

2.1.2 Abstract 26

2.1.3 Introduction 27

2.1.4 Results and Discussion 29

2.1.5 Conclusion 35

2.1.6 Experimental Appendix: Supplementary Information 36

I. Synthesis 36

II. Structural Characterization 38

III. Optoelectronic Properties 42

IV. Host-Guest Binding with C_{60} 48

V. Electrochemical Details 50

VI. Computational Analysis 51

2.1.7 Citations 56

2.2 Mechanistic Investigation into Strain Mediated S_NAr Pathways 61

2.2.1 Introduction 61

2.2.2 Results and Discussion 63
2.2.3 Conclusion and Bridge to Chapter III 66
2.2.4 Experimental Appendix: Supplementary Information 67
I. Synthesis 68
II. Structural Characterization 78
2.2.5 Citations 99
Chapter III: Diels-Alder Strategies for Late-Stage Property Tuning of CPPs 102
3.1.1 Contributions 102
3.1.2 Abstract 102
3.1.3 Introduction 102
3.1.4 Discussion 104
3.1.5 Conclusion and Bridge to Chapter IV 107
3.1.6 Experimental Appendix: Supplementary Information 107
I. Synthesis 108
II. Structural Characterization 110
III. Optoelectronic Properties 117
IV. Solvatochromic Study 120
V. Computational Analysis 121
3.1.7 Citations 125
Chapter IV: Developing CPPs as a Bioconjugation Handle 129
4.1 CPPs as Fluorophores for Multiplexed Imaging in Biological Systems 129
4.1.1 Contributions 129
4.1.2 Abstract 129
4.1.3 Introduction 130
4.1.4 Results and Discussion 131
4.1.5 Conclusion and Future Work 133
4.1.6 Bridge to Chapter V 133

4.1.7 Experimental Appendix: Supplementary Information 133
I. Synthesis 137
II. Structural Characterization 138
4.1.8 Citations 143
Chapter V: Additional Work 146
5.1 Statistical Optimization of Hydrazone-Crosslinked Hyaluronic Acid Hydrogels for Protein Delivery 146
5.1.1 Contributions 146
5.1.2 Introduction 146
5.1.3 Experimental Appendix: Supplementary Information 150
I. Synthesis 150
II. Degree of modification (DOM) determination 152
III. Hydrogel Analysis 153
IV. Design of Experiments 155
5.1.4 Results and Discussion 158
5.1.5 Conclusion 170
5.1.6 Citations 171
Chapter VI: Summary 178
6.1 Concluding Remarks 178
6.2 Acknowledgements 178
6.2.1 Redox-Active Multi-Thianthrene-Containing Cycloparaphenylenes 178
6.2.2 Statistical Optimization of Hydrazone-Crosslinked Hyaluronic Acid Hydrogels for Protein Delivery 179

List of Figures

1.1 Comparison of linear vs curved paraphenylene systems 15

1.2 CPP applications 16

1.3 Meisenheimer S_NAr mechanism 17

1.4 Alkyne CPP modifications 18

1.5 One-photon versus two-photon microscopy 20

2.6 Thianthrene systems 28

2.7 Single crystal X-ray diffraction of structure **2**. 32

2.8 Host-Guest complexation with thianthrene CPPs 34

2.9 Redox analysis of thianthrene CPPs 35

2.10 Previous examples modifying cycloparaphenylenes with S_NAr. 62

2.11 Competition study between linear tetrafluorinated system compared to fluorinated CPP. 62

2.12 Photophysical study for single fluorine [*n*]CPPs (*n*=8,10, and 12). 64

2.13 Single crystal x-ray diffraction of structure **7b**. 65

2.14 S_NAr on single fluorine systems 66

2.15 DFT geometry and energy analysis for S_NAr on single fluorine systems 67

3.16 Examples of late-stage modifications on alkyne cycloparaphenylenes. 104

3.17 Photophysics for Diels-Alder products 106

4.18 Photophysical properties of bioconjugated CPPs 134

4.19 Synthesis of novel benzothiadiazole CPP derivate 135

4.20 m-alkyne CPP conjugation proposal 136

5.21 Functionalization of HA hydrogels 159

5.22 Physicochemical properties of hydrogel formulations 162

5.23 3D response surface response factors for hydrogel formulations 164

5.24 Validation of predictive models to optimize HA hydrogels 167

5.25 Synthesis of norbornene modified HA and affibody conjugation 168

5.26 Release of BMP-2 from HA hydrogel. 168

List of Tables

3.1 Synthetic conditions for [9+1]CPP to product1a, and [11+1]CPP to product 2a . . 104

3.2 Compiled optoelectronic values for derivatized CPPs and parent compounds. . . . 105

4.3 Synthetic conditions for different thiolate peptides. 132

5.4 DOE hydrogel formulations using D-optimal regression model 156

5.5 Ranges of physicochemical properties exhibited by HA hydrogels. 162

5.6 ANOVA assessment of regression models. Excluded non-significant values are indicated with a dash (–). 166

5.7 Formulations for optimal and pessimal hydrogels. 167

List of Schemes

1.1 2008 proposed reductive elimination pathway 14

2.2 Synthesis of thianthrene CPPs 30

2.3 Synthesis pathway for library of single fluorine [*n*]CPPs (*n*=8,10, and 12). 64

3.4 Diels-Alder [4+2] cycloaddition between CPP and tetraphenylcyclopentadienone. . . . 105

4.5 Thiol-ene mechanism 132

Chapter I: Background

1.1 The Inception of Cycloparaphenylenes (CPPs)

Carbon nanomaterials such as graphene, carbon nanotubes (CNTs), and fullerenes exhibit unique electronic, optical, and mechanical properties that make them attractive for applications ranging from electronics to drug delivery.[1,2] However, conventional synthetic and fabrication methods often provide limited control over structural features such as size, chirality, and functionalization, frequently resulting in heterogeneous mixtures that complicate property tuning and application development.[3–5] Bottom-up molecular approaches offer an alternative strategy for achieving structural precision in carbon nanomaterials. Cycloparaphenylenes (CPPs), cyclic arrays of para-linked benzene rings, represent molecularly defined fragments of carbon nanotubes and provide a promising platform for constructing nanocarbon architectures with atomic-level control. Owing to their strained cyclic structure and radially oriented π-systems, CPPs exhibit distinctive electronic and photophysical properties and have become attractive scaffolds for the development of functional nanomaterials.[6–8] While significant progress has been made in the synthesis of CPPs, strategies to broadly diversify their structure and precisely tune their properties remain comparatively limited. CPP synthesis relies on bottom-up assembly from small organic building blocks to construct highly strained macrocycles. In 2008, Jasti and Bertozzi introduced a key strategy incorporating a cyclohexadiene unit as a masked aromatic group (**Scheme 1.1**), enabling controlled aryl–aryl coupling followed by deprotection and reduction to generate fully aromatic CPPs. In 2010, Yamago and co-workers reported an alternative Pt-mediated macrocyclization using linear precursors; however, this approach can lead to limitations including restricted symmetry control, broad product distributions, and high material costs associated with excess platinum reagents.[9,10] Since these foundational reports, substantial efforts have focused on improving the efficiency, scalability, and structural diversity of CPP synthesis.

CPPs synthesized through bottom-up strategies provide precise control over ring size, with each nanohoop exhibiting a characteristic fluorescence signature while maintaining a similar absorption

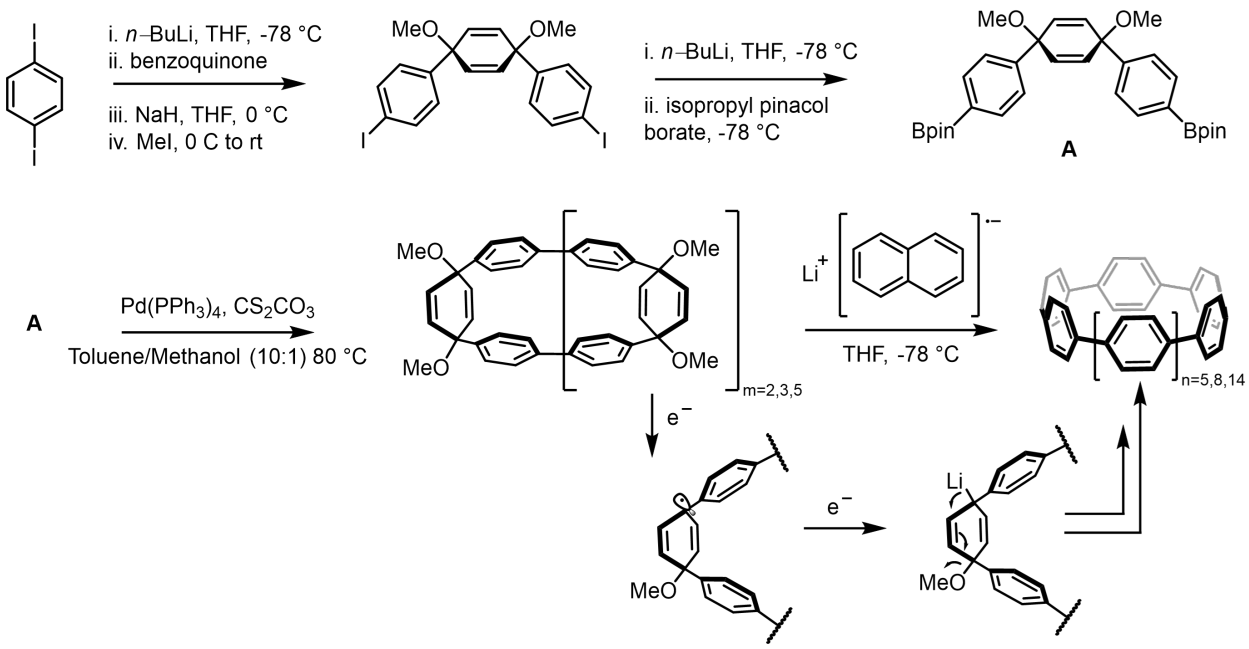

Scheme 1.1: Jasti reported a reductive elimination pathway in 2008 that used masked arene rings in precursor building blocks to successfully install unfavorable strain in the final paraphenylene structure (adapted from ref. 6).

energy near 340 nm, a feature attributed to their high symmetry and strained cyclic architecture.[6,7,11] Compared to linear paraphenylene analogues, CPPs exhibit significantly lower HOMO–LUMO energy gaps. The trend for lowering the HOMO-LUMO gap is inverse to linear analogues, smaller CPPs have more orbital overlap because the strained architecture minimizes dihedral angles (**Figure 1.1**). These unique photophysical properties, combined with their radially oriented π-systems, have made CPPs attractive scaffolds for a variety of emerging applications including fluorescent probes, strain-promoted reactivity, and organic electronic materials such as OLEDs.[12] Consequently, significant effort has been devoted to modifying CPP structures to tune their physical and chemical properties (**Figure 1.2**).

Many functionalized CPPs have been accessed through incorporation of substituents during precursor synthesis using modular strategies. While this approach enables installation of diverse functional groups prior to macrocyclization, certain substituents remain incompatible with the reaction conditions required for macrocycle formation or aromatization, often resulting in reduced yields or limited substrate scope. For example, to access soluble CPPs for cell imaging applications, White

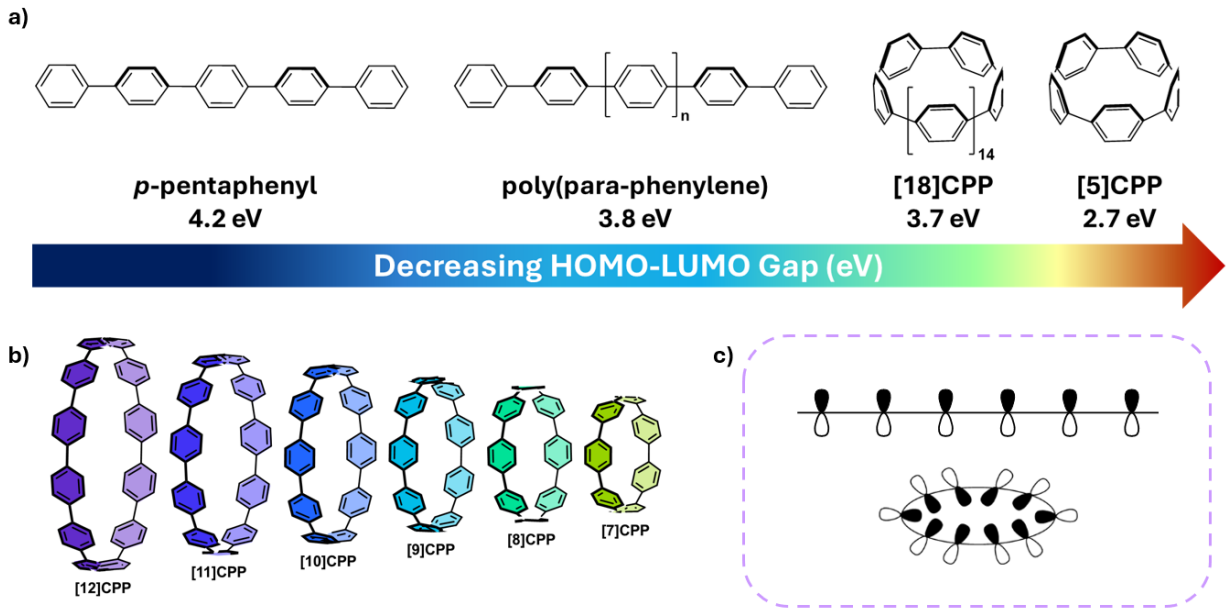

Figure 1.1: a) Comparison of HOMO-LUMO gap energies in eV of linear paraphenylene systems versus cyclic paraphenylene systems. b) Color representations of [*n*]CPPs. c) Linear versus axial orbital generalized diagram representation.

et al. carried through a protected hydroxy functional group with limited yield.[13,14] Further, to access new applications and properties, it becomes costly with time and materials to optimize through early-functionalization methods. These constraints restrict the accessible chemical diversity of CPP derivatives and present challenges for expanding nanohoop functionality. As a result, the broader utility of CPPs as structurally precise nanocarbon scaffolds is limited by the lack of strategies for modular, post-synthetic modification. To address this challenge, this dissertation develops *late-stage synthetic strategies* that enable *tunable* **host–guest interactions, photophysical properties, and biological conjugation**. This work aims to adapt existing scalable CPP platforms that allow for broad diversification of CPPs to harness new properties and reactivities.

1.2 S_NAr Chemistry for Modular CPP Diversification and Host–Guest Tuning

To address limitations of early precursor incorporation, recent efforts have explored late-stage modification strategies in which stable, fully aromatized CPPs are diversified through post-synthetic transformations. One particularly promising platform includes fluorinated cy-

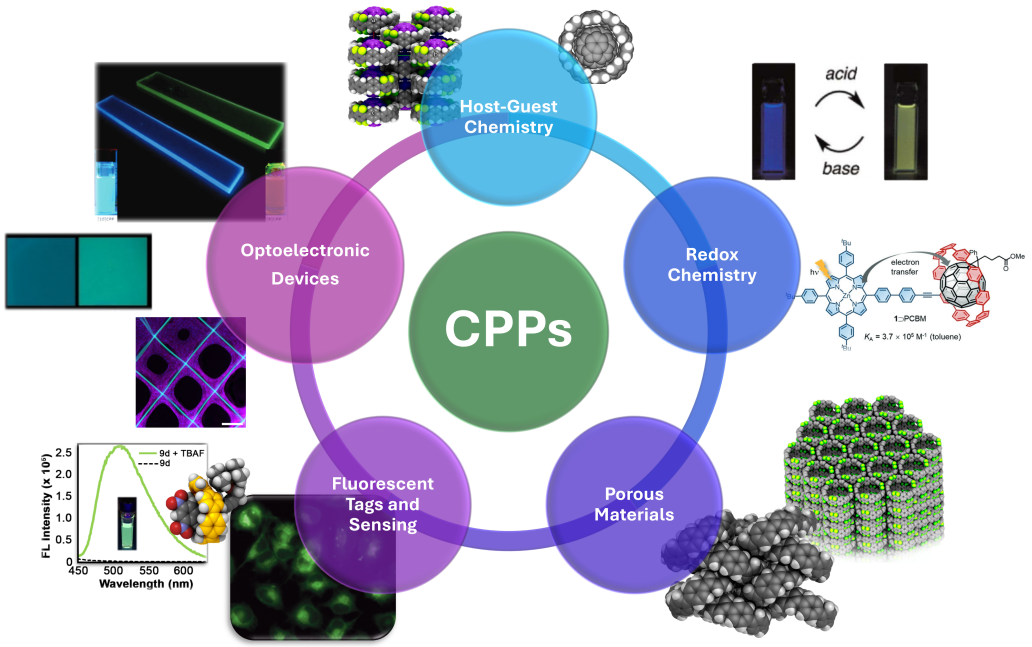

Figure 1.2: CPPs have possibilities for a wide array of nanomaterial applications, adding to the diversification of the CPP library will enable new technologies to be developed in areas such as porous materials, fluorescent tags, and many others.

cloparaphenylenes (F[*n*]CPPs). Dr. Van Raden and Dr. Leonhardt expanded the CPP library by introducing fluorinated CPPs that exhibit exceptional stability throughout synthesis, enabling gram-scale preparation.[10,12] In addition to improving synthetic robustness, the fluorine substituents serve as versatile handles for post-aromatization functionalization through nucleophilic aromatic substitution (S_NAr), positioning F[n]CPPs as a modular platform for late-stage diversification of CPP nanomaterials.[14–17] Nucleophilic Aromatic Substitution (S_NAr) is a fundamental organic reaction taught briefly in undergraduate courses but is used extensively in broader areas such as therapeutic and agricultural chemistry.[18,19] Progress in the field has focused on elucidating the mechanistic pathway, initially proposed to go through the Meisenheimer intermediate in 1902, but has since been revealed to be more complex.[19–26] In an S_NAr reaction, the nucleophile attacks an aromatic substrate, and substitutes in place of a leaving group. The mechanism proposed by Meisenheimer indicates that it undergoes a stepwise addition-elimination stabilized by ortho- and para-substituted electron withdrawing groups (EWG) (**Figure 1.3**). Blaziak and Makosza

reported a faster equilibrium pathway possible at EWG ortho- positions which can lead to other adducts under certain conditions.[26,27] Recent studies have revealed nucleophilic substitution with poor EWG or even electron donating groups on the substrate, yet it proceeds through a concerted pathway.[22,28–30]

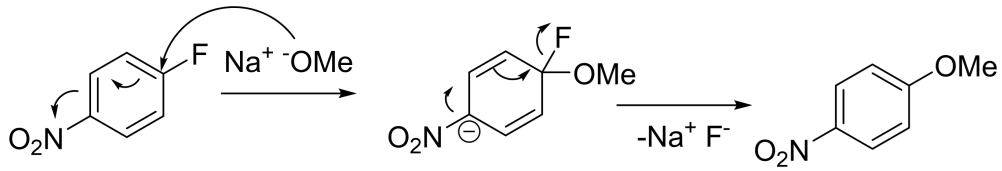

Figure 1.3: In the Meisenheimer pathway for S_NAr a nucleophile attacks an aromatic substrate; the incoming negative charge is further stabilized when there is an adequate electron withdrawing group ortho or para to the site of attack.

In 2018, the Swager group published in *Nature Chemistry* novel thianthrene synthesis using the S_NAr reaction between fluoro-arenes and thiobenzenes.[31] They analyzed the dynamic nature of the S_NAr reaction with thianthrene nucleophiles finding that a single substitution could be resubmitted to form di-substituted products. This dynamic reforming of bonds proved useful to form planar extended thianthrene systems which typically requires thermodynamic equilibrium conditions to form crystalline structures with error correcting behavior. Inspired by these planar systems, we've applied this method to CPPs, where S_NAr provides a useful strategy to diversify CPP architectures, discussed in depth in Chapter 2. This work was recently accepted by the journal *Chemical Communications* and co-authored with Tara D. Clayton, Audrey M. Davenport, Lev N. Zakharov, Carl K. Brozek, and Ramesh Jasti.

1.3 Diels-Alder Strategies for Late-Stage Property Tuning of CPPs

Another strategy for diversifying CPPs involves leveraging their inherent *strain-promoted reactivity* to enable post-synthetic modification. In particular, strained alkyne embedded CPPs represent a versatile platform for late-stage functionalization.[16,32,33] In 2018, Schaub and co-workers demonstrated that the reactivity of these systems increases with decreasing ring size, consistent with increased strain energy. This trend was later quantified by Fehr and co-workers, who further

showed that electronic effects also contribute to the enhanced reactivity of alkyne-functionalized CPPs.[33] These findings position strained alkyne CPPs as scalable and modular scaffolds for post-aromatization diversification. To date, functionalization of alkyne CPPs has primarily relied on transformations such as azide–alkyne cycloaddition and metal-mediated cyclotrimerization (**Figure 1.4**).[32] While effective, these are only two approaches for systematically tuning the electronic structure of the CPP framework. Expanding the scope of reactivity at these strained alkynes would enable new strategies for modifying CPP properties.

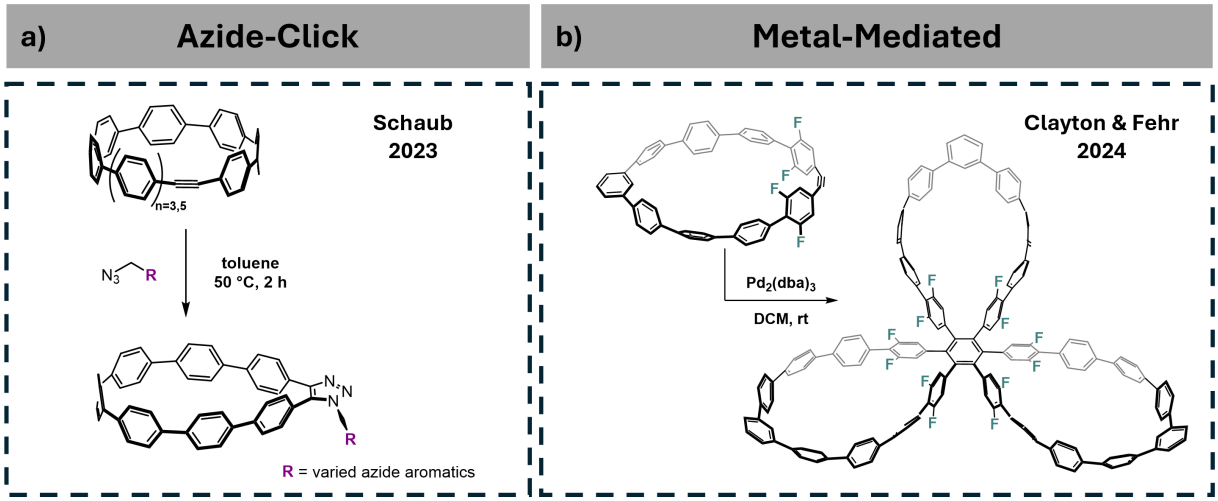

Figure 1.4: a) In 2023, alkyne CPPs were studied with varied azide aromatics to determine substitution effects (adapted from ref. 16) b) Metal-mediated cyclotrimerization was accomplished using strained CPPs with varying electronic modifications, an example *m*-fluorinated CPP is demonstrated (adapted from ref. 32)

Another route for alkyne CPP modification is the use of [4+2] Diels–Alder cycloadditions. This reaction offers a metal-free, high-yielding, and broadly applicable method for introducing structural complexity, while also enabling π-extension of the CPP framework. Such modifications provide a direct route to tuning photophysical properties, including emission behavior and Stokes shifts. In Chapter 3, we report the first example of a Diels–Alder reaction on strained alkyne CPPs, establishing this transformation as a new tool for late-stage diversification and property control in CPP nanomaterials. This research is being prepared for a manuscript co-authored with Tara D. Clayton, Victor Salpino, Leyla Gillette, and Ramesh Jasti.

1.4 Developing CPPs as a Bioconjugation Handle

CPPs are positioned for multiple applications; however, translation from academic study to industry has been slow. To date, few studies have specifically explored their potential as biological fluorophores.[12,13,34] Fluorescence imaging is widely used to increase spatial resolution in biological systems and better understand complex cellular processes. Common microscopy methods include widefield and confocal microscopy, which are valued for their speed and accessibility. Widefield microscopy is generally more affordable but is best suited for thin samples, as it illuminates the entire field of view, often reducing resolution and producing blurred images.[35] Confocal microscopy improves resolution by filtering out background fluorescence through a pinhole mechanism, although signals originating near the focal plane can still contribute to background noise. Two-photon excitation (TPE) provides an alternative strategy for improving imaging resolution.[36,37] In conventional one-photon microscopy, as used in widefield and confocal techniques, a single high-energy photon excites a fluorescent molecule (**Figure 1.5a-b**). In biological samples, this excitation often overlaps with endogenous absorption and autofluorescence, which can reduce image clarity. In contrast, longer-wavelength light interacts less with biological molecules. TPE exploits this property by using two lower-energy photons that are simultaneously absorbed to excite a fluorophore, typically using focused pulsed lasers. This approach enables excitation specifically at the focal plane and allows deeper tissue penetration with near-infrared light.[38] Two-photon absorption was first theorized in 1931 by Maria Goeppert-Mayer, who estimated the probability of this process to be ~10^{-50} cm^4 s $photon^{-1}$ (1 GM).[39] TPE offers several advantages, including precise focal-plane excitation and reduced photobleaching outside the imaging region, enabling deeper tissue imaging, though imaging speed can be limited.

In 2021, the Jasti laboratory demonstrated that CPPs could function as two-photon imaging agents, reporting a two-photon fluorescence (TPF) cross-section of 65 GM—comparable to commercial fluorophores typically ranging from 20–200 GM.[34] They also observed improved photostability relative to a commercial standard, with approximately half the photobleaching at 100 mW laser power.

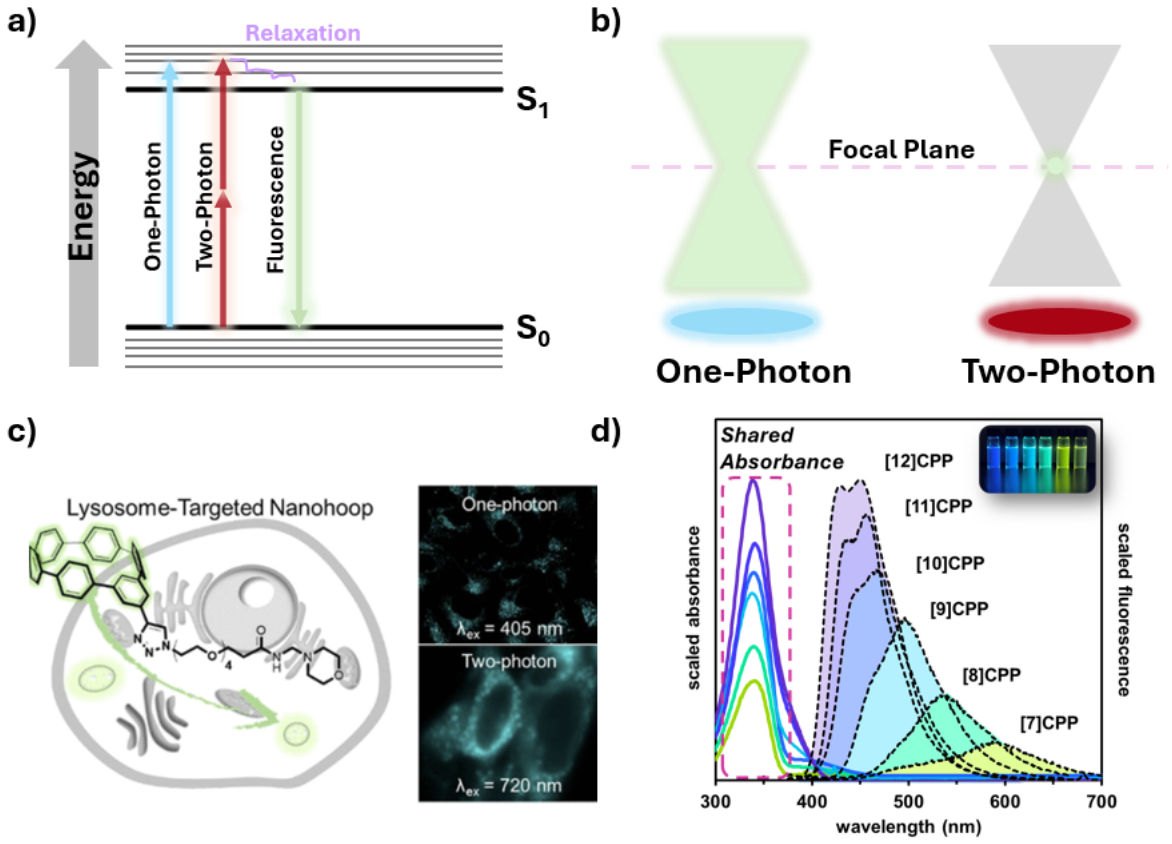

Figure 1.5: a) Simplified Jablonski diagram demonstrating one vs two-photon absorption. b) Example excitation of the focal plane for one vs two-photon microscopy. c) CPP as a one and two-photon fluorophore in a target cell system. (adapted from ref. 34) d) Common absorption of hydrocarbon cpps and their relative emission profiles.

These results highlight the potential of CPPs as promising fluorophores for biological imaging applications. To further expand the potential biological applications of CPPs, we explore their use as *multiplexed* fluorophores – expanding research with new CPP sizes and emissions. As CPPs also exhibit shared absorption profiles and large effective Stokes shifts, this makes them promising candidates for multiplexed imaging strategies (**Figure 1.5c-d**). In this approach, multiple fluorophores can be excited at a single wavelength while producing distinct emission signals, enabling improved analysis of temporal and spatial relationships within biological systems. This concept and its implementation are discussed in greater detail in Chapter 4. This chapter contains collaborative work with Katy Wyatt, Gabriela Bailey, Katelyn Alley, and Justin Svendsen.

1.5 Bridge to Chapter II

Overall, we develop a set of late-stage synthetic strategies that aim to establish CPPs as programmable nanocarbon scaffolds, enabling precise control over their structural, electronic, and functional properties without requiring de novo synthesis, as detailed in the following chapters.

1.6 Citations

(1) Hong, G.; Diao, S.; Antaris, A. L.; Dai, H. Carbon Nanomaterials for Biological Imaging and Nanomedicinal Therapy. *Chem. Rev.* **2015**, 115 (19), 10816–10906. https://doi.org/10.1021/acs.chemrev.5b00008.

(2) Salah, L. S.; Ouslimani, N.; Bousba, D.; Huynen, I.; Danlée, Y.; Aksas, H. Carbon Nanotubes (CNTs) from Synthesis to Functionalized (CNTs) Using Conventional and New Chemical Approaches. *J. Nanomater.* **2021**, 2021, e4972770. https://doi.org/10.1155/2021/4972770.

(3) Banerjee, S.; Hemraj-Benny, T.; Wong, S. S. Covalent Surface Chemistry of Single-Walled Carbon Nanotubes. *Adv. Mater.* **2005**, 17 (1), 17–29. https://doi.org/10.1002/adma.200401340.

(4) Leith, G. A.; Rice, A. M.; Yarbrough, B. J.; Kittikhunnatham, P.; Mathur, A.; Morris, N. A.; Francis, M. J.; Berseneva, A. A.; Dhull, P.; Adams, R. D.; Bobo, M. V.; Vannucci, A. A.;

Smith, M. D.; Garashchuk, S.; Shustova, N. B. “Broken-Hearted” Carbon Bowl via Electron Shuttle Reaction: Energetics and Electron Coupling. *Chem. Sci.* **2021**, 12 (19), 6600–6606. https://doi.org/10.1039/D0SC06755E.

(5) Handbook of Carbon Nanotubes; Abraham, J., Thomas, S., Kalarikkal, N., Eds.; *Springer International Publishing: Cham*, **2022**. https://doi.org/10.1007/978-3-030-91346-5.

(6) Jasti, R.; Bhattacharjee, J.; Neaton, J. B.; Bertozzi, C. R. Synthesis, Characterization, and Theory of [9]-, [12]-, and [18]Cycloparaphenylene: Carbon Nanohoop Structures. *J. Am. Chem. Soc.* **2008**, 130 (52), 17646–17647. https://doi.org/10.1021/ja807126u.

(7) Iwamoto, T.; Watanabe, Y.; Sakamoto, Y.; Suzuki, T.; Yamago, S. Selective and Random Syntheses of [n]Cycloparaphenylenes (n = 8–13) and Size Dependence of Their Electronic Properties. *J. Am. Chem. Soc.* **2011**, 133 (21), 8354–8361. https://doi.org/10.1021/ja2020668.

(8) Matsui, K.; Segawa, Y.; Itami, K. Synthesis and Properties of Cycloparaphenylene-2,5-Pyridylidene: A Nitrogen-Containing Carbon Nanoring. *Org. Lett.* **2012**, 14 (7), 1888–1891. https://doi.org/10.1021/ol3005112.

(9) Xia, J.; Bacon, J. W.; Jasti, R. Gram-Scale Synthesis and Crystal Structures of [8]- and [10]CPP, and the Solid-State Structure of C60@[10]CPP. *Chem. Sci.* **2012**, 3 (10), 3018–3021. https://doi.org/10.1039/C2SC20719B.

(10) Van Raden, J. M.; Leonhardt, E. J.; Zakharov, L. N.; Pérez-Guardiola, A.; Pérez-Jiménez, A. J.; Marshall, C. R.; Brozek, C. K.; Sancho-García, J. C.; Jasti, R. Precision Nanotube Mimics via Self-Assembly of Programmed Carbon Nanohoops. *J. Org. Chem.* **2020**, 85 (1), 129–141. https://doi.org/10.1021/acs.joc.9b02340.

(11) Adamska, L.; Nayyar, I.; Chen, H.; Swan, A. K.; Oldani, N.; Fernandez-Alberti, S.; Golder, M. R.; Jasti, R.; Doorn, S. K.; Tretiak, S. Self-Trapping of Excitons, Violation of Condon Approximation, and Efficient Fluorescence in Conjugated Cycloparaphenylenes. *Nano Lett.* **2014**, 14 (11), 6539–6546. https://doi.org/10.1021/nl503133e.

(12) Leonhardt, E. J.; Jasti, R. Emerging Applications of Carbon Nanohoops. *Nat. Rev. Chem.*

2019, 3 (12), 672–686. https://doi.org/10.1038/s41570-019-0140-0.

(13) White, B. M.; Zhao, Y.; Kawashima, T. E.; Branchaud, B. P.; Pluth, M. D.; Jasti, R. Expanding the Chemical Space of Biocompatible Fluorophores: Nanohoops in Cells. *ACS Cent. Sci.* **2018**, 4 (9), 1173–1178. https://doi.org/10.1021/acscentsci.8b00346.

(14) Shudo, H.; Kuwayama, M.; Segawa, Y.; Yagi, A.; Itami, K. Half-Substituted Fluorocycloparaphenylenes with High Symmetry: Synthesis, Properties and Derivatization to Densely Substituted Carbon Nanorings; preprint; *Chemistry*, **2023**. https://doi.org/10.26434/chemrxiv-2023-zsvnt.

(15) A. Kamin, A.; D. Clayton, T.; E. Otteson, C.; M. Gannon, P.; Krajewski, S.; Kaminsky, W.; Jasti, R.; J. Xiao, D. Synthesis and Metalation of Polycatechol Nanohoops Derived from Fluorocycloparaphenylenes. *Chem. Sci.* **2023**, 14 (36), 9724–9732. https://doi.org/10.1039/D3SC03561A.

(16) Terabayashi, T.; Kayahara, E.; Zhang, Y.; Mizuhata, Y.; Tokitoh, N.; Nishinaga, T.; Kato, T.; Yamago, S. Synthesis of Twisted [n]Cycloparaphenylene by Alkene Insertion. *Angew. Chem. Int. Ed.* **2023**, 62 (2), e202214960. https://doi.org/10.1002/anie.202214960.

(17) Hashimoto, S.; Kayahara, E.; Mizuhata, Y.; Tokitoh, N.; Takeuchi, K.; Ozawa, F.; Yamago, S. Synthesis and Physical Properties of Polyfluorinated Cycloparaphenylenes. *Org. Lett.* **2018**, 20 (18), 5973–5976. https://doi.org/10.1021/acs.orglett.8b02715.

(18) Brown, D. G.; Boström, J. Analysis of Past and Present Synthetic Methodologies on Medicinal Chemistry: Where Have All the New Reactions Gone? *J. Med. Chem.* **2016**, 59 (10), 4443–4458. https://doi.org/10.1021/acs.jmedchem.5b01409.

(19) Fernández, I.; Frenking, G.; Uggerud, E. Rate-Determining Factors in Nucleophilic Aromatic Substitution Reactions. *J. Org. Chem.* **2010**, 75 (9), 2971–2980. https://doi.org/10.1021/jo100195w.

(20) Meisenheimer, J. Ueber Reactionen aromatischer Nitrokörper. *Justus Liebigs Ann. Chem.* **1902**, 323 (2), 205–246. https://doi.org/10.1002/jlac.19023230205.

(21) Bartoli, G.; Todesco, P. E.; Ciminale, F.; Fiorentino, M. Electronic and Steric Effects in

Nucleophilic Aromatic Substitution. Kinetic Studies on the Reactions between Ethers and Thioethers of 2,4-Dinitrophenol and Nucleophiles. *J. Org. Chem.* **1975**, 40 (25), 3777–3778. https://doi.org/10.1021/jo00913a034.

(22) Rohrbach, S.; Smith, A. J.; Pang, J. H.; Poole, D. L.; Tuttle, T.; Chiba, S.; Murphy, J. A. Concerted Nucleophilic Aromatic Substitution Reactions. *Angew. Chem. Int. Ed.* **2019**, 58 (46), 16368–16388. https://doi.org/10.1002/anie.201902216.

(23) Terrier, F. Rate and Equilibrium Studies in Jackson-Meisenheimer Complexes. *Chem. Rev.* **1982**, 82 (2), 77–152. https://doi.org/10.1021/cr00048a001.

(24) Terrier, F.; Mokhtari, M.; Goumont, R.; Hallé, J.-C.; Buncel, E. High Brønsted Bnuc Values in SNAr Displacement. An Indicator of the SET Pathway? *Org. Biomol. Chem.* **2003**, 1 (10), 1757–1763. https://doi.org/10.1039/B301031G.

(25) Ong, D. Y.; Tejo, C.; Xu, K.; Hirao, H.; Chiba, S. Hydrodehalogenation of Haloarenes by a Sodium Hydride–Iodide Composite. *Angew. Chem. Int. Ed.* **2017**, 56 (7), 1840–1844. https://doi.org/10.1002/anie.201611495.

(26) Błaziak, K.; Danikiewicz, W.; Mąkosza, M. How Does Nucleophilic Aromatic Substitution Really Proceed in Nitroarenes? Computational Prediction and Experimental Verification. *J. Am. Chem. Soc.* **2016**, 138 (23), 7276–7281. https://doi.org/10.1021/jacs.5b13365.

(27) Błaziak, K.; Danikiewicz, W.; Mąkosza, M. How Do Aromatic Nitro Compounds React with Nucleophiles? Theoretical Description Using Aromaticity, Nucleophilicity and Electrophilicity Indices. *Molecules* **2020**, 25 (20), 4819. https://doi.org/10.3390/molecules25204819.

(28) Handel, H.; Pasquini, M. A.; Pierre, J. L. Effets de cryptands et activation de bases—VII. Tetrahedron 1980, 36 (22), 3205–3208. https://doi.org/10.1016/0040-4020(80)80166-9.

(29) Kwan, E. E.; Zeng, Y.; Besser, H. A.; Jacobsen, E. N. Concerted Nucleophilic Aromatic Substitutions. *Nat. Chem.* **2018**, 10 (9), 917–923. https://doi.org/10.1038/s41557-018-0079-7.

(30) Rohrbach, S.; Murphy, J. A.; Tuttle, T. Computational Study on the Boundary Between the

Concerted and Stepwise Mechanism of Bimolecular SNAr Reactions. *J. Am. Chem. Soc.* **2020**, 142 (35), 14871–14876. https://doi.org/10.1021/jacs.0c01975.

(31) Ong, W. J.; Swager, T. M. Dynamic Self-Correcting Nucleophilic Aromatic Substitution. *Nat. Chem.* **2018**, 10 (10), 1023–1030. https://doi.org/10.1038/s41557-018-0122-8.

(32) Clayton, T. D.; Fehr, J. M.; Price, T. W.; Zakharov, L. N.; Jasti, R. Pinwheel-like Curved Aromatics from the Cyclotrimerization of Strained Alkyne Cycloparaphenylenes. *J. Am. Chem. Soc.* **2024**, 146 (44), 30607–30614. https://doi.org/10.1021/jacs.4c12272.

(33) Fehr, J. M.; Myrthil, N.; Garrison, A. L.; Price, T. W.; Lopez, S. A.; Jasti, R. Experimental and Theoretical Elucidation of SPAAC Kinetics for Strained Alkyne-Containing Cycloparaphenylenes. *Chem. Sci.* **2023**, 14 (11), 2839–2848. https://doi.org/10.1039/D2SC06816H.

(34) Lovell, T. C.; Bolton, S. G.; Kenison, J. P.; Shangguan, J.; Otteson, C. E.; Civitci, F.; Nan, X.; Pluth, M. D.; Jasti, R. Subcellular Targeted Nanohoop for One- and Two-Photon Live Cell Imaging. *ACS Nano* **2021**, 15 (9), 15285–15293. https://doi.org/10.1021/acsnano.1c06070.

(35) St. Croix, C. M.; Shand, S. H.; Watkins, S. C. Confocal Microscopy: Comparisons, Applications, and Problems. *BioTechniques* **2005**, 39 (sup6), S2–S5. https://doi.org/10.2144/000112089.

(36) Luu, P.; Fraser, S. E.; Schneider, F. More than Double the Fun with Two-Photon Excitation Microscopy. *Commun. Biol.* **2024**, 7 (1), 364. https://doi.org/10.1038/s42003-024-06057-0.

(37) Kim, H. M.; Cho, B. R. Small-Molecule Two-Photon Probes for Bioimaging Applications. *Chem. Rev.* **2015**, 115 (11), 5014–5055. https://doi.org/10.1021/cr5004425.

(38) Kaiser, W.; Garrett, C. G. B. Two-Photon Excitation in Ca F 2 : Eu 2 +. *Phys. Rev. Lett.* **1961**, 7 (6), 229–231. https://doi.org/10.1103/PhysRevLett.7.229.

(39) Göppert-Mayer, M. Über Elementarakte mit zwei Quantensprüngen. *Ann. Phys.* **1931**, 401 (3), 273–294. https://doi.org/10.1002/andp.19314010303.

Chapter II: S_NAr Chemistry for Modular CPP Diversification and Host–Guest Tuning

2.1 Redox-Active Multi-Thianthrene-Containing Cycloparaphenylenes

2.1.1 Contributions

In collaboration with Dr. Tara Clayton (Jasti Lab) and Audrey Davenport (Brozek Lab) we explored the use of S_NAr to synthesize thianthrene modified CPPs for fullerene host systems. Dr. Tara Clayton led project design, synthesis, characterization, manuscript writing and editing. My contributions included synthesis, characterization, DFT computation and analysis, as well as manuscript writing and editing. Audrey Davenport performed the cyclic voltammetry experiments and analysis as well as manuscript writing and editing. Dr. Ramesh Jasti contributed to project design, manuscript editing and writing. Dr. Carl Brozek contributed to manuscript editing and CV analysis. All citations for this paper can be found at the end of section 2.1.

2.1.2 Abstract

Thianthrene is a widely used building block used in p-type organic semiconductors. The rich electrochemistry of thianthrene enables a switch between its characteristic nonplanar and planar forms, and its incorporation into macrocyclic systems can provide increased solubility and improved host–guest complexation. Cycloparaphenylenes (CPPs) are a relatively new class of nonplanar aromatic macrocycles whose stepwise synthesis enables precise control over their properties. In this work, we report high-yielding transformations of fluorinated CPPs into multi-thianthrene-containing strained macrocyclic nanocarbons. Single crystal X-ray diffraction of our dodeca-substituted CPP (**2**) reveals tub-shaped 5,7,12,14-tetrathiapentacene (TTP) units that curve around neighboring CPPs to form hexagonal crystals. Host–guest complexation with C_{60} shows increased binding constants upon TTP inclusion, with **2** strongly binding C_{60}, and cyclic voltammetry reveals that TTP incorporation lowers oxidation potentials. This efficient strategy for introducing functional heterocycles into CPPs expands the toolkit for designing strained, π-rich,

redox-active macrocycles with tunable supramolecular properties.

2.1.3 Introduction

[*n*]CPPs (*n* = the number of phenyl units) are a class of curved aromatic macrocycles that display size dependent optoelectronic properties that are unlike other small molecules or carbon nanomaterials.[1,2] First synthesized in 2008,[3] CPPs and their derivatives have garnered interest as bright and versatile chromophores,[4,5] participants in supramolecular and host–guest chemistry,[6] novel monomers,[7,8] organic ligands,[9–12] and components in organic electronics.[5,13,14] It is expected that future applications of CPP nanomaterials will continue to grow with advancements in derivatization, synthesis, and characterization.[15] New methods for CPP derivatization include nucleophilic aromatic substitution (S_NAr), first shown on CPPs in 2023 by Yamago et al. who reported late-stage functionalization of an alkene-inserted CPP with a pyrrole nucleophile.[16] This was followed by work done by Itami et al. also using pyrrole on highly fluorinated CPPs.[17] In 2023 Xiao et al., in collaboration with our group, demonstrated that sulfur and oxygen nucleophiles also work efficiently to derivatize fluorinated CPPs.[11]

Thianthrene and thianthrene-containing systems are versatile scaffolds with diverse applications in materials science and related fields. Thianthrenes continue to be explored in the development of functional polymers,[18–20] room-temperature phosphorescent materials,[21–24] participants in supramolecular chemistry,[25–28] and redox-active materials. Thianthrene has one of the highest redox potentials amongst organic cathode materials (4.1 V vs. Li+/Li, 0.84 V vs. Fc/Fc+ for the first half-wave oxidation) making it a promising candidate for high-potential organic electrodes.[19,29] Unlike the planar oxygen-containing analogue 1,4-dibenzodioxin, neutral thianthrene has a bent geometry of 128 degrees which planarizes to 180 degrees upon its first and second oxidation to the cation and dictation respectively (**Fig. 2.6a**).[30] This planarization and increase in aromaticity upon oxidation helps provide stability while also affording a redox-activated isomerization that can be harnessed for applications requiring conformational flexibility.

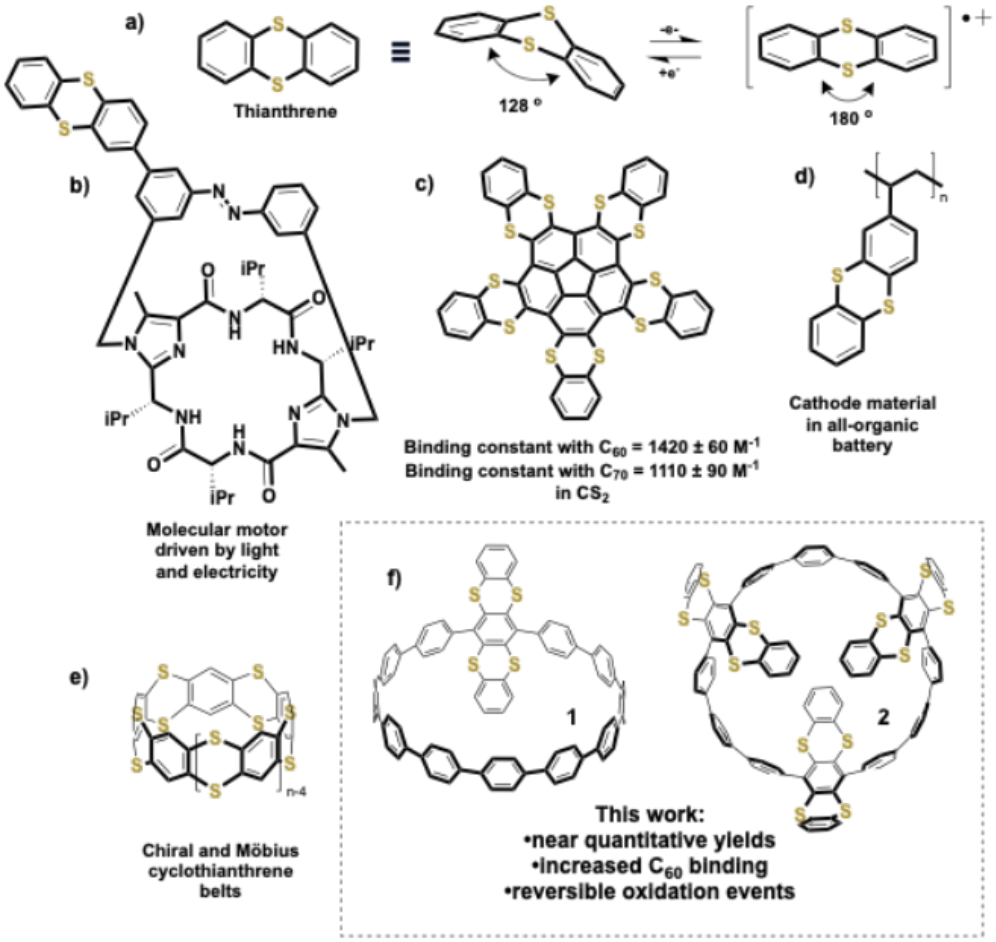

Figure 2.6: a) Oxidation-induced planarization of thianthrene. b-e) Representative examples of diversly functioned thianthrene-containing systems. f) multi-thianthrene-containing CPPs **1** and **2** synthesized in this work.

Representative applications of thianthrene span molecular motion, supramolecular chemistry, energy storage, and redox-active macrocycles (**Fig. 2.6b–e**). In molecular machines, thianthrene's redox-driven isomerization has been coupled with azobenzene photoisomerization to create the first electro- and photo-responsive motor.[31] Its bent geometry has also been leveraged with curved polyaromatics to enhance fullerene binding.[28] Beyond supramolecular systems, thianthrene-based polymers have been developed as cathode materials in all-organic batteries, providing stable cycling performance.[32] The curved morphology of thianthrene has further enabled the construction of sulfur-embedded hydrocarbon belts (cyclothianthrenes) that display quasi-reversible oxidations and potential for host–guest chemistry and porous materials.[32] Collectively, these examples underscore the versatility of the thianthrene motif and motivated our design of CPPs decorated with thianthrene units. Here, we report the first synthesis of redox-active TTP-containing CPPs 1 and 2 (**Fig. 2.6f**), analogues of [12]CPP with one or three TTP units, obtained in near-quantitative yields. This work positions thianthrene-decorated CPPs as a versatile platform for functional nanocarbon design.

2.1.4 Results and Discussion

The TTP units were incorporated into the CPP backbone via S_NAr of fluorinated CPPs **3** and **4** with 1,2-benzenedithiol (**Scheme 2.2**). This synthetic approach was inspired by Swager and coworkers, who demonstrated that ortho-aryldithiols and ortho-aryldifluorides efficiently undergo S_NAr to afford a series of molecules and polymer networks with multiple thianthrene moieties.[33] The fluorinated CPPs **3** and **4** used as electrophilic precursors to the TTP-containing CPPs were prepared via stepwise synthetic techniques previously reported by our lab.[15] Molecules **3** and **4** were dissolved in a 1:1 mixture of THF and DMF, treated with 1,2-benzenedithiol, heated to 120 degrees Celsius via microwave irradiation, and allowed to stir at this temperature for 24 hours. Upon completion, a basic aqueous workup to remove excess 1,2-benzenedithiol was performed followed by a short plug on basic alumina. Despite the synthetically taxing formation of 4 or 12 new bonds respectively, TTP-containing CPPs **1** and **2** were afforded in 96 and 91 percent isolated

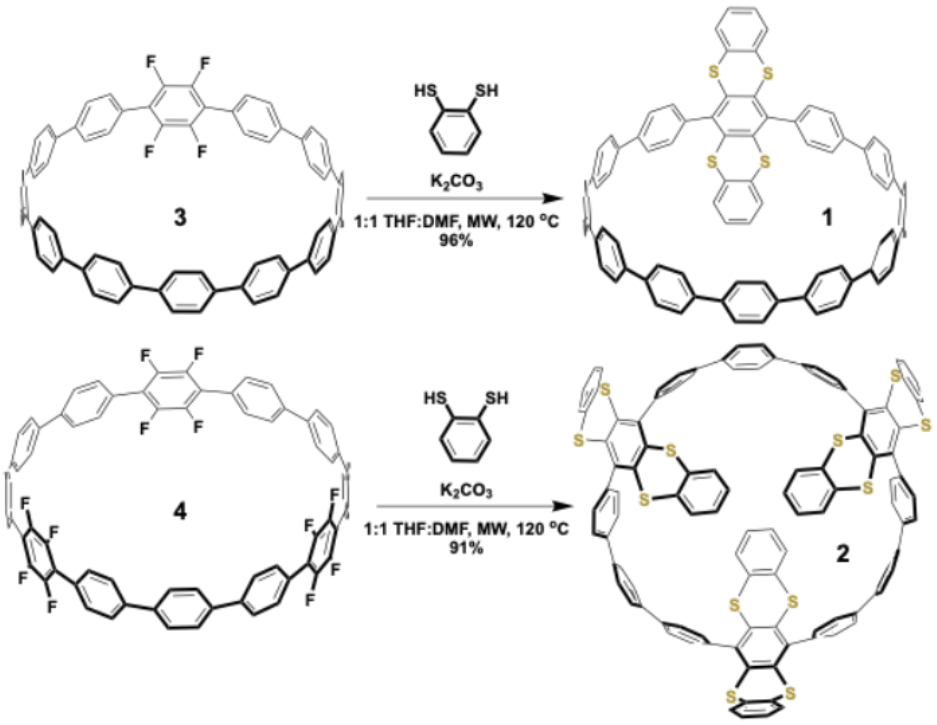

Scheme 2.2: Synthesis of multi-thianthrene-containing CPPs (**1** and **2**) from fluorinated CPP precursors (**3** and **4**) via nucleophilic aromatic substitution with 1,2-benzenedithiol.

yield. The efficiency of this transformation and the ease of isolation highlight the utility of S_NAr as a powerful and general method for derivatizing CPPs with functional heterocycles.

Compounds **1** and **2** were readily characterized by mass spectrometry and NMR spectroscopy. High resolution MALDI-TOF MS spectra displayed the expected parent-ion signals at m/z = 1188.30 for **1** and m/z = 1740.14 for **4**, confirming successful incorporation of TTP units. The ^{1}H NMR spectrum of **1** showed two characteristic upfield-shifted doublets of doublets at 7.06 and 6.95 ppm corresponding to the protons on the TTP unit. In contrast, the ^{1}H NMR spectrum of the highly functionalized macrocycle **2** was more complex, with overlapping resonances and reduced magnetic equivalence arising from the non-planarity of the TTP units; nevertheless, all expected proton signals were observed, consistent with the proposed structure. Single-crystal X-ray diffraction of compound **2** further confirmed its structure and connectivity (**Fig. 2.7**). Crystals of **2** were obtained via solvent layering of chloroform and pentane in an NMR tube. Although significant solvent disorder was present, two chloroform molecules could be resolved, and the remainder was treated by

SQUEEZE; one of the S_2C_6H groups (C91-C96) was also highly disordered and refined as an idealized C6 fragment. The X-ray data were sufficient to confirm the structure and hexagonal crystal packing motif. Notably, two of the three TTP units display the less commonly favored tub conformation, curving around neighboring CPP backbones, while the third adopts a chair conformation. The central benzene rings of the tub-shaped TTPs engage in slightly offset π–π interactions with unsubstituted benzene rings of adjacent CPPs at 3.4 Å, whereas the chair conformer exhibits a π–π distance of 3.7 Å. The dihedral angles between the TTP and adjacent CPP phenyl units are 61.6° (tub) and 54.0° (chair), compared to 23.3° in unfunctionalized [12]CPP. Out-of-plane bending angles are 118.8° for the tub conformers and 130.6° for the chair. The reduced angle of the tub form likely arises from favorable noncovalent interactions with neighboring CPPs. While compound **1** also crystallized, the crystals were unsuitable for single-crystal analysis. These structural insights demonstrate how TTP incorporation profoundly alters CPP conformation and directs solid-state packing.

We next examined the photophysical properties of **1** and **2** to assess the influence of thianthrene incorporation on the [12]CPP scaffold (**Fig. 2.8**). As with the fluorinated parent CPPs, absorbance and emission maxima were only modestly affected. Compound **1** exhibited a maximum absorption at 330 nm in dichloromethane (vs. 339 nm for [12]CPP) with a slightly reduced extinction coefficient (1.2×10^5 vs. 1.4×10^5 M^{-1} cm^{-1}) and nearly identical fluorescence, showing a maximum at 448 nm compared to 450 nm for [12]CPP. Compound **2** displayed a stronger perturbation, with an absorption maximum at 316 nm, an extinction coefficient of 1.2×10^5 $M^{-1}cm^{-1}$, and a fluorescence maximum at 428 nm in DCM. The hypsochromic shift of **2** likely arises from backbone distortion reducing effective conjugation. Solvatochromism was observed, with emission red-shifted to 448 nm in DMF but unchanged in toluene (**Fig. S7**). DFT analysis of the molecular orbitals suggests donor–acceptor behavior in **2**, wherein excitation involves electron transfer from the electron-rich thianthrene units to the more electron-deficient CPP backbone (**Fig. S14 and S15**). This interpretation is consistent with the slight solvatochromism, reduced brightness, and broadened fluorescence profile of **2**. Collectively, these results indicate that thianthrene incorporation minimally

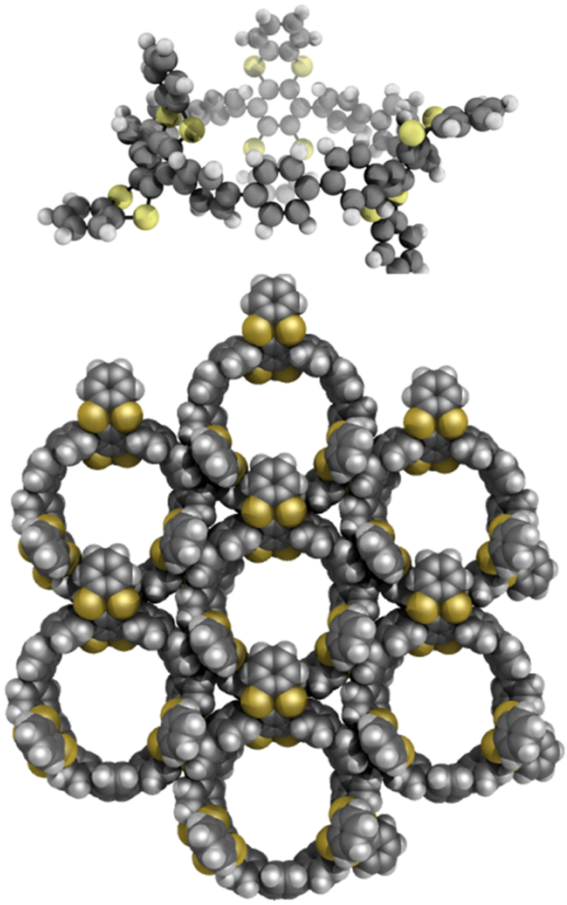

Figure 2.7: Single crystal X-ray diffraction of structure **2**.

perturbs the photophysics of CPPs while introducing tunable donor–acceptor character. We next investigated the effect of TTP incorporation on the host–guest properties of **1** and **2** with C_{60}. Fluorescence titration experiments in toluene revealed complete quenching of both compounds upon addition of C_{60}. Analysis with BindFit gave 1:1 binding constants of 7.3×10^4 M^{-1} (error 4.8%) for **1** and 1.0×10^5 M^{-1} (error 5.3%) for **2**, indicating that TTP incorporation enhances fullerene affinity relative to unsubstituted [12]CPPs (nonbinding). The increased binding strength of **2** highlights how thianthrene units provide an additional design element—beyond CPP size—for tuning host–guest interactions. These findings, combined with the redox-switchable isomerization of thianthrene, point toward the development of dynamic and responsive CPP–fullerene complexes with potential applications in sensing, separation, and molecular delivery.

Electrochemical properties of **1** and **2** were examined by cyclic voltammetry (CV) in a 1:4 mixture of acetonitrile and dichlorobenzene with 0.01 M $TBAPF_6$ at room temperature and a scan rate of 50 mV/s (**Fig. 2.9**). Higher concentrations of $TBAPF_6$ electrolyte led to diminished solubility of both **1** and **2**. Both compounds displayed reversible oxidations (**Fig. 2.9**), with half-wave oxidation potentials of 0.75 V vs Fc/Fc^+ for **1** and 0.70 V vs Fc/Fc^+ for **2**. In comparison, all-hydrocarbon [12]CPP oxidizes at 0.85 V vs Fc/Fc^+, indicating that TTP incorporation lowers the oxidation potential and facilitates electron removal. This effect likely arises from the stabilization of TTP cations through increased aromaticity upon oxidation.

Notably, the oxidation potentials of **1** and **2** are similar to those of smaller CPPs, [10]CPP (0.74 V) and [9]CPP (0.70 V), despite their larger ring size. Thus, incorporation of TTP units offers a complementary handle to CPP size for tuning redox properties. Given the characteristic redox-activated isomerization of thianthrene and the enhanced fullerene binding observed, these systems represent promising candidates for the design of redox-switchable host–guest complexes.

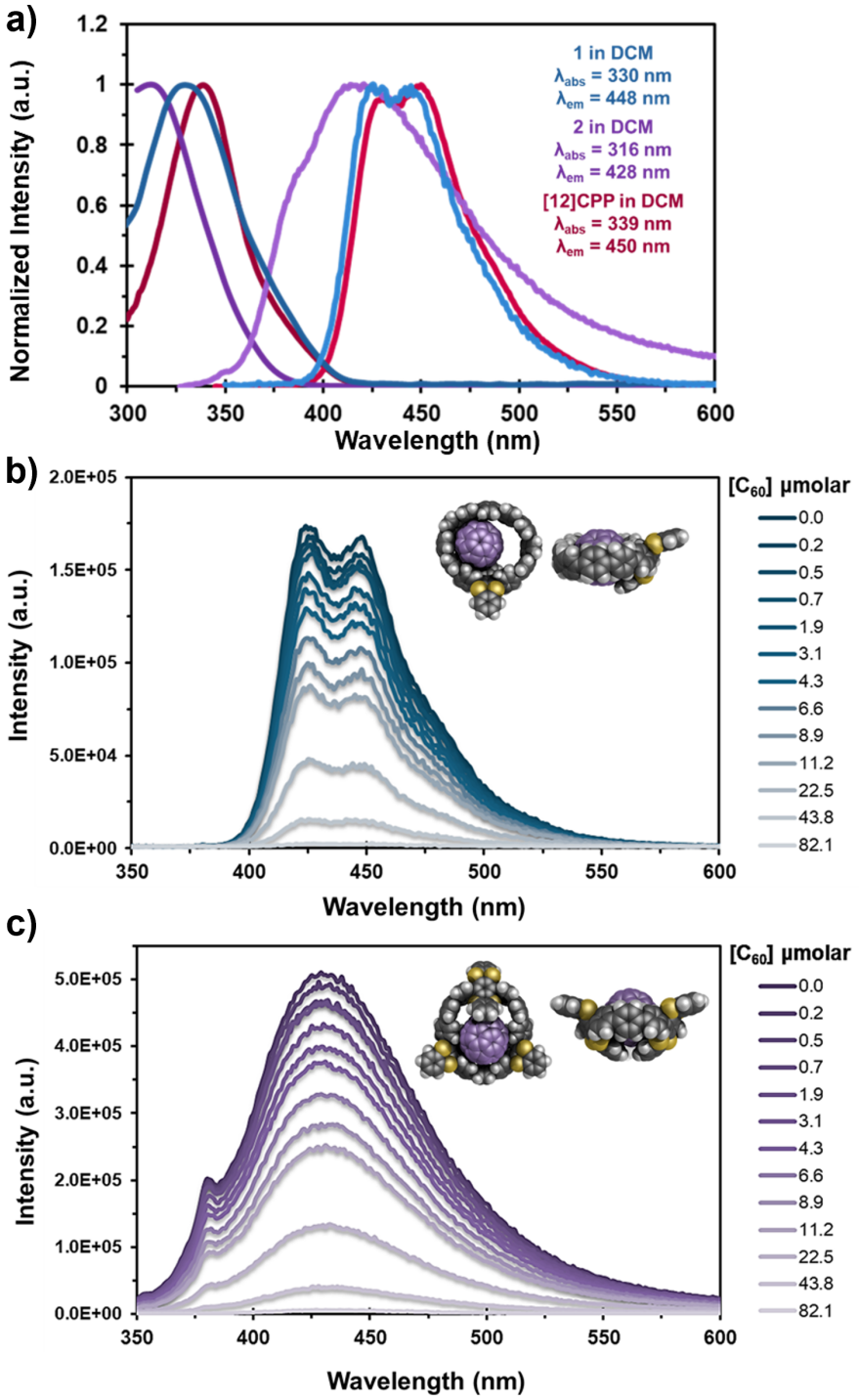

Figure 2.8: a) Normalized absorbance (solid lines) and emission (dashed lines) of 1, 2, and all-hydrocarbon [12]CPP in DCM. b) DFT space-filling model of **1** hosting C_{60} and fluorescence quenching upon increased addition of C_{60}. c) DFT space-filling model of **2** hosting C_{60} and fluorescence quenching upon increased addition of C_{60}.

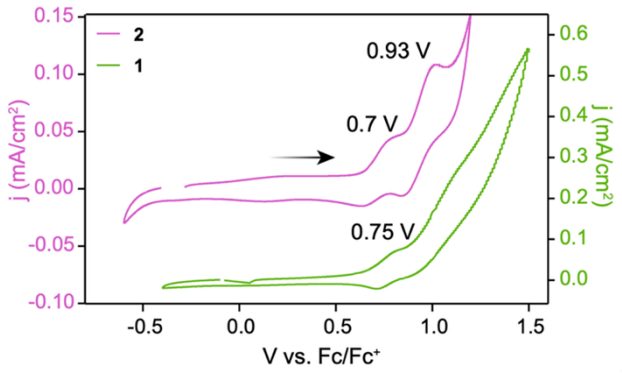

Figure 2.9: Cyclic voltammetry of colloidal suspensions of **1** (2 mM) and **2** (0.7 mM) in 0.01 M $TBAPF_6$ in a 1:4 mixture of acetonitrile and dichlorobenzene at 50 mV/s using a glassy carbon working electrode and a graphitic counter electrode. Scans were collected versus a Ag/Ag^+ pseudo reference electrode then referenced to the Fc/Fc^+ redox couple.

2.1.5 Conclusion

In summary, we have demonstrated that nucleophilic aromatic substitution of fluorinated CPPs with 1,2-benzenedithiol is a highly efficient derivatization that furnishes TTP-appended macrocycles. The resulting compounds show enhanced binding to C_{60}, altered solid-state packing, and lower oxidation potentials relative to all-hydrocarbon CPPs. Structures **1** and **2** were fully characterized by NMR spectroscopy, high-resolution mass spectrometry, and optical measurements, and the packing of **2** was elucidated by single-crystal X-ray diffraction. Both macrocycles are soluble in common organic solvents, underscoring their processability and potential utility in materials applications. Importantly, the availability of fluorinated CPP precursors on gram scale makes this strategy broadly practical, offering access to a diverse family of functional CPP derivatives that are typically difficult to obtain in large quantities. Importantly, the dynamic, self-correcting nature of the S_NAr reaction[34] paired with its high efficiency suggests that this chemistry could be extended toward polymers and covalent organic frameworks. More broadly, the thianthrene motif imparts switchable motion, nonplanar geometry, electron donation, and reactive handles for further derivatization, positioning TTP-CPPs as versatile platforms for building π-rich, adaptive, and functional nanomaterials.

2.1.6 Experimental Appendix: Supplementary Information

Unless otherwise noted, commercially available materials were used without purification. Compounds **3** and **4** were prepared according to the literature.[35–38] Moisture and oxygen sensitive reactions were carried out in flame-dried glassware and under an inert atmosphere of purified nitrogen using syringe/septa technique. Tetrahydrofuran (THF) and dimethylformamide (DMF) were dried by filtration through alumina according to the methods described by Grubbs.[39] Alumina column chromatography was conducted with SorbTech basic alumina (pH 10), Act. II-III, 50-200 μm. ^{1}H and ^{13}C NMR spectra were recorded on a Bruker Avance III HD 500 (^{1}H: 500 MHz, ^{13}C: 126 MHz) NMR spectrometer. The chemical shifts (δ) were reported in parts per million (ppm) and were referenced to the residual protio-solvent (CD_2Cl_2, ^{1}H: δ = 5.32 ppm and ^{13}C: δ = 53.84 ppm; deuterated 1,1,2,2-tetrachloroethane (TCE-d_2), ^{1}H: δ = 6.00 ppm and ^{13}C: δ = 73.78 ppm) or to tetramethylsilane (for $CDCl_3$, TMS, δ = 0.00 ppm). Coupling constants (J) are given in Hz and the apparent resonance multiplicity is reported as s (singlet), d (doublet), t (triplet), q (quartet), dd (doublet of doublets) or m (multiplet). UV/Vis absorption and fluorescence spectra were recorded on an Agilant Cary 100 spectrophotometer and a Horiba Jobin Yvon Fluoromax-4 Fluorimeter, respectively. All measurements were carried out under ambient conditions in a Spectrocell RF-1010-T threaded top vacuum formed borosilicate fluorometer cell (10 mm light path). Supplementary raw data files available via Figshare: https://figshare.com/account/articles/31259227.

I. Synthesis

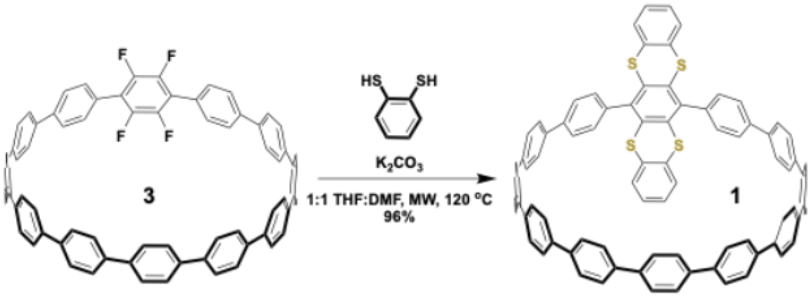

Compound 1: 3 (16.4 mg, 0.017 mmol, 1 eq), 1,2-Benzenedithiol (0.019 mL, 0.166 mmol, 10 eq), and K_2CO_3 (13.8 mg, 0.01 mmol, 6 eq) were added to a microwave flask and dissolved in THF

(0.55 mL, 0.03 M) and DMF (0.55 mL, 0.03 M). The reaction mixture was heated with microwave to 120 °C and allowed stir for 24 hrs. It was then cooled to room temperature and diluted with DCM and water. A 1M aqueous solution of K_2CO_3 was added until the solution was basic, and the product was extracted with DCM (4 X 50 mL), washed with water (2 X 50 mL), washed with brine (2 X 50 mL), dried over sodium sulfate, filtered, and concentrated. Finally, the material was rinsed with methanol and dried to afford the product as an off-white powder (19 mg) in 96% yield. ^{1}H NMR (500 MHz, Methylene Chloride-d_2) δ 7.77 – 7.63 (m, 40H), 7.26 (d, J = 8.2 Hz, 4H), 7.06 (dd, J = 5.8, 3.4 Hz, 4H), 6.95 (dd, J = 5.8, 3.4 Hz, 4H). ^{13}C NMR (126 MHz, CD_2Cl_2) δ 141.05, 140.05, 139.23, 138.59, 138.56, 138.54, 138.52, 138.49, 138.45, 138.38, 137.49, 135.79, 135.54, 130.99, 128.36, 127.98, 127.60, 127.42, 127.36, 127.34, 127.29, 127.27, 127.12.

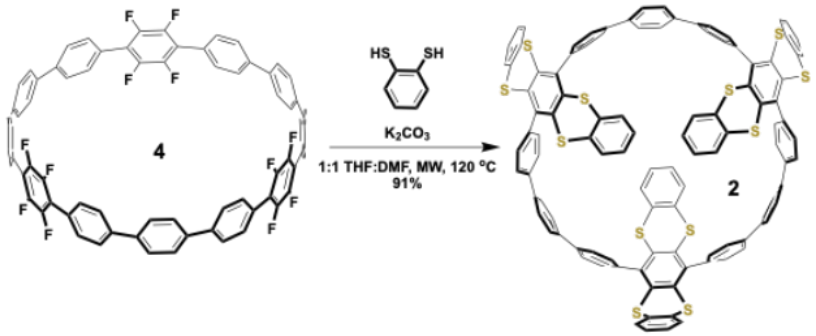

Compound 2: 4 (9.3 mg, 0.008 mmol, 1 eq), 1,2-Benzenedithiol (0.008 mL, 0.066 mmol, 8 eq), and K_2CO_3 (20 mg, 0.148 mmol, 18 eq) were added to a microwave flask and dissolved in THF (0.55 mL, 0.015 M) and DMF (0.55 mL, 0.015 M). The reaction mixture was heated with microwave to 120 °C and allowed stir for 24 hrs. It was then cooled to room temperature and diluted with DCM and water. A 1M aqueous solution of K_2CO_3 was added until the solution was basic, and the product was extracted with DCM (4 X 50 mL), washed with water (2 X 50 mL), washed with brine (2 X 50 mL), dried over sodium sulfate, filtered, and adsorbed onto basic alumina. An alumina plug eluted with DCM in hexanes (0-100%) afforded the product as an off-white powder (13 mg) in 91% yield. ^{1}H NMR (500 MHz, Methylene Chloride-d_2) δ 7.78 – 7.57 (m, 24H), 7.53 (s, 4H), 7.41 (dd, J = 21.4, 7.3 Hz, 6H), 7.29 (dd, J = 25.7, 8.2 Hz, 12H), 7.16 (dd, J = 5.7, 3.4 Hz, 2H), 7.13 – 7.06 (m, 6H), 6.97 (dd, J = 13.2, 5.7 Hz, 6H). ^{13}C NMR (126 MHz, CD_2Cl_2) δ 141.01, 140.11,

139.66, 136.40, 135.93, 135.83, 135.75, 135.64, 131.74, 131.48, 129.13, 128.67, 128.49, 128.30, 127.79, 127.22, 127.06, 126.88.

II. Structural Characterization

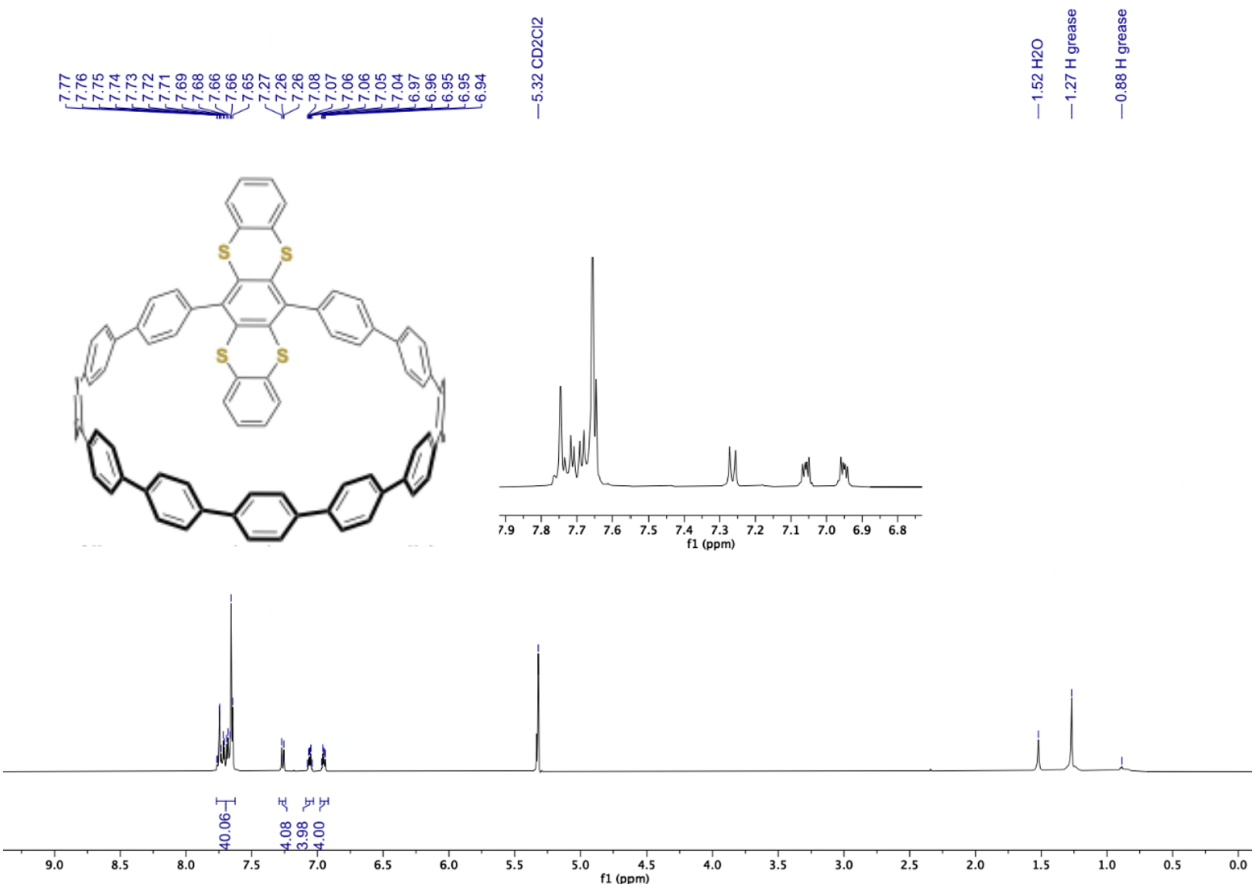

Figure S1. ^{1}H NMR Spectrum of **1**.

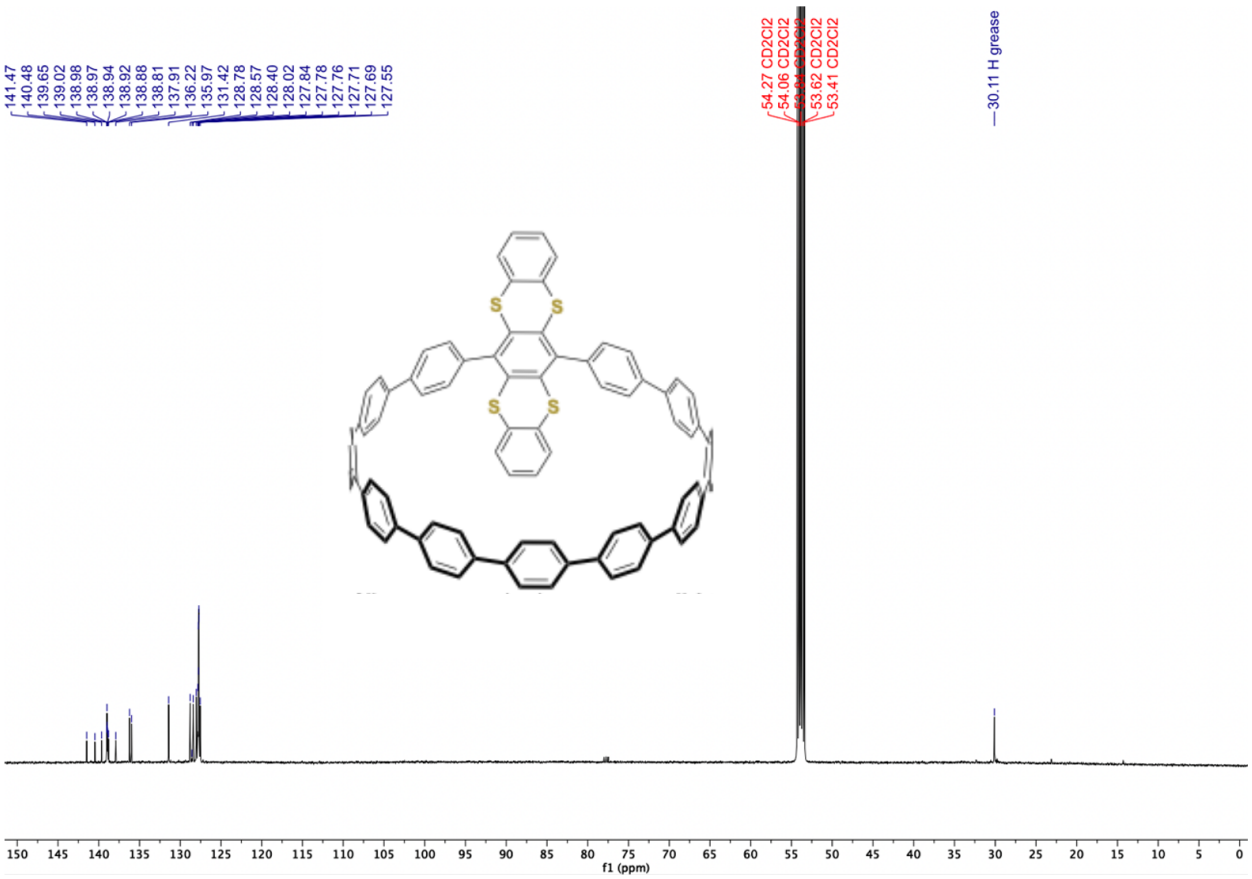

Figure S2. ^{13}C NMR Spectrum of **1**.

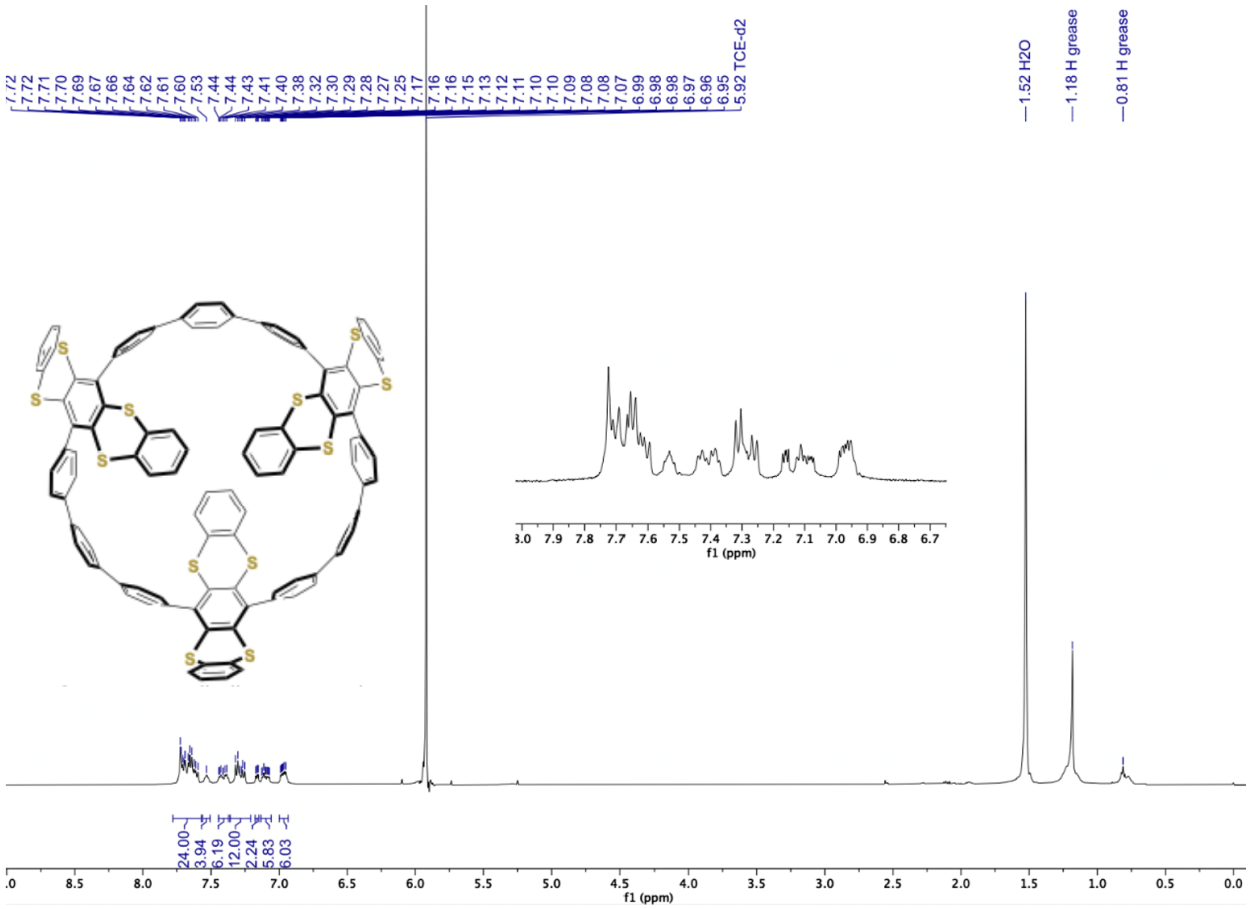

Figure S3. ^{1}H NMR Spectrum of **2**.

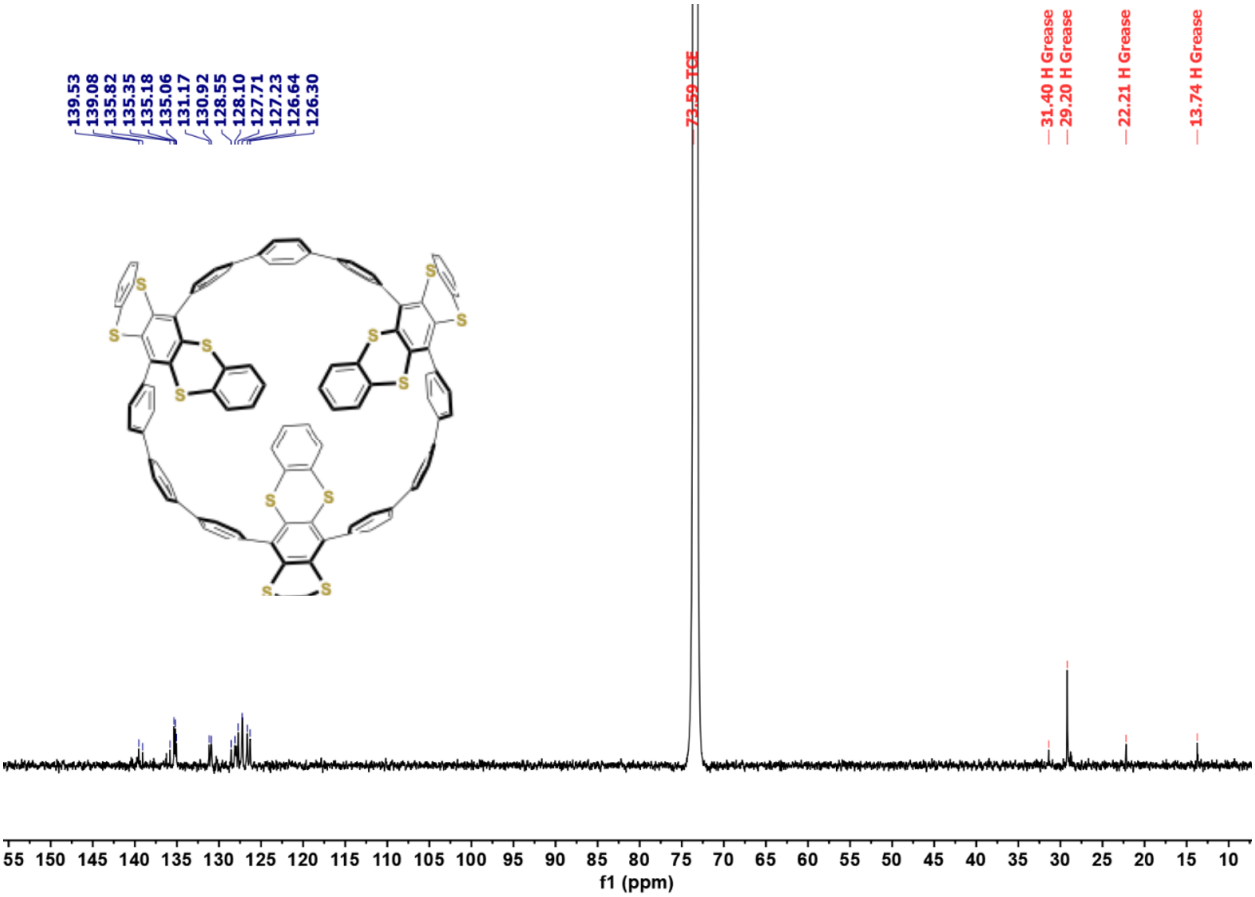

Figure S4. ^{13}C NMR Spectrum of **2**.

X-ray Crystallography. Diffraction intensities for 2 were collected at 173 K on a Bruker Apex2 single crystal diffractometer using CuKa radiation, 1.54178 Å. Space group was determined based on systematic absences. Absorption correction was applied by *SADABS*. Structure was solved by direct methods and Fourier techniques and refined on F2 using full matrix least-squares procedures. All non-H atoms were refined with anisotropic thermal parameters. H atoms in the structure were refined in calculated positions in a rigid group model. The diffraction data at high angles are very weak due to a strong disorder of solvent molecules. They were collected only up to resolution 1.01 Å even by using a strong *Incoatec* Cu-source. However, it provides the appropriate ratio of the number of the measured reflections per the number of the refined parameters, 12202/1142. Two $CHCl_3$ solvent molecules located outside the hoop were found from the XRD data and refined. Others solvent molecules located inside the hoop are highly disordered and were treated by *SQUEEZE*.

Solvent molecules treated by *SQUEEZE* were not included in the total formula of the compound given in the CIF file. The structure was determined in a non-centrosymmetrical space group as a racemic twin: the Flack is 0.12(3). One of the $S_2C_6H_4$ groups is highly disordered. Atomic thermal parameters in this group are elongated, and this group was refined as a C6-group with the ideal geometry. The RIGU option was used in the structure refinement. The structure is determined with a low resolution. However, the X-ray structure provides the clear chemical results. All calculations were performed by the *Bruker SHELXL-2014/7 package*. Crystallographic Data for Jastirr212: $C_{110}H_{62}Cl_6S_{12}$, M = 1981.01, 0.15 x 0.14 x 0.08 mm, T = 173(2) K, Hexagonal, space group P65, a = 19.6392(4) Å, b = 19.6392(4) Å, c = 53.6698(19) Å, α = 90°, β = 90°, γ = 120.0°, V = 17927.0(10) $Å^3$, Z = 6, Dc = 1.101 Mg/m^3, μ(Cu) = 3.582 mm-1, F(000) = 6096, 2θmax = 100.134°, 87596 reflections, 12202 independent reflections [Rint = 0.1647], R1 = 0.0717, wR2 = 0.1832 and GOF = 1.028 for 12202 reflections (1142 parameters) with I>2σ(I), R1 = 0.1057, wR2 = 0.2059 and GOF = 1.001 for all reflections, the Flack = 0.12(3), max/min residual electron density +0.268/-0.293 $eÅ^{-3}$.

III. Optoelectronic Properties

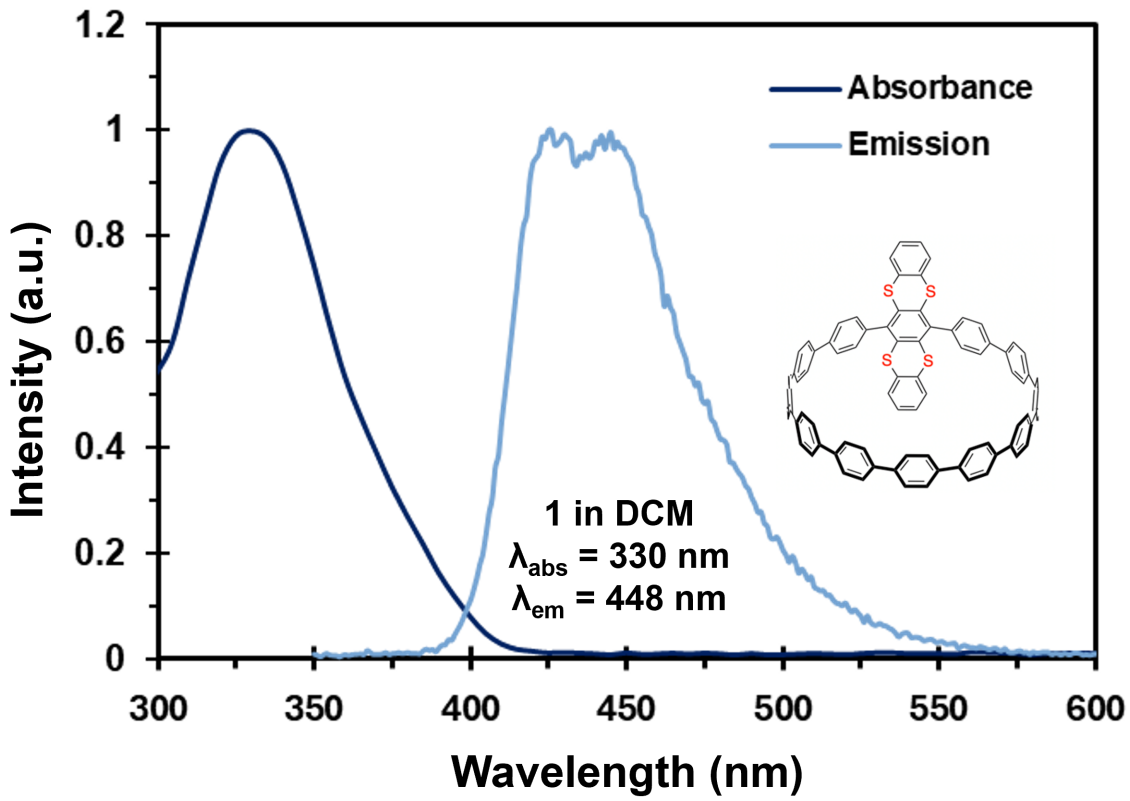

Figure S5. Scaled absorbance (solid) and fluorescence (dotted) of **1** in dichloromethane with λ_{max} at 330 nm and λ_{em} at 425, 448 nm.

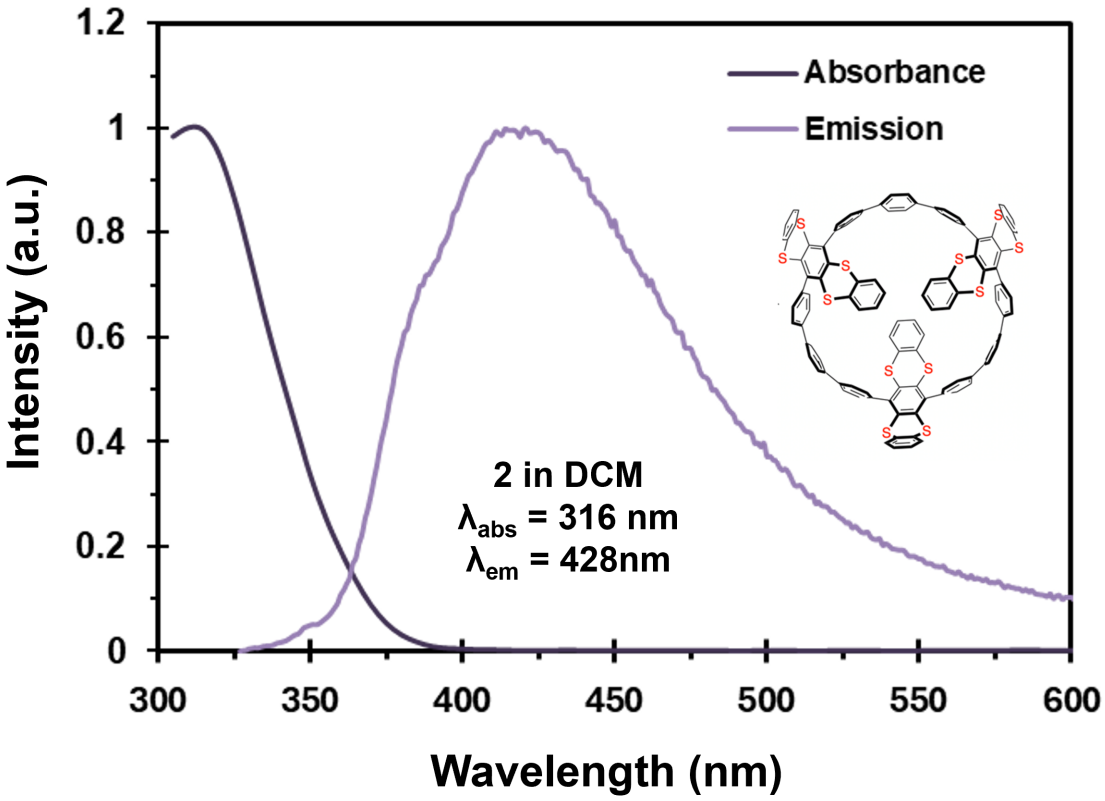

Figure S6. Scaled absorbance (solid) and fluorescence (dotted) of **2** in dichloromethane with λ_{max} at 315 nm and λ_{em} at 421 nm.

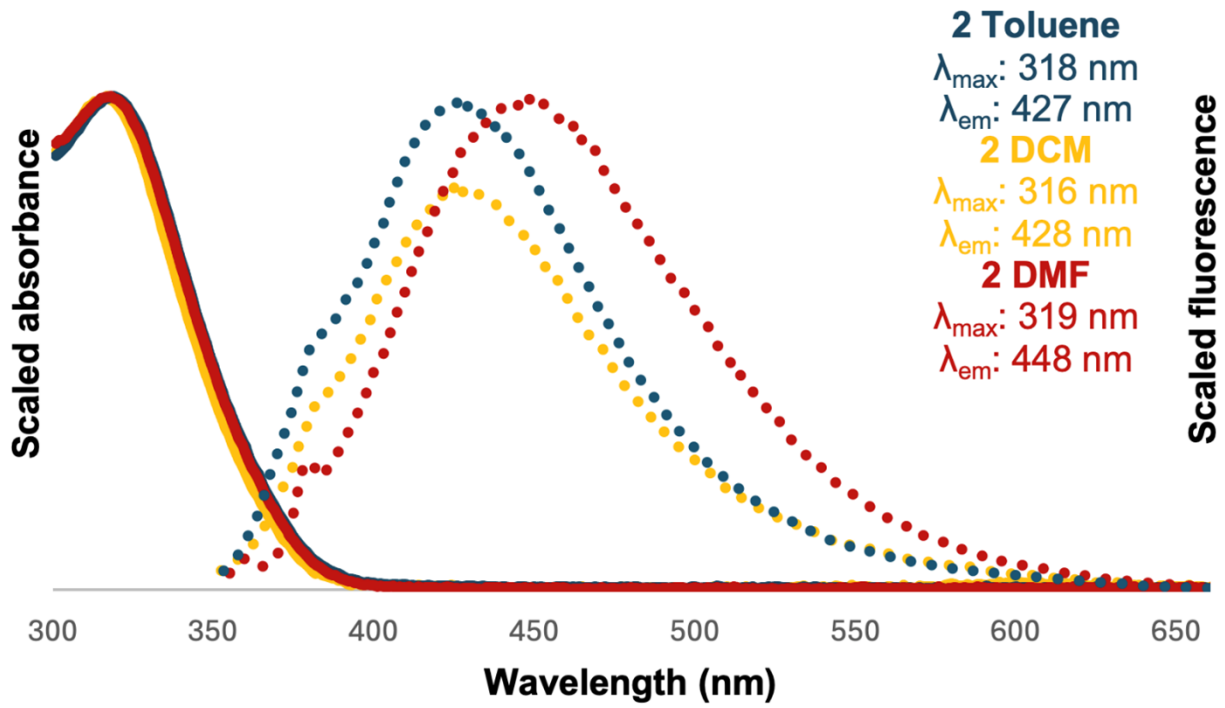

Figure S7. Scaled absorbance (solid) and fluorescence (dotted) of **2** in various solvents excited at 340 nm to study the solvatochromic properties of structure **2**.

Molar Absorptivity For extinction coefficient measurements, **1** and **2** were dissolved at known concentrations in dichloromethane. Solutions of **1** and **2** were then added incrementally to a cuvette containing a known amount of dichloromethane and absorbance measurements were taken after each addition. The whole process was repeated three times for **1** and **2** respectively. Data was worked up by dividing the absorbance value at the absorbance maxima by the solution's concentration. Measurements from each trial were averaged together, and the standard deviation between trials was determined.

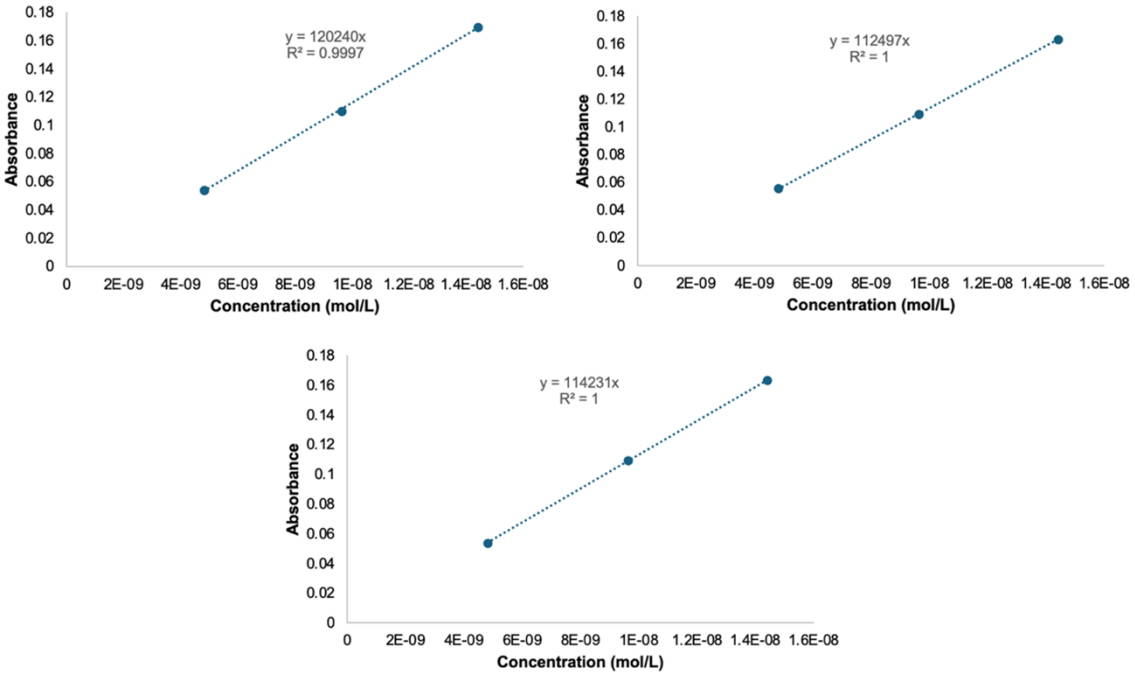

Figure S8. Absorbance versus concentration for extinction coefficient determination of **1** in DCM at the absorbance maximum.

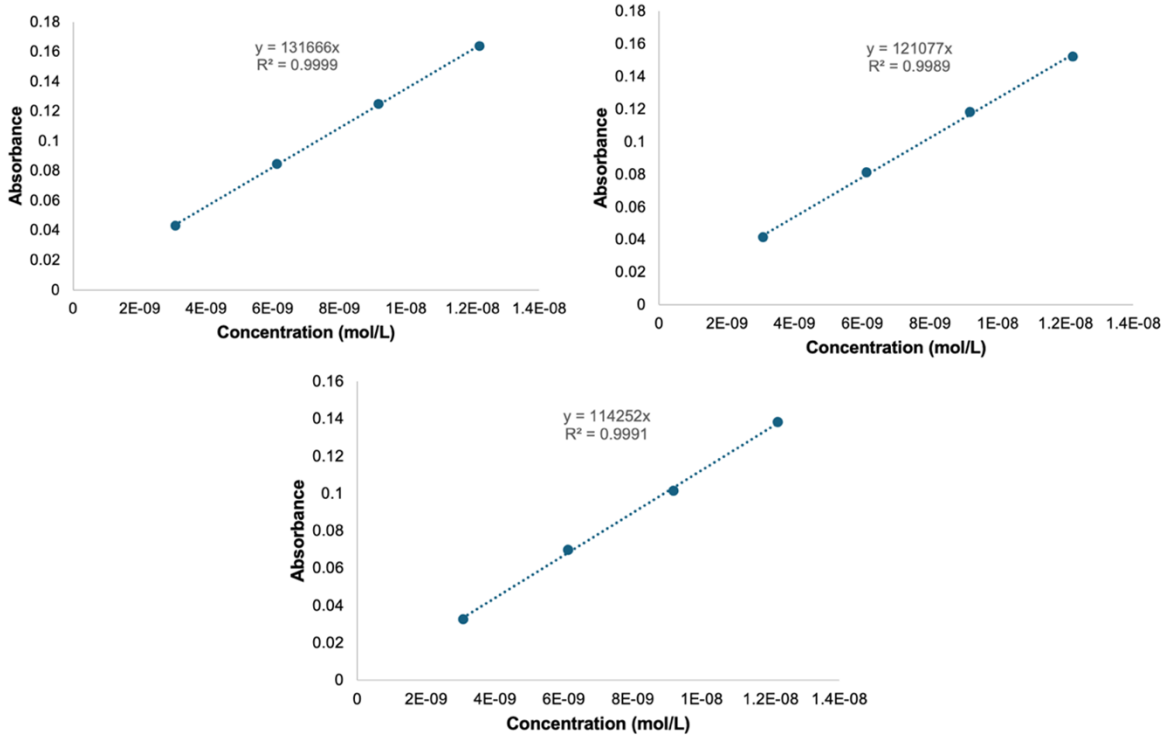

Figure S9. Absorbance versus concentration for extinction coefficient determination of **2** in DCM at the absorbance maximum.

Quantum Yield Quantum yield measurements were performed according to literature procedures.[40,41] Anthracene and quinine were used as standards and found to be within 10% error from their literature values following established procedures. Parent CPPs (1p and 2p) and Compounds **1** and **2** were all run in CH_2Cl_2. Given the donor-acceptor nature of the thianthrene modified compounds, we see an expected decrease in the QY values. QY values were calculated according to this equation:

$$\varphi_x = \varphi_{ST}\left(\frac{Grad_x}{Grad_{ST}}\right)\left(\frac{\eta_x^2}{\eta_{ST}^2}\right)$$

Where ST = standard and x = test solution, Φ is the fluorescent quantum yield, Grad is the gradient from the plot of the integrated fluorescence intensity vs absorbance, and η is the refractive index of the solvent.

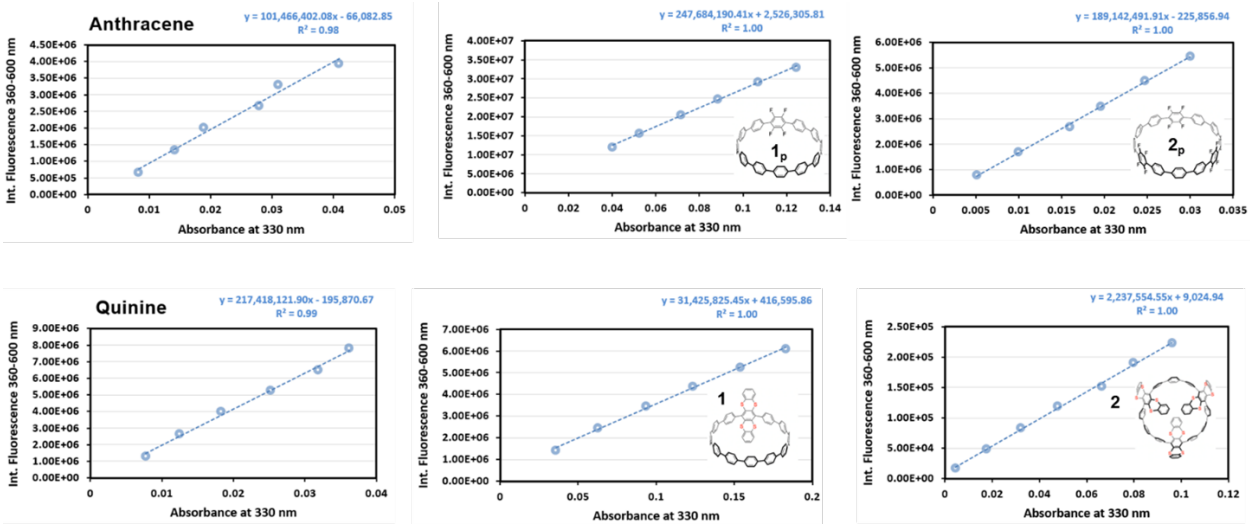

	Lit Val.	n	n^2	Slope	Slope Div	n^2 Div	QY	% error
Quinine	0.54	1.33	1.78	2.17E+08	2.1E+00	9.6E-01	0.55	2.6
Anthracene	0.27	1.36	1.85	1.01E+08	4.7E-01	1.0E+00	0.26	-2.7
1p	w.r.tq	1.42	2.03	2.48E+08	1.1E+00	1.1E+00	0.70	
1p	w.r.ta	1.42	2.03	2.48E+08	2.4E+00	1.1E+00	0.72	
1	w.r.tq	1.42	2.03	3.14E+07	1.4E-01	1.1E+00	0.09	
1	w.r.ta	1.42	2.03	3.14E+07	3.1E-01	1.1E+00	0.09	
2p	w.r.tq	1.42	2.03	1.89E+08	8.7E-01	1.1E+00	0.54	
2p	w.r.ta	1.42	2.03	1.89E+08	1.9E+00	1.1E+00	0.55	
2	w.r.tq	1.42	2.03	2.24E+06	1.0E-02	1.1E+00	0.01	
2	w.r.ta	1.42	2.03	2.24E+06	2.2E-02	1.1E+00	0.01	

Figure S10. Gradients of integrated fluorescent in DCM for quantum yield determination of compounds **1** and **2** (QY = 1% and 9% respectively).

IV. Host-Guest Binding with C_{60} Fluorescence titration experiments were used to determine the association constant (K) between the CPP host (H) **1** and **2** and $\mathbf{C_{60}}$ guest (G). Stock solutions of **1**, **2**, and $\mathbf{C_{60}}$ were made in toluene at room temperature. Varying concentrations of the $\mathbf{C_{60}}$ solution were added to a known concentration of the CPP solution until fluorescence was quenched. All samples were excited at 340 nm. Emission spectra were collected from 345 nm - 800 nm and the fluorescence signal was measured at 426 nm, 448 nm, and 474 nm for **1** and 381 nm, 429 nm, and 450 nm for **2**. Open-source software BindFit was used to fit the data with the Nelder-Mead method.[42] The association constants were derived by applying a non-linear 1:1 and 2:1 binding model.

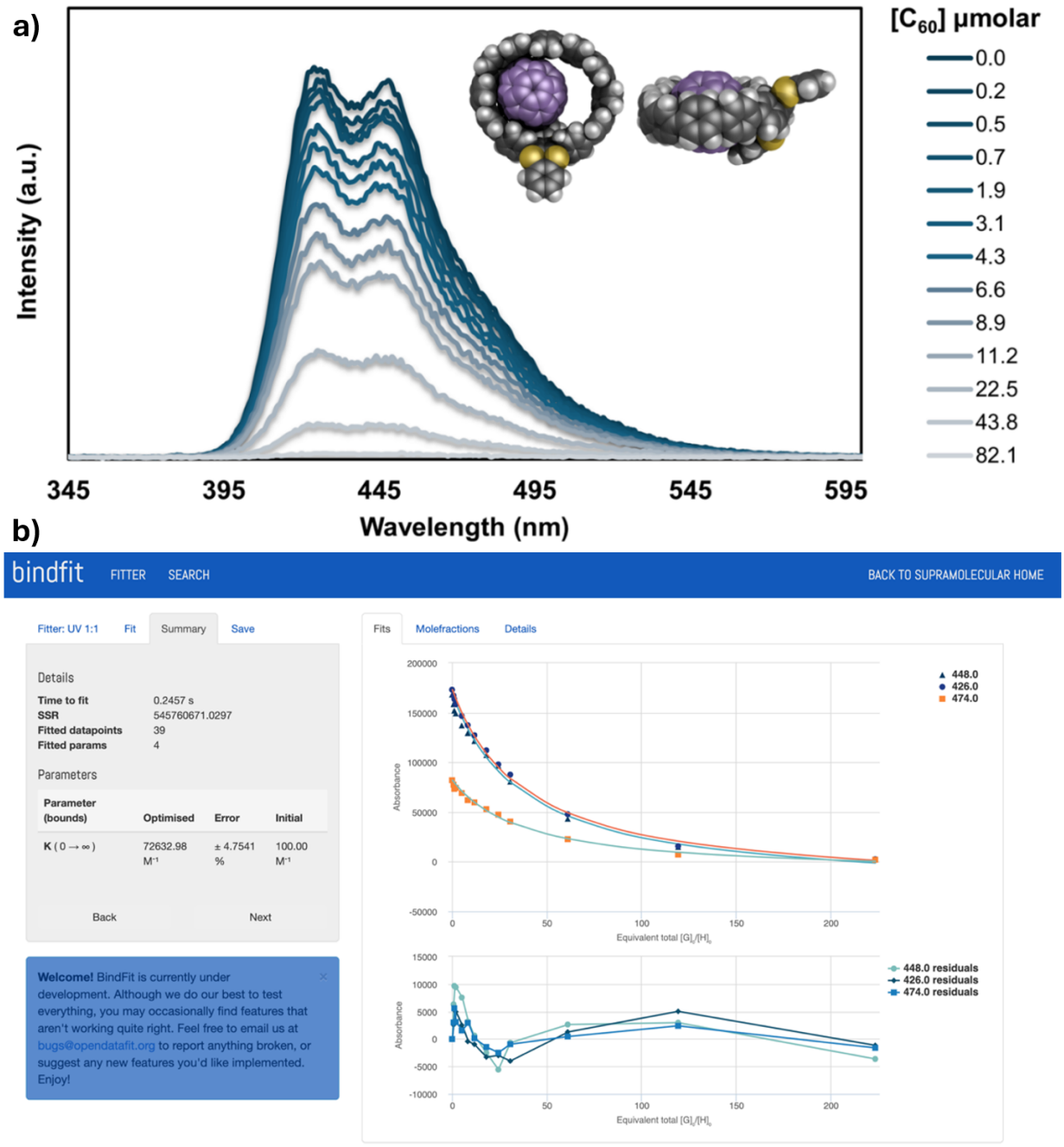

Figure S11. (a) Fluorescence quenching experiment of **1** with increasing amounts of C_{60} guest. (b) Bindfit model demonstrating 1:1 host–guest complexation and binding $K_a = 7.26 \times 10^4\ M^{-1}$.

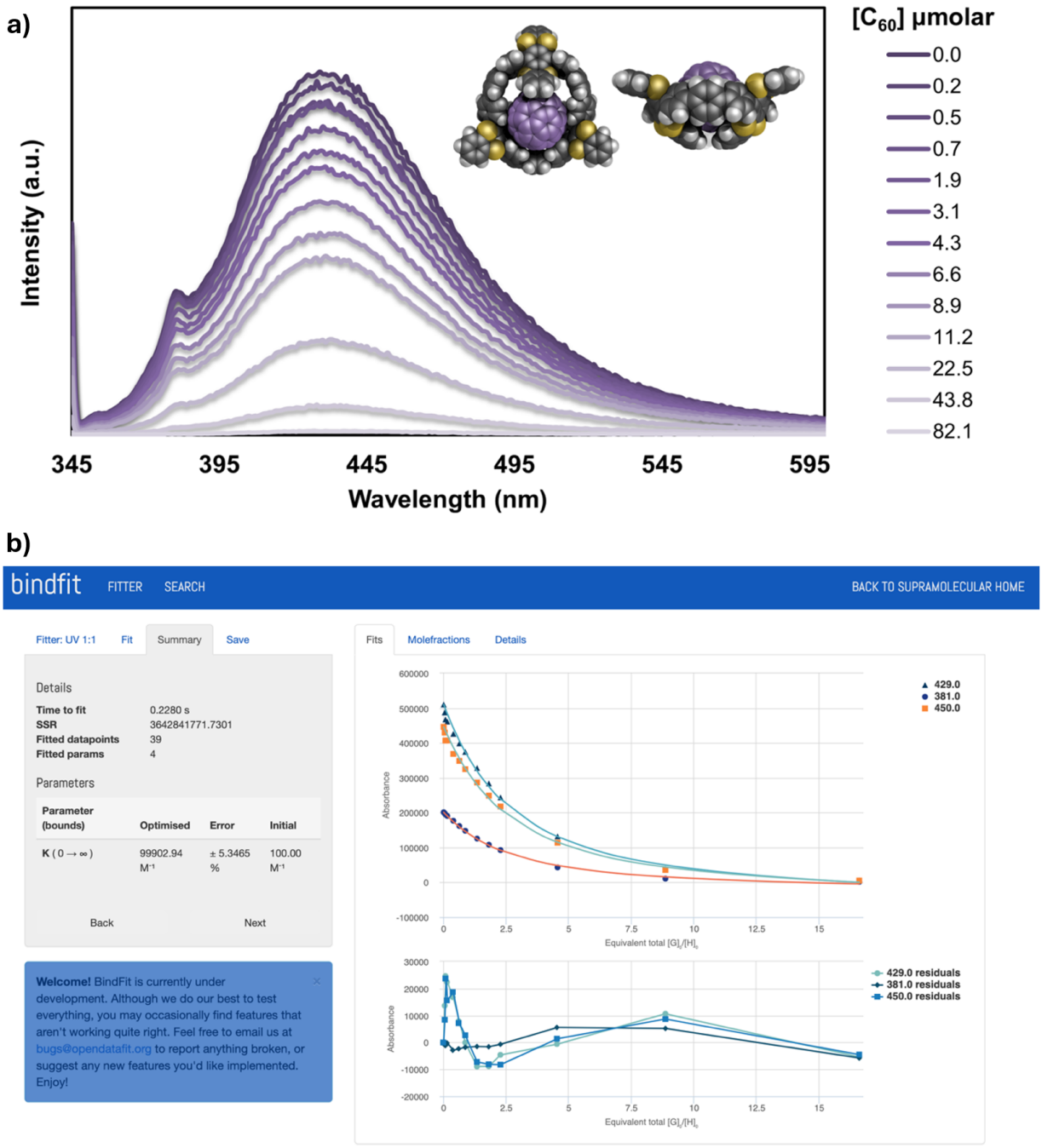

Figure S12. (a) Fluorescence quenching experiment of **2** with increasing amounts of C_{60} guest. (b) Bindfit model demonstrating 1:1 host-guest complexation and binding $K_a = 9.99 \times 10^4\ M^{-1}$.

V. Electrochemical Details Solutions of **1** and **2** were solubilized separately with $TBAPF_6$ in 1:4 mixtures of acetonitrile:dichlorobenzene to afford 2 mM and 0.7 mM of the compounds, re-

spectively. Cyclic voltammetry scans were collected at a scan rate of 50 mV/s. A graphitic counter electrode and a Ag/Ag^+ pseudo reference electrode were used. Data was all referenced to the Fc/Fc^+ redox couple in the same solvent mixture. Mixtures were sparged with N_2 for 5 minutes prior to data collection.

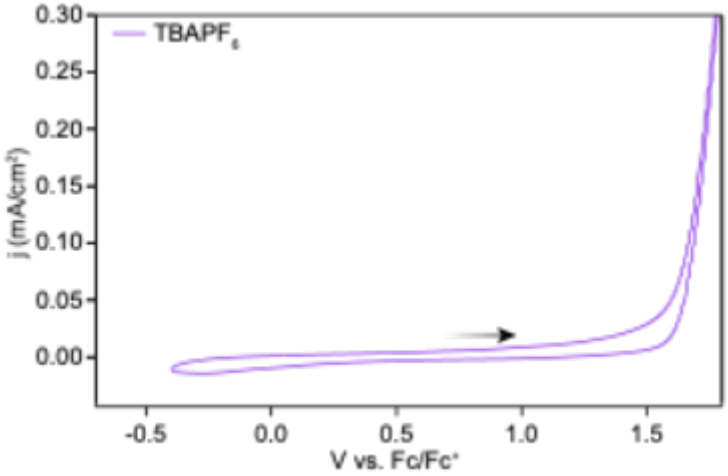

Figure S13. Cyclic voltammetry scan of $TBAPF_6$ in 1:4 mixture of acetonitrile:dichlorobenzene without compounds **1** and **2**. Referenced to the Fc/Fc^+ redox couple.

VI. Computational Analysis Gaussian 09[43] was used for structural geometry minimization, optical vertical transitions, and frequency calculations. All input files are available for download via Figshare at https://figshare.com/account/articles/31259227?file=61649173.

Keywords –

a) Geometry Optimization

B3LYP/6-31G (d,p) Opt Freq

b) Vertical Transitions

B3LYP/6-31G(d,p) TD=NSTATES=12 scrf=(solvent=dichloromethane)

CAM-B3LYP/6-31G(d,p) Opt TD scrf=(solvent=dichloromethane)

Vertical transitions were determined using the time-dependent DFT method to probe excited states when exposed to an external field. Optical absorption spectra were observed for 12 states, and emission spectra were found by optimizing the time-dependent excited states. A polarizable continuum

model (PCM) was used to better match experimental solvent conditions ran in dichloromethane. Major transitions include degenerate HOMO orbitals to LUMO unoccupied states; similar to parent CPP systems.[44] However, substitution introduces orbital localization on the TTP unit stabilizing occupied orbitals and leads to a hypsochromic shifts the typical CPP 340 nm absorption.

Compound 1 No.	Energy (cm-1)	Wavelength (nm)	Osc. Strength	Symmetry	Major Contributions
1	26474.34258	377.7242049	0.3397	Singlet-A	H-1->L+1 (12%), HOMO->LUMO (83%)
2	28127.77916	355.520425	2.3988	Singlet-A	H-1->LUMO (44%), HOMO->L+1 (48%)
3	29592.482	337.9236659	0.0078	Singlet-A	H-1->LUMO (51%), HOMO->L+1 (45%)
4	29978.82157	333.5688154	0.8715	Singlet-A	H-1->L+1 (62%), HOMO->L+2 (13%)
5	30803.1202	324.6424367	0.5565	Singlet-A	H-1->L+1 (16%), HOMO->L+2 (64%)
6	30954.75243	323.0521718	0.0147	Singlet-A	H-3->LUMO (44%), H-3->L+2 (15%), H-2->LUMO (13%)
7	31198.33187	320.5299579	0.0081	Singlet-A	H-3->L+1 (22%), H-3->L+3 (38%), H-2->L+3 (12%)
8	31294.31185	319.5468892	0.0912	Singlet-A	H-3->LUMO (21%), H-2->LUMO (53%), HOMO->L+2 (16%)
9	31980.68966	312.6886914	0.0063	Singlet-A	H-1->L+2 (13%), HOMO->L+3 (71%)
10	32057.31234	311.9413098	0.0078	Singlet-A	H-1->L+2 (77%)
11	32418.64872	308.46443	0.151	Singlet-A	H-3->L+1 (12%), H-2->L+1 (65%), HOMO->L+3 (11%)
12	32423.48805	308.4183906	0.0006	Singlet-A	H-3->L+1 (52%), H-3->L+3 (21%)

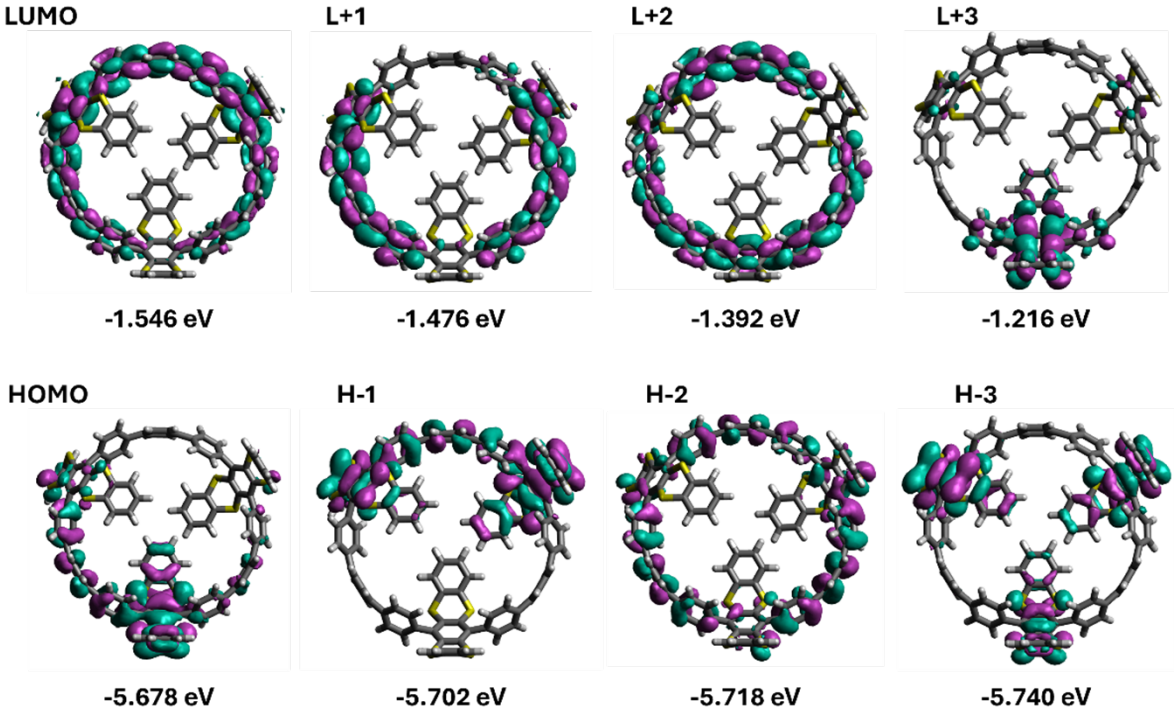

Figure S14. Calculated orbital localization (top) LUMO and (bottom) HOMO for single substitution of tetrathiapentacene on [12]CPP.

Compound 2 No.	Energy (cm-1)	Wavelength (nm)	Osc. Strength	Symmetry	Major Contributions
1	29151.3	343	0.1798	Singlet-A	H-1->LUMO (36%), H-1->L+1 (14%)
2	29296.5	341	0.1835	Singlet-A	H-3->LUMO (27%), H-1->LUMO (12%), HOMO->LUMO (11%)
3	29387.6	340	0.0479	Singlet-A	H-2->LUMO (48%), HOMO->L+1 (13%)
4	30123.2	332	0.8993	Singlet-A	H-2->L+1 (17%), HOMO->LUMO (27%), HOMO->L+2 (18%)
5	30199.8	331	0.1445	Singlet-A	H-3->L+3 (14%), HOMO->L+3 (57%)
6	30453.1	328	0.0035	Singlet-A	H-3->L+5 (24%), H-1->L+5 (47%)
7	30547.4	327	0.0191	Singlet-A	H-3->L+4 (33%), H-1->L+4 (24%)
8	30647.5	326	0.4774	Singlet-A	H-4->LUMO (17%), H-2->L+1 (20%)
9	30832.2	324	0.9958	Singlet-A	H-5->LUMO (25%), H-2->L+2 (19%), HOMO->L+1 (16%)
10	31425.8	318	0.1251	Singlet-A	H-4->L+1 (14%), HOMO->L+1 (39%)
11	31638.7	316	0.0397	Singlet-A	H-3->L+2 (22%), H-1->L+1 (34%), HOMO->L+2 (11%)
12	31725.8	315	0.0205	Singlet-A	H-3->L+1 (17%), H-1->L+2 (33%)

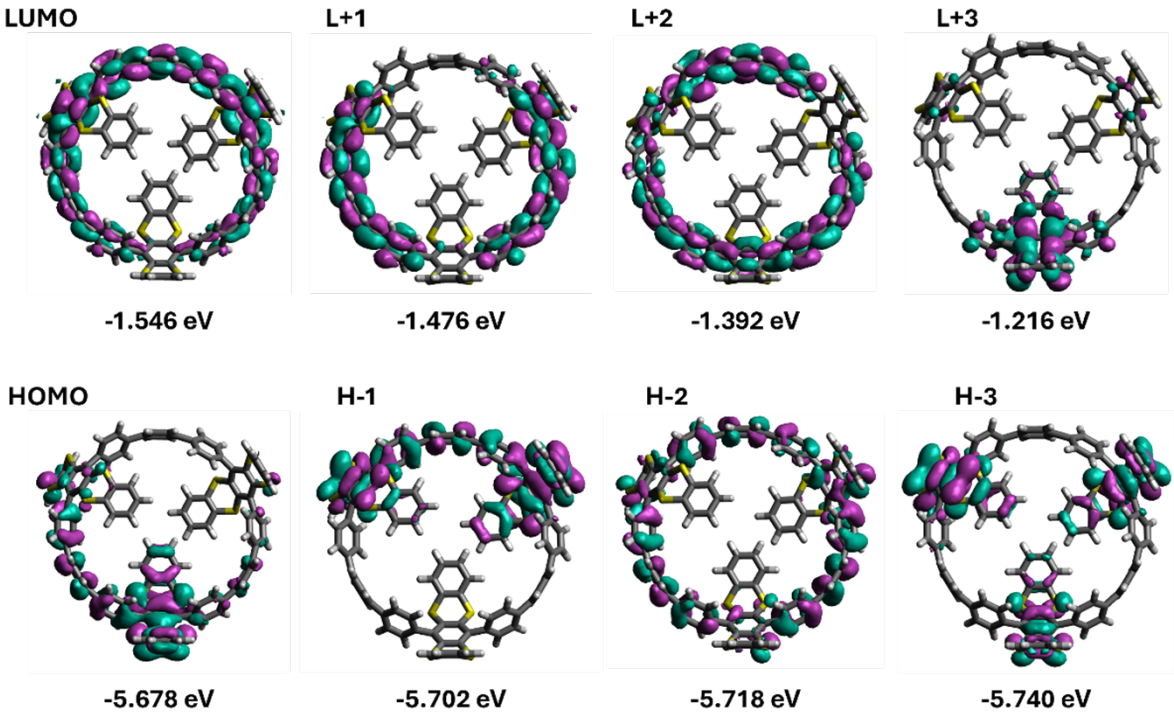

Figure S15. TD-DFT orbital localization for (top) LUMO and (bottom) HOMO for trisubstituted tetrathiapentacene on [12]CPP.

c) Binding Energy

M062X/6-31G(d,p) Opt Freq scrf=(solvent=toluene)

Binding energy calculations were performed using G098 at the M06-2X level of theory to compare to literature values of cycloparaphenylenes and visualized using PyMOL.[45,46] Frequency calculations were performed with the polarizable continuum model (PCM) to better represent toluene solvation. Binding analysis was performed by computing the difference of the sums of values for the reactants (Host, Guest) and products (Complex) to derive corrected Gibbs free energy values, see equation 1.12 We see that as we increased the number of thianthrene units we can increase [12]CPPs binding to C_{60}. M06-2X is known to overestimate binding energy, in the case for [10]CPP it is highly overestimated ($\Delta G°lit$=37 kj/mol, ~121% overestimate) perhaps due to closer H contacts as seen in previous literature DFT results.[45,46] However, with substituted [12]CPP variations it better estimates C_{60} binding compared to experimental observations (~6 to 21% differences -See Table S1). Although there is error in the computations, we see the same trend of an increase in host binding upon TTP substitution as observed experimentally.

$$\Delta_r G°(298K) = \sum(\mathcal{E}_0 + G_{corr})_{\text{products}} - \sum(\mathcal{E}_0 + G_{corr})_{\text{reactants}}$$

Equation 1. Describes the free energy calculation for guest binding.

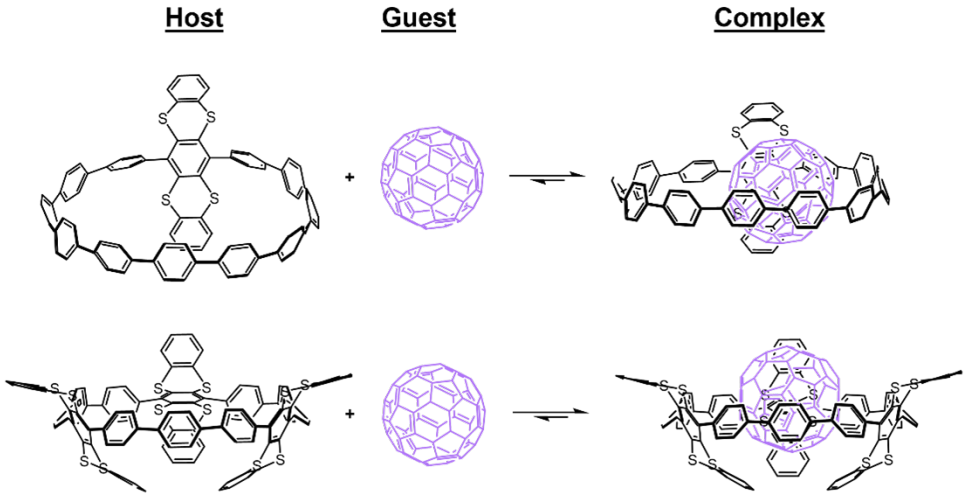

Complex	ΔG Total (kJ/mol)	Error (%)
[10]CPP DFT	-82	
[10]CPP Lit. EXP	-37	-121.6
2 DFT	-31	
2 EXP (1:1)	-29	6.9
1 DFT	-22	
1 EXP (1:1)	-27.7	20.6

Table S1. Free energy comparisons for computed and experimental binding of C_{60} guest complexation.

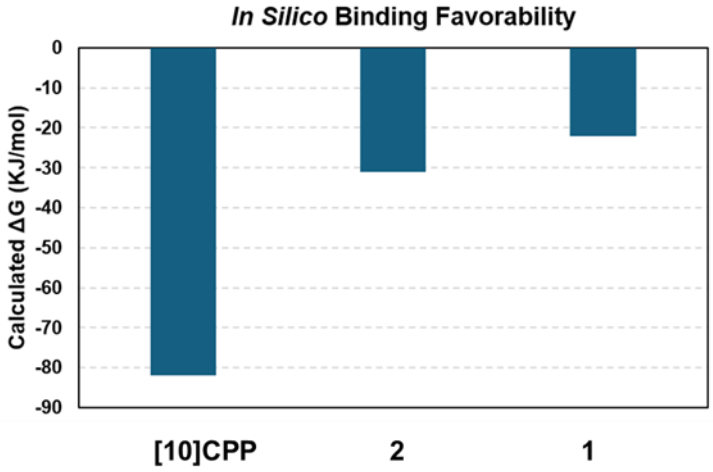

Figure S16. DFT calculated free energy for complex **1**, **2**, and **[10]CPP**. Computed with G09 at the M06-2X level of theory in a toluene solvation model.

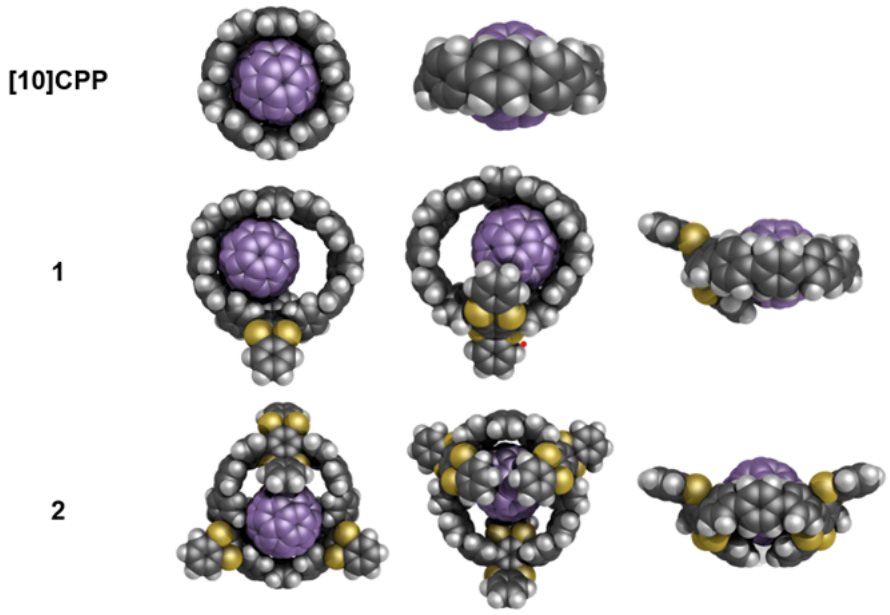

Figure S17. G09 minimized geometry structures of hydrocarbon and TTP-CPPs visualized in PyMOL.

2.1.7 Citations

(1) Darzi, E. R.; Jasti, R. The Dynamic, Size-Dependent Properties of [5]–[12]Cycloparaphenylenes. *Chem. Soc. Rev.* **2015**, 44 (18), 6401–6410.

(2) Fujitsuka, M.; Cho, D. W.; Iwamoto, T.; Yamago, S.; Majima, T. Size-Dependent Fluorescence Properties of [n]Cycloparaphenylenes (n = 8–13), Hoop-Shaped π-Conjugated Molecules. *Phys. Chem. Chem. Phys.* **2012**, 14 (42), 14585–14588.

(3) Jasti, R.; Bhattacharjee, J.; Neaton, J. B.; Bertozzi, C. R. Synthesis, Characterization, and Theory of [9]-, [12]-, and [18]Cycloparaphenylene: Carbon Nanohoop Structures. *J. Am. Chem. Soc.* **2008**, 130 (52), 17646–17647.

(4) Lovell, T. C.; Bolton, S. G.; Kenison, J. P.; Shangguan, J.; Otteson, C. E.; Civitci, F.; Nan, X.; Pluth, M. D.; Jasti, R. Subcellular Targeted Nanohoop for One- and Two-Photon Live Cell Imaging. *ACS Nano* **2021**, 15 (9), 15285–15293.

(5) Chen, D.; Wada, Y.; Kusakabe, Y.; Sun, L.; Kayahara, E.; Suzuki, K.; Tanaka, H.; Yamago, S.; Kaji, H.; Zysman-Colman, E. A Donor–Acceptor 10-Cycloparaphenylene and Its Use as

an Emitter in an Organic Light-Emitting Diode. *Org. Lett.* **2023**, 25 (6), 998–1002.

(6) Lu, D.; Huang, Q.; Wang, S.; Wang, J.; Huang, P.; Du, P. The Supramolecular Chemistry of Cycloparaphenylenes and Their Analogs. *Front. Chem.* **2019**, 7.

(7) Peters, G. M.; Grover, G.; Maust, R. L.; Colwell, C. E.; Bates, H.; Edgell, W. A.; Jasti, R.; Kertesz, M.; Tovar, J. D. Linear and Radial Conjugation in Extended π-Electron Systems. *J. Am. Chem. Soc.* **2020**, 142 (5), 2293–2300.

(8) Zhang, J.; Cheng, H.; Meng, Z.; Zhang, H.; Luo, Z.; Muddassir, M.; Li, X.; Sha, Y. Side-Chain Meta [6]Cycloparaphenylene-Based Nanoring-Containing Polymers. *Polym. Chem.* **2023**, 14 (45), 5029–5033.

(9) Heras Ojea, M. J.; Van Raden, J. M.; Louie, S.; Collins, R.; Pividori, D.; Cirera, J.; Meyer, K.; Jasti, R.; Layfield, R. A. Spin-Crossover Properties of an Iron(II) Coordination Nanohoop. *Angew. Chem. Int. Ed.* **2021**, 60 (7), 3515–3518.

(10) Van Raden, J. M.; Louie, S.; Zakharov, L. N.; Jasti, R. 2,2′-Bipyridyl-Embedded Cycloparaphenylenes as a General Strategy To Investigate Nanohoop-Based Coordination Complexes. *J. Am. Chem. Soc.* **2017**, 139 (8), 2936–2939.

(11) A. Kamin, A.; D. Clayton, T.; E. Otteson, C.; M. Gannon, P.; Krajewski, S.; Kaminsky, W.; Jasti, R.; J. Xiao, D. Synthesis and Metalation of Polycatechol Nanohoops Derived from Fluorocycloparaphenylenes. *Chem. Sci.* **2023**, 14 (36), 9724–9732.

(12) Kayahara, E.; Patel, V. K.; Mercier, A.; Kündig, E. P.; Yamago, S. Regioselective Synthesis and Characterization of Multinuclear Convex-Bound Ruthenium-[n]Cycloparaphenylene (N=5 and 6) Complexes. *Angew. Chem. Int. Ed.* **2016**, 55 (1), 302–306.

(13) Lv, Y.; Lin, J.; Song, K.; Song, X.; Zang, H.; Zang, Y.; Zhu, D. Single Cycloparaphenylene Molecule Devices: Achieving Large Conductance Modulation via Tuning Radial π-Conjugation. *Sci. Adv.* **2021**. 7 (52), eabk3095.

(14) Roy, R.; Brouillac, C.; Jacques, E.; Quinton, C.; Poriel, C. π-Conjugated Nanohoops: A New Generation of Curved Materials for Organic Electronics. *Angew. Chem.* **2024**, 136 (30), e202402608.

(15) Leonhardt, E. J.; Jasti, R. Emerging Applications of Carbon Nanohoops. Nat. Rev. Chem. 2019, 3 (12), 672–686.

(16) Terabayashi, T.; Kayahara, E.; Zhang, Y.; Mizuhata, Y.; Tokitoh, N.; Nishinaga, T.; Kato, T.; Yamago, S. Synthesis of Twisted [n]Cycloparaphenylene by Alkene Insertion. *Angew. Chem. Int. Ed.* **2023**, 62 (2), e202214960.

(17) Shudo, H.; Kuwayama, M.; Segawa, Y.; Yagi, A.; Itami, K. Half-Substituted Fluorocycloparaphenylenes with High Symmetry: Synthesis, Properties and Derivatization to Densely Substituted Carbon Nanorings. *Chem. Commun.* **2023**, 59 (90), 13494–13497.

(18) Mohamed, M. G.; Chaganti, S. V.; Li, M.-S.; Samy, M. M.; Sharma, S. U.; Lee, J.-T.; Elsayed, M. H.; Chou, H.-H.; Kuo, S.-W. Ultrastable Porous Organic Polymers Containing Thianthrene and Pyrene Units as Organic Electrode Materials for Supercapacitors. *ACS Appl. Energy Mater.* **2022**, 5 (5), 6442–6452.

(19) E. Speer, M.; Kolek, M.; Jacques Jassoy, J.; Heine, J.; Winter, M.; M. Bieker, P.; Esser, B. Thianthrene-Functionalized Polynorbornenes as High-Voltage Materials for Organic Cathode-Based Dual-Ion Batteries. *Chem. Commun.* **2015**, 51 (83), 15261–15264.

(20) Ren, J.; Wang, X.; Liu, H.; Hu, Y.; Zhang, X.; Masuda, T. Poly(Phenylacetylene)s Bearing Thianthrene Groups as High-Voltage Organic Cathode Materials for Lithium Batteries. *React. Funct. Polym.* **2020**, 146, 104365.

(21) Pander, P.; Swist, A.; Soloducho, J.; Dias, F. B. Room Temperature Phosphorescence Lifetime and Spectrum Tuning of Substituted Thianthrenes. *Dyes Pigments* **2017**, 142, 315–322.

(22) Wen, Y.; Liu, H.; Zhang, S.-T.; Pan, G.; Yang, Z.; Lu, T.; Li, B.; Cao, J.; Yang, B. Modulating Room Temperature Phosphorescence by Oxidation of Thianthrene to Achieve Pure Organic Single-Molecule White-Light Emission. *CCS Chem.* **2020**, 3 (7), 1940–1948.

(23) Yang, Z.; Zhao, S.; Zhang, X.; Liu, M.; Liu, H.; Yang, B. Efficient Room-Temperature Phosphorescence from Discrete Molecules Based on Thianthrene Derivatives for Oxygen Sensing and Detection. *Front. Chem.* **2022**, 9.

(24) Li, N.; Wang, Y.; Li, Z. Photo-Induced Room Temperature Phosphorescence and Thermally

Activated Photochromism Based on Thianthrene Derivatives. *J. Mater. Chem. C* **2024**, 12 (31), 12045–12053.

(25) Yuan, J.; Lv, W.; Li, A.; Zhu, K. A Self-Assembled M2L2 Truncated Square and Its Application as a Container for Fullerenes. *Chem. Commun.* **2021**, 57 (95), 12848–12851.

(26) Georghiou, P. E.; Dawe, L. N.; Tran, H.-A.; Strübe, J.; Neumann, B.; Stammler, H.-G.; Kuck, D. C3v-Symmetrical Tribenzotriquinacenes as Hosts for C60 and C70 in Solution and in the Solid State. *J. Org. Chem.* **2008**, 73 (22), 9040–9047.

(27) Amthor, S.; Lambert, C.; Graser, B.; Leusser, D.; Selinka, C.; Stalke, D. Synthesis and Ligand Properties of Thianthrenophane. *Org. Biomol. Chem.* **2004**, 2 (20), 2897–2901.

(28) Georghiou, P. E.; Tran, A. H.; Mizyed, S.; Bancu, M.; Scott, L. T. Concave Polyarenes with Sulfide-Linked Flaps and Tentacles: New Electron-Rich Hosts for Fullerenes. *J. Org. Chem.* **2005**, 70 (16), 6158–6163.

(29) Heiska, J.; Nisula, M.; Karppinen, M. Organic Electrode Materials with Solid-State Battery Technology. *J. Mater. Chem. A* **2019**, 7 (32), 18735–18758.

(30) Etkind, S. I.; Swager, T. M. The Properties, Synthesis, and Materials Applications of 1,4-Dithiins and Thianthrenes. *Synthesis* **2022**, 4843–4863.

(31) Burkhart, C.; Haberhauer, G. A Light- and Electricity-Driven Molecular Pushing Motor. *Eur. J. Org. Chem.* **2017** (10), 1308–1317.

(32) Wang, S.; Yuan, J.; Xie, J.; Lu, Z.; Jiang, L.; Mu, Y.; Huo, Y.; Tsuchido, Y.; Zhu, K. Sulphur-Embedded Hydrocarbon Belts: Synthesis, Structure and Redox Chemistry of Cyclothianthrenes. *Angew. Chem.* **2021**, 133 (34), 18591–18595.

(33) Ong, W. J.; Swager, T. M. Dynamic Self-Correcting Nucleophilic Aromatic Substitution. *Nat. Chem.* **2018**, 10 (10), 1023–1030.

(34) Leonhardt, E. J.; Van Raden, J. M.; Miller, D.; Zakharov, L. N.; Alemán, B.; Jasti, R. A Bottom-Up Approach to Solution-Processed, Atomically Precise Graphitic Cylinders on Graphite. *Nano Lett.* **2018**, 18 (12), 7991–7997.

(35) Schaub, T. A.; Margraf, J. T.; Zakharov, L.; Reuter, K.; Jasti, R. Strain-Promoted Reactivity

of Alkyne-Containing Cycloparaphenylenes. *Angew. Chem. Int. Ed.* **2018**, 57 (50), 16348–16353.

(36) Bruno, N. C.; Tudge, M. T.; Buchwald, S. L. Design and Preparation of New Palladium Precatalysts for C–C and C–N Cross-Coupling Reactions. *Chem. Sci.* **2013**, 4 (3), 916–920.

(37) Fehr, J. M.; Myrthil, N.; Garrison, A. L.; Price, T. W.; Lopez, S. A.; Jasti, R. Experimental and Theoretical Elucidation of SPAAC Kinetics for Strained Alkyne-Containing Cycloparaphenylenes. *Chem. Sci.* **2023**, 14 (11), 2839–2848.

(38) Pangborn, A. B.; Giardello, M. A.; Grubbs, R. H.; Rosen, R. K.; Timmers, F. J. Safe and Convenient Procedure for Solvent Purification. *Organometallics* **1996**, 15 (5), 1518–1520.

(39) Clayton, T. D.; Fehr, J. M.; Price, T. W.; Zakharov, L. N.; Jasti, R. Pinwheel-like Curved Aromatics from the Cyclotrimerization of Strained Alkyne Cycloparaphenylenes. *J. Am. Chem. Soc.* **2024**, 146 (44), 30607–30614.

(40) Scientific, H. A Guide to Recording Fluorescence Quantum Yields.

(41) Hibbert, D. B.; Thordarson, P. The Death of the Job Plot, Transparency, Open Science and Online Tools, Uncertainty Estimation Methods and Other Developments in Supramolecular Chemistry Data Analysis. *Chem. Commun.* **2016**, 52 (87), 12792–12805.

(42) Frisch, M. J.; Trucks, G. W.; Schlegel, H. B.; Scuseria, G. E.; Robb, M. A.; Cheeseman, J. R.; Scalmani, G.; Barone, V.; Petersson, G. A.; Nakatsuji, H.; Li, X.; Caricato, M.; Marenich, A. V.; Bloino, J.; Janesko, B. G.; Gomperts, R.; Mennucci, B.; Hratchian, H. P.; Ortiz, J. V.; Izmaylov, A. F.; Sonnenberg, J. L.; Williams; Ding, F.; Lipparini, F.; Egidi, F.; Goings, J.; Peng, B.; Petrone, A.; Henderson, T.; Ranasinghe, D.; Zakrzewski, V. G.; Gao, J.; Rega, N.; Zheng, G.; Liang, W.; Hada, M.; Ehara, M.; Toyota, K.; Fukuda, R.; Hasegawa, J.; Ishida, M.; Nakajima, T.; Honda, Y.; Kitao, O.; Nakai, H.; Vreven, T.; Throssell, K.; Montgomery Jr., J. A.; Peralta, J. E.; Ogliaro, F.; Bearpark, M. J.; Heyd, J. J.; Brothers, E. N.; Kudin, K. N.; Staroverov, V. N.; Keith, T. A.; Kobayashi, R.; Normand, J.; Raghavachari, K.; Rendell, A. P.; Burant, J. C.; Iyengar, S. S.; Tomasi, J.; Cossi, M.; Millam, J. M.; Klene, M.; Adamo, C.; Cammi, R.; Ochterski, J. W.; Martin, R. L.; Morokuma, K.; Farkas, O.; Foresman, J. B.;

Fox, D. J. Gaussian 16 Rev. C.01, **2016**.

(43) Adamska, L.; Nayyar, I.; Chen, H.; Swan, A. K.; Oldani, N.; Fernandez-Alberti, S.; Golder, M. R.; Jasti, R.; Doorn, S. K.; Tretiak, S. Self-Trapping of Excitons, Violation of Condon Approximation, and Efficient Fluorescence in Conjugated Cycloparaphenylenes. *Nano Lett.* **2014**, 14 (11), 6539–6546.

(44) Iwamoto, T.; Watanabe, Y.; Sadahiro, T.; Haino, T.; Yamago, S. Size-Selective Encapsulation of C60 by [10]Cycloparaphenylene: Formation of the Shortest Fullerene-Peapod. *Angew. Chem. Int. Ed.* **2011**, 50 (36), 8342–8344.

(45) Schrödinger, LLC. The PyMOL Molecular Graphics System, Version 1.8, **2015**.

(46) Ochterski, J. W. Thermochemistry in Gaussian.

2.2 Mechanistic Investigation into Strain Mediated S_NAr Pathways

2.2.1 Introduction

Using S_NAr for late-stage functionalization shows ample promise to modify CPP properties, without the need for new pre-synthetic optimizations as we see with thianthrene substituted CPPs (**Figure 2.10**).[1–3] Despite S_NAr's application in CPP late-stage functionalization, the mechanistic role of S_NAr with CPPs remains unexplored. Our goal of effectively synthesizing discrete carbon nanostructures through S_NAr reactivity necessitates a deeper understanding of optimal reaction conditions, given the diverse nucleophile and donor group chemistries at play. *Accordingly, we aimed to further elucidate the impact of strain and radial conjugation on the mechanistic pathway of S_NAr with CPPs. This chapter covers the progress made toward understanding the CPPs role within S_NAr contexts.*

CPPs have many unique properties given their curved geometry and axially strained molecular orbitals which differ in many ways from planar aromatic systems.[4–6] CPPs exhibit size-dependent features resulting from distinct strain-induced reactivity patterns and varying redox properties.[6–9] We hypothesized that these unique CPP structure properties may change S_NAr reactivity so we per-

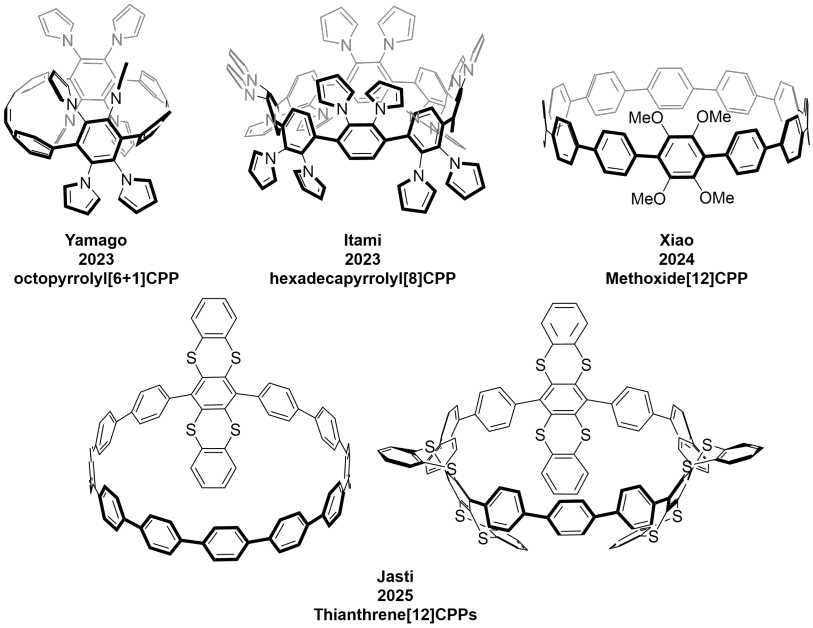

Figure 2.10: Previous examples modifying cycloparaphenylenes with S_NAr.

formed a competition reaction to probe this idea. These preliminary competition studies do indicate a preferential substitution with **TF[12]CPP** when mixed with a model linear analogue (**Figure 2.11**). **TF[12]CPP** was mixed with equal molar ratio of the *linear analogue*, 2 molar equivalents of dithiobezene, and subjected to microwave (MW) heating for 24 hours. NMR was taken to identify if the CPP or linear system was substituted. In the NMR we see peaks consistent with linear starting material of linear analogue and from the thianthrene substituted CPP, **TT[12]CPP**.

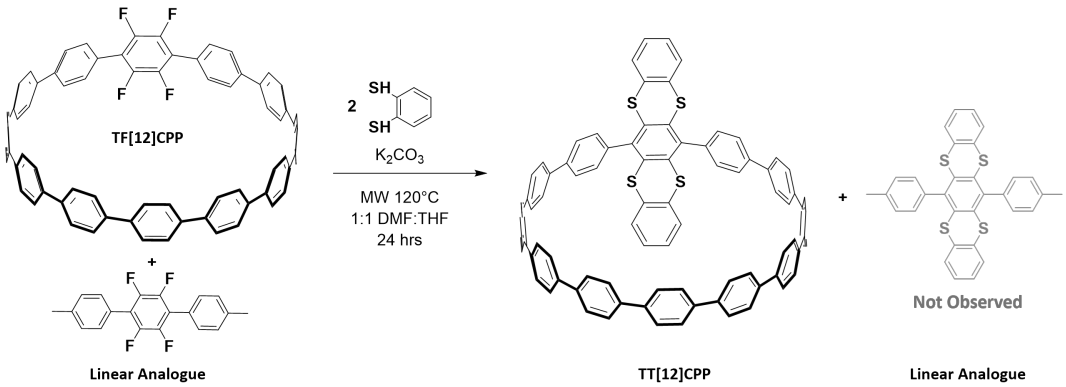

Figure 2.11: Competition study between linear tetrafluorinated system compared to fluorinated CPP.

Thin layer chromatography revealed spots corresponding to starting materials **TF[12]CPP** and **lin-**

ear analogue as well as the substituted CPP **TT[12]CPP**. Interestingly, no spots were observed for the linear substitution product. This material was resubjected for another 24 hrs with 3 more molar equiv. of dithiobenzene and we see full consumption of **TF[12]CPP** into **TT[12]CPP** as well as 3 spots for a mixture of incomplete substitutions on the linear system. We hypothesized this result was due to the CPPs ability to stabilize other systems through charge delocalization; in the case of a Meisenheimer intermediate the CPP may better stabilize an anionic charge build up, and increase the rate of reaction.[4,10] Smaller CPP sizes have also been shown to exhibit increased reactivity due to their ring strain and narrow HOMO-LUMO gap.[6] Given this result, we aimed to investigate S_NAr reactivity further by analyzing the impact of *strain* and *aromaticity* for a library of monofluorinated [*n*]CPPs (*n* = 8, 10, and 12) on the substitution rate of thiobenzene. This study aimed to remove the electronic influence of para fluorine stabilization groups to focus solely on the effect of CPP size. It's also worth analyzing the specific role of dihedral angle in S_NAr reaction rate. Taking from Hammond's postulate, stabilization of the transition state structure could aid in faster reactivity. [11,12]

2.2.2 Results and Discussion

A library of single fluorine CPPs was created following the conventional modular bottom-up synthetic method (**Scheme 2.3**). To synthesize F[8]CPP, **4**, the small fluorine building block undergoes lithium halogen exchange at the bromine position and inserts into the carbonyl on the chloroketone precursor. This is followed by Miyaura borylation and Suzuki coupling to form the TES protected macrocycle **3**. TBAF is used to deprotect and form the hydroxy macrocycle which then undergoes reductive-aromatization with H_2SnCl_4 to form **4** in 54% yield. To synthesize F[10]CPP and F[12]CPP (**7a** and **7b** respectively) the small fluorine building block undergoes a double Suzuki reaction with the known [3]ClBpin coupling partner. This 7-ring intermediate **5** then gets coupled with another borylated 3-ring or 5-ring intermediate to form the TES protected macrocycles **6a** and **6b**. These protected macrocycles undergo a similar deprotection then reductive-elimination step to form **7a** in 55% yield and **7b** in 36% yield.

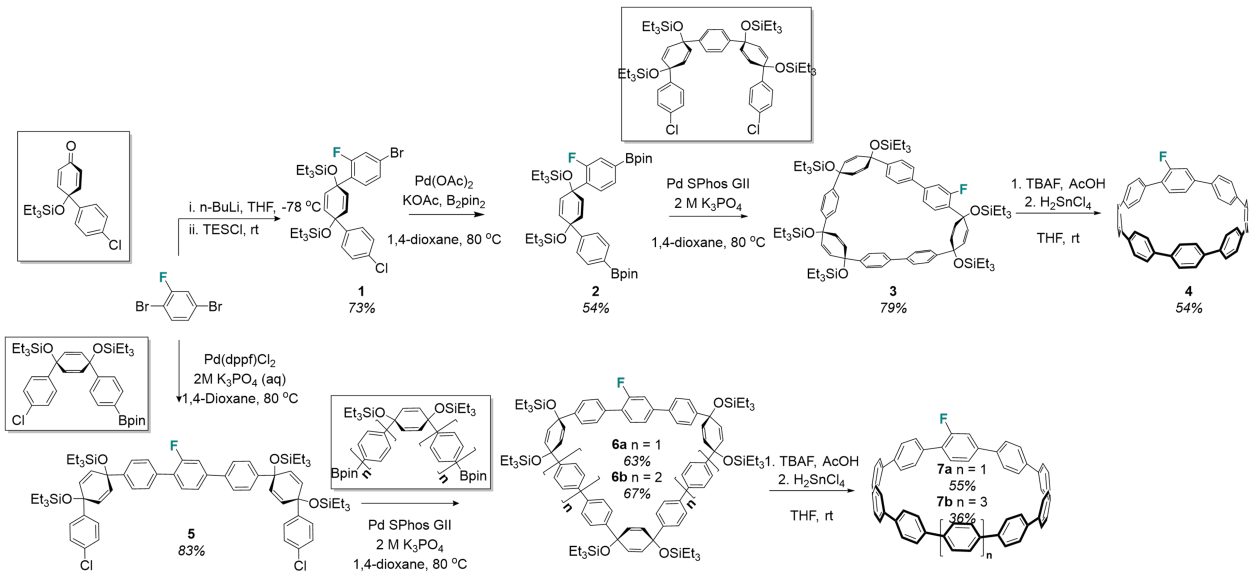

Scheme 2.3: Synthesis pathway for library of single fluorine [*n*]CPPs (*n*=8,10, and 12).

Absorption and emission spectrum were taken for the single fluorine family and showed no change in opto-electronics as observed from hydrocarbon CPP analogues of the same size (**Figure 2.12**). The single F[n]CPPs share a similar absorption (λ_{abs}= 340 nm) and red-shifting emissions as size decreases from 12 to 10 to 8 (λ_{em}= 450, 470, and 540 nm respectively). They appear as light-tan to yellow powders and when irradiated emit in both solid and solution state.

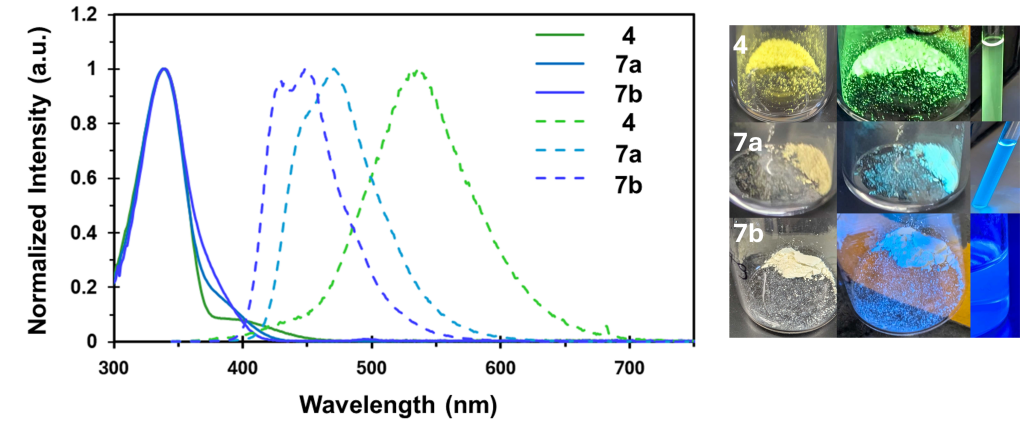

Figure 2.12: Photophysical study for single fluorine [*n*]CPPs (*n*=8,10, and 12).

Structure Elucidation Through X-Ray Crystallography

Single crystal x-ray diffraction was performed by Lev Zakharov on compound **7b** (F[12]CPP) whose crystals were obtained through slow evaporation in a methanol/dichloromethane co-solvent

system (**Figure 2.13**). The crystal forms columns in the $P2_1/c$ space group. Six solvent CH_2Cl_2 molecules are located between the main molecules in the packing. Solvent molecules inside the hoops are highly disordered and were treated by SQUEEZE, and conformation slightly varies between hoops.

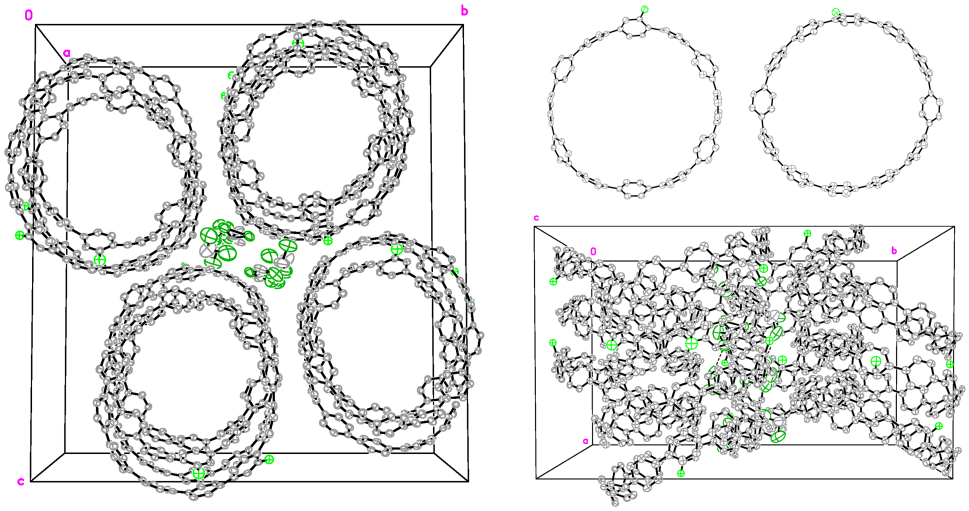

Figure 2.13: Single crystal x-ray diffraction of structure **7b**.

Nucleophilic Aromatic Substitution on Single Fluorinated CPPs Having fully characterized single fluorinated CPPs, we next aimed to probe reactivity with thiophenol as the chosen nucleophile (**Figure 2.14**). This reaction is run in a microwave at 120 °C for 24 hours. K_3PO_4 facilitates deprotonation and the thiophenol attacks the carbon-fluorine bond. For all CPP species we observed thiophenol substitution readily characterized by ^1H, ^{19}F NMR and mass spec (**Methods Section**). Attempts were made to monitor reactivity using VT NMR, however, without microwave conditions we could accurately monitor product formation. Still, a single fluorine linear analogue subjected to the same microwave conditions won't undergo S_NAr. Thus, we are observing new reactivity likely due to the CPPs strained architecture.

Dihedral Angle Comparison

CPPs strain influences the dihedral angle (Φ), as strain increases, it forces the dihedral angle to

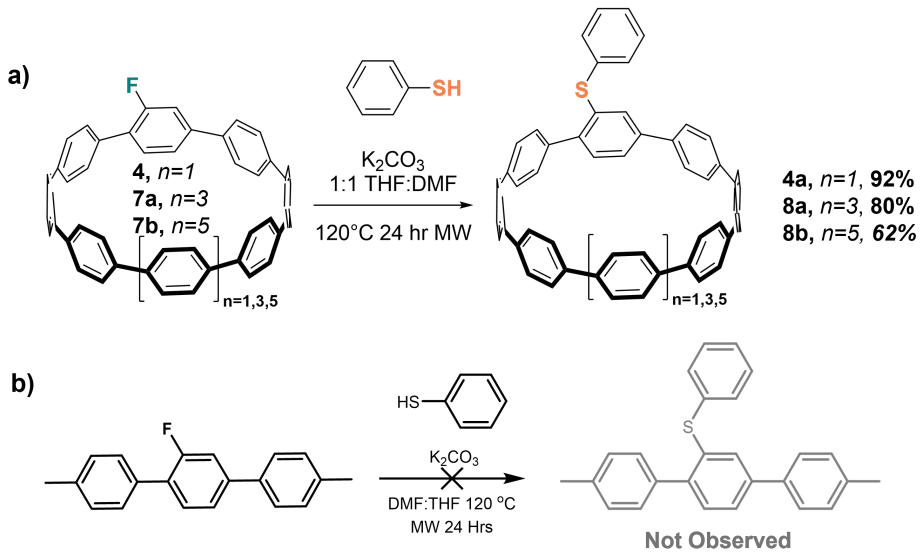

Figure 2.14: A) Synthesis of thiophenol substituted [*n*]CPPs (*n*=8,10,12). B) Single fluorine linear analogue doesn't undergo S_NAr.

shrink. In hydrocarbon systems the dihedral angle decreases from 36° in [12]CPP to 28° for [6]CPP.[6] In S_NAr, geometry of precursors could be expected to affect the transition state energy, and therefore the expected rate of the reaction. Accordingly, a DFT computational study was run to compare HOMO-LUMO energies and dihedral angles of the single fluorine library, linear single fluorine analogue, and TF[12]CPP (as comparison given its high reactivity). Calculations were performed using Gaussian G09[13] software with B3LYP/6-31(d,p) theory and basis set combinations. Geometries were all verified to be lowest ground state energies by ensuring positive frequency vibrations. Dihedral angles were measured in GaussView and HOMO-LUMO gap energies measured by subtracting the HOMO level from LUMO level. The difference between the HOMO of the nucleophile (thiophenol) and LUMO of aromatic substrate was used to determine Frontier Molecular Orbital (FMO) energy interaction for reaction compared to TF[12]CPP as a standard (i.e. how much energy offset are the single fluorine substrates compared to the TF[12]CPP), (**Figure 2.15**).

2.2.3 Conclusion and Bridge to Chapter III

Given linear deactivated aromatic systems are quite unreactive toward S_NAr, it is surprising we observe substitution on the single fluorine CPPs, with varying yields. Although we couldn't

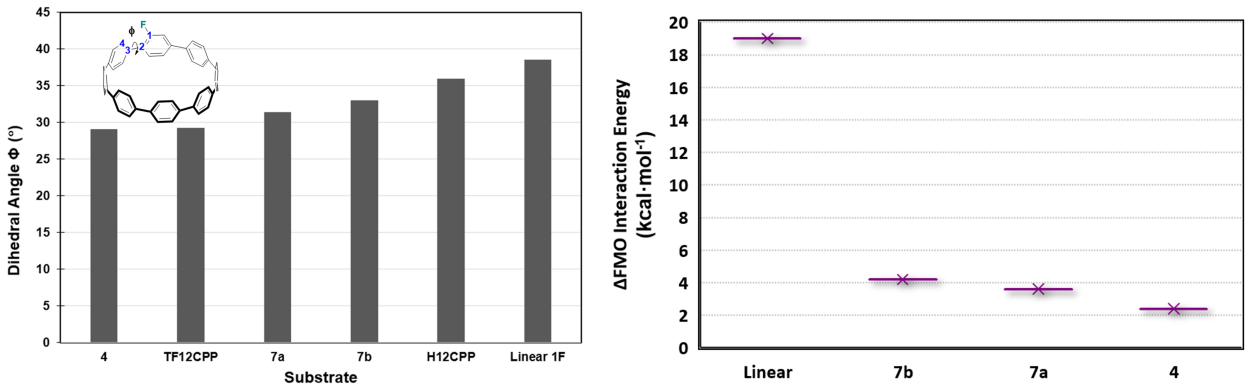

Figure 2.15: (*left*) DFT analysis on the dihedral angles for F[*n*]CPPs, linear analogue, and TF[12]CPP as a standard. (*right*) Energy analysis for FMO interaction energy calculated in ref. to TF[12]CPP (LUMO) subtracted from Thiophenol (HOMO) in kcal/mol.

quantify the rate of the system due to instrument limitations, CPPs proved to be more reactive than their linear counterparts. Work is on-going to investigate this rate relationship more thoroughly, as we aim to use S_NAr for extended CPPs due to its dynamic bond formation showed by Swager and its versatility with a wide array of nucleophiles available.[14] S_NAr is shown as an efficient method to modify CPPs in the late-stage due the stability of the C-F bond through early reaction conditions. In this chapter we were able to show how modifying CPPs using S_NAr opened new tunability toward host–guest chemistry, increasing affinity for C_{60} binding. In the next chapter, we explore using the Diels-Alder [4+2] as another late-stage synthetic strategy on strained-alkyne CPPs. This is another class of functionalized CPPs that scales well, and maintains a handle for post-synthetic transformations. This handle opens an additional library of reagents to use for CPP π-extension, in our study specifically one that increases the overall Stokes Shift also accessing a range of photophysical properties.

2.2.4 Experimental Appendix: Supplementary Information

Commercially available materials were used without purification unless otherwise indicated. Moisture and oxygen sensitive reactions were carried out in flame-dried glassware and under an inert atmosphere of purified nitrogen using syringe/septa technique. Tetrahydrofuran (THF) and dimethylformamide (DMF) were dried by filtration through alumina according to the methods de-

scribed by Grubbs.[15] Alumina column chromatography was conducted with SorbTech basic alumina (pH 10), Act. II-III, 50-200 μm. ^{1}H and ^{13}C NMR spectra were recorded on a Bruker Avance III HD 500 (^{1}H: 500 MHz, ^{13}C: 126 MHz) NMR spectrometer. The chemical shifts (δ) were reported in parts per million (ppm) and were referenced to the solvent (CD_2Cl_2, ^{1}H: δ = 5.32 ppm and ^{13}C: δ = 53.84 ppm or $CDCl_3$, ^{1}H: δ = 7.26 ppm and ^{13}C: δ = 77.801 ppm). Coupling constants (J) are given in Hz and the apparent resonance multiplicity is reported as s (singlet), d (doublet), t (triplet), q (quartet), dd (doublet of doublets) or m (multiplet). UV/Vis absorption and fluorescence spectra were recorded on an Agilant Cary 100 spectrophotometer and a Horiba Jobin Yvon Fluoromax-4 Fluorimeter, respectively. All measurements were carried out under ambient conditions in a Spectrocell RF-1010-T threaded top vacuum formed borosilicate fluorometer cell (10 mm light path).

I. Synthesis

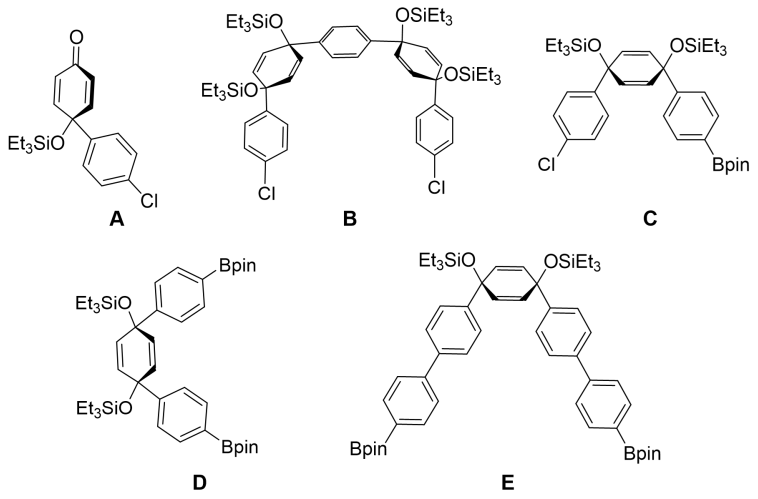

Compounds **A-E** were synthesized according to literature methods.[16,17]

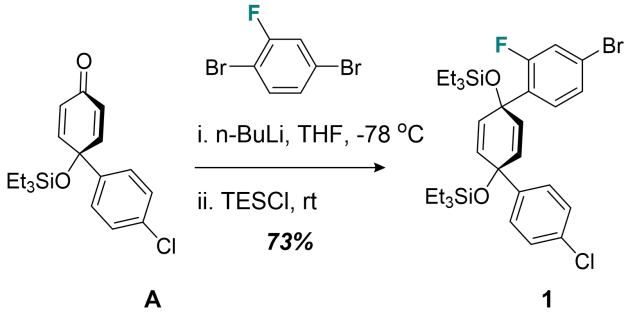

Compound 1. 1,4-dibromo-2-fluorobenzene (1.82 g, 7.2 mmol) was added to a flame dried round bottom flask, which was put under high vac for 30 mins. The rbf was cycled with N2 and high vac (x3) then dissolved in dry THF (11 mL). Compound A (2g, 6.0 mmol) was tared in a glass scintillation vial, and dissolved separately in THF (2 mL). Both vessels were cooled in acetone:dry ice baths kept at -78C. After allowing temperature equilibration (~30 mins), n-BuLi (4.5 mL, 6.3 mmol) was added dropwise to the vessel containing 1,4-dibromo-2-fluorobenzene. Compound A was then cannulated into the reaction flask. The mixture turned yellow and was allowed to stir at -78C for one hour at which point chlorotriethylsilane was added and the mixture warmed to rt and stirred overnight. In the morning, the reaction was checked for completion then quenched with sodium bicarbonate. Reduced pressure was used to removed THF then the solution was extracted with hexanes (3x30mL), washed with brine and water, then organic layers combined and dried over sodium sulfate. The organic phase was concentrated down and purified further on a short silica plug (~20%DCM:80%Hexanes). Concentrated the product fraction down to yield a light yellow oil (2.8 g, 75% yield, 94% purity). ^{1}H NMR (500 MHz, Chloroform-*d*) δ 7.30 – 7.11 (m, 7H), 6.21 (dd, J = 10.1, 1.4 Hz, 2H), 5.99 (d, J = 10.1 Hz, 2H), 0.93 (dt, J = 22.5, 7.9 Hz, 18H), 0.61 (dt, J = 32.8, 7.9 Hz, 12H). ^{13}C NMR (126 MHz, Methylene Chloride-d_2) δ 161.42 (d, J = 256.1 Hz), 144.56, 134.17, 133.13, 132.29 (d, J = 4.6 Hz), 131.98, 131.83, 129.96 (d, J = 1.8 Hz), 129.29 (d, J = 4.7 Hz), 128.62, 128.00, 127.82, 127.31 (d, J = 3.6 Hz), 121.88, 120.72, 114.80 – 112.00 (m), 71.48 (d, J = 5.9 Hz), 70.33 (d, J = 2.3 Hz), 8.77 – 5.09 (m). ^{19}F NMR (471 MHz, Methylene Chloride-d_2) δ -107.80 (dd, J = 10.8, 8.0 Hz).

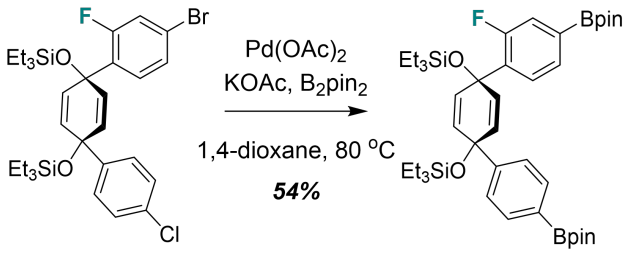

1 **2**

Compound 2. Compound 1 was added as an oil into a tared 100 mL RBF with DCM. Reduced the volume under pressure and dried on high vac for an extended period of time, then used a bunsen burner to carefully dry off the solvent. Let cool to rt then weighed the flask for the mass of Compound 1 (1.445 g, 2.3 mmol). Added dry KOAc (1.364 g, 13.9 mmol), Pd(OAc)2 (0.052 g, 0.23 mmol), B2pin2 (1.411 g, 5.6 mmol), Sphos (0.143 g, 0.35 mmol). The reaction vessel was then flame dried again with all solids present. Dioxane (15 mL) was added and the reaction was placed in a pre-heated 80C oil bath for 24 hrs. The reaction was allowed to cool to room temperature, and solvent removed at reduced pressure. The black sludge was taken up in DCM (sonicated) and ran through a celite plug topped with a thin pad of silica. The resulting filtrate was light orange and volume reduced under-pressure. A crude NMR was taken and the oil was further dried under high vac. Triturated out with cold methanol and filtered through a Buchner funnel, product is a white to off-white product (0.962 g, 54% yield). ^{1}H NMR (500 MHz, Methylene Chloride-d2) δ 7.59 – 7.53 (m, 2H), 7.43 – 7.33 (m, 2H), 7.30 – 7.20 (m, 3H), 6.27 (dd, J = 10.1, 1.4 Hz, 2H), 6.01 – 5.95 (m, 2H), 1.38 – 1.21 (m, 24H), 0.93 (dt, J = 34.4, 7.9 Hz, 18H), 0.70 – 0.43 (m, 12H).^{13}C NMR (126 MHz, Methylene Chloride-d_2) δ 160.95 (d, J = 252.0 Hz), 148.67, 135.17, 134.33 (d, J = 2.8 Hz), 132.60, 131.47 (d, J = 70.8 Hz), 129.83 (d, J = 3.4 Hz), 129.62 – 129.32 (m), 127.18 (d, J = 3.6 Hz), 124.95 (d, J = 7.1 Hz), 122.25, 122.08, 116.57 (d, J = 22.5 Hz), 114.45 – 112.32 (m), 83.67, 71.61, 70.31 (d, J = 2.2 Hz), 67.04, 29.68, 24.63 (d, J = 4.5 Hz), 6.80, 6.63, 6.35, 6.22. ^{19}F NMR (471 MHz, Methylene Chloride-d_2) δ -111.85 (dd, J = 12.2, 7.7 Hz). HRMS (ESI,TOF), m/z calculated for $C_{42}H_{65}B_2FO_6Si_2$ $(M+H)^+$ 762.4490, found 762.4484.

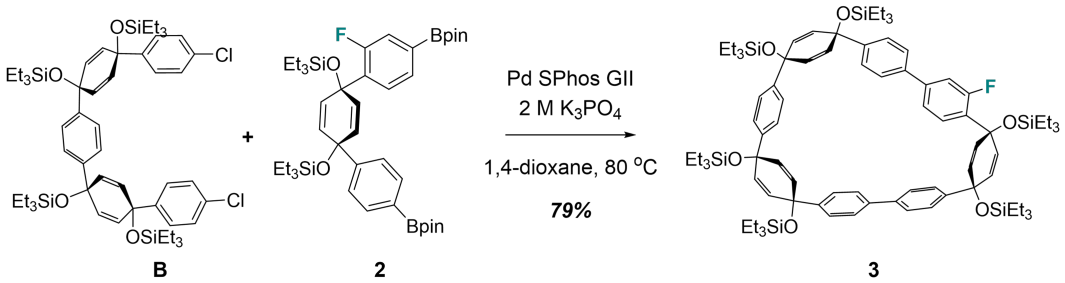

Compound 3. Compound 2(0.305 g, 0.40 mmol) was added with compound B (0.390 g, 0.40 mmol), Pd Sphos GII (0.062 g, 20 mol%) to a flame-dried rbf and put under high vac for 1 hour. The reaction vessel was purged with nitrogen 3 times, then 1,4-dioxane (400 mL, 1 mM) added via cannula then heated to 80 °C. Sparged 2M K3PO4 (40 mL, 1 mM) was added dropwise and the reaction was allowed to stir overnight. The next morning the reaction was reduced under pressure to remove the dioxane solvent. DCM was added to the crude sludge left behind and sonicated. This solution was then poured over a celite plug topped with a thin pad of silica on top. The plug was sufficiently flushed with 100 % DCM. Added filtered reaction solution to a rbf and concentrated down to afford a brown sticky oil. After being on high vac for 30 mins took a sample and ran crude NMR. Showed some bpin byproduct, checked TLC and saw that MeOH separated something off. Added DCM to dissolve the oil and then slowly added meoh to triturate out a solid in the sonication bath. Retrieved a pale yellow solid recovered through vacuum filtration (445 mg, 78% yield). 1H NMR (500 MHz,) δ 7.51 (s, 2H), 7.49 – 7.14 (m, 12H), 7.02 – 6.70 (m, 3H), 6.39 (dd, J = 10.0, 1.9 Hz, 1H), 6.13 – 5.88 (m, 14H), 1.06 – 0.84 (m, 54H), 0.77 – 0.51 (m, 35H).

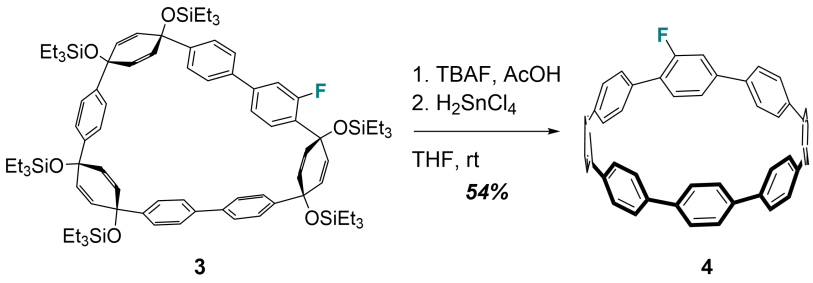

Compound 4. In flame dried flask, dissolved Compound 3 (0.165 g, 0.12 mmol) in dry THF (12 mL), acetic acid (0.334 mL, 5.8 mmol) was added quickly dropwise, followed by Tetrabutyl

ammonia fluoride (TBAF) (2.916 mL, 2.9 mmol) very slowly dropwise. The reaction was allowed to stir at roomtemp for 48 hrs. After completion diH_2O (10 mL) was added to reaction mixture, resulting in an off-white suspension, and the solution was subsequently rotovapped to remove THF. Vacuum filtration afforded a beige solid rinsed with more water and DCM. The solid and the filter paper it was on was dried under vacuum and collected (0.085 g, 99%). To a solution of $SnCl_2$•$2H_2O$ (0.27 g, 1.2 mmol) in THF (1.5 mL) was added conc. HCl (0.20 mL, 12 N, 2.4 mmol) at room temperature. After stirring for 30 min., the resulting solution of H_2SnCl_4 (0.881 mL, 0.72 mmol) was added to a suspension of macrocycle (0.085 g, 0.12 mmol) in THF (12 mL), and the resulting mixture was stirred at room temp. overnight. The solvent was removed under reduced pressure at 40C, and the residue was taken up in DCM (sonicated) and purified by passing over a short alumina plug with DCM as an eluent (~100 mL). The filtrate was subsequently reduced with roto-evaporation at 40C and resulting solid was dispersed in diethyl ether then collected with vacuum filtration resulting in a yellow-green product (0.040 g, 54% yield). HRMS (ESI,TOF), m/z calculated for $C_{48}H_{31}F$ $(M+H)^+$ 626.2410, found 626.2404.

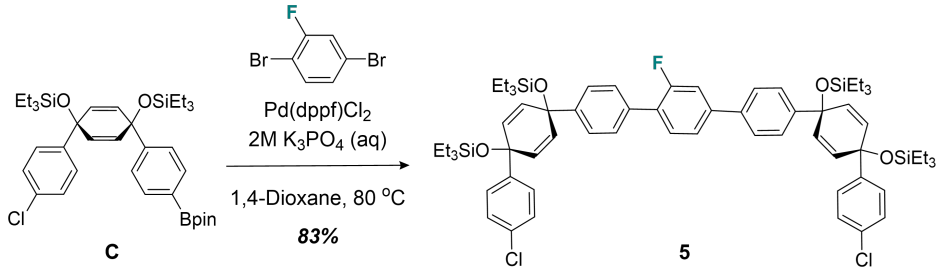

Compound 5. 1,4-dibromo-2-fluorobenzene (125 mg, 0.49 mmol), compound C (0.674 mg, 1.0 mmol), and Pd(dppf)Cl2 (36 mg, 10 mol %) were added to a flame dried round bottom flask, which was put under high vac for an hour. The rbf was cycled with N2 and high vac (x3) then solids dissolved in dioxane resulting in an orange solution and heated to 80C. Once heated, 2M K3PO4 that had been sparged for 5 minutes prior was added dropwise, turning the solution dark brown. This mixture was allowed to stir at 80C overnight. In the morning the reaction was cooled to rt then solvent was removed under reduced pressure. Suspended the crude sludge in hexanes and

passed through a plug of celite topped with silica then eluted with 20% DCM 80% hexanes. The filtrate was then concentrated down to a light-yellow oil and triturated with DCM:MeOH, filtered through a Buchner funnel to retrieve a flakey white solid (513 mg, 91% yield). ^{1}H NMR (500 MHz, Acetone-d_6) δ 7.72 (d, J = 8.4 Hz, 2H), 7.66 – 7.53 (m, 5H), 7.49 (dd, J = 8.4, 1.6 Hz, 4H), 7.42 (dd, J = 8.6, 3.0 Hz, 4H), 7.36 (dd, J = 8.6, 1.8 Hz, 4H), 6.20 – 6.09 (m, 8H), 0.97 (td, J = 7.9, 5.9 Hz, 36H), 0.73 – 0.63 (m, 24H).^{13}C NMR (126 MHz, Methylene Chloride-d_2) δ 160.72 (d, J = 247.3 Hz), 146.40, 146.11, 145.46 (d, J = 2.9 Hz), 142.42 (d, J = 8.0 Hz), 138.87 (d, J = 1.9 Hz), 135.02, 133.50, 132.42 (d, J = 9.6 Hz), 131.95 (d, J = 6.5 Hz), 131.57 (d, J = 4.1 Hz), 129.33 (d, J = 3.2 Hz), 128.83, 127.98, 127.27, 127.11, 126.63, 123.45 (d, J = 3.1 Hz), 115.02 (d, J = 2.9 Hz), 114.84, 71.79, 7.03 (d, J = 3.7 Hz). ^{19}F NMR (471 MHz, Methylene Chloride-d_2) δ -118.31 (t, J = 11 Hz). HRMS (ESI,TOF), m/z calculated for $C_{66}H_{87}Cl_2FO_4Si_4$ $(M+H)^+$ 1144.5043, found 1144.5037.

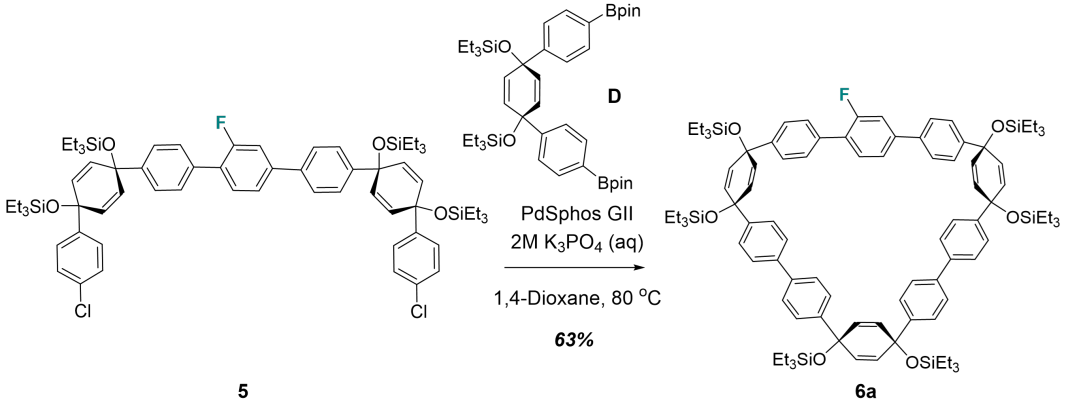

Compound 6a. Compound D (0.157 g, 0.32 mmol) was added with compound 5 (0.35 g, 0.31 mmol), Pd Sphos GII (0.048 g, 20 mol%) to a flame-dried rbf and put under high vac for 1 hour. The reaction vessel was purged with nitrogen 3 times, then 1,4-dioxane (305 mL, 1 mM) added via cannula then heated to 80 °C. Sparged 2M K3PO4 (31 mL, 1 mM) was added dropwise and the reaction was allowed to stir overnight. The next morning the reaction was reduced under pressure to remove the dioxane solvent. DCM was added to the crude sludge left behind and sonicated. This solution was then poured over a celite plug topped with a thin pad of silica on top. The plug was sufficiently flushed with 100 % DCM. Added filtered reaction solution to a rbf and concentrated down to afford a brown sticky oil. This oil was then dissolved in small amount of DCM to be

adsorbed on silica for column purification. Rotovapped the dcm+silica down then put on high vac until completely dry. Column purification was performed (30-50% DCM:Hexanes), product fractions were combined reduced on vacuum, then triturated out with methanol to afford an off-white solid (0.301 g, 63%). ^{1}H NMR (500 MHz, Methylene Chloride-d_2) δ 7.59 – 7.39 (m, 27H), 6.15 – 5.94 (m, 12H), 1.05 – 0.88 (m, 54H), 0.72 – 0.57 (m, 36H).^{13}C NMR (126 MHz, Chloroform-d) δ 160.08 (d, J = 248.0 Hz), 147.02 – 145.80 (m), 145.62 – 145.32 (m), 145.11, 144.65 (d, J = 7.0 Hz), 141.93 (d, J = 28.6 Hz), 139.58, 138.66, 138.27, 134.74 – 133.87 (m), 131.71, 131.64, 131.57, 131.52, 131.46, 131.41, 131.37, 130.89, 128.67, 128.16, 127.26, 126.78, 126.75, 126.67, 126.63, 126.54, 126.48, 126.31, 126.20, 126.02, 125.95, 125.91, 122.77, 120.08 (d, J = 49.2 Hz), 114.57, 114.38, 71.39. ^{19}F NMR (471 MHz, Methylene Chloride-d_2) δ -118.35 (d, J = 64.9 Hz). HRMS (MALDI,TOF), m/z calculated for $C_{96}H_{129}FO_6Si_6$ $(M+H)^+$ 1564.8389, found 1564.9000.

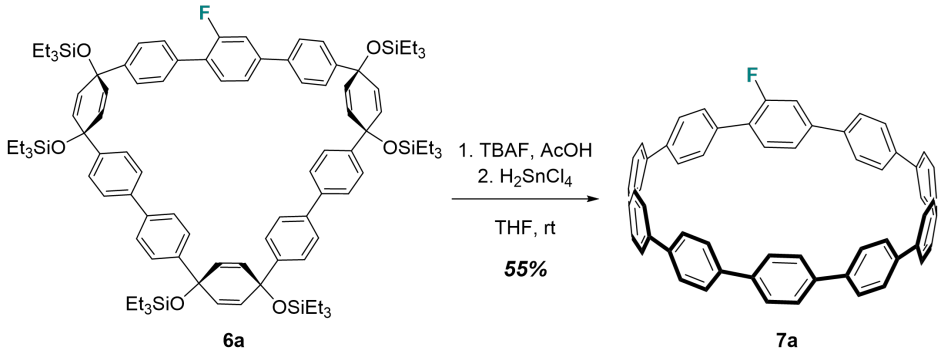

6a 7a

Compound 7a. In flame dried flask, dissolved compound 6a (0.116 g, 7.4x10^{-2} mmol) in dry THF (25 mL), resulting in clear solution. Acetic acid (0.2 mL) added quickly dropwise, followed by Tetrabutyl ammonia fluoride (TBAF) (2 mL) very slowly dropwise, allowed to stir at roomtemp overnight. Next day ~10 mL DI water added to reaction mixture, resulting in a yellow-white suspension, and the solution was subsequently rotovapped to remove THF. Vacuum filtration afforded a beige solid rinsed with more water and DCM. The solid and the filter paper it was on was left on house vac for a few hours then left overnight to air dry (no vac). Solid was transferred to a weigh paper for yield then to be moved on for aromatization (quant. yield). SnCl2•2H2O (0.41 g, 1.82 mmol) was dried on high-vac for 30 mins then added to a flame-dried 25 mL round-bottom flask. The flask was cycled with nitrogen and THF (2.5 mL) was added followed by conc. HCl (0.30 mL,

12 N, 3.63 mmol) at room temperature. After stirring for 30 min., the resulting solution was added to a suspension of macrocycle (0.048 g, $4.6x10^{-2}$ mmol) in THF (9 mL), and the resulting mixture was stirred at room temp overnight. The solvent was removed under reduced pressure at 40 C, and the residue was taken up in DCM (sonicated) and purified by passing over a short alumina plug with DCM as an eluent (~300 mL). The filtrate was reduced with roto-evaporation at 40 C. The resulting solid was dispersed in MeOH, and let air dry then put on high-vac to remove grease impurities to give pure CPP (0.02 g, 55%) as a pale-yellow solid. ^{1}H NMR (600 MHz, Methylene Chloride-d_2) δ 7.72 – 7.56 (m, 36H), 7.42 (dd, J = 13.5, 1.9 Hz, 1H), 7.37 (t, J = 8.4 Hz, 1H), 7.29 (dd, J = 8.5, 1.9 Hz, 1H). ^{13}C NMR (126 MHz, Methylene Chloride-d_2) δ 161.14 (d, J = 248.3 Hz), 141.28 (d, J = 8.3 Hz), 139.62, 139.22, 138.84, 138.51, 138.31, 137.68, 135.52, 134.11 (d, J = 17.4 Hz), 131.86, 130.17, 128.66, 127.69, 126.44, 124.65, 114.50, 114.30. ^{19}F NMR (471 MHz, Methylene Chloride-d_2) δ -115.65 – -115.75 (m). HRMS (MALDI,TOF), m/z calculated for $C_{60}H_{39}F$ $(M)^+$ 778.3036, found 778.3030.

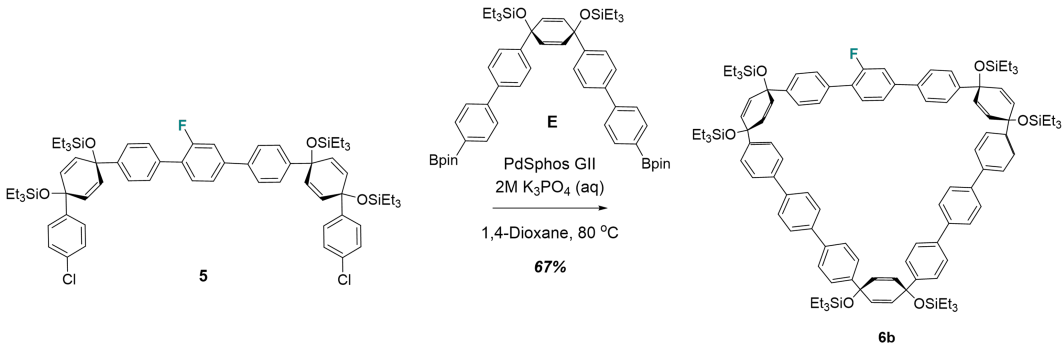

Compound 6b. Compound E (0.157 g, 0.32 mmol) was added with compound 5 (0.35 g, 0.31 mmol), Pd Sphos GII (0.048 g, 20 mol%) to a flame-dried rbf and put under high vac for 1 hour. The reaction vessel was purged with nitrogen 3 times, then 1,4-dioxane (305 mL, 1 mM) added via cannula then heated to 80 °C. Sparged 2M K3PO4 (31 mL, 1 mM) was added dropwise and the reaction was allowed to stir overnight. The next morning the reaction was reduced under pressure to remove the dioxane solvent. DCM was added to the crude sludge left behind and sonicated. This solution was then poured over a celite plug topped with a thin pad of silica on top. The plug was sufficiently flushed with 100 % DCM. Added filtered reaction solution to a rbf and concentrated

down to afford a brown sticky oil. This oil was then dissolved in small amount of DCM to be adsorbed on silica for column purification. Rotovapped the dcm+silica down then put on high vac until completely dry. Column purification was performed (30-50% DCM:Hexanes), product fractions were combined reduced on vacuum, then triturated out with methanol to afford an off-white solid (0.301 g, 63%). ^{1}H NMR (500 MHz, Methylene Chloride-d_2) δ 7.96 – 7.17 (m, 35H), 6.23 – 5.54 (m, 12H), 0.97 (q, J = 7.1, 6.2 Hz, 53H), 0.65 (ddt, J = 14.7, 10.6, 5.4 Hz, 36H).^{13}C NMR (126 MHz, Methylene Chloride-d_2) δ 159.59 (d, J = 256.7 Hz), 146.49, 146.21, 145.85, 139.92, 134.66, 132.06, 132.00, 131.94, 131.83, 131.31, 129.08, 127.68, 127.66, 127.05, 127.01, 126.94, 126.83, 126.46, 123.19, 71.92, 71.90, 71.76, 7.26, 6.86, 6.83. ^{19}F NMR (471 MHz, Methylene Chloride-d_2) δ -118.21 (dd, J = 12.0, 7.9 Hz). HRMS (MALDI,TOF), m/z calculated for $C_{108}H_{137}FO_6Si_6$ $(M+H)^+$ 1716.9015, found 1716.9009.

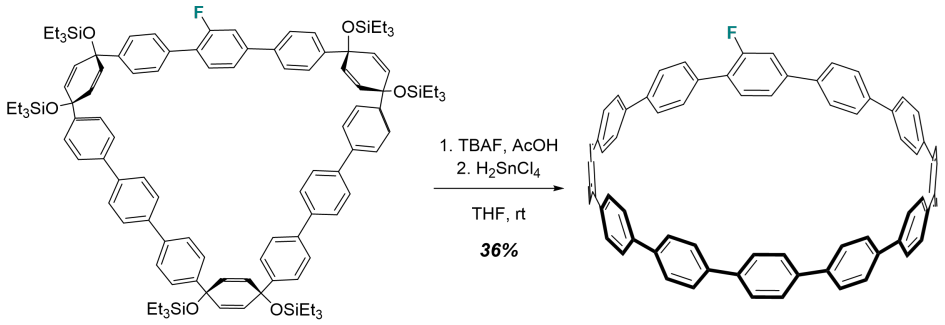

6b 7b

Compound 7b. In flame dried flask, dissolved compound 6b (0.31 g, 1.8x10^{-1} mmol) in dry THF (23 mL), resulting in clear solution. Acetic acid (0.5 mL) added quickly dropwise, followed by Tetrabutyl ammonia fluoride (TBAF) (4.5 mL) very slowly dropwise, allowed to stir at roomtemp overnight. Next day ~10 mL DI water added to reaction mixture, resulting in a yellow-white suspension, and the solution was subsequently rotovapped to remove THF. Vacuum filtration afforded a beige solid rinsed with more water and DCM. The solid and the filter paper it was on was left on house vac for a few hours then left overnight to air dry (no vac). Solid was transferred to a weigh paper for yield then to be moved on for aromatization (quant. yield). SnCl2•2H2O (0.41 g, 1.82 mmol) was dried on high-vac for 30 mins then added to a flame-dried 25 mL round-bottom flask. The flask was cycled with nitrogen and THF (2.5 mL) was added followed by conc. HCl (0.30 mL,

12 N, 3.63 mmol) at room temperature. After stirring for 30 min., the resulting solution was added to a suspension of macrocycle (0.162 g, 0.16 mmol) in THF (30 mL), and the resulting mixture was stirred at room temp overnight. #The solvent was removed under reduced pressure at 40 C, and the residue was taken up in DCM (sonicated) and purified by passing over a short alumina plug with DCM as an eluent (~300 mL). The filtrate was reduced with roto-evaporation at 40 C. The resulting solid was dispersed in MeOH, and let air dry then put on high-vac to remove grease impurities to give pure CPP (0.053 g, 36%) as a pale-yellow solid. ~50:50 DCM:Hex should give pretty good separation). ^{1}H NMR (500 MHz, Methylene Chloride-d_2) δ 7.71 – 7.59 (m, 44H), 7.48 – 7.38 (m, 2H), 7.34 (dd, J = 8.4, 1.8 Hz, 1H).^{13}C NMR (126 MHz, Methylene Chloride-d_2) δ 160.44 (d, J = 248.5 Hz), 141.05 (d, J = 8.1 Hz), 139.32, 138.55, 138.50, 138.48, 138.45, 134.34, 131.32, 128.87, 128.84, 127.40, 127.36, 127.33, 127.30, 127.28, 127.24, 127.09, 123.87, 119.34, 114.14, 113.95. ^{19}F NMR (471 MHz, Methylene Chloride-d_2) δ -115.85 (m). HRMS (MALDI,TOF), m/z calculated for $C_{72}H_{47}F$ $(M)^+$ 930.3662, found 930.3656.

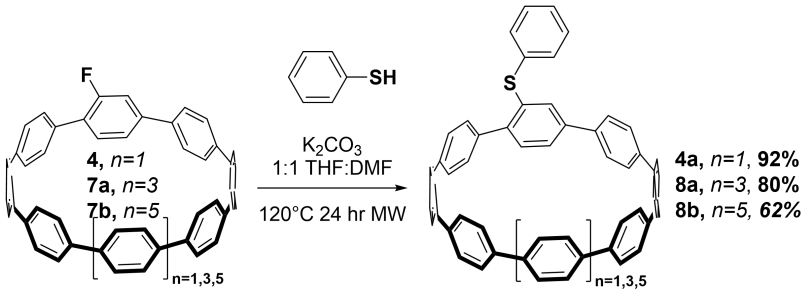

General procedure for S_NAr Substitution. **4a.:** Solid CPP **4** (1.8 mg, 2.9x10^{-3} mmol) and K_2CO_3 (5 mg, 3.4x10^{-2} mmol crushed) were added to a microwave flask, which was then evacuated and backfilled with nitrogen three times. 1:1 Dry THF and DMF (0.25mL:0.25mL) was added via syringe followed by thiophenol (2 microliters, 1.7x10^{-2} mmol). The mixture was allowed to react for 24 hrs in a microwave reactor at 120°C. After 24 hr the mixture (yellowish solids and solvent) was removed from vial with water, further basified with 1M K_2CO_3, yellow solids collected via vacuum filtration rinsed with water and methanol. The residue was dissolved in DCM and washed with basic water, dried over sodium sulfate and reduced under pressure to afford an tan solid (2 mg, 97% yield). ^{1}H NMR (500 MHz, Methylene Chloride-d_2) δ 7.61 – 7.47 (m, 19H), 7.45 – 7.40

(m, 4H), 7.32 (ddd, J = 7.7, 6.7, 4.5 Hz, 9H), 7.29 – 7.22 (m, 5H). HRMS (MALDI,TOF), m/z calculated for $C_{54}H_{36}S$ $(M)^+$ 716.2538, found 716.2532. **8a.:** The titled compound was prepared from **7a** (3.6 mg, $4.6x10^{-3}$ mmol), K_2CO_3 (12 mg, $8.3x10^{-2}$ mmol crushed), DMF:THF (0.5 mL 1:1), thiophenol (5 microliters, $4.6x10^{-2}$ mmol) according to the general procedure. Yellow solid recovered (3.2 mg, 80% yield). ^{1}H NMR (500 MHz, Acetone-d_6) δ 7.98 (s, 1H), 7.83 – 7.63 (m, 7H), 7.59 – 7.53 (m, 8H), 7.51 – 7.43 (m, 6H), 7.38 (ddd, J = 15.4, 8.4, 7.1 Hz, 14H), 7.34 – 7.25 (m, 8H).HRMS (MALDI,TOF), m/z calculated for $C_{66}H_{44}S$ $(M)^+$ 868.3158, found 868.3164. **8b.:** The titled compound was prepared from **7b** (3.1 mg, $3.3x10^{-3}$ mmol), K_2CO_3 (11 mg, $8.3x10^{-2}$ mmol crushed), DMF:THF (0.5 mL 1:1), thiophenol (4 microliters, $4.6x10^{-2}$ mmol) according to the general procedure. Yellow solid recovered (2.1 mg, 62% yield). ^{1}H NMR (500 MHz, Methylene Chloride-d2) δ 7.65 (d, J = 6.4 Hz, 33H), 7.58 – 7.37 (m, 9H), 7.32 (t, J = 7.5 Hz, 7H), 7.28 – 7.21 (m, 3H).HRMS (MALDI,TOF), m/z calculated for $C_{78}H_{52}S$ $(M)^+$ 1020.3790, found 1020.3784.

II. Structural Characterization *^{1}H NMR*

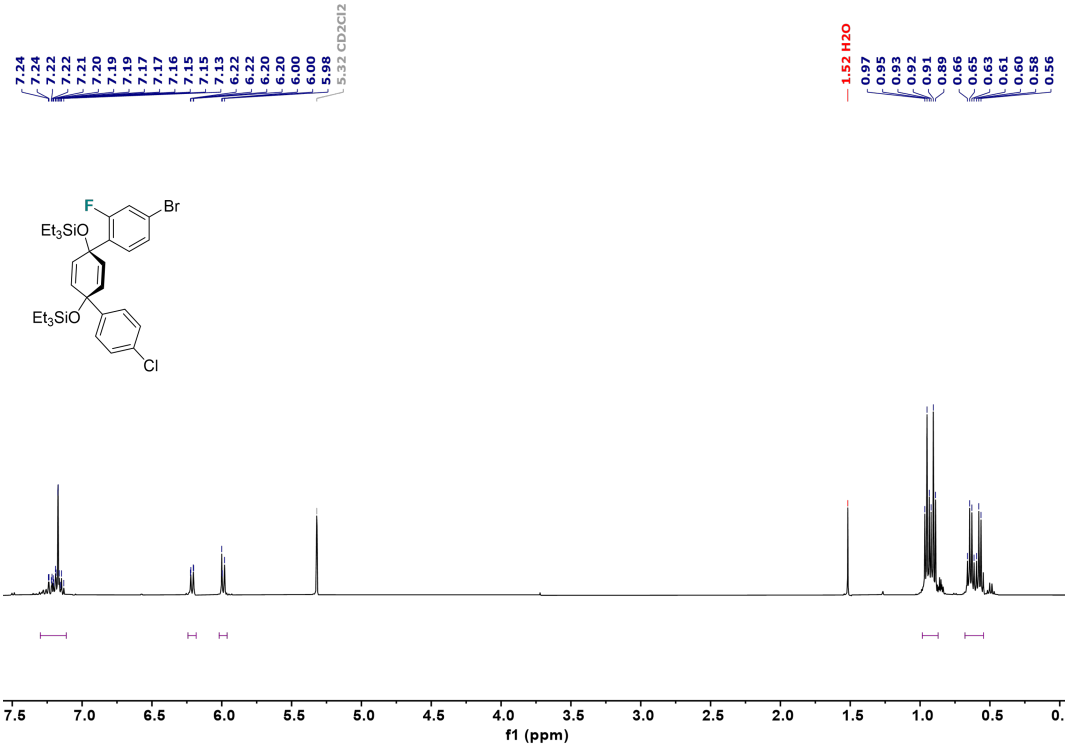

Figure S1. ^{1}H NMR of compound **1**.

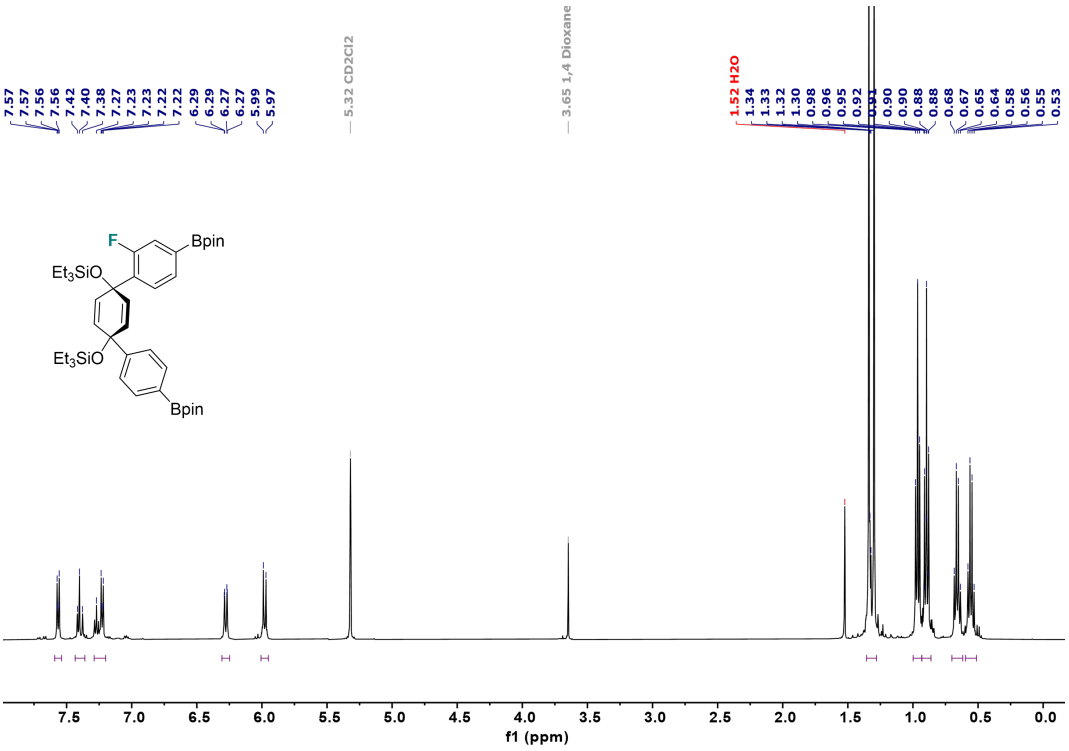

Figure S2. ^{1}H NMR of compound **2**.

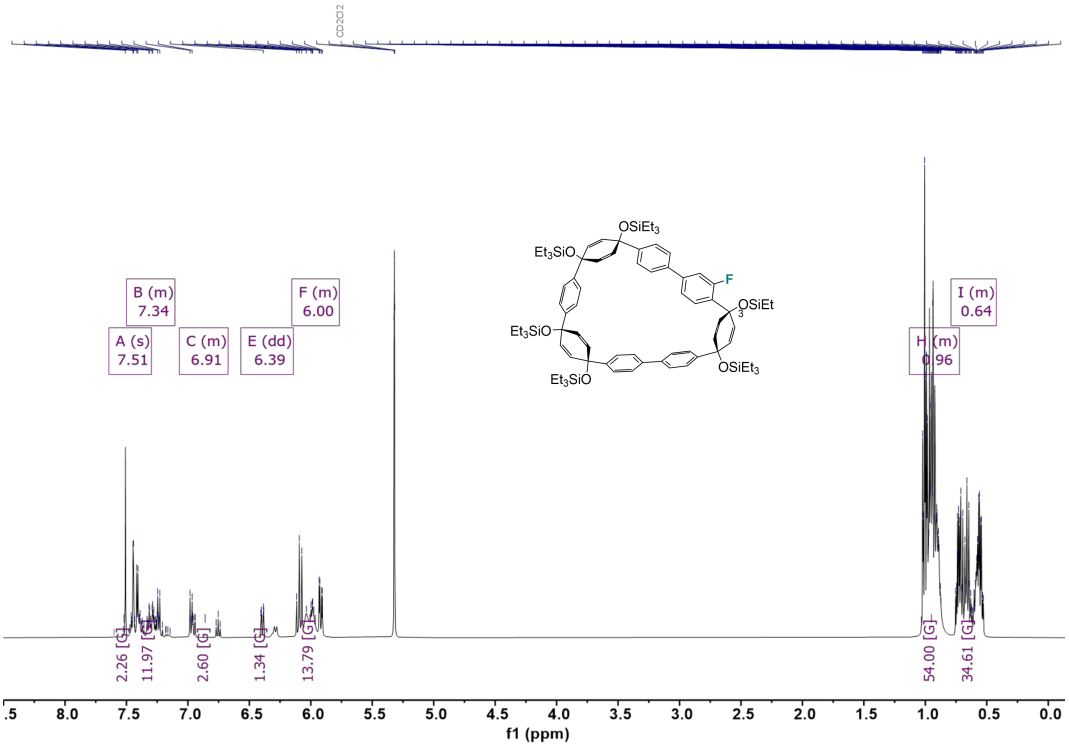

Figure S3. ^{1}H NMR of compound **3**.

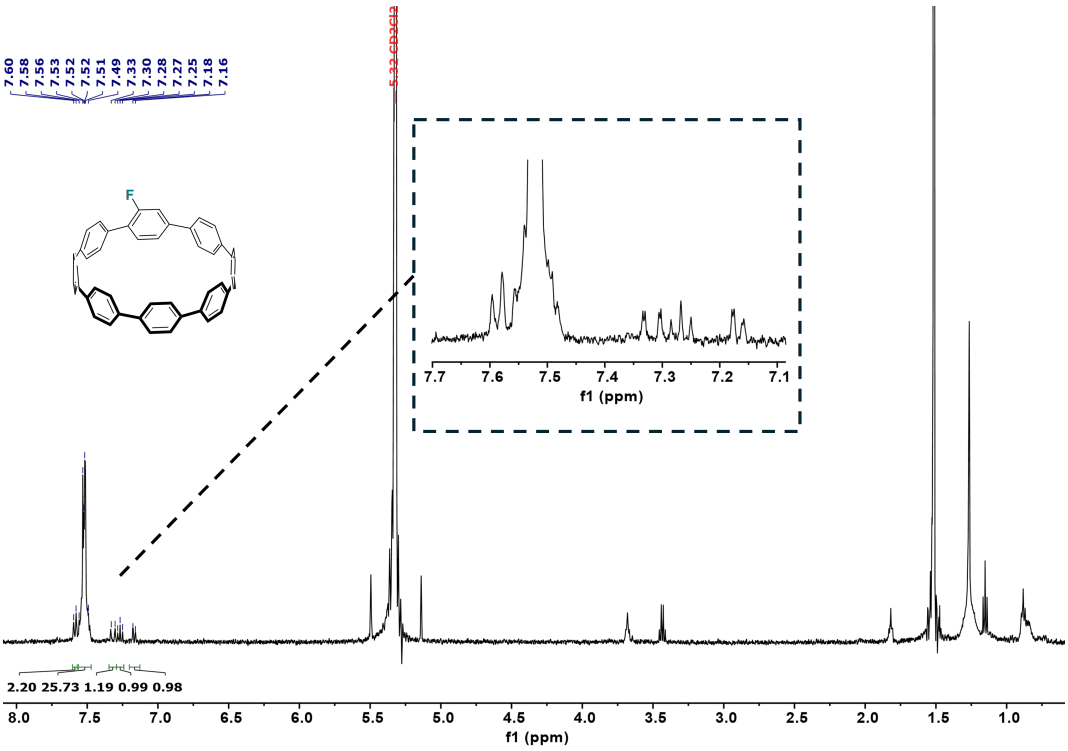

Figure S4. ^{1}H NMR of compound **4**.

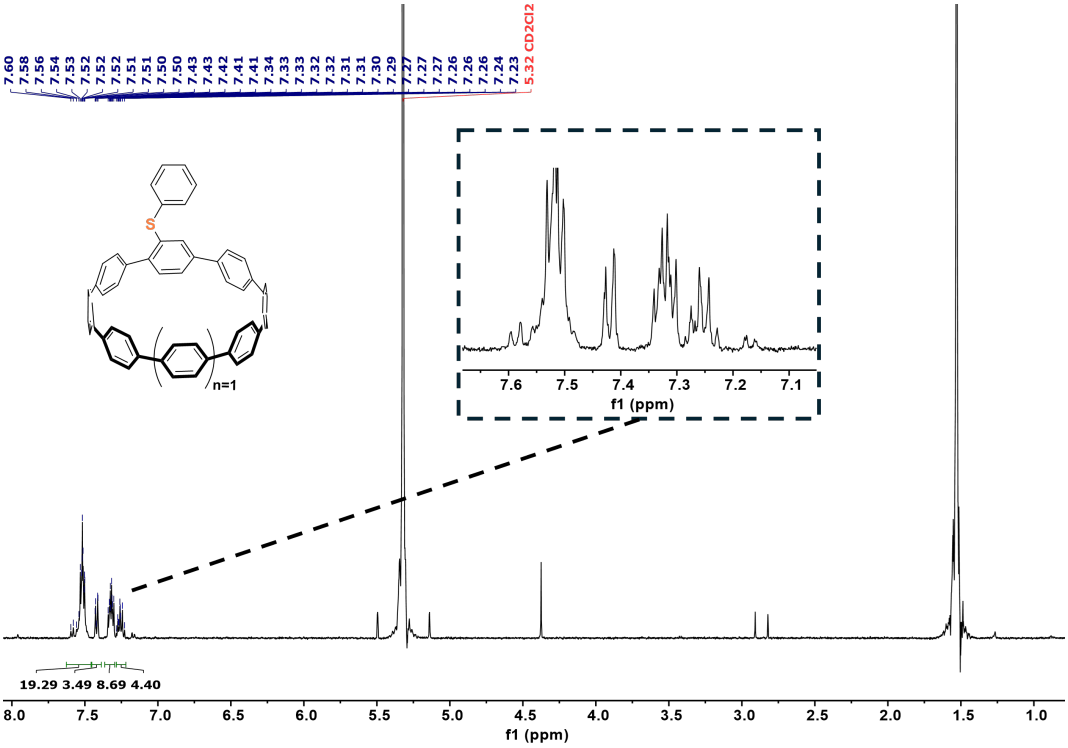

Figure S5. ^{1}H NMR of compound **4a**.

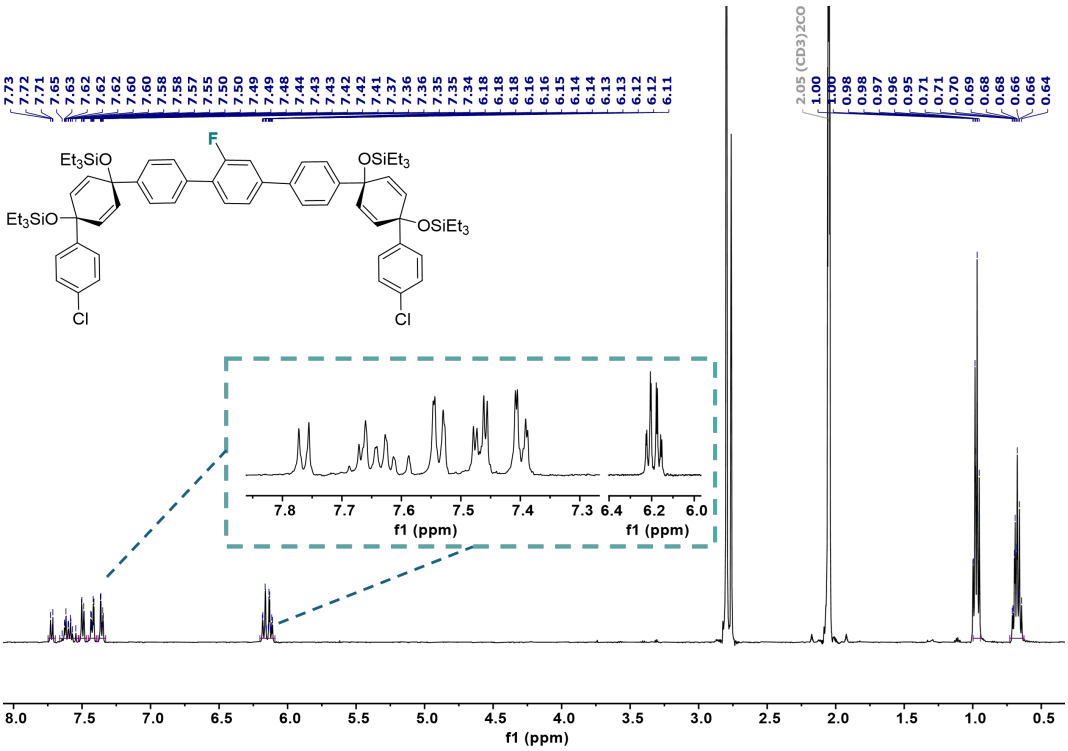

Figure S6. ^{1}H NMR of compound **5**.

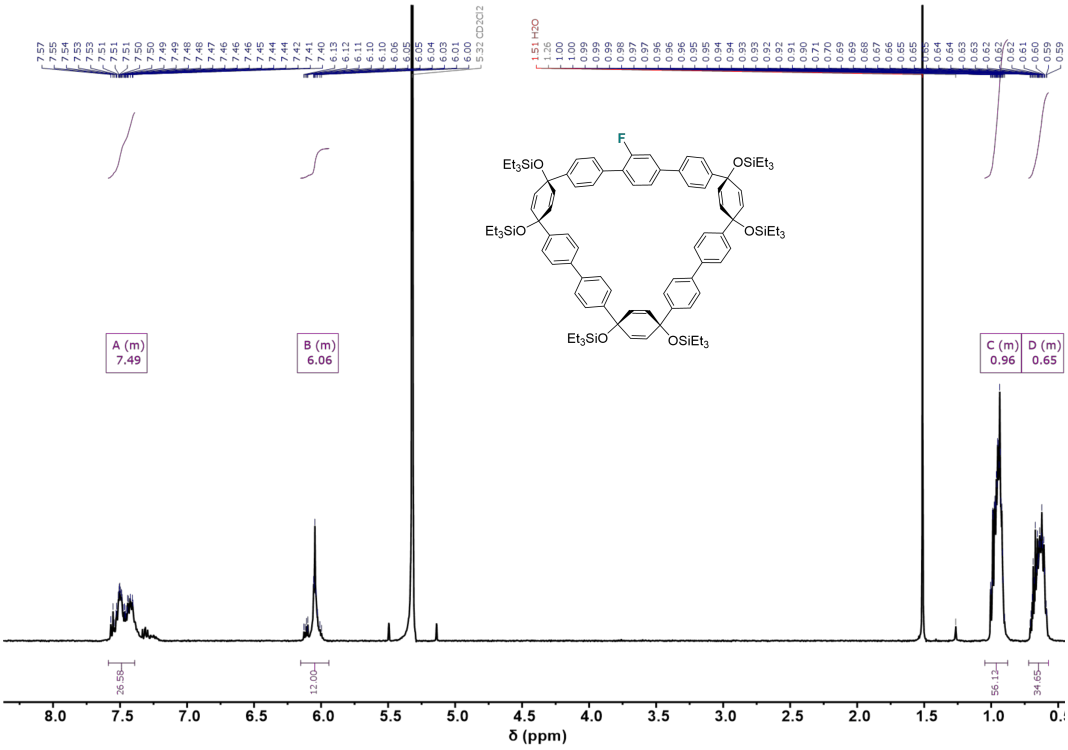

Figure S7. ^{1}H NMR of compound **6a**.

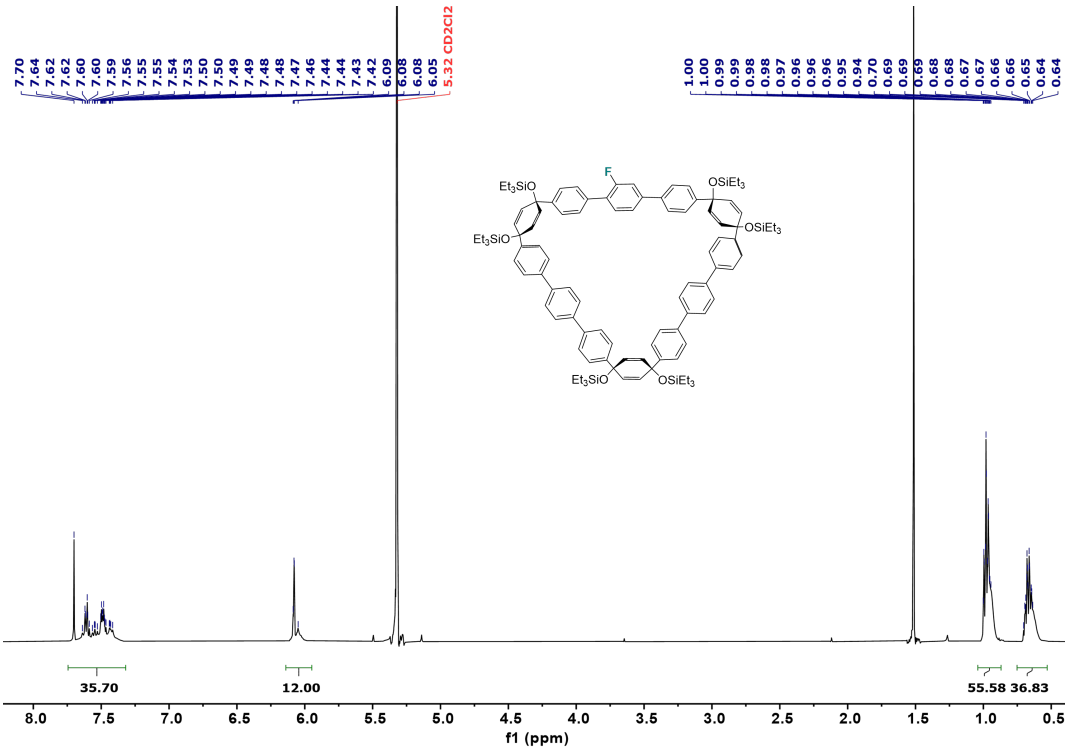

Figure S8. ^{1}H NMR of compound **6b**.

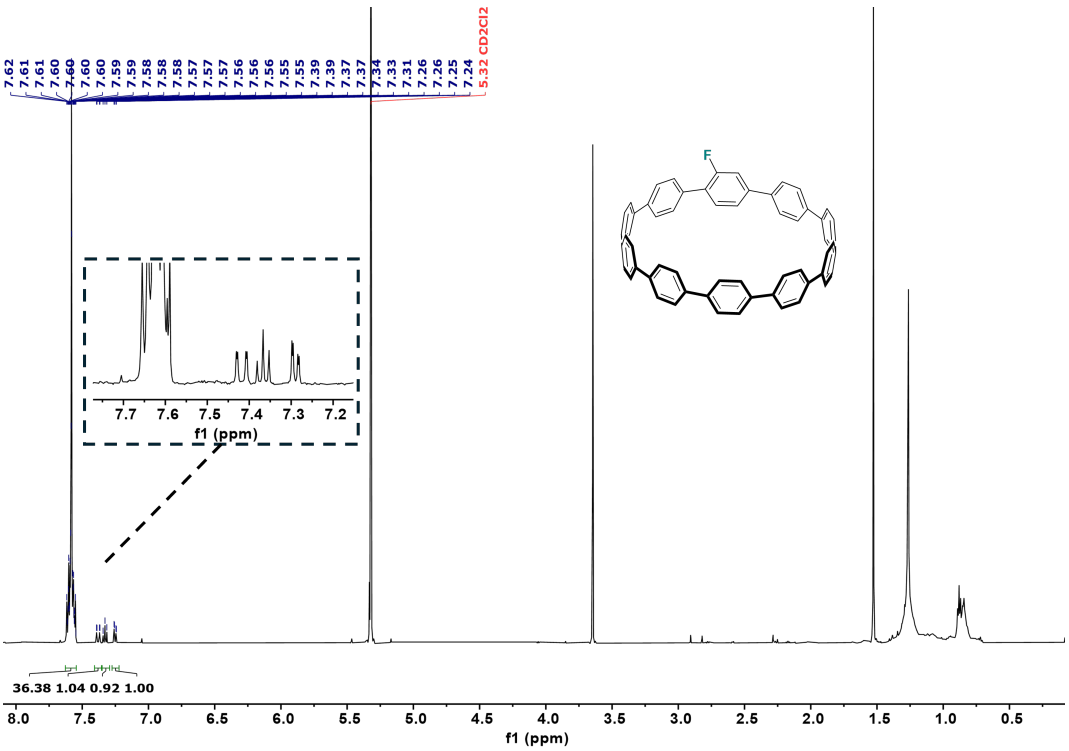

Figure S9. ^{1}H NMR of compound **7a**.

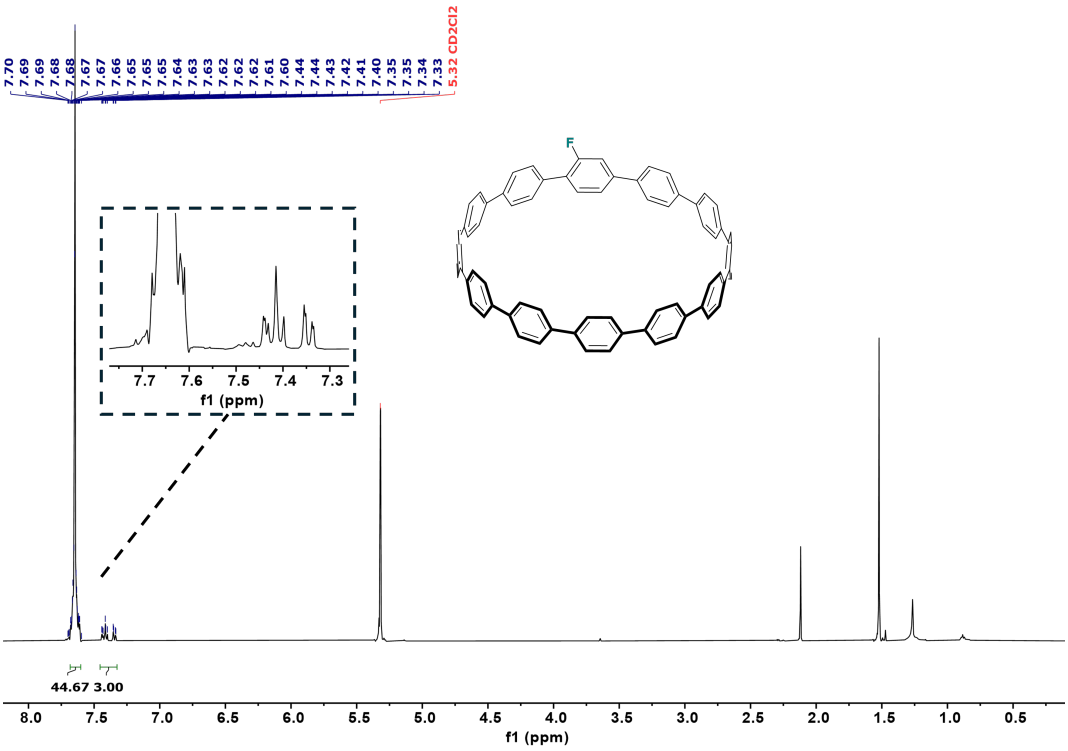

Figure S10. ^{1}H NMR of compound **7b**.

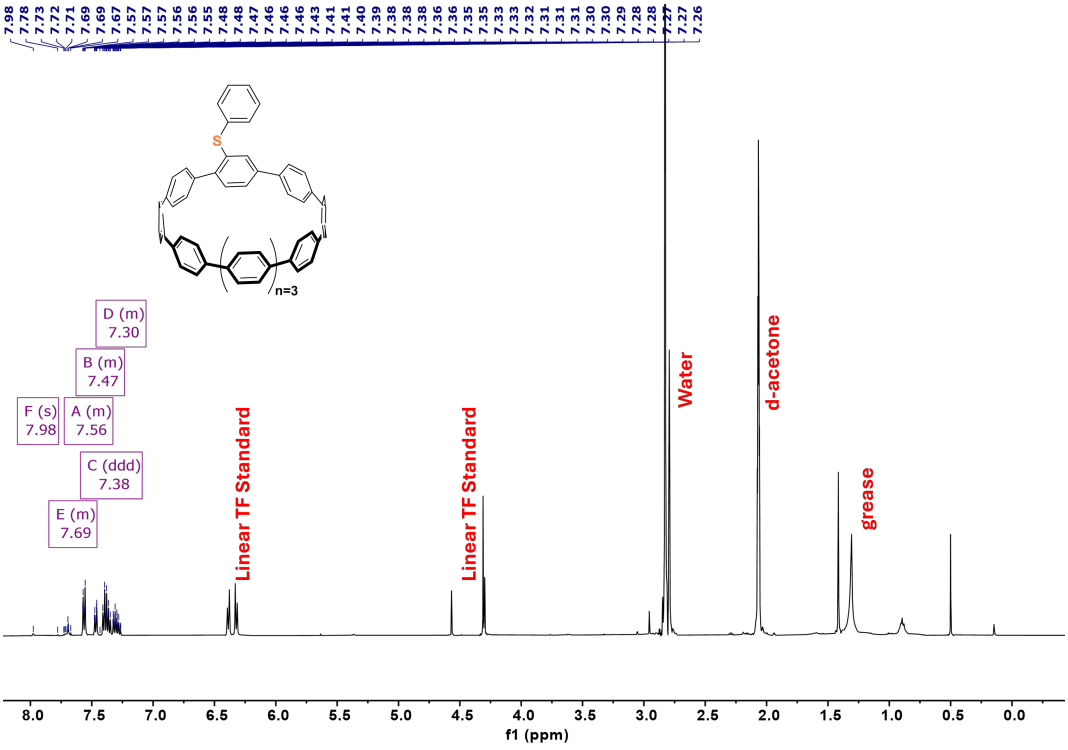

Figure S11. ^{1}H NMR of compound **8a**.

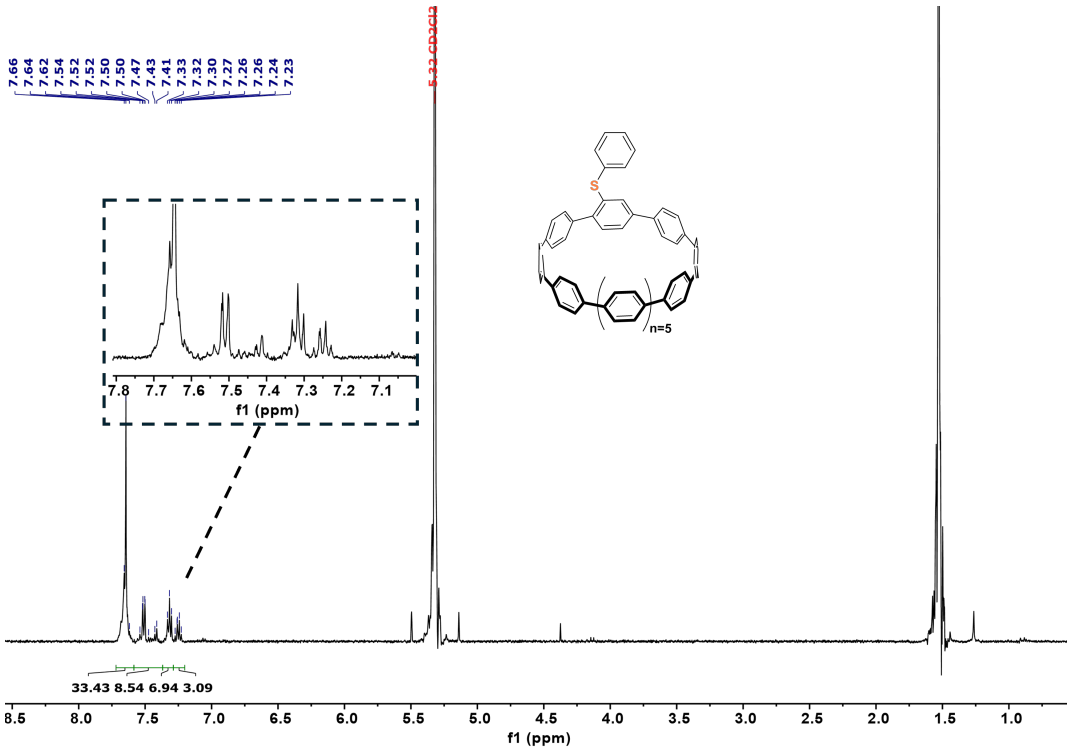

Figure S12. ^{1}H NMR of compound **8b**.

^{13}C NMR

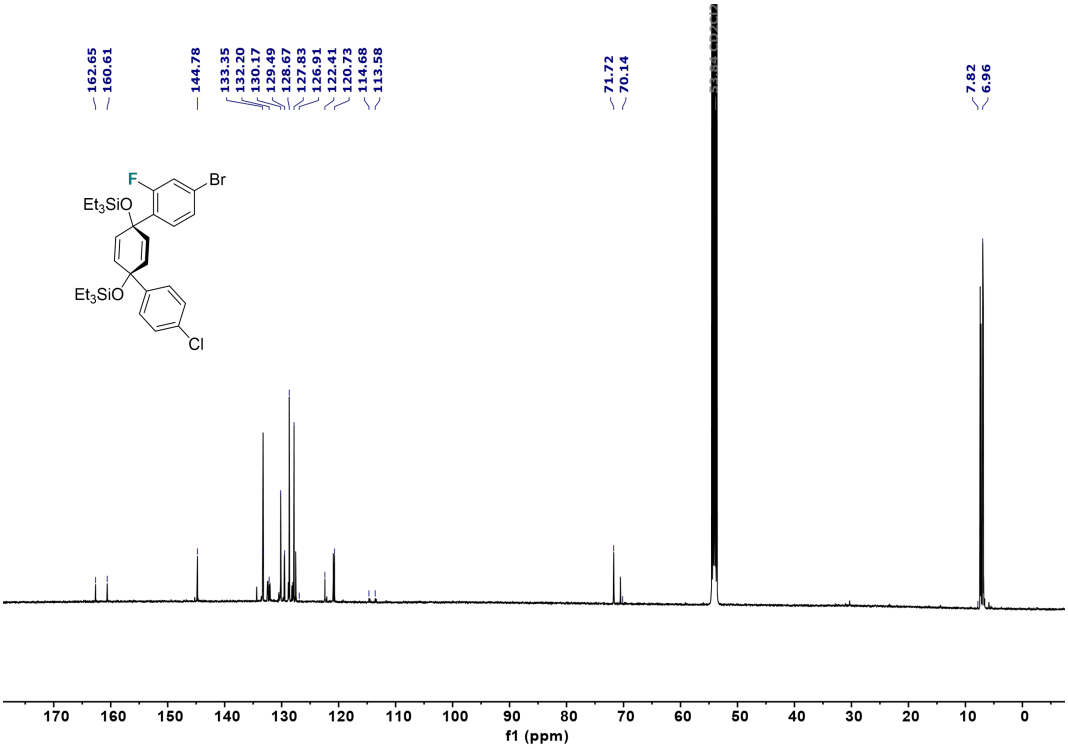

Figure S13. ^{13}C NMR of compound **1**.

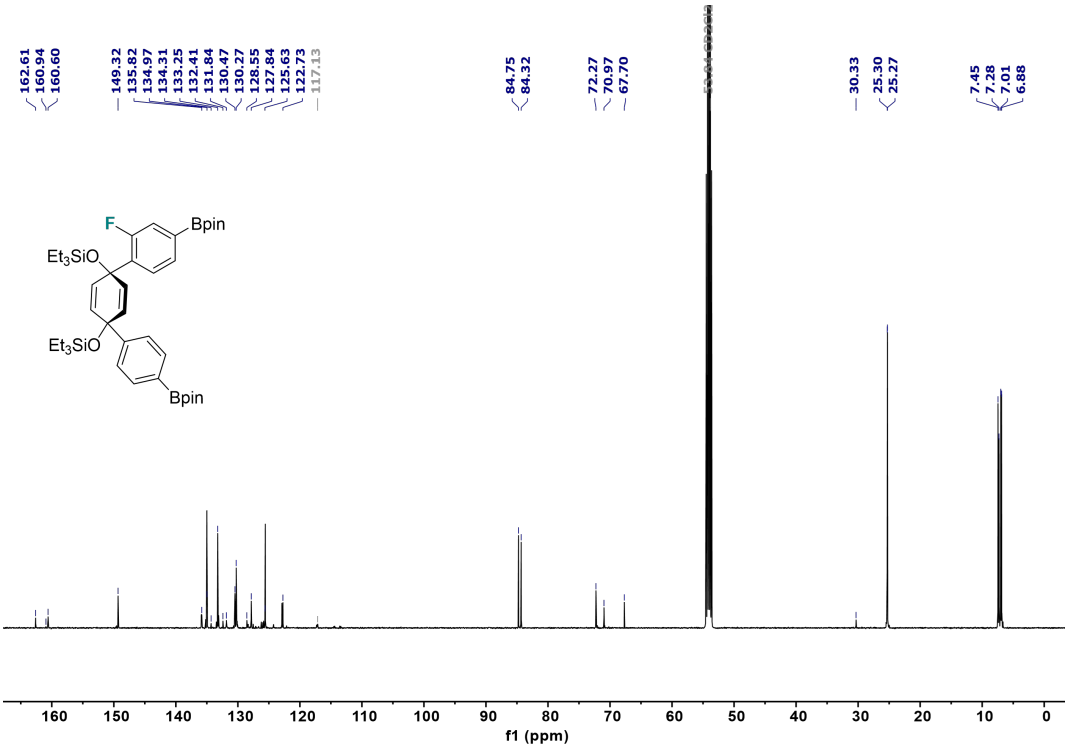

Figure S14. ^{13}C NMR of compound **2**.

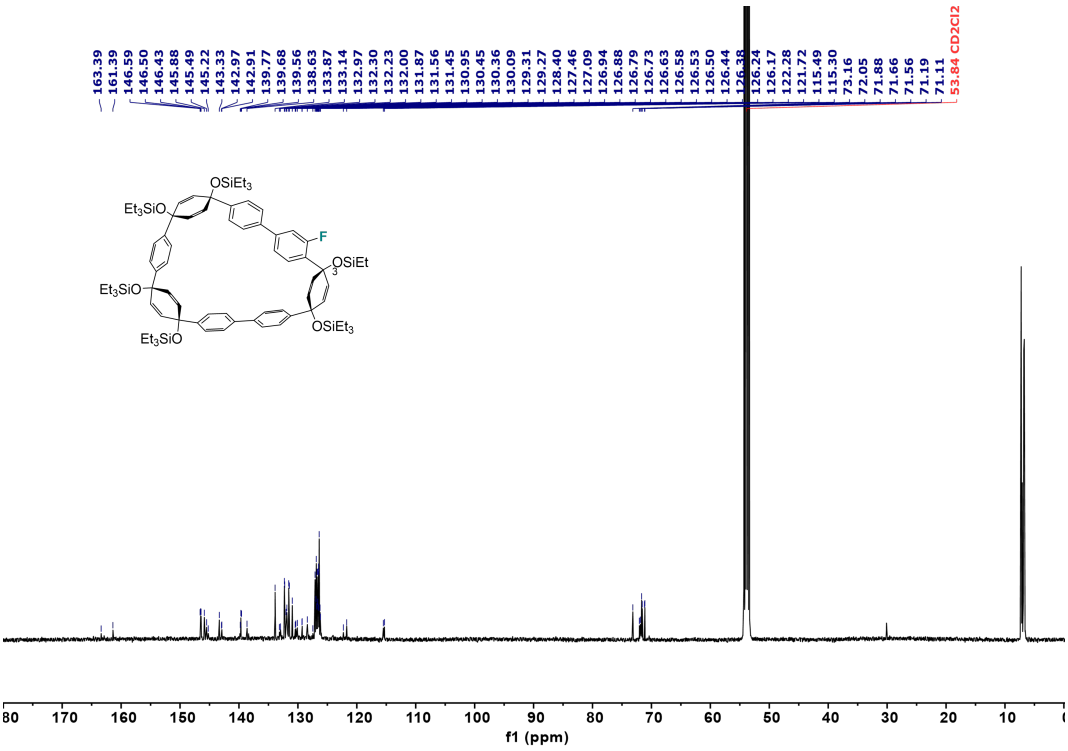

Figure S15. ^{13}C NMR of compound **3**.

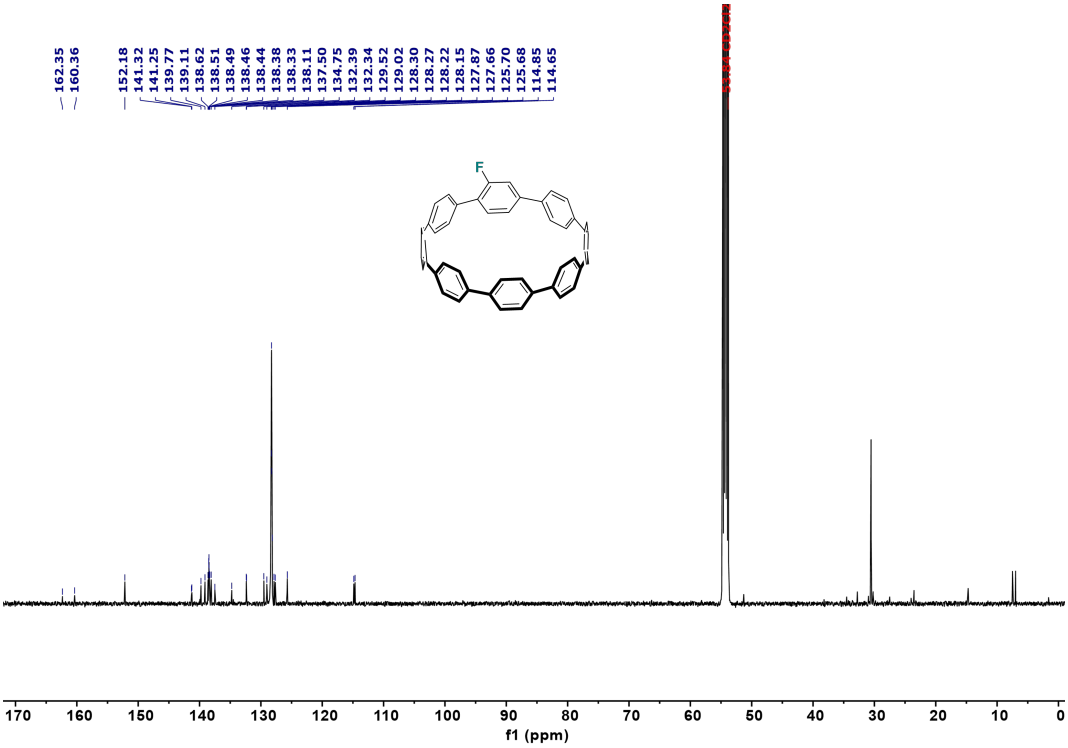

Figure S16. ^{13}C NMR of compound **4**.

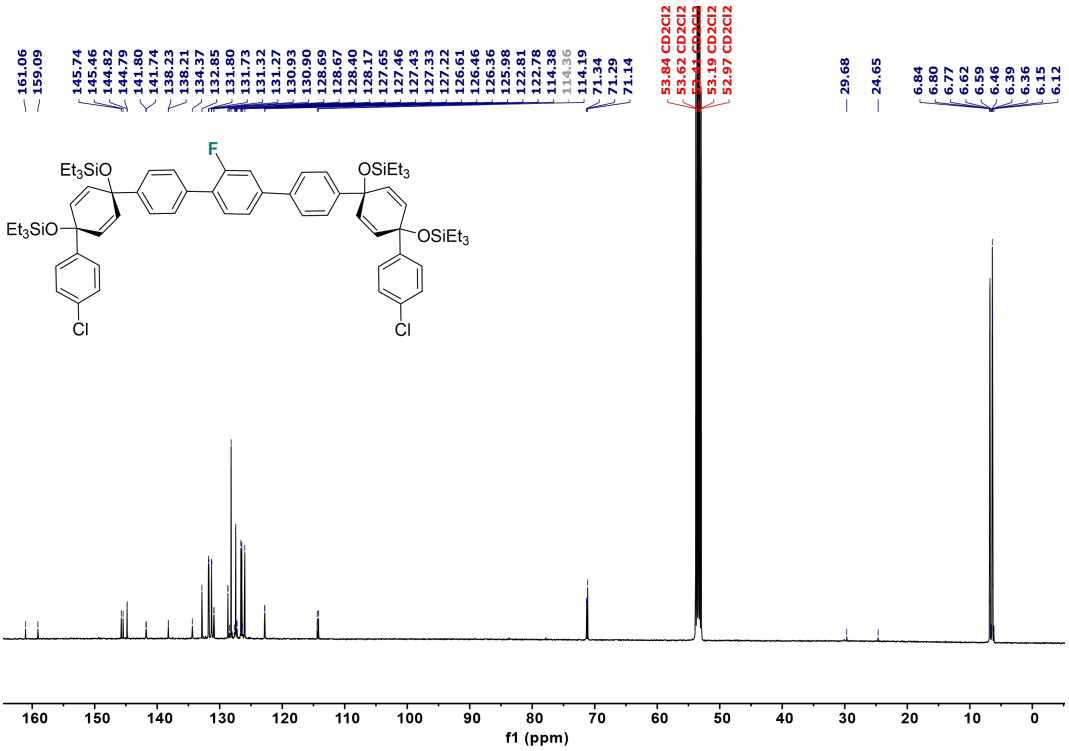

Figure S17. ^{13}C NMR of compound **5**.

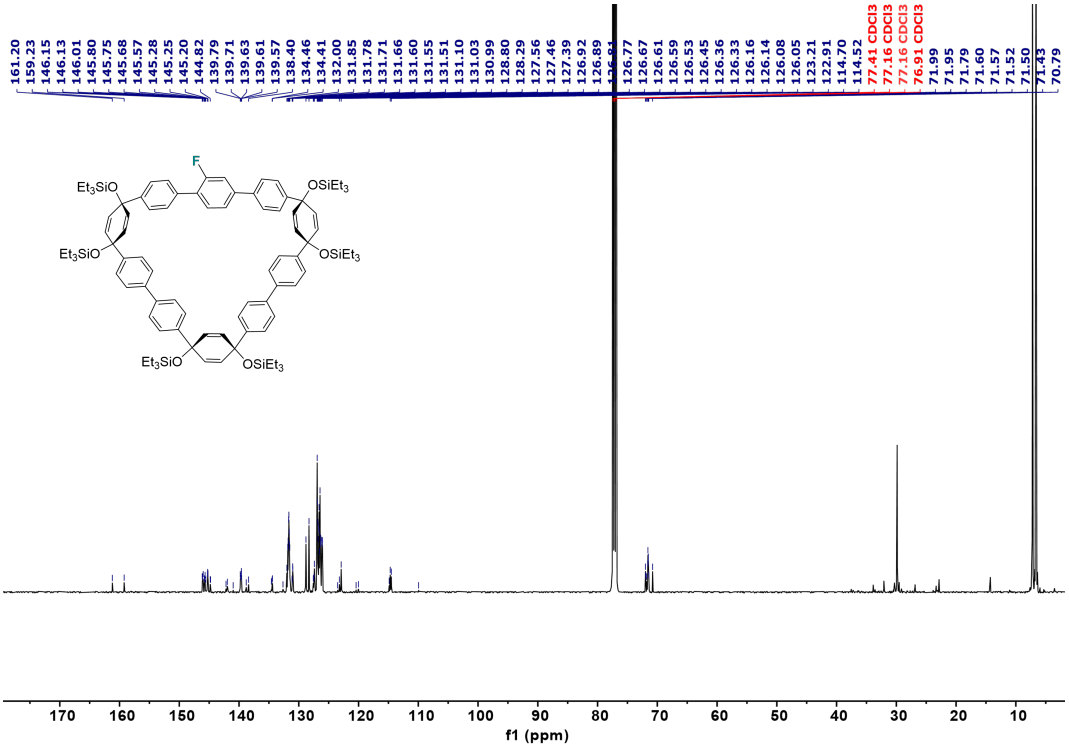

Figure S18. ^{13}C NMR of compound **6a**.

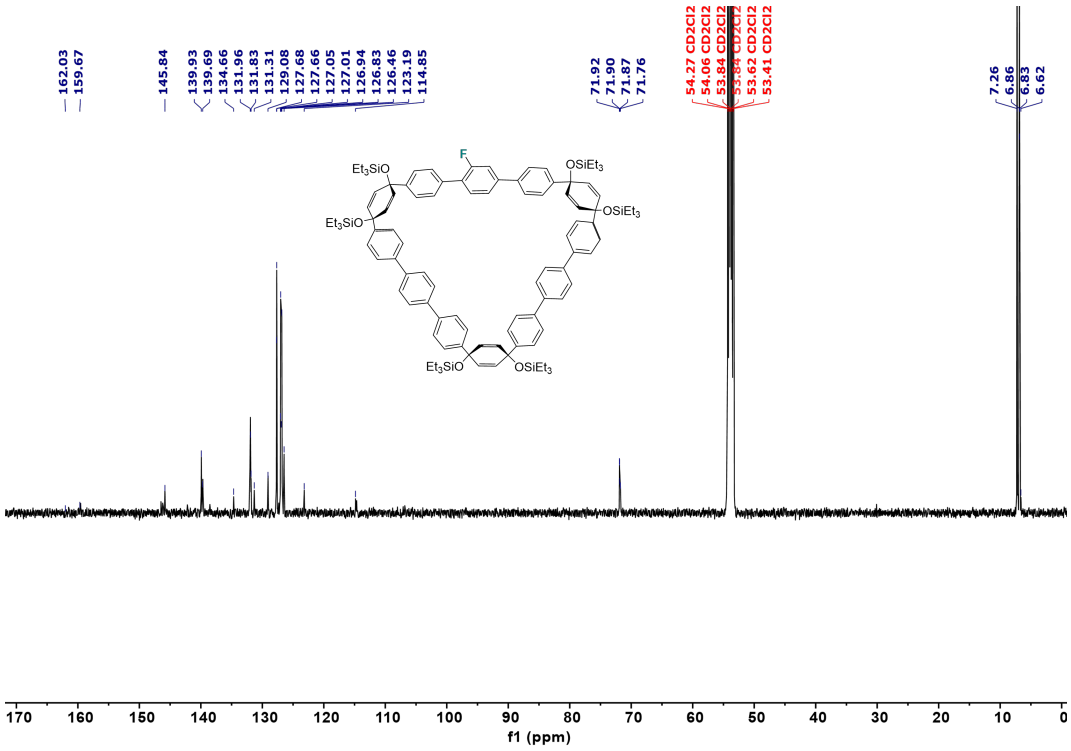

Figure S19. ^{13}C NMR of compound **6b**.

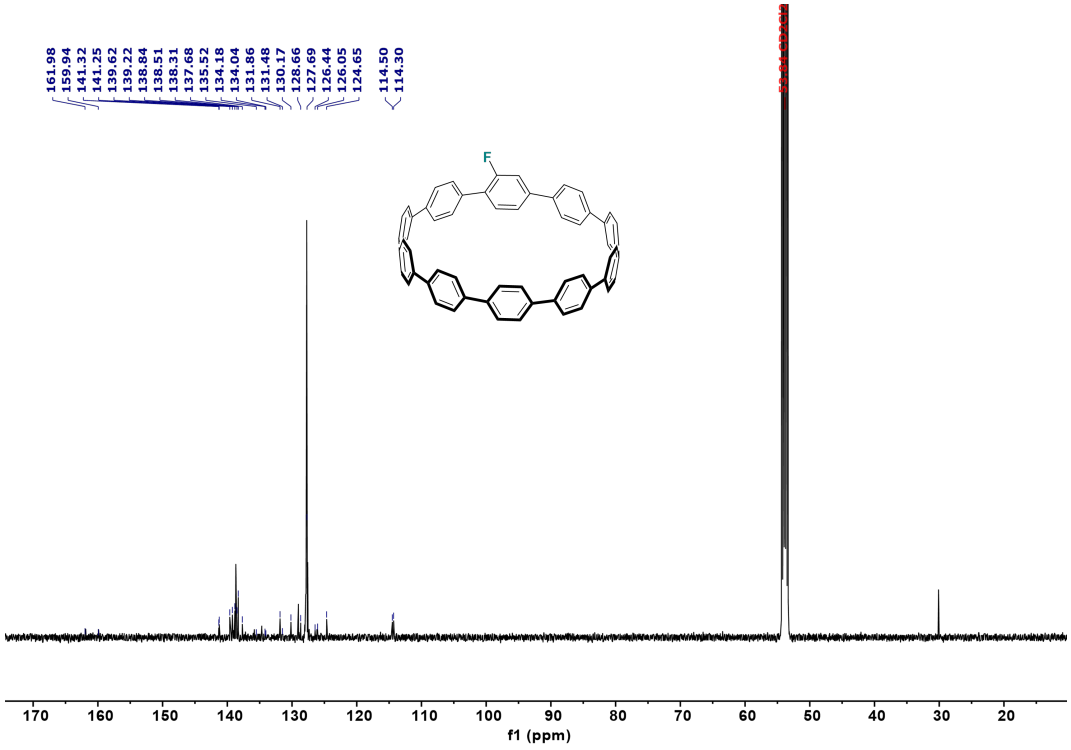

Figure S20. ^{13}C NMR of compound **7a**.

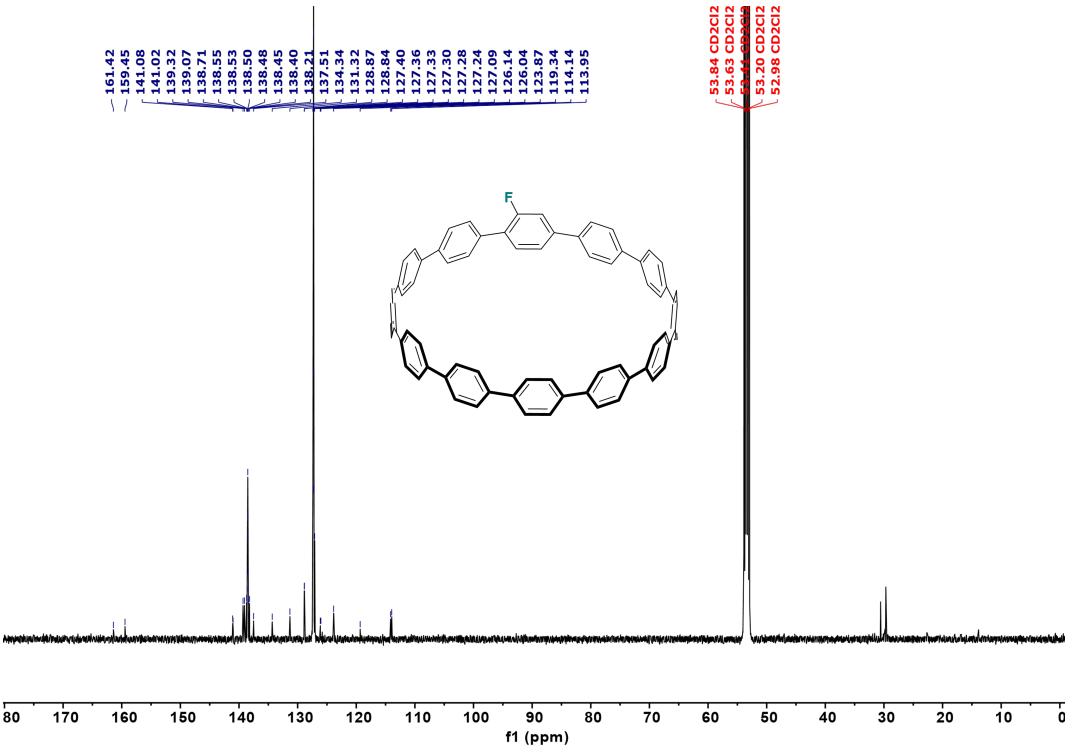

Figure S21. ^{13}C NMR of compound **7b**.

^{19}F NMR

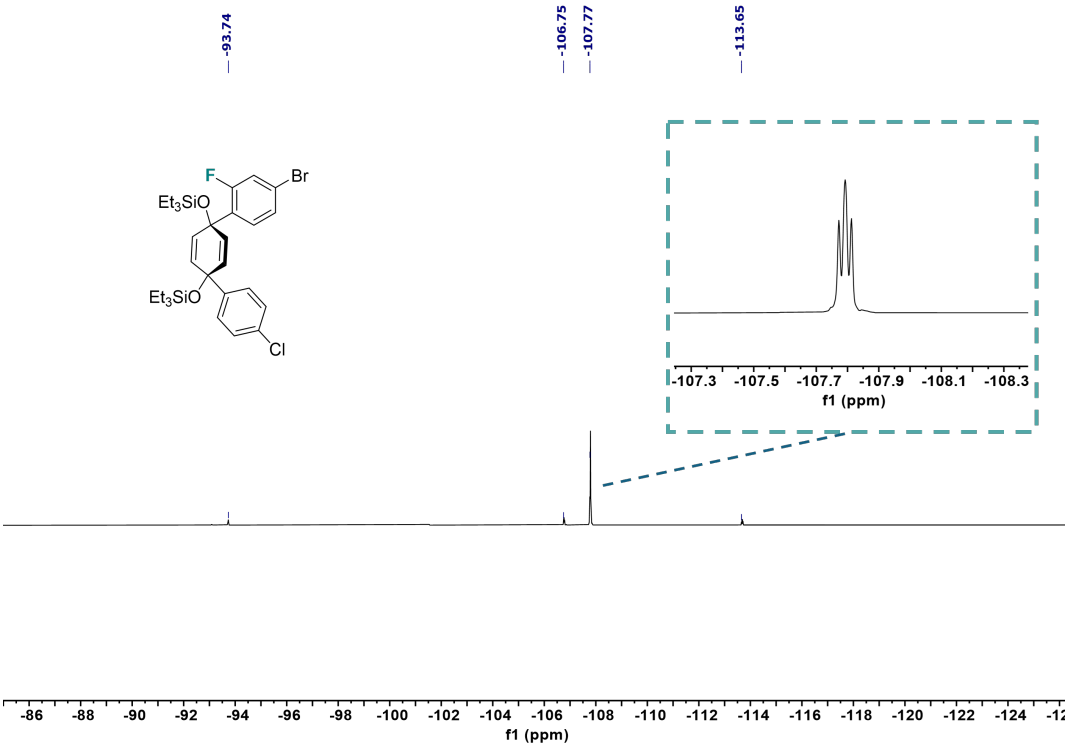

Figure S22. ^{19}F NMR of compound **1**.

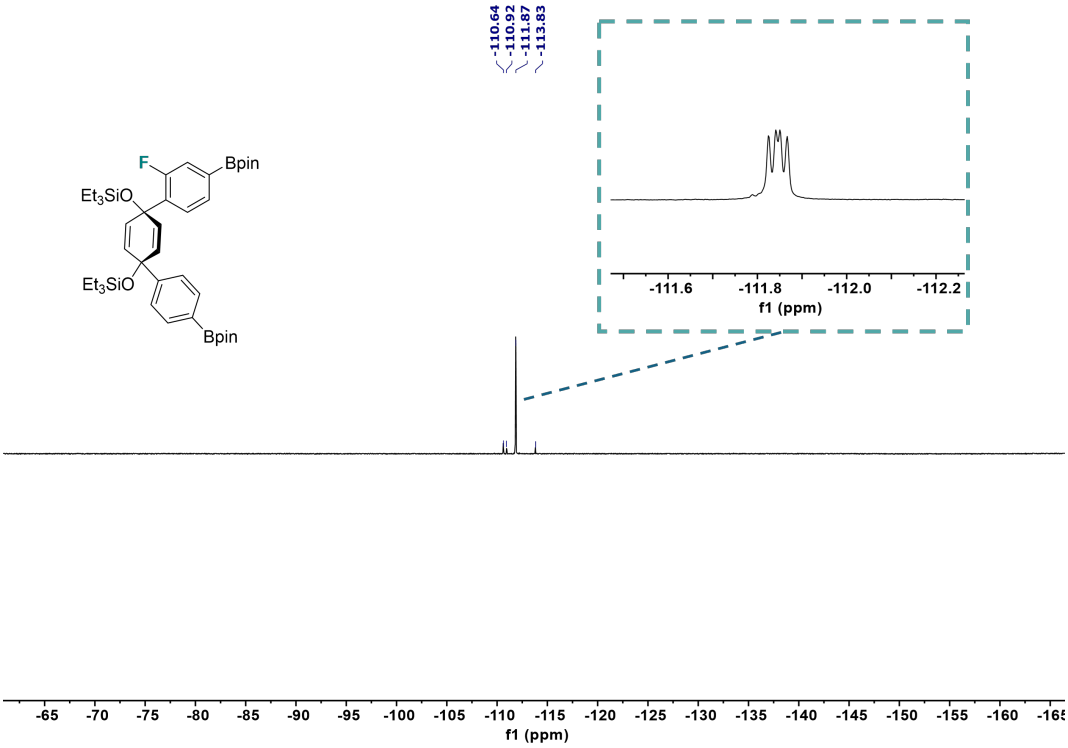

Figure S23. ^{19}F NMR of compound **2**.

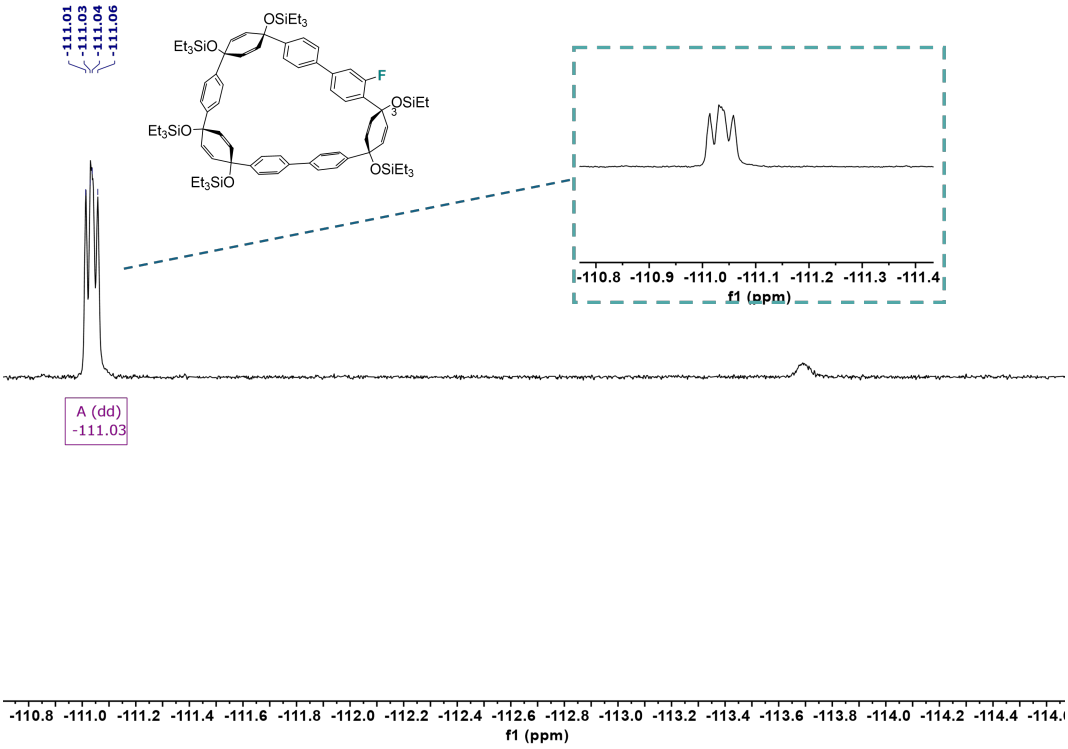

Figure S24. ^{19}F NMR of compound **3**.

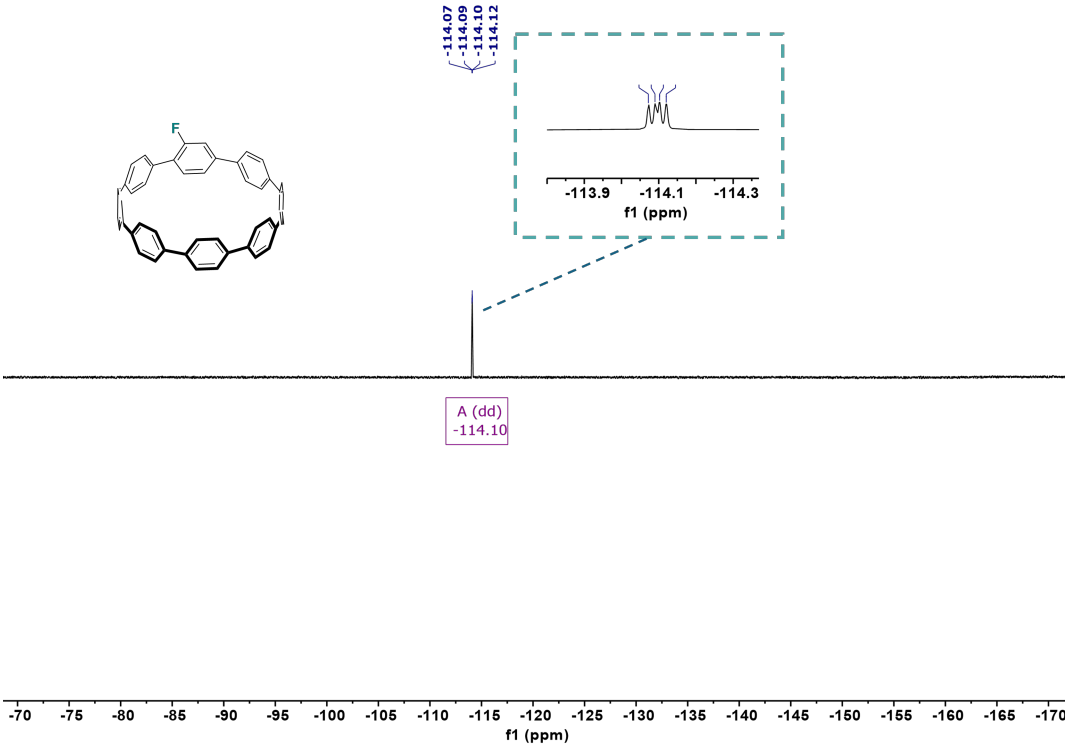

Figure S25. ^{19}F NMR of compound **4**.

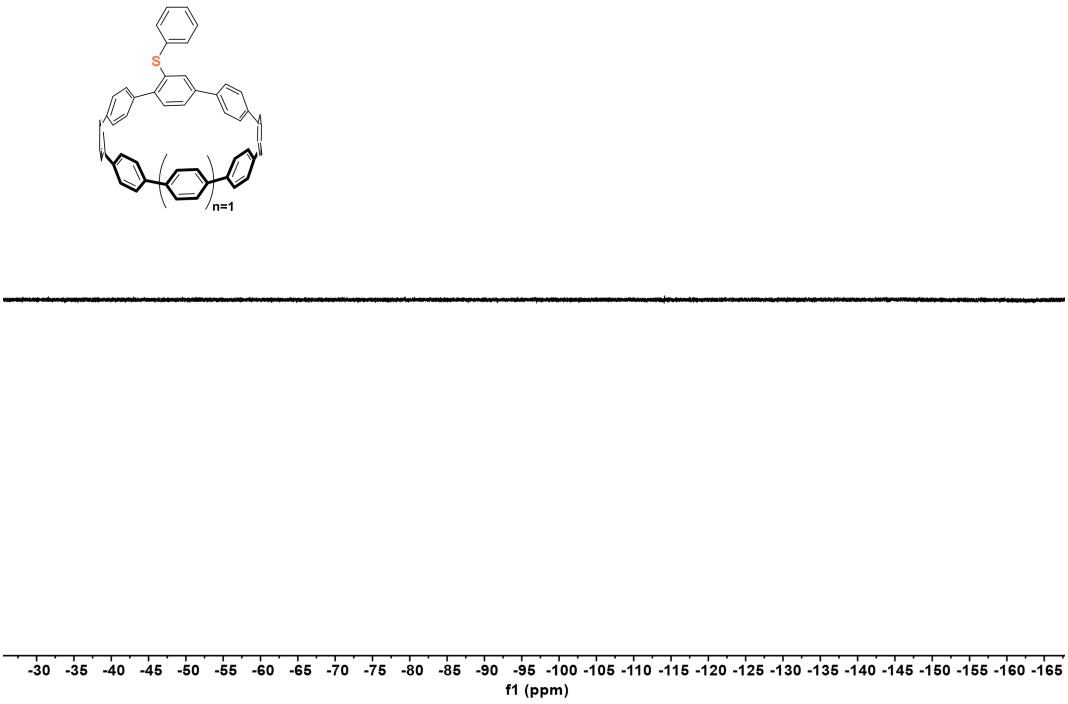

Figure S26. ^{19}F NMR of compound **4a**.

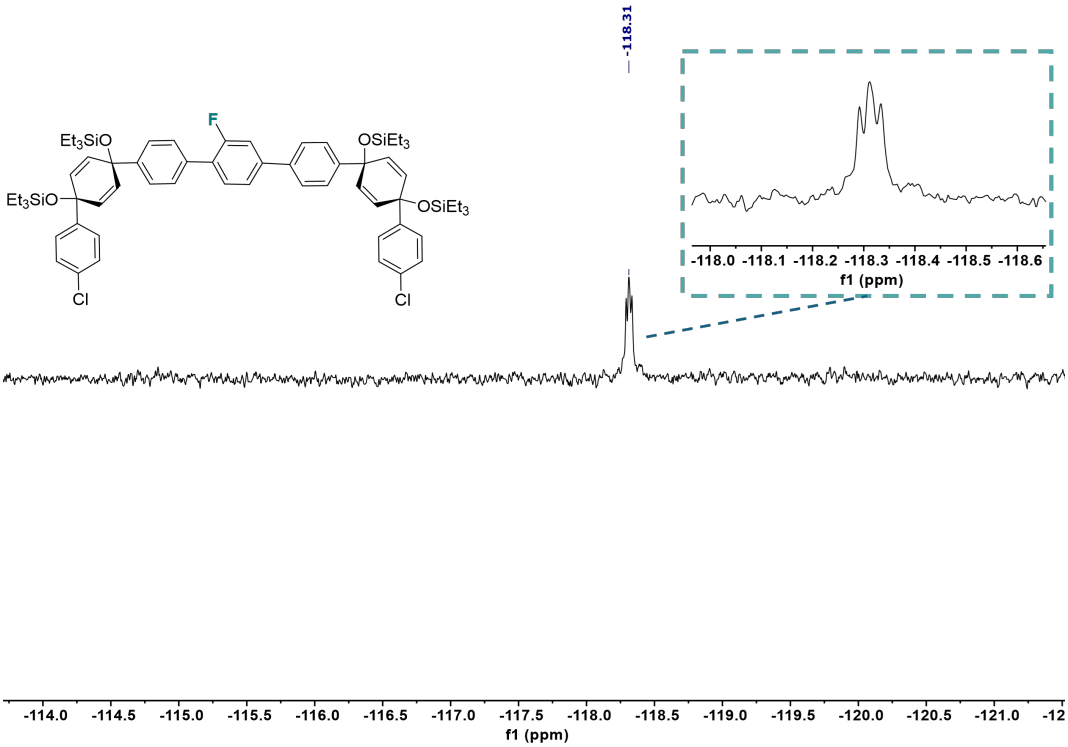

Figure S27. ^{19}F NMR of compound **5**.

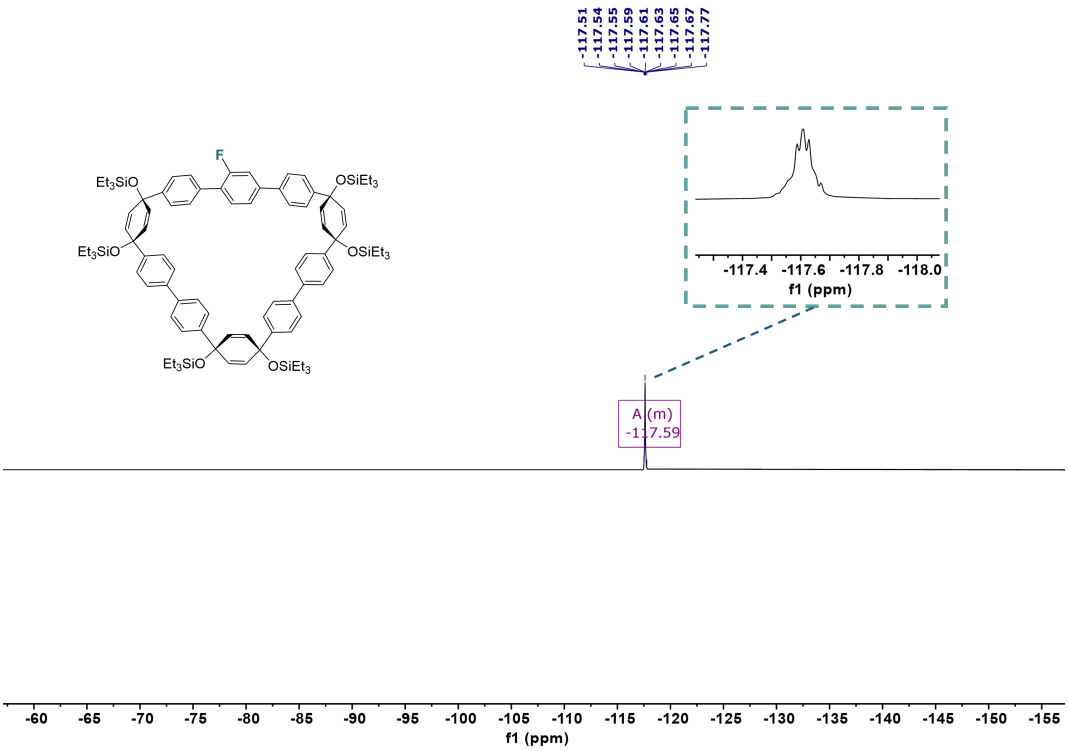

Figure S28. ^{19}F NMR of compound **6a**.

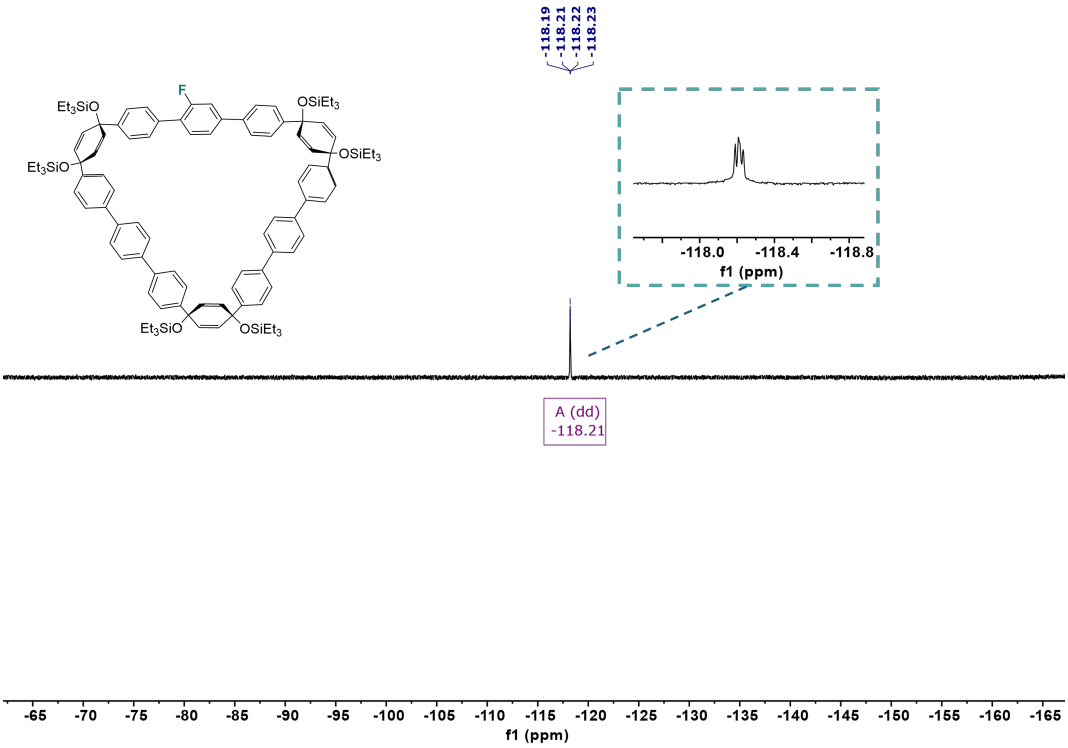

Figure S29. ^{19}F NMR of compound **6b**.

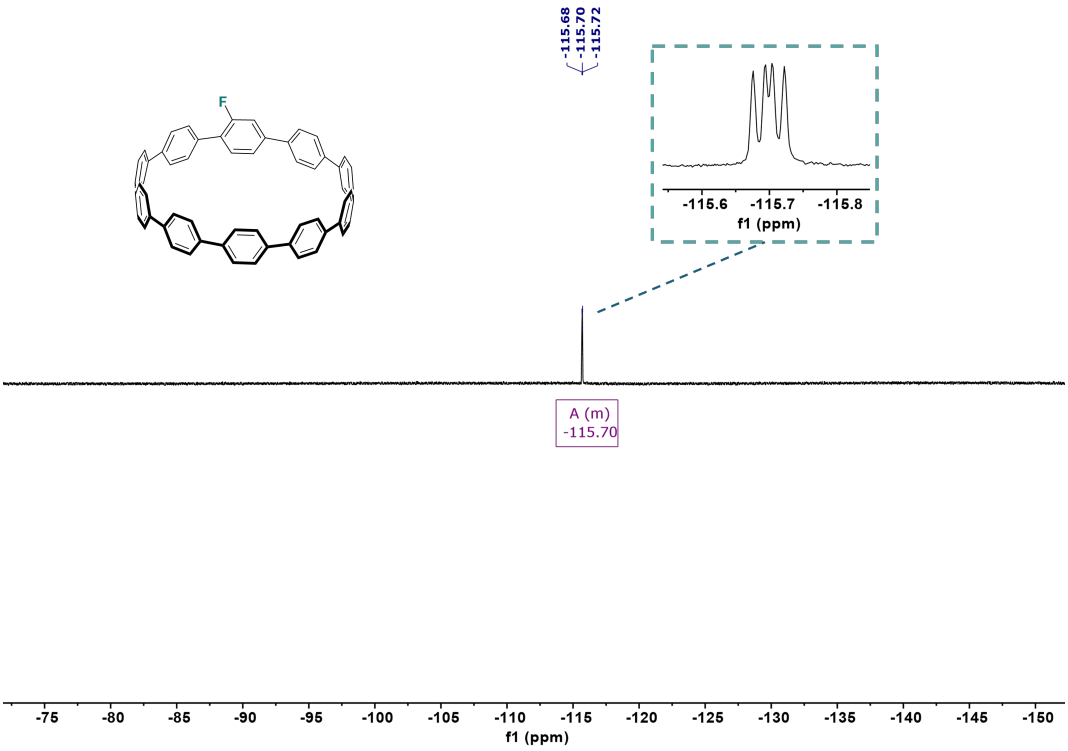

Figure S30. ^{19}F NMR of compound **7a**.

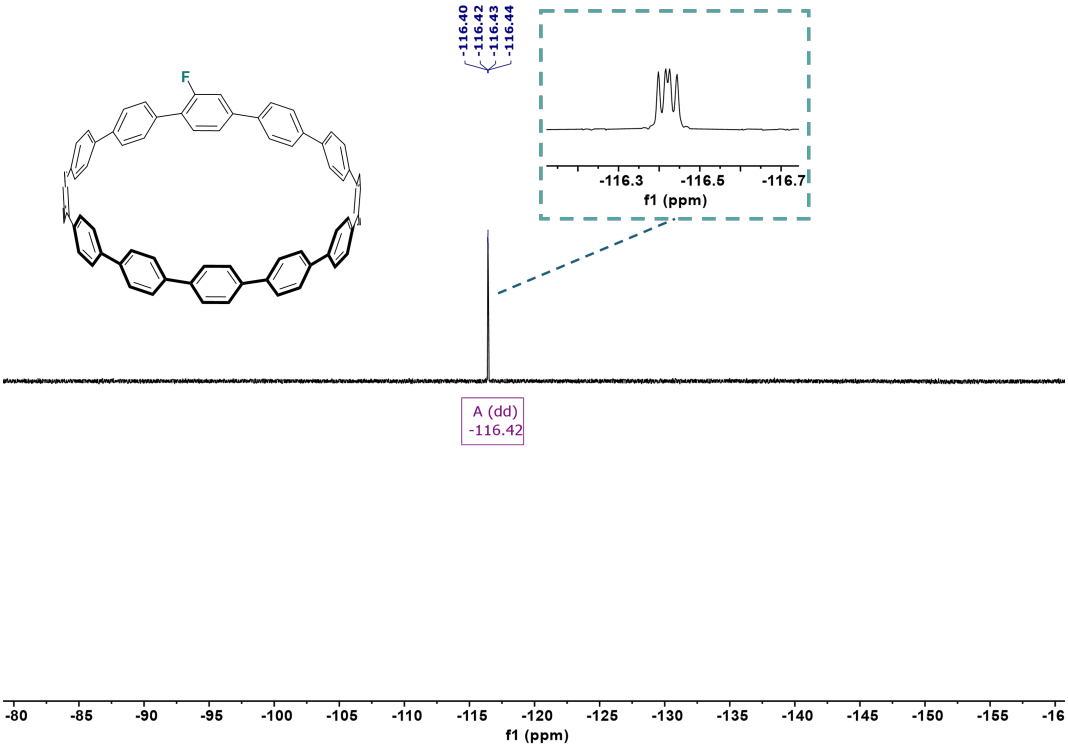

Figure S31. ^{19}F NMR of compound **7b**.

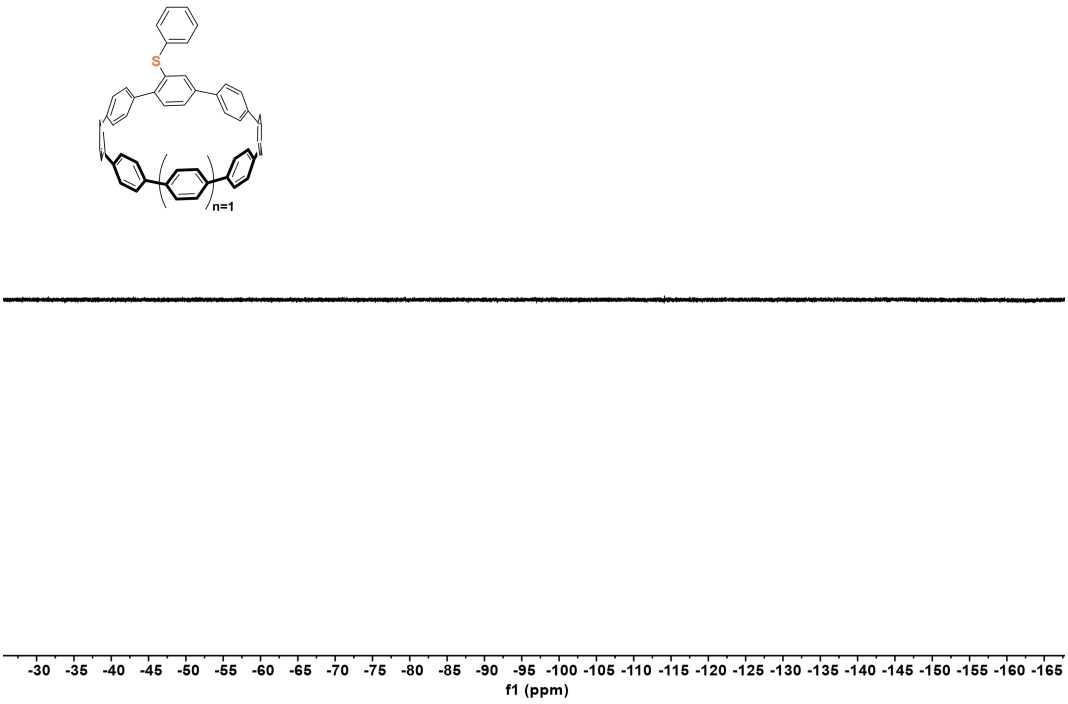

Figure S14. ^{19}F NMR of compound **8a**.

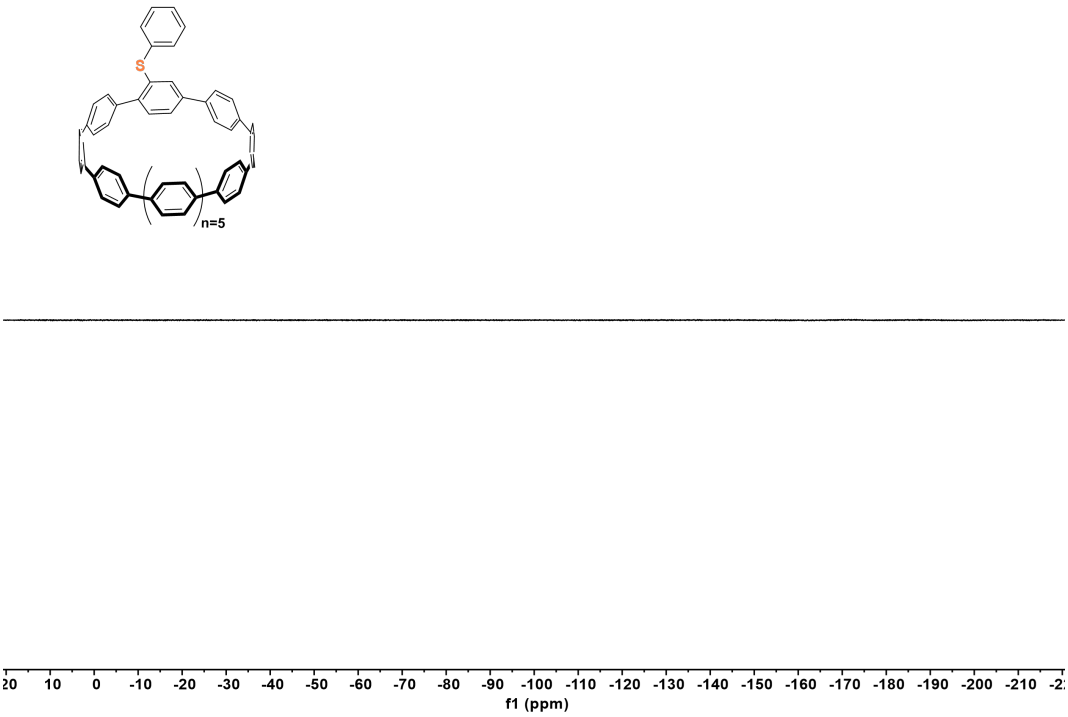

Figure S15. ^{19}F NMR of compound **8b**.

Mass Spectroscopy

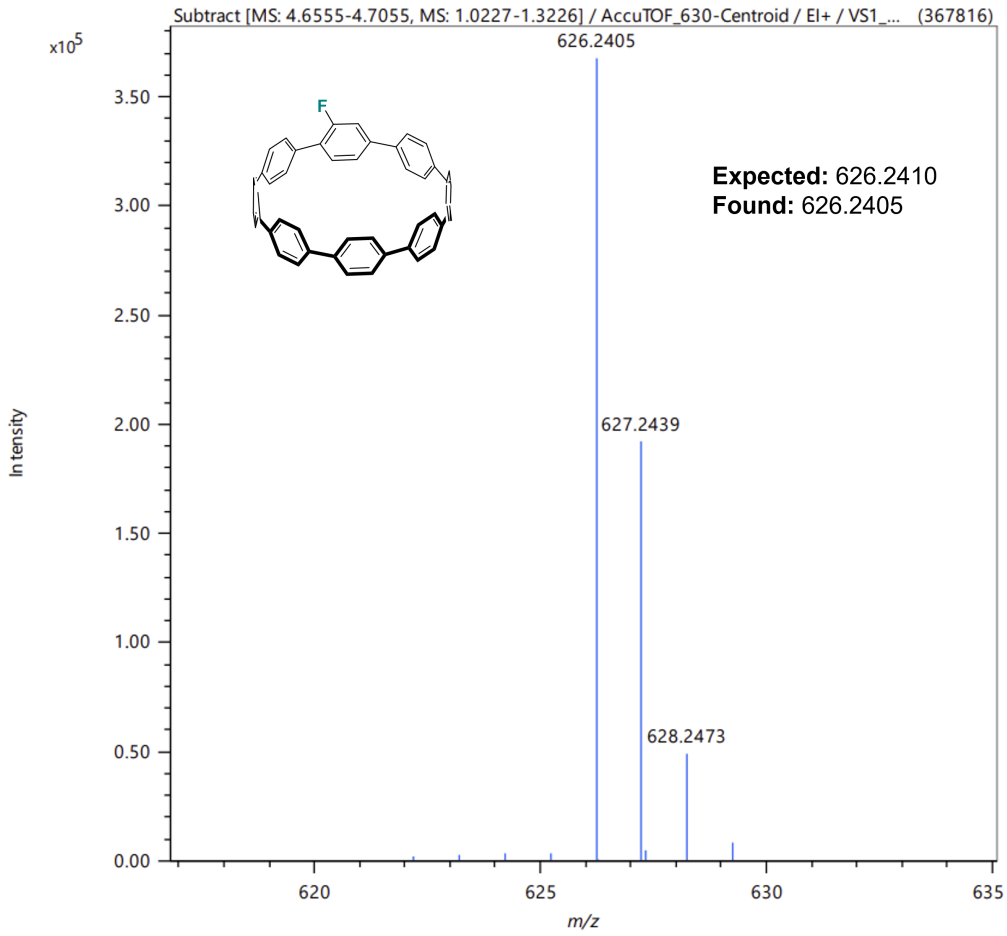

Figure S16. Mass determination of compound **4**.

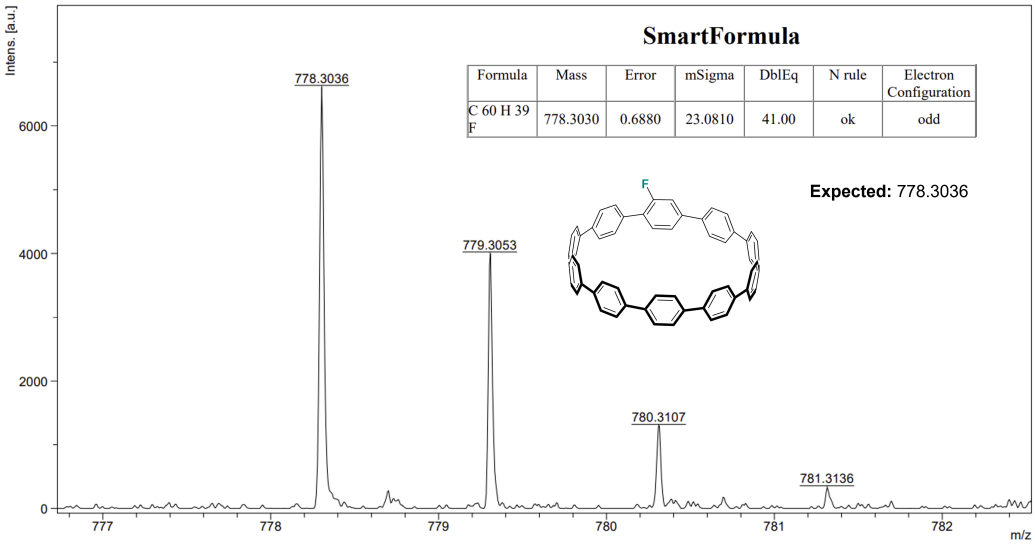

Figure S17. Mass determination of compound **7a**.

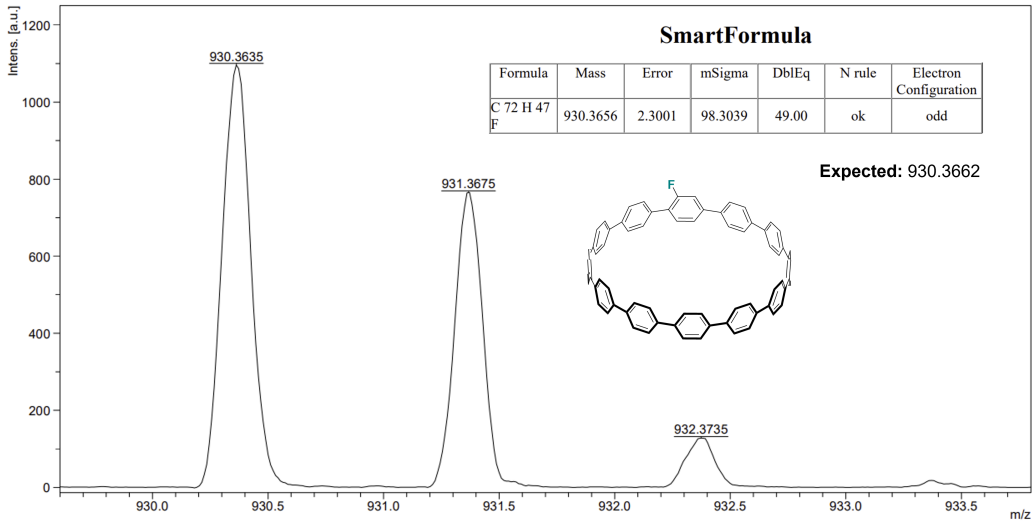

Figure S18. Mass determination of compound **7b**.

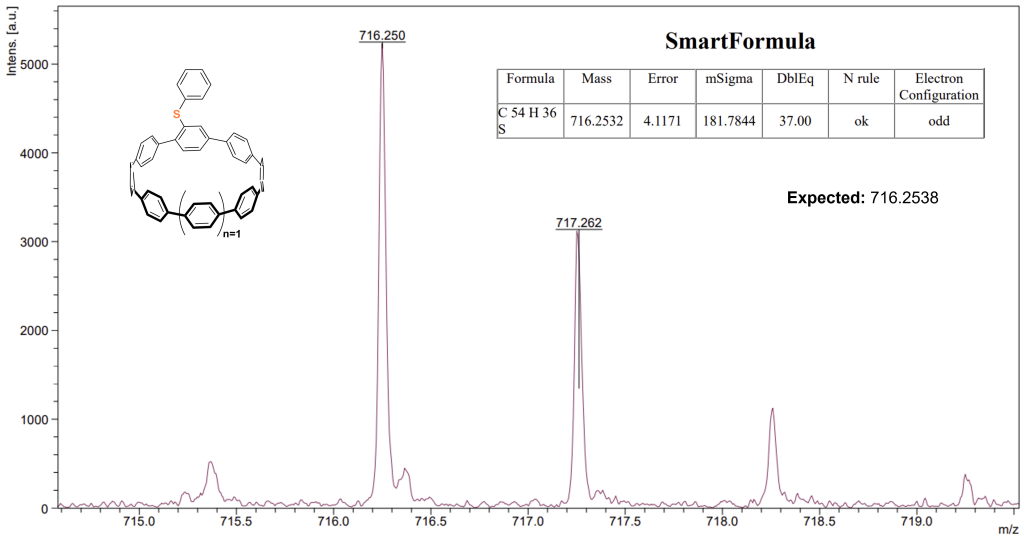

Figure S19. Mass determination of compound **4a**.

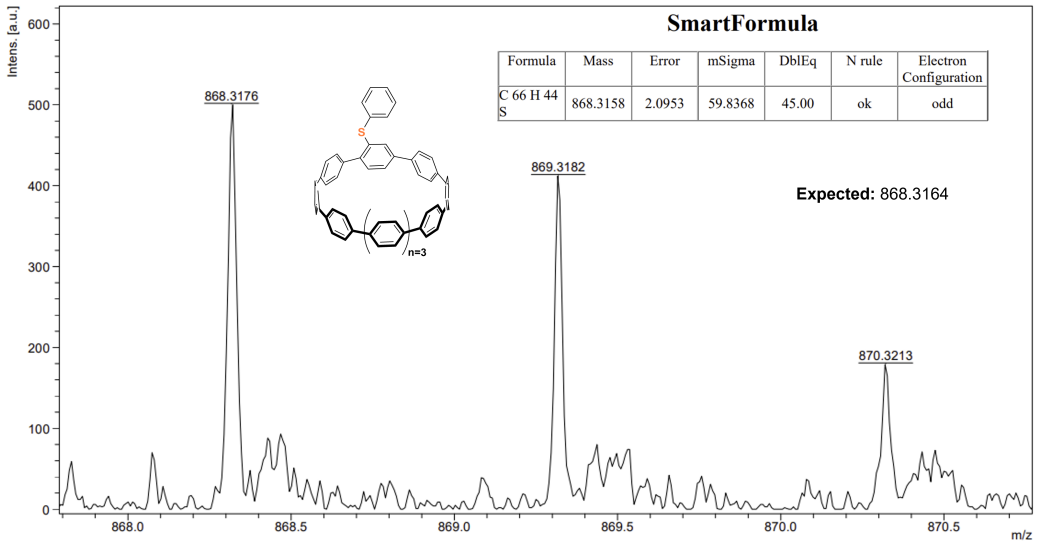

Figure S20. Mass determination of compound **8a**.

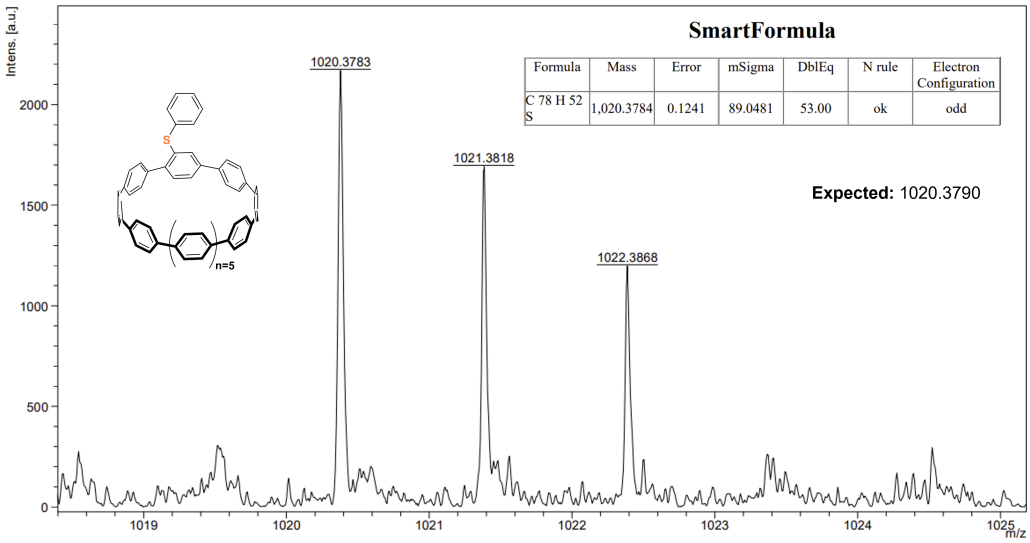

Figure S21. Mass determination of compound **8b**.

2.2.5 Citations

(1) A. Kamin, A.; D. Clayton, T.; E. Otteson, C.; M. Gannon, P.; Krajewski, S.; Kaminsky, W.; Jasti, R.; J. Xiao, D. Synthesis and Metalation of Polycatechol Nanohoops Derived from Fluorocycloparaphenylenes. *Chem. Sci.* **2023**, 14 (36), 9724–9732. https://doi.org/10.1039/D3SC03561A.

(2) Shudo, H.; Kuwayama, M.; Segawa, Y.; Yagi, A.; Itami, K. Half-Substituted Fluorocycloparaphenylenes with High Symmetry: Synthesis, Properties and Derivatization to Densely Substituted Carbon Nanorings; preprint; *Chemistry*, **2023**. https://doi.org/10.26434/chemrxiv-2023-zsvnt.

(3) Terabayashi, T.; Kayahara, E.; Zhang, Y.; Mizuhata, Y.; Tokitoh, N.; Nishinaga, T.; Kato, T.; Yamago, S. Synthesis of Twisted [n]Cycloparaphenylene by Alkene Insertion. *Angew. Chem. Int. Ed.* **2023**, 62 (2), e202214960. https://doi.org/10.1002/anie.202214960.

(4) Golder, M. R.; Wong, B. M.; Jasti, R. Photophysical and Theoretical Investigations of the [8]Cycloparaphenylene Radical Cation and Its Charge-Resonance Dimer. *Chem. Sci.* **2013**, 4 (11), 4285. https://doi.org/10.1039/c3sc51861b.

(5) Jasti, R.; Bertozzi, C. R. Progress and Challenges for the Bottom-up Synthesis of Carbon Nanotubes with Discrete Chirality. *Chem. Phys. Lett.* **2010**, 494 (1), 1–7. https://doi.org/10.1016/j.cplett.2010.04.067.

(6) Darzi, E. R.; Jasti, R. The Dynamic, Size-Dependent Properties of [5]–[12]Cycloparaphenylenes. *Chem. Soc. Rev.* **2015**, 44 (18), 6401–6410. https://doi.org/10.1039/C5CS00143A.

(7) Fehr, J. M.; Myrthil, N.; Garrison, A. L.; Price, T. W.; Lopez, S. A.; Jasti, R. Experimental and Theoretical Elucidation of SPAAC Kinetics for Strained Alkyne-Containing Cycloparaphenylenes. *Chem. Sci.* **2023**, 14 (11), 2839–2848. https://doi.org/10.1039/D2SC06816H.

(8) Iwamoto, T.; Watanabe, Y.; Sakamoto, Y.; Suzuki, T.; Yamago, S. Selective and Random Syntheses of [n]Cycloparaphenylenes (n = 8–13) and Size Dependence of Their Electronic Properties. *J. Am. Chem. Soc.* **2011**, 133 (21), 8354–8361. https://doi.org/10.1021/ja2020668.

(9) E. Lewis, S. Cycloparaphenylenes and Related Nanohoops. *Chem. Soc. Rev.* **2015**, 44 (8), 2221–2304. https://doi.org/10.1039/C4CS00366G.

(10) Jiang, Z.; Duan, W.; Lin, W.; Yang, L.; Wu, Z.; Wang, J.; Wang, S.; Du, P.; Li, Q. Cycloparaphenylene and Their Radicals Anchored to a Metal−organic Framework. *Mater. Today Chem.* **2022**, 25, 100973. https://doi.org/10.1016/j.mtchem.2022.100973.

(11) Hammond, G. S. A Correlation of Reaction Rates. *J. Am. Chem. Soc.* **1955**, 77 (2), 334–338. https://doi.org/10.1021/ja01607a027.

(12) Lennox, A. J. J. Meisenheimer Complexes in SNAr Reactions: Intermediates or Transition States? *Angew. Chem. Int. Ed.* **2018**, 57 (45), 14686–14688. https://doi.org/10.1002/anie.201809606.

(13) Frisch, M. J.; Trucks, G. W.; Schlegel, H. B.; Scuseria, G. E.; Robb, M. A.; Cheeseman, J. R.; Scalmani, G.; Barone, V.; Petersson, G. A.; Nakatsuji, H.; Li, X.; Caricato, M.; Marenich, A. V.; Bloino, J.; Janesko, B. G.; Gomperts, R.; Mennucci, B.; Hratchian, H. P.; Ortiz, J. V.; Izmaylov, A. F.; Sonnenberg, J. L.; Williams; Ding, F.; Lipparini, F.; Egidi, F.; Goings, J.; Peng, B.; Petrone, A.; Henderson, T.; Ranasinghe, D.; Zakrzewski, V. G.; Gao, J.; Rega, N.;

Zheng, G.; Liang, W.; Hada, M.; Ehara, M.; Toyota, K.; Fukuda, R.; Hasegawa, J.; Ishida, M.; Nakajima, T.; Honda, Y.; Kitao, O.; Nakai, H.; Vreven, T.; Throssell, K.; Montgomery Jr., J. A.; Peralta, J. E.; Ogliaro, F.; Bearpark, M. J.; Heyd, J. J.; Brothers, E. N.; Kudin, K. N.; Staroverov, V. N.; Keith, T. A.; Kobayashi, R.; Normand, J.; Raghavachari, K.; Rendell, A. P.; Burant, J. C.; Iyengar, S. S.; Tomasi, J.; Cossi, M.; Millam, J. M.; Klene, M.; Adamo, C.; Cammi, R.; Ochterski, J. W.; Martin, R. L.; Morokuma, K.; Farkas, O.; Foresman, J. B.; Fox, D. J. Gaussian 16 Rev. C.01, **2016**.

(14) Ong, W. J.; Swager, T. M. Dynamic Self-Correcting Nucleophilic Aromatic Substitution. *Nat. Chem.* **2018**, 10 (10), 1023–1030. https://doi.org/10.1038/s41557-018-0122-8.

(15) Pangborn, A. B.; Giardello, M. A.; Grubbs, R. H.; Rosen, R. K.; Timmers, F. J. Safe and Convenient Procedure for Solvent Purification. *Organometallics* **1996**, 15 (5), 1518–1520. https://doi.org/10.1021/om9503712.

(16) Patel, V. K.; Kayahara, E.; Yamago, S. Frontispiece: Practical Synthesis of [n]Cycloparaphenylenes (N=5, 7–12) by H2SnCl4-Mediated Aromatization of 1,4-Dihydroxycyclo-2,5-Diene Precursors. *Chem. – Eur. J.* **2015**, 21 (15). https://doi.org/10.1002/chem.201581562.

(17) Darzi, E. R.; Sisto, T. J.; Jasti, R. Selective Syntheses of [7]–[12]Cycloparaphenylenes Using Orthogonal Suzuki–Miyaura Cross-Coupling Reactions. *J. Org. Chem.* **2012**, 77 (15), 6624–6628. https://doi.org/10.1021/jo3011667.

Chapter III: Diels-Alder Strategies for Late-Stage Property Tuning of CPPs

3.1.1 Contributions

In collaboration with Dr. Tara D. Clayton, Victor Salpino, Leyla Gillette, and Dr. Ramesh Jasti we've reported a novel late-stage synthetic approach to modify CPPs through a Diels-Alder (DA) transformation. In this work Tara, Victor, Leyla and I synthesized the starting building blocks, CPP parent complexes, and Diels-Alder products. I characterized these products through mass spectrometry, nuclear magnetic resonance spectroscopy (NMR), photophysical properties, and ran DFT computational analysis on all structures. I led manuscript writing and edits along with Dr. Clayton and Dr. Jasti contributing to peer editing as well. Through this project we demonstrated the first Diels-Alder transformations on CPPs as a late-stage derivatization method.

3.1.2 Abstract

Cycloparaphenylenes (CPPs) are strained, curved π-conjugated macrocycles whose reactivity enables late-stage functionalization, yet [4+2] Diels–Alder reactions on alkyne-embedded CPPs have not been experimentally demonstrated. Here, we report the first Diels–Alder transformations of alkyne-containing CPPs, providing efficient access to π-extended, ortho-modified nanohoops. Reaction efficiency and temperature dependence vary systematically with CPP size, consistent with strain-promoted reactivity. The resulting adducts preserve high molar absorptivity and quantum yield while exhibiting increased effective Stokes shifts relative to the parent CPPs. These results establish Diels–Alder cycloaddition as a viable late-stage modification strategy for strained alkyne CPPs.

3.1.3 Introduction

Cycloparaphenylenes (CPPs) are a class of curved aromatic macrocycles constructed via bottom-up rational design.[1,2] By assembling small molecular building blocks with complementary geometries, strain can be introduced through masked benzene units, which are subsequently

deprotected and aromatized to form the CPP. CPPs feature radially oriented π-orbitals, resulting in size-dependent optoelectronic properties distinct from their linear analogues. Since their initial synthesis in 2008, the CPP library has expanded through diverse functionalization strategies.[1,3–10] However, derivatization of CPPs is most commonly achieved through incorporation of functional groups early in synthesis, an approach that can often be low yielding, time-consuming, and limited by reaction compatibility. Consequently, increased attention has shifted towards late-stage modification strategies for tuning CPP properties.[9,11–13] Although hydrocarbon CPPs possess attractive optoelectronic properties, they are comparatively inert toward late-stage derivatization in the absence of a reactive handle. For example, extension of the sidewall of a hydrocarbon CPP toward carbon nanotube growth was previously observed only in situ and could not be isolated.[14] As a result, recent work has shifted to incorporating stable functional groups during synthesis that enable post-aromatization modification.[9,11,13,15–19] Among these platforms, alkyne-containing CPPs represent a particularly versatile class of molecules due to their strain-dependent reactivity, enabling transformations such as strain-promoted azide-alkyne cycloaddition (SPAAC) and palladium-catalyzed cyclotrimerization reaction (**Figure 3.16a**).[11,15,16] Notably, computational studies have predicted that alkyne-embedded CPPs should exhibit enhanced [4+2] Diels–Alder reactivity relative to linear alkynes as a consequence of backbone strain. (**Figure 3.16b**).[12] Despite these predictions, experimental Diels-Alder reactions on alkyne-embedded CPPs have not been reported. Here, we report the first Diels–Alder transformations of alkyne-embedded cyclopara-phenylenes. Alkyne-containing CPPs [9+1]CPP and [11+1]CPP were synthesized following reported procedures[15] and subjected to cycloaddition with 2,3,4,5-tetraphenylcyclopentadienone to afford π-extended, ortho-modified CPPs (**Scheme 3.4**). The reaction proceeds efficiently and exhibits size-dependent reactivity consistent with the strain char-acteristics of the parent nanohoops. In particular, the larger [11+1]CPP required higher temperatures to achieve full conversion relative to [9+1]CPP, consistent with reduced strain in the larger macrocycle. These observations align with prior computational predictions that strain in alkyne-embedded CPPs can promote [4+2] cycloaddition reactivity.

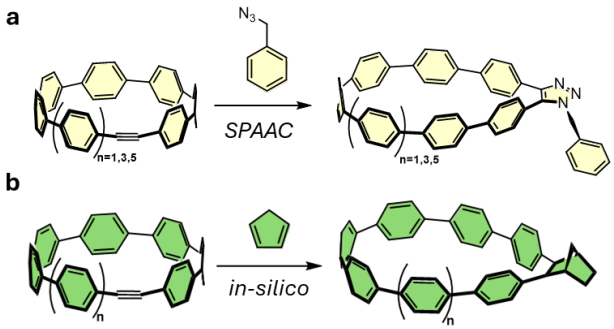

Figure 3.16: Examples of late-stage modifications on alkyne cycloparaphenylenes.

3.1.4 Discussion

To evaluate this reactivity experimentally, alkyne-embedded cycloparaphenylenes [9+1]CPP and [11+1]CPP were synthesized according to reported procedures[15] and subjected to Diels–Alder cycloaddition with 2,3,4,5-tetraphenylcyclopentadienone (**Scheme 3.4**). In this transformation, the strained alkyne undergoes a [4+2] cycloaddition followed by extrusion of CO to install an ortho-tetraphenylene unit on the CPP framework. Both nano-hoop sizes undergo efficient conversion to the corresponding π-extended adducts, although clear differences in reactivity were observed: the smaller [9+1]CPP reacts under milder conditions, whereas the larger [11+1]CPP requires higher temperatures to achieve full conversion, consistent with reduced strain in the larger macrocycle. Additional studies were performed to further probe the strain-promoted nature of this transformation, including variation of reaction temperature and heating conditions (**Table 3.1**). These results support the conclusion that embedded alkyne strain plays a central role in enabling Diels–Alder reactivity in CPP frameworks.

Compound	source	Δ	t	yield
Product 1a	MW	180 °C	12 hr	80%
Product 2a	MW	220 °C	12 hr	99%

Table 3.1: Synthetic conditions for [9+1]CPP to product1a, and [11+1]CPP to product 2a

With these π-extended CPP derivatives in hand, we next examined how tetraphenylene incorporation influences their optoelectronic properties. UV–vis absorption and fluorescence spectroscopy were performed on both the parent CPPs and the Diels–Alder adducts (**Figure 3.17**). Relative to

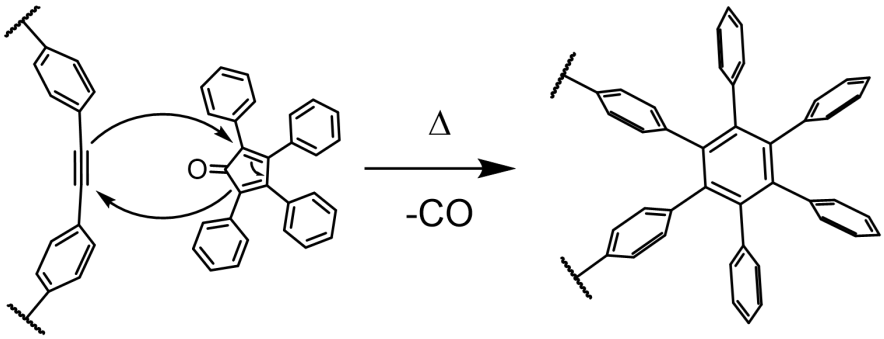

Scheme 3.4: Diels-Alder [4+2] cycloaddition between CPP and tetraphenylcyclopentadienone.

the parent nanohoops, the tetraphenylene-modified CPPs exhibit increased effective Stokes shifts while maintaining high molar absorptivity and quantum yield (**Table 3.2**). For example, modification of [9+1]CPP increases the Stokes shift from 112 nm to 147 nm while retaining a relatively high quantum yield (ϕ = 0.46 vs 0.76 for the parent). Similarly, the [11+1]CPP derivative displays an increased Stokes shift of 126 nm compared to 107 nm for the parent CPP, while maintaining a high quantum yield (ϕ = 0.74). This combination of large Stokes shift and high emissive efficiency is desirable for imaging and sensing applications because it minimizes self-absorption while preserving signal brightness. Interestingly, while isolated tetra-phenylbenzene derivatives typically exhibit low emissive efficiency due to non-radiative rotational pathways, incorporation within the rigid CPP framework appears to enhance emissive behavior.

Compound	ε ($M^{-1}cm^{-1}$)	Φ	Δλ
1,2,3,4-tetraphenylbenzene	----------	0.04	54
[9+1]CPP**	$1.2x10^5$	0.76	112
1A	$1.2x10^5$	0.46	147
[11+1]CPP**	$1.7x10^5$	0.80	107
2A	$2.6x10^5$	0.74	126

Table 3.2: Compiled optoelectronic values for derivatized CPPs and parent compounds.

To gain insight into the observed photophysical changes, density functional theory (DFT) calculations were performed on the tetraphenylene-modified CPP derivatives. The calculations suggest that incorporation of the tetraphenylene unit perturbs π-conjugation and lowers the symmetry of the CPP framework, leading to changes in the HOMO–LUMO transition. In addition, the calculations indicate an inversion of the molecular dipole upon excitation, which stabilizes the emissive excited

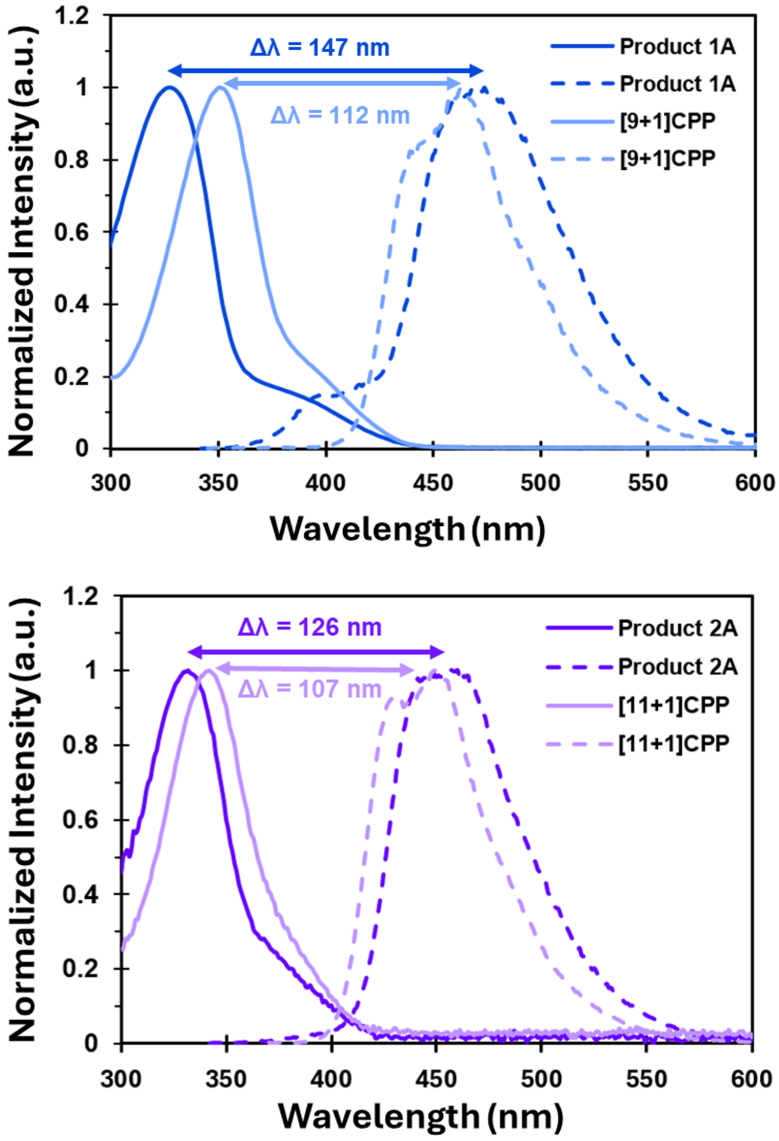

Figure 3.17: Absorption and emission profiles for alkyne CPPs and their tetraphenylene products.

state and contributes to the increased Stokes shifts observed experimentally.

3.1.5 Conclusion and Bridge to Chapter IV

In summary, we demonstrated that alkyne-embedded cycloparaphenylenes undergo efficient Diels–Alder cycloaddition with tetraphenylcyclopentadienone, providing the first experimental example of this transformation on CPP frameworks. The reaction proceeds through cycloaddition followed by CO extrusion to generate ortho-tetraphenylene-modified nanohoops. Reactivity varies with CPP size, consistent with strain-promoted activation of the embedded alkyne. The resulting π-extended CPP derivatives display increased Stokes shifts while maintaining high molar absorptivity and quantum yield. These results establish Diels–Alder chemistry as a viable late-stage functionalization strategy for alkyne-embedded CPPs and provide a platform for expanding the structural and photophysical diversity of CPP-based fluorophores. More broadly, this strain-enabled derivatization strategy may facilitate the development of tailored curved π-systems for applications in optoelectronic materials and fluorescence imaging. In the next chapter we explore using thiol-ene photochemistry to modify norbornene functionalized CPPs toward applications in biological imaging. This is another late-stage functionalization route we can use to access room temperature and biological relevant reaction conditions to expand CPPs into new research spaces.

3.1.6 Experimental Appendix: Supplementary Information

Commercially available materials were used without purification unless otherwise indicated. Moisture and oxygen sensitive reactions were carried out in flame-dried glassware and under an inert atmosphere of purified nitrogen using syringe/septa technique. Tetrahydrofuran (THF) and dimethylformamide (DMF) were dried by filtration through alumina according to the methods described by Grubbs.[21] Alumina column chromatography was conducted with SorbTech basic alumina (pH 10), Act. II-III, 50-200 μm. 1H and 13C NMR spectra were recorded on a Bruker Avance III HD 500 (^{1}H: 500 MHz, ^{13}C: 126 MHz) NMR spectrometer. The chemical shifts (δ) were reported in parts per million (ppm) and were referenced to the solvent (CD2Cl2, ^{1}H: δ = 5.32

ppm and ^{13}C: δ = 53.84 ppm or $CDCl_3$, ^{1}H: δ = 7.26 ppm and ^{13}C: δ = 77.801 ppm). Coupling constants (J) are given in Hz and the apparent resonance multiplicity is reported as s (singlet), d (doublet), t (triplet), q (quartet), dd (doublet of doublets) or m (multiplet). UV/Vis absorption and fluorescence spectra were recorded on an Agilant Cary 100 spectrophotometer and a Horiba Jobin Yvon Fluoromax-4 Fluorimeter, respectively. All measurements were carried out under ambient conditions in a Spectrocell RF-1010-T threaded top vacuum formed borosilicate fluorometer cell (10 mm light path). Mass spectroscopy HRMS measurements were performed on Bruker Daltonics UltrafleXtreme MALDI TOF/TOF by a third-party lab. Supporting raw data files can be accessed via FigShare at https://figshare.com/account/articles/31286152.

I. Synthesis

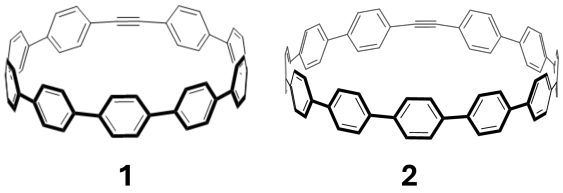

Compounds **1** and **2** were synthesized according to literature methods.[22]

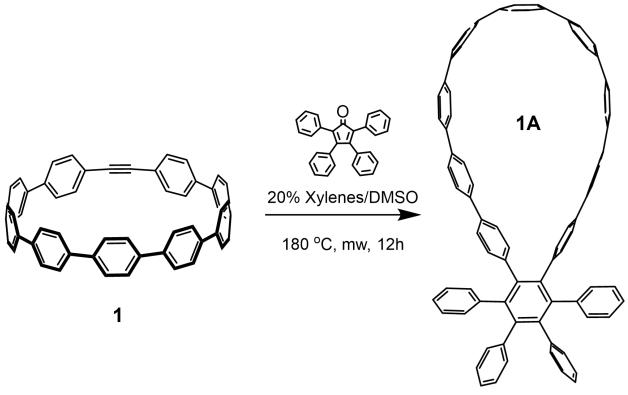

Compound 1A. Solid 2,3,4,5-Tetraphenylcyclopentadienone (3 mg, 0.008 mmols) and compound 1 (5 mg, 0.007 mmols) were added to a small microwave vial with a stir bar. The vial was back-filled with nitrogen x3 then solvent added via syringe: xylenes (0.141 mL), DMSO (0.564 mL). Reaction was set to normal absorption in a MW reactor at 180 °C for 12 hours. The crude solu-

tion was filtered over an alumina plug with 100% DCM then purified on alumina prep plate with 50:50 DCM:Hexanes solvent system to yield a flaky yellow solid (6 mg, 80%).^{1}H NMR (500 MHz, Chloroform-d) δ 7.60 (s, 5H), 7.55 (q, J = 8.9 Hz, 8H), 7.49 – 7.40 (m, 15H), 7.17 – 7.07 (m, 8H), 6.95 – 6.83 (m, 20H). ^{13}C NMR (126 MHz, CDCl3) δ 140.68, 140.61, 140.52, 139.84, 139.81, 138.79, 138.59, 138.57, 138.09, 137.63, 137.50, 136.37, 131.78, 131.44, 131.40, 127.70, 127.65, 127.55, 127.34, 126.96, 126.84, 126.73, 126.68, 126.59, 125.26, 125.21, 124.82. HRMS (MALDI, TOF), m/z calculated for C84H56 $(M)^+$ Expected: 1064.4382, Found: 1064.4377.

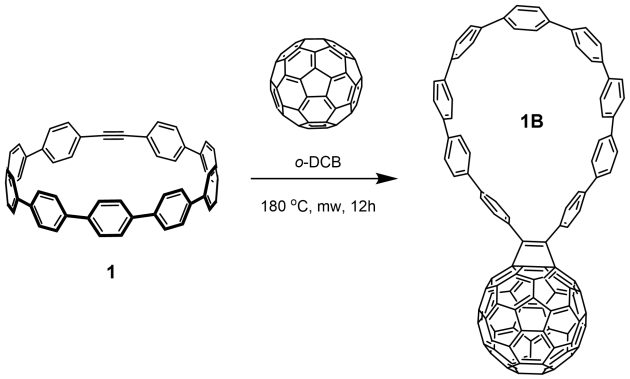

Compound 1B. Weighed out precise amount of fullerene (0.075 mg, 0.012 mmol) in a scintillation vial then added 0.7 mL of o-DCB solvent. Added 0.7 mL of o-DCB to the vial containing [9+1]CPP (made by victor) transferred both of these solutions to the medium sized MW vial (0.5 mL to 2 mL vol capacity). Purged with N2 for ~ 15mins before setting up in the MW reactor. Added the vial to the reactor and set temp at 180C for a 12 hour reaction with normal absorption to compare to the tetraphenylene DA experiments. Filtered through buchner funnel to remove black solid, rinse with 100% DCM. Reduced volume under vacuum. Filtrate showed a brown solution, that irradiates blue under UV lamp. Ran through an alumina column with DCM to try to separate out some spots but didn't work very well. Ended up doing a prep plate with 50:50 DCM:Hex which cleaned it up nicely. Seems stable in d-DCM for at least 24 hrs.

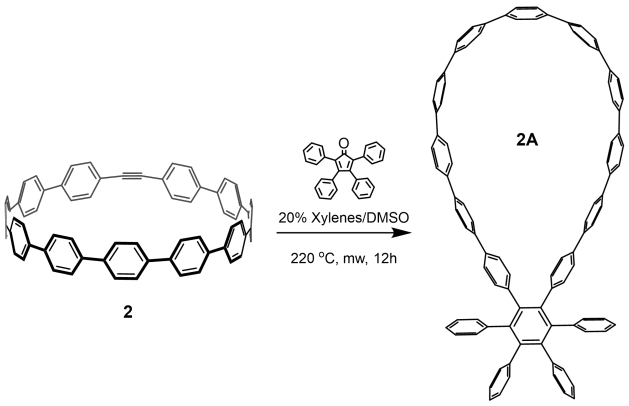

Compound 2A. Solid 2,3,4,5-Tetraphenylcyclopentadienone (1 mg, 0.003 mmols) and compound 2 (2 mg, 0.002 mmols) were added to a small microwave vial with a stir bar. The vial was backfilled with nitrogen x3 then solvent added via syringe: xylenes (0.05 mL), DMSO (0.2 mL). Reaction was set to normal absorption in a MW reactor at 220 °C for 12 hours. The mixture was directly applied to CC (basic allox, 0 - 100% DCM/Hex) to afford the product as a colorless solid (2.8 mg, 99%). 1H NMR (500 MHz, Methylene Chloride-d2) δ 7.71 – 7.61 (m, 26H), 7.61 – 7.49 (m, 10H), 7.25 (d, J = 8.4 Hz, 4H), 7.06 – 7.01 (m, 4H), 6.98 – 6.87 (m, 20H). 13C NMR (126 MHz, CD2Cl2) δ 140.74, 140.72, 140.66, 140.52, 140.01, 139.77, 138.91, 138.76, 138.67, 138.64, 138.30, 137.96, 137.91, 136.41, 131.91, 131.41, 131.35, 127.52, 127.48, 127.37, 127.29, 127.21, 127.16, 127.01, 126.83, 126.59, 126.50, 125.25, 125.18, 124.61. HRMS (MALDI, TOF), m/z calculated for C96H64 (M)+ Expected: 1216.5008, Found: 1216.5003.

II. Structural Characterization ^{1}H NMR

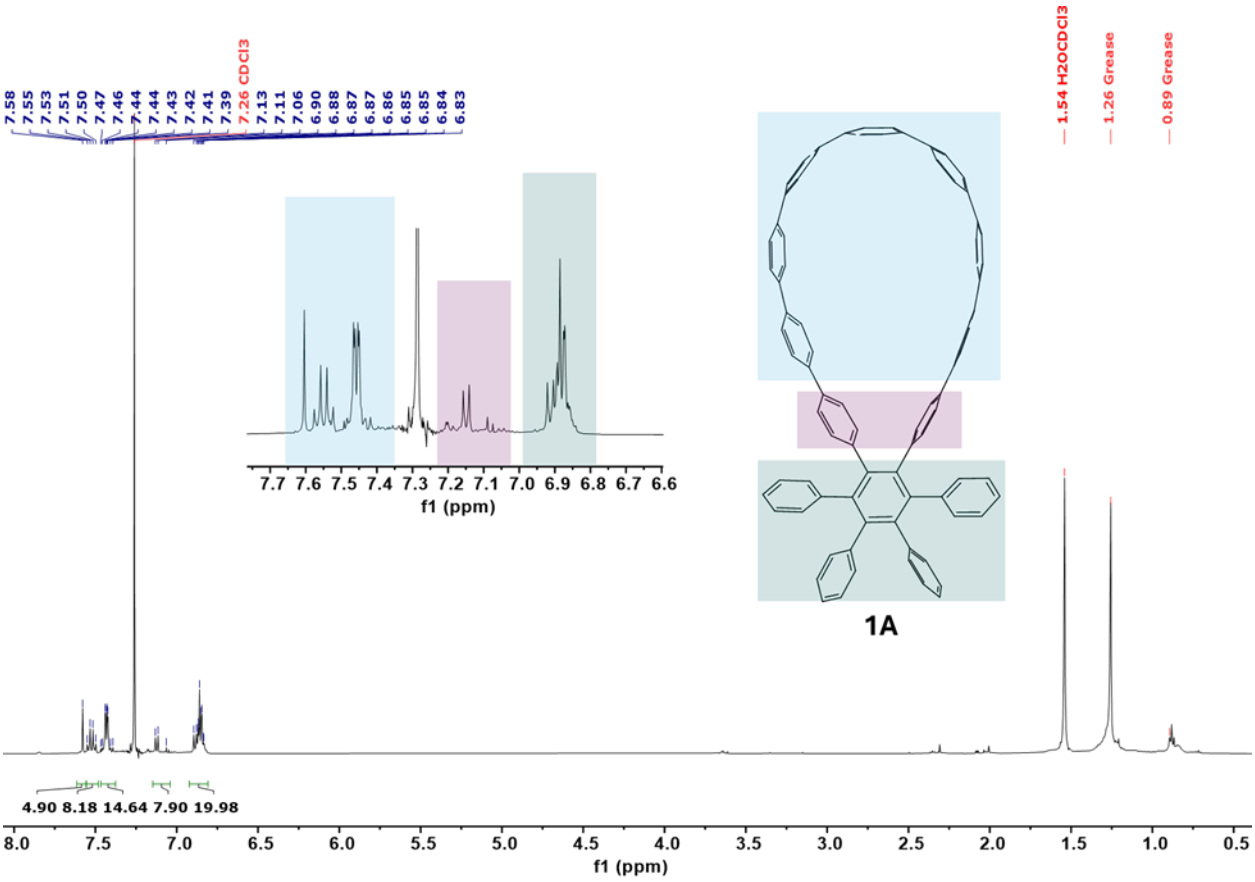

Figure S1. Proton NMR spectra for 1A tetraphenyl modified CPP.

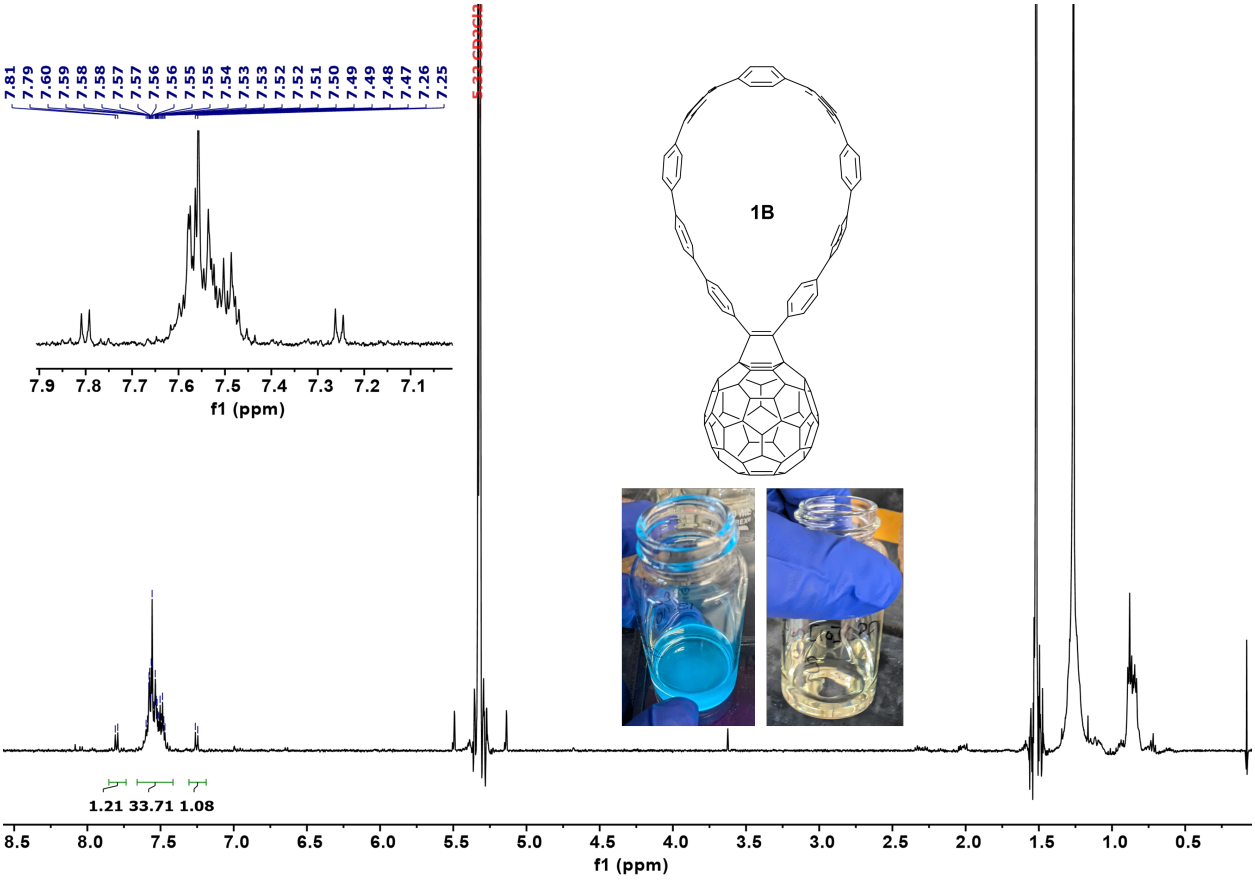

Figure S2. Proton NMR spectra for 1B C_{60} modified CPP.

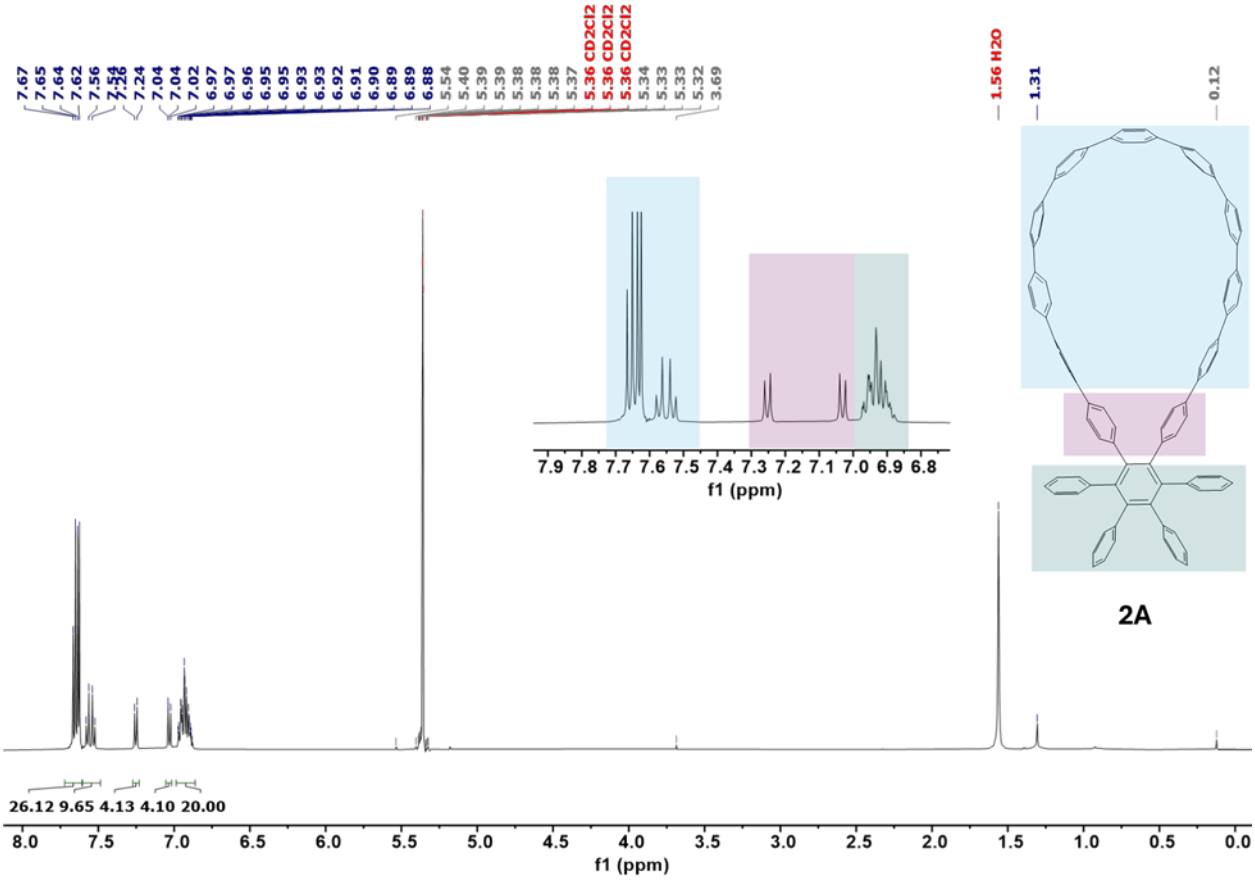

Figure S3. Proton NMR spectra for 2A tetraphenyl modified CPP.

^{13}C NMR

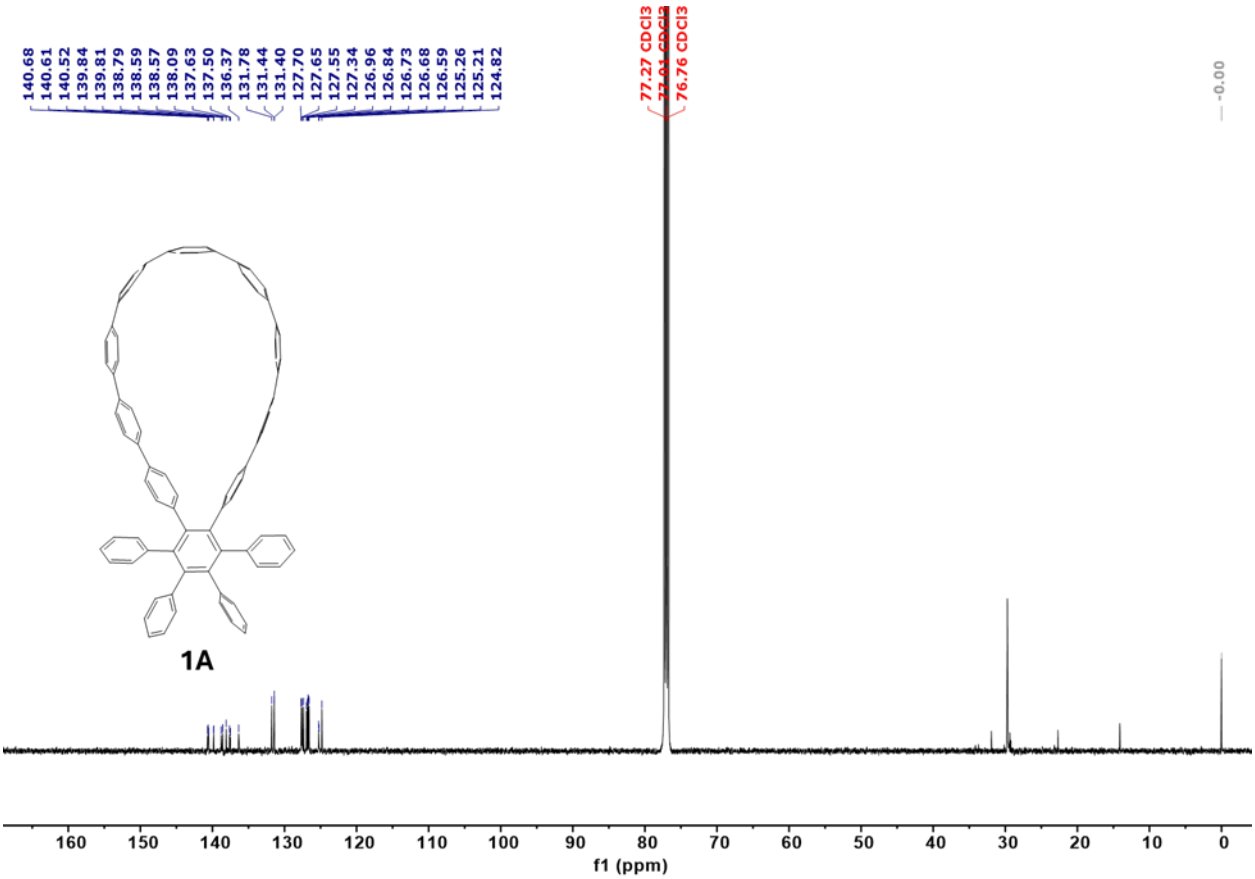

Figure S4. Carbon NMR spectra for 1A tetraphenyl modified CPP.

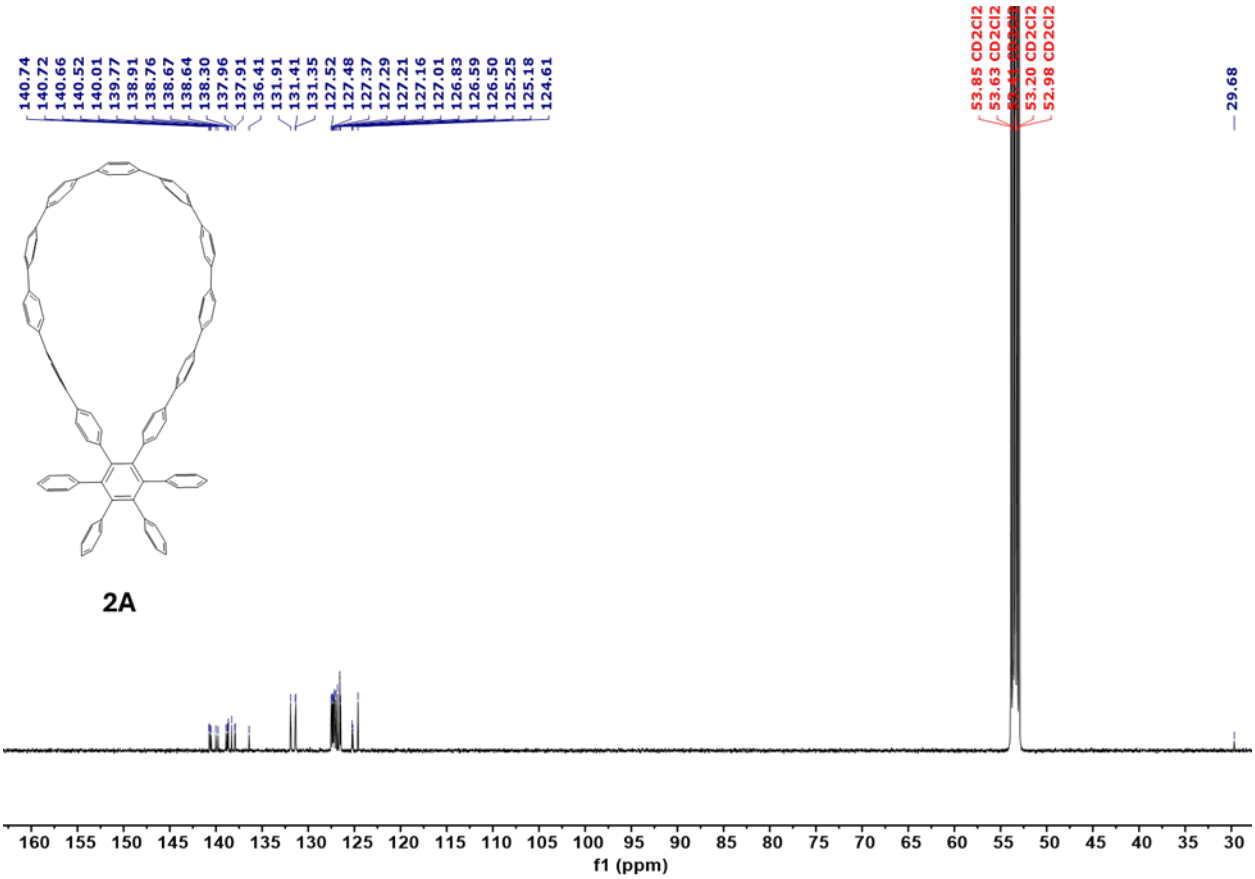

Figure S5. Carbon NMR spectra for 2A tetraphenyl modified CPP.

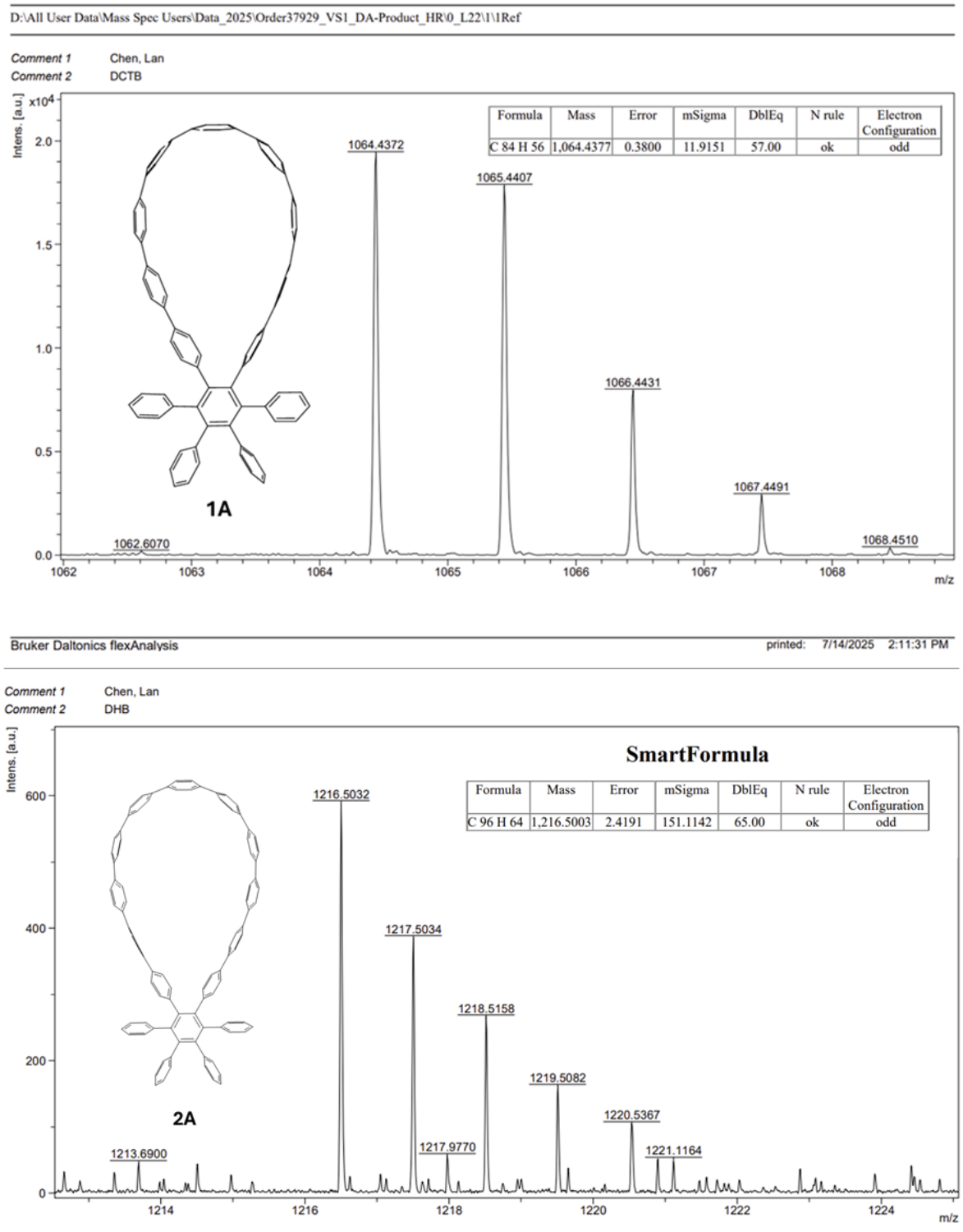

Figure S6. Mass spectral characterization for tetraphenyl modified CPPs.

III. Optoelectronic Properties Molar Absorptivity A known amount of CPP solid in a glass scintillation vial was dissolved with dry DCM via Hamilton syringe. A quartz UV-Vis cuvette was filled with 2.4 to 2.5 mL of dry DCM (recorded by trial for calculations). A blank background was taken to remove the baseline. Specified amounts of sample solution were added in 5-20 uL aliquots (depending on signal and trial, recorded amount) via Hamilton syringe. Spectra were recorded and sample addition steps repeated for 4-5 measurements. Raw data was processed in excel and slopes of concentration vs. absorbance were extracted for molar absorptivity.

1A Concentration (M)	Trial 1	Trial 2	Trial 3
1.41E-07	0.0151	0.0173	0.0154
2.81E-07	0.0323	0.0315	0.0339
4.22E-07	0.0485	0.0483	0.0521
5.62E-07	0.0663	0.0598	0.07031
7.02E-07	0.0834	0.0779	0.0909
ε	122000	106000	133000
average			120333
std dev			13577

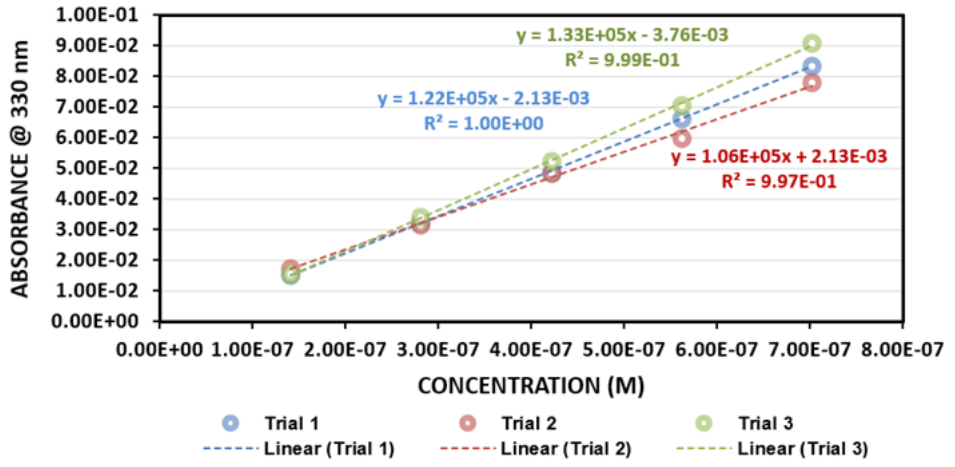

2A Concentration (M)	Trial 1	Trial 2	Trial 3
5.43E-08	0.0166	0.0158	0.0144
1.09E-07	0.0312	0.0296	0.0302
1.63E-07	0.0442	0.0487	0.0399
2.17E-07	0.0589	0.0627	0.0499
2.71E-07	0.0745	0.0770	0.0641
ε	265000	287000	220000
average			257333
std dev			34152

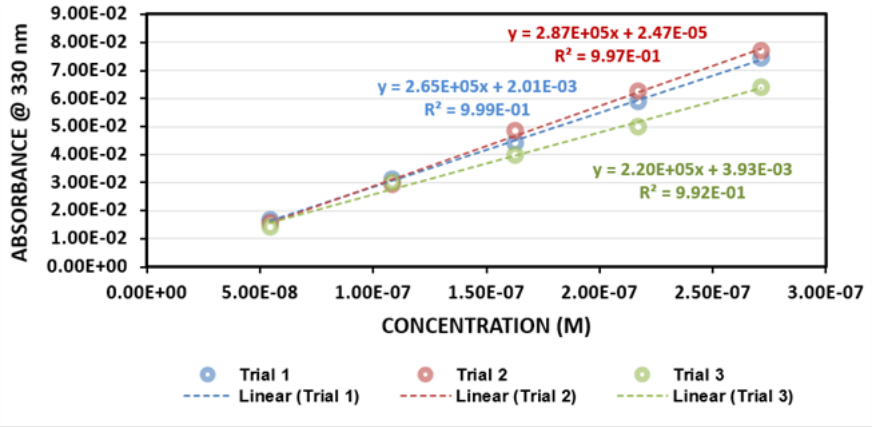

Figure S7. Tables and graphs for molar absorptivity trials for compounds 1A and 2A (ε=1.20x10^5 M^{-1}cm^{-1} and 2.57x10^5 M^{-1}cm^{-1} respectively).

Quantum Yield Quantum yields were measured following standardized procedures with guidance from "A Guide to Recording Fluorescence Quantum Yields" by Horiba Scientific.[23] Two standards, anthracene in ethanol (QY = 0.27) and quinine in 0.1 M H2SO4 (QY ≈ 0.54 based on literature), were used for calibration. The fluorimeter and UV-Vis spectrophotometer were turned on at least 30 minutes prior to measurements. A quinine solution was prepared by adding approximately 1 mL of 0.1 M H2SO4 to a vial containing ~2 mg quinine, which was wrapped in aluminum foil alongside an empty foil-wrapped vial. Anthracene was prepared by adding ~2 mg to a cuvette and sonicating until dissolved in ethanol. A blank was prepared for the quinine trials using a cuvette filled about two-thirds with 0.1 M H2SO4 and capped. UV-Vis spectra were recorded to establish a baseline followed by a baseline fluorescence measurement that was then taken with 1 nm slit widths, excited at 340 nm, collecting emission from 345 nm to 800 nm. A drop of the prepared quinine solution was added to the cuvette, which was shaken and checked for bubbles and cleanliness before measurement. UV-Vis spectra were recorded again to ensure absorbance at 340 nm was within 0.01–0.02. If necessary, the quinine solution was further diluted, or the process was restarted. Multiple data points were collected across absorbance values ranging from approximately 0.02 to 0.1, with at least five measurements spaced evenly (e.g., at 0.02, 0.04, 0.06, 0.08, and 0.1 abs). Data were saved in both .batch and .csv formats, then transferred to a computer for analysis. A plot

of absorbance at 340 nm versus integrated fluorescence (400–600 nm for quinine, 360–480 nm for anthracene) was generated to ensure linearity. Fluorescence data were baseline-corrected and integrated, with UV-Vis absorbance recorded at a consistent wavelength (e.g., 330 nm). The entire procedure was repeated for anthracene in ethanol and for the compound of interest in each solvent of choice, such as DCM and DMSO. Quantum yields of the sample relative to quinine and anthracene standards were calculated using the appropriate equations and compared against literature values, ensuring within 10% accuracy. Throughout the experiment, the instruments were kept powered on, and any baseline fluctuations in the UV-Vis were addressed by cleaning the cuvette and re-measuring. Changes in slit widths or excitation wavelength during measurements were avoided to maintain consistency.

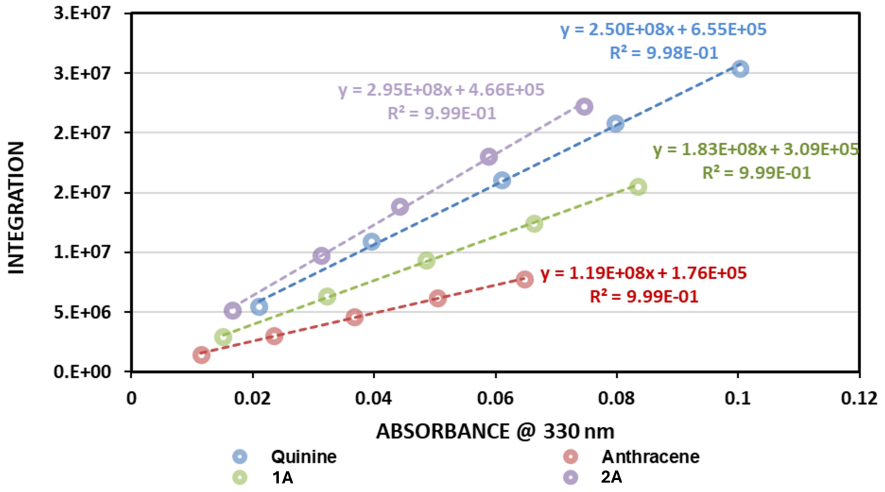

Compound	Solvent	Slope	Φ w.r.t. quinine	Φ w.r.t. anthracene	% err. Φ
quinine	0.1 M H_2SO_4	2.50 x 10^8	0.54 (lit)	0.55	1.22
anthracene	ethanol	1.19 x 10^8	0.26	0.27 (lit)	1.24
1A	DCM	1.83 x 10^8	0.45	0.46	---
2A	DCM	2.95 x 10^8	0.73	0.74	---

Figure S8. Quantum yield traces for standards and compounds 1A and 2A (Φ= 46 and 74% respectively). The gradients of the graph above were used to calculate the quantum yields of the different samples. Absolute values were calculated first using the standard samples which have a fixed and known fluorescence quantum yield value using this equation:

$$\varphi_x = \varphi_{ST}(\frac{Grad_x}{Grad_{ST}})(\frac{\eta_x^2}{\eta_{ST}^2})$$

Where ST = standard and x = test solution, Φ is the fluorescent quantum yield, Grad is the gradient from the plot of the integrated fluorescence intensity vs absorbance, and η is the refractive index of the solvent.

IV. Solvatochromic Study

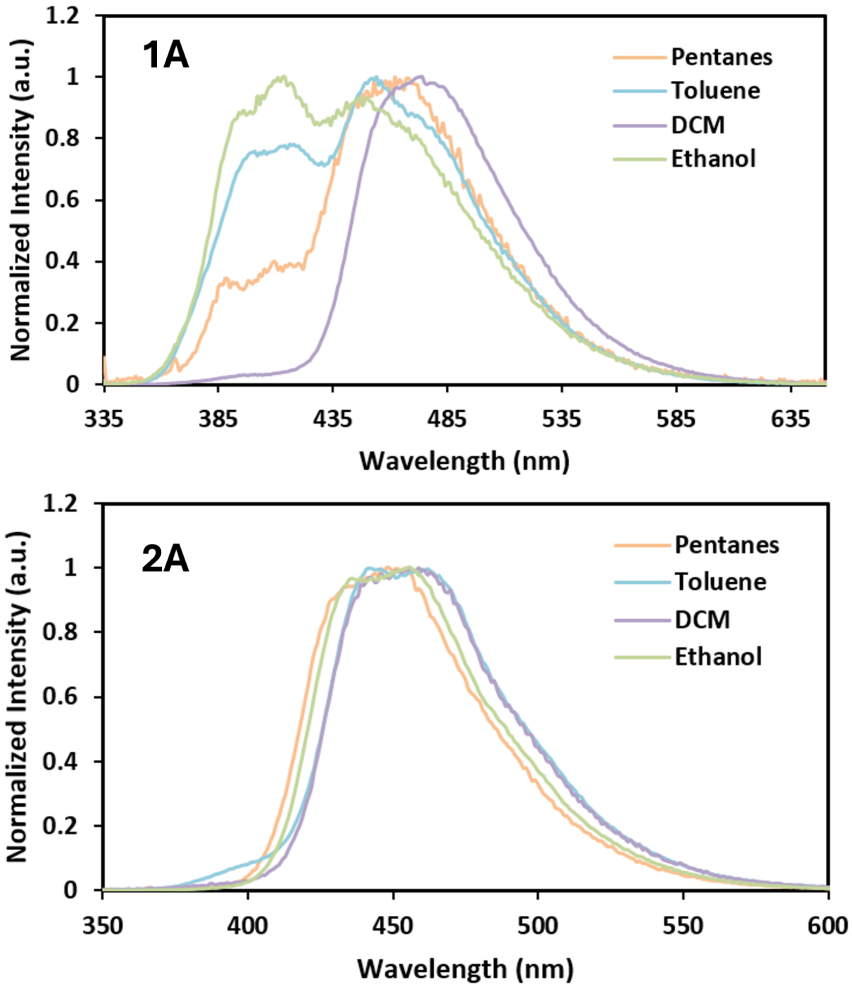

Figure S9. Varying solvent polarity for compound 1A and 2A shows a shift in maximum emission wavelength.

V. Computational Analysis Calculations were performed using Gaussian G09[24] software at a theory level and basis set as indicated for each method. Geometries were all verified to be lowest ground state energies by ensuring positive frequency vibrations. Input data files can be accessed via FigShare at: https://figshare.com/account/articles/31286152.

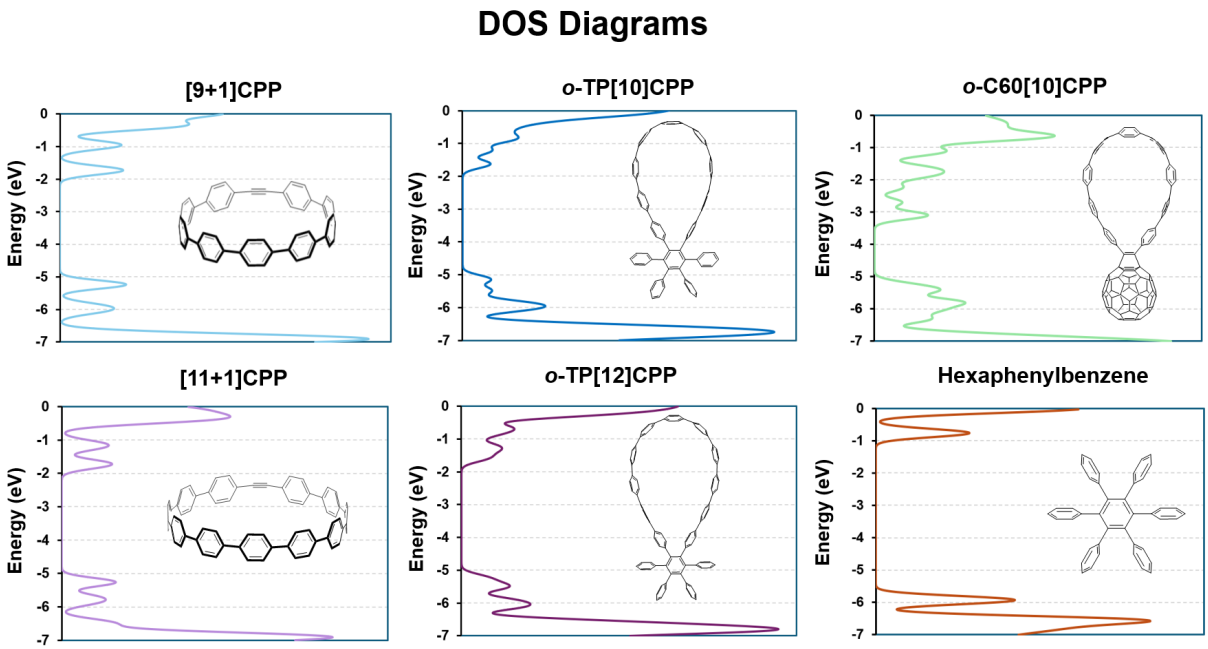

Density functional theory (DFT) *in-silico* computations were ran using Gaussian G09 software. Structural geometry optimization and frequency calculations were performed at the B3LYP level of theory with a 6-31G(d,p) basis set which were then processed using GaussSum software to generate DOS profiles and determine the HOMO and LUMO frontier orbital energies (Figure XX). In the energy diagrams we see that compared to the small molecule analogue hexaphenylbenzene (HPB), additional states are accessed due to CPP orbital contributions, shrinking the HOMO-LUMO energy gap relative to HPB. HPB compared to o-TP[10]CPP shows a 1.652 eV decrease, and o-TP[12]CPP shows a 1.509 eV decrease in the H-L gap. However, when looking at CPP parent complexes, [9+1] and [11+1] CPPs, the H-L gap slightly widens and the states become more diffuse, owing to the break in symmetry via the constraint of the strain on the molecule (+0.045 and 0.175 eV respectively). A theoretical structure with fullerene (C_{60}) was also calculated and showed we could further modify the effect on the H-L gap and decrease it by 1.348 eV compared to its [9+1]CPP

parent compound (Table XX). These results show the flexibility of using diels-alder methodology to tune the H-L gap and open more possibilities for CPPs in different opto-electronic applications.

Absorptions – *B3LYP/6-31 (d,p) TD=NSTATES=12*

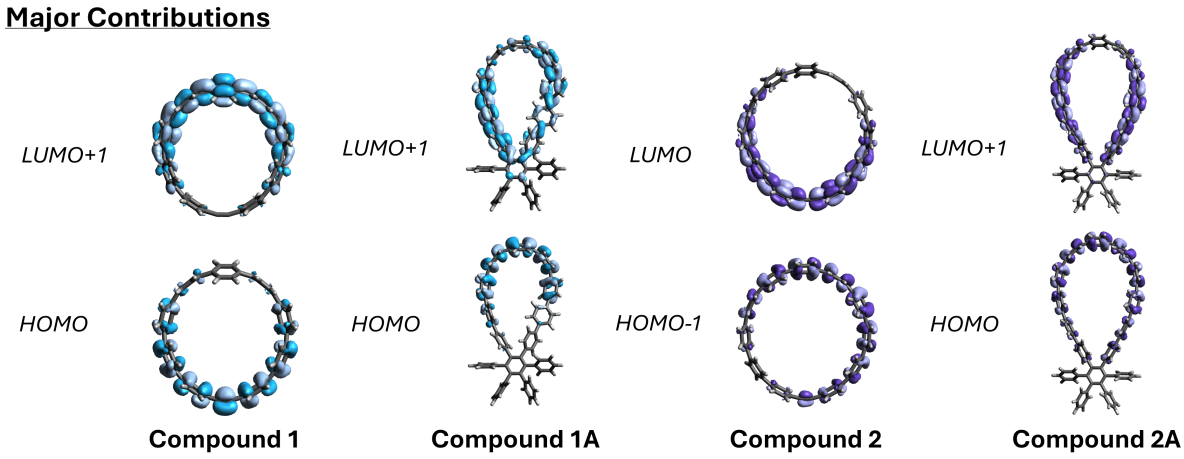

Figure S10. Major contributions for frontier orbital transitions for parent and product compounds.\

Compound 1

No.	Wavelength (nm)	Osc. Strength	Major contribs
1	425.828386	0.0414	H-1->LUMO (62%), HOMO->L+1 (36%)
2	393.413273	0.4175	HOMO->LUMO (98%)
3	386.846156	1.7317	H-1->LUMO (37%), HOMO->L+1 (62%)
4	378.046692	0.73	H-1->L+1 (98%)
5	328.104671	0.1281	H-2->LUMO (88%)
6	323.955354	0.066	H-3->LUMO (25%), H-2->L+1 (49%), HOMO->L+2 (20%)
7	319.02067	1.0466	H-3->LUMO (17%), H-2->L+1 (10%), HOMO->L+2 (65%)
8	316.520367	0.3728	H-1->L+2 (66%), HOMO->L+3 (26%)
9	312.791243	0.0365	H-3->LUMO (38%), H-2->L+1 (33%), H-1->L+3 (26%)
10	308.372365	0.009	H-3->L+1 (32%), H-1->L+2 (22%), HOMO->L+3 (42%)
11	303.666984	0.1213	H-3->L+1 (61%), HOMO->L+3 (29%)
12	302.821466	0.0877	H-3->LUMO (18%), H-1->L+3 (57%), HOMO->L+2 (12%)

Compound 1a

No.	Wavelength (nm)	Osc. Strength	Major contribs
1	410.000638	0.4605	HOMO->LUMO (96%)
2	350.772911	0.401	H-1->LUMO (86%), HOMO->L+1 (11%)
3	348.387639	1.655	H-1->LUMO (11%), HOMO->L+1 (85%)
4	323.220608	0.2669	H-1->L+1 (89%)
5	316.682059	0.0288	H-2->LUMO (16%), HOMO->L+2 (72%)
6	314.856501	0.106	H-2->LUMO (75%), HOMO->L+2 (18%)
7	311.455469	0.0023	H-3->LUMO (41%), HOMO->L+3 (35%)
8	306.701776	0.0609	H-10->LUMO (11%), HOMO->L+5 (61%)
9	304.293025	0.3969	H-3->LUMO (32%), HOMO->L+3 (42%)
10	301.115223	0.0757	H-1->L+2 (67%), HOMO->L+3 (10%)
11	296.968127	0.2979	H-4->LUMO (23%), H-2->L+1 (46%)
12	295.566399	0.151	H-4->LUMO (58%), H-3->LUMO (14%), H-2->L+1 (17%)

Compound 2

No.	Wavelength (nm)	Osc. Strength	Major contribs
1	417.062006	0.1684	H-1->LUMO (41%), H-1->L+1 (10%), HOMO->LUMO (31%), HOMO->L+1 (16%)
2	385.750888	1.4485	H-1->LUMO (54%), HOMO->LUMO (16%), HOMO->L+1 (23%)
3	384.840901	1.4934	H-1->L+1 (20%), HOMO->LUMO (49%), HOMO->L+1 (26%)
4	371.755549	0.6906	H-1->L+1 (63%), HOMO->L+1 (30%)
5	340.382136	0.191	H-2->LUMO (94%)
6	333.685523	0.601	H-3->LUMO (39%), H-2->L+1 (55%)
7	332.754141	0.5602	H-1->L+2 (14%), HOMO->L+2 (74%)
8	328.957795	0.2715	H-1->L+2 (73%), HOMO->L+2 (14%)
9	324.616937	0.0015	H-3->LUMO (53%), H-2->L+1 (40%)
10	317.44423	0.022	H-3->L+1 (13%), H-1->L+3 (19%), HOMO->L+3 (56%)
11	317.062687	0.1421	H-3->L+1 (23%), H-1->L+3 (33%), HOMO->L+3 (32%)
12	316.342696	0.221	H-3->L+1 (58%), H-1->L+3 (34%)

Compound 2a

No.	Wavelength (nm)	Osc. Strength	Major contribs
1	391.092653	0.2953	HOMO->LUMO (90%)
2	355.489844	3.2479	H-1->LUMO (39%), HOMO->L+1 (55%)
3	344.295335	0.0379	H-1->LUMO (55%), HOMO->L+1 (41%)
4	341.05629	0.9796	H-2->LUMO (60%), HOMO->L+2 (25%)
5	330.483508	0.0449	H-2->LUMO (35%), HOMO->L+2 (53%)
6	328.94034	0.0059	H-1->L+1 (74%), HOMO->L+2 (16%)
7	320.521672	0.0836	H-2->L+1 (82%)
8	314.106691	0.3434	H-1->L+2 (76%)
9	309.064196	0.0071	H-2->L+2 (74%)
10	307.538616	0.0105	H-3->LUMO (37%), HOMO->L+3 (38%)
11	303.600061	0.1029	H-3->LUMO (36%), HOMO->L+3 (45%)
12	296.421434	0.0009	H-6->LUMO (12%), H-4->LUMO (11%), H-3->L+1 (15%), H-3->L+2 (11%), H-2->L+3 (16%), HOMO->L+5 (10%)

Table S11. List of all major contributions and strength of absorption transitions for each compound.

Absorption Relaxations – *CAM-B3LYP/6-31 (d,p) opt TD*

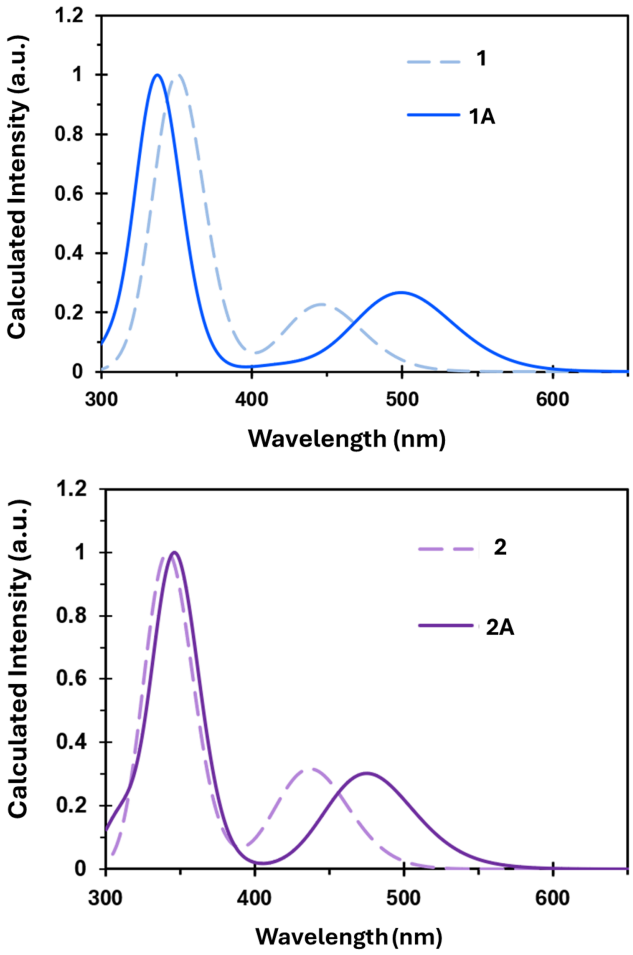

Figure S12. Comparison graphs for computational opt TD DFT calculations, we see a similar trend verifying the experimental observations of widening the effective Stokes Shift. Calculations were done using PCM in dichloromethane to match experimental protocols.

Dipole Moments – *B3LYP/6-31G (d,p) opt*

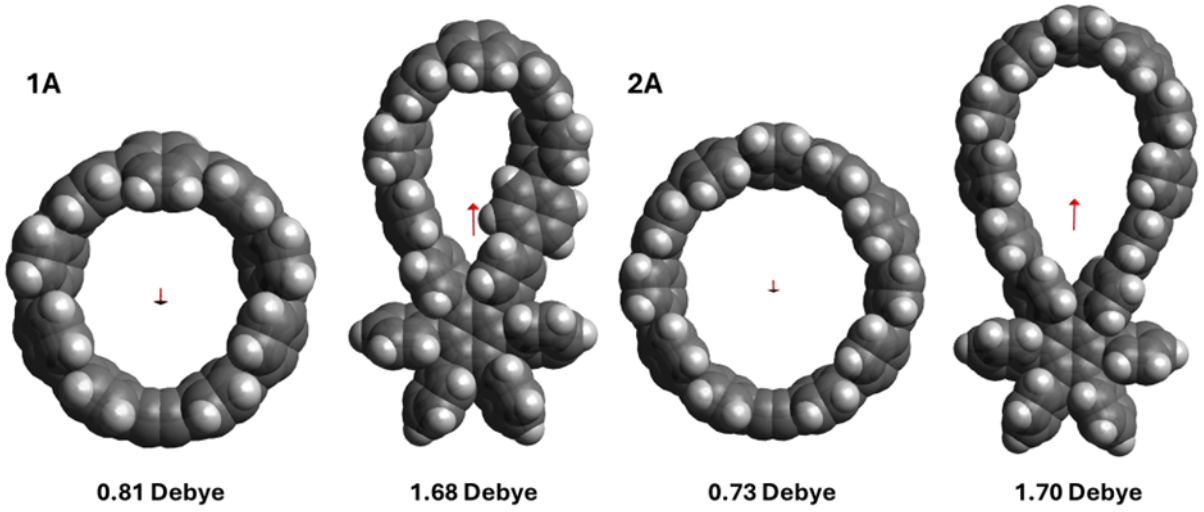

Figure S13. Inversion of dipole following tetraphenyl CPP modification.

3.1.7 Citations

(1) Jasti, R.; Bhattacharjee, J.; Neaton, J. B.; Bertozzi, C. R. Synthesis, Characterization, and Theory of [9]-, [12]-, and [18]Cycloparaphenylene: Carbon Nano-hoop Structures. *J. Am. Chem. Soc.* **2008**, 130 (52), 17646–17647. https://doi.org/10.1021/ja807126u.

(2) Patel, V. K.; Kayahara, E.; Yamago, S. Practical Synthesis of [n]Cycloparaphenylenes (N=5, 7–12) by H2SnCl4-Mediated Aromatization of 1,4-Dihydroxycyclo-2,5-Diene Precursors. *Chem. – Eur. J.* **2015**, 21 (15), 5742–5749. https://doi.org/10.1002/chem.201406650.

(3) Iwamoto, T.; Watanabe, Y.; Sakamoto, Y.; Suzuki, T.; Yamago, S. Selective and Random Syntheses of [n]Cycloparaphenylenes (n = 8–13) and Size De-pendence of Their Electronic Properties. *J. Am. Chem. Soc.* **2011**, 133 (21), 8354–8361. https://doi.org/10.1021/ja2020668.

(4) Ishii, Y.; Nakanishi, Y.; Omachi, H.; Matsuura, S.; Matsui, K.; Shinohara, H.; Segawa, Y.; Itami, K. Size-Selective Synthesis of [9]–[11] and [13]Cycloparaphenylenes. *Chem. Sci.* **2012**, 3 (7), 2340–2345. https://doi.org/10.1039/C2SC20343J.

(5) Xu, Y.; Wang, B.; Kaur, R.; Minameyer, M. B.; Bo-the, M.; Drewello, T.; Guldi, D. M.; von Delius, M. A Supramolecular [10]CPP Junction Enables Effi-cient Electron Transfer in

Modular Porphyrin–[10]CPP□Fullerene Complexes. *Angew. Chem.* **2018**, 130 (36), 11723–11727. https://doi.org/10.1002/ange.201802443.

(6) Pedersen, V. B. R.; Woodcock, L. B.; Dünweber, P. G. I. L.; Mikkelsen, K. V.; Jasti, R.; Nielsen, M. B. [11]Cycloparaphenylene Incorporating a Redox-Active Dithiafulvene Moiety Provides Access to a Carbon Nanohoop with an Unpaired Electron along the Core. *Chem. Commun.* **2026**. https://doi.org/10.1039/D5CC06226H.

(7) Liang, J.; Zhu, L.; Li, Y.; Xu, G.; Han, H.; Li, Y.; Zhou, Z. Abnormal Anti-Kasha Emission and TADF in Anionic Cycloarylenes. *Angew. Chem.* **2025**, e202512344. https://doi.org/10.1002/ange.202512344.

(8) Xu, Z.; Liu, X.; Ge, C.; Tian, X.; Ma, X.; Sun, Z. Controlling the Flipping Motion of Cyclopara-phenylene Dimers. *J. Org. Chem.* **2025**, acs.joc.5c01164. https://doi.org/10.1021/acs.joc.5c01164.

(9) A. Kamin, A.; D. Clayton, T.; E. Otteson, C.; M. Gannon, P.; Krajewski, S.; Kaminsky, W.; Jasti, R.; J. Xiao, D. Synthesis and Metalation of Poly-catechol Nanohoops Derived from Fluorocyclopara-phenylenes. *Chem. Sci.* **2023**, 14 (36), 9724–9732. https://doi.org/10.1039/D3SC03561A.

(10) Kręcijasz, R. B.; Malinčík, J.; Mathew, S.; Štacko, P.; Šolomek, T. Strain-Induced Photochemical Opening of Ferrocene[6]Cycloparaphenylene: Un-caging of Fe2+ with Green Light. *J. Am. Chem. Soc.* **2025**, 147 (12), 10231–10237. https://doi.org/10.1021/jacs.4c15818.

(11) Fehr, J. M.; Myrthil, N.; Garrison, A. L.; Price, T. W.; Lopez, S. A.; Jasti, R. Experimental and Theo-retical Elucidation of SPAAC Kinetics for Strained Alkyne-Containing Cycloparaphenylenes. *Chem. Sci.* **2023**, 14 (11), 2839–2848. https://doi.org/10.1039/D2SC06816H.

(12) García-Rodeja, Y.; Fernández, I. Factors Controlling the Reactivity of Strained-Alkyne Embedded Cyclo-paraphenylenes. *J. Org. Chem.* **2019**, 84 (7), 4330–4337. https://doi.org/10.1021/acs.joc.9b00292.

(13) Shudo, H.; Kuwayama, M.; Segawa, Y.; Yagi, A.; Itami, K. Half-Substituted Fluorocyclopara-

phenylenes with High Symmetry: Synthesis, Proper-ties and Derivatization to Densely Substituted Car-bon Nanorings; preprint; *Chemistry*, **2023**. https://doi.org/10.26434/chemrxiv-2023-zsvnt.

(14) Jackson, E. P.; Sisto, T. J.; Darzi, E. R.; Jasti, R. Probing Diels–Alder Reactivity on a Model CNT Sidewall. *Tetrahedron* **2016**, 72 (26), 3754–3758. https://doi.org/10.1016/j.tet.2016.03.077.

(15) Schaub, T. A.; Margraf, J. T.; Zakharov, L.; Reuter, K.; Jasti, R. Strain-Promoted Reactivity of Alkyne-Containing Cycloparaphenylenes. *Angew. Chem. Int. Ed.* **2018**, 57 (50), 16348–16353. https://doi.org/10.1002/anie.201808611.

(16) Clayton, T. D.; Fehr, J. M.; Price, T. W.; Zakharov, L. N.; Jasti, R. Pinwheel-like Curved Aromatics from the Cyclotrimerization of Strained Alkyne Cy-cloparaphenylenes. *J. Am. Chem. Soc.* **2024**, 146 (44), 30607–30614. https://doi.org/10.1021/jacs.4c12272.

(17) Kayahara, E.; Qu, R.; Yamago, S. Bromination of Cycloparaphenylenes: Strain-Induced Site-Selective Bis-Addition and Its Application for Late-Stage Functionalization. *Angew. Chem. Int. Ed.* **2017**, 56 (35), 10428–10432. https://doi.org/10.1002/anie.201704982.

(18) Bliksted Roug Pedersen, V.; Price, T. W.; Kofod, N.; Zakharov, L. N.; Laursen, B. W.; Jasti, R.; Brønd-sted Nielsen, M. Synthesis and Properties of Flu-orenone-Containing Cycloparaphenylenes and Their Late-Stage Transformation. *Chem. – Eur. J.* **2024**, 30 (5), e202303490. https://doi.org/10.1002/chem.202303490.

(19) Kinoshita, N.; Kotani, N.; Sugiura, M.; Matsumura, K.; Sakamaki, D.; Tauchi, D.; Hasegawa, M.; Kawai, H.; Tsuchido, Y. A Precisely Bromo-Functionalized [9]Cycloparaphenylene as a Platform for Late-Stage Multi-Site π-Extension toward Chiral Nanohoops. *Chemistry* **2025**. https://doi.org/10.26434/chemrxiv-2025-3f5nd.

(20) Clayton, T. D.; Fehr, J. M.; Price, T. W.; Zakharov, L. N.; Jasti, R. Pinwheel-like Curved Aromatics from the Cyclotrimerization of Strained Alkyne Cycloparaphenylenes. *J. Am. Chem. Soc.* **2024**, 146 (44), 30607–30614. https://doi.org/10.1021/jacs.4c12272.

(21) Pangborn, A. B.; Giardello, M. A.; Grubbs, R. H.; Rosen, R. K.; Timmers, F. J. Safe and

Convenient Procedure for Solvent Purification. *Organometallics* **1996**, 15 (5), 1518–1520. https://doi.org/10.1021/om9503712.

(22) Schaub, T. A.; Margraf, J. T.; Zakharov, L.; Reuter, K.; Jasti, R. Strain-Promoted Reactivity of Alkyne-Containing Cycloparaphenylenes. *Angew. Chem. Int. Ed.* **2018**, 57 (50), 16348–16353. https://doi.org/10.1002/anie.201808611.

(23) Scientific, H. A Guide to Recording Fluorescence Quantum Yields.

(24) Frisch, M. J.; Trucks, G. W.; Schlegel, H. B.; Scuseria, G. E.; Robb, M. A.; Cheeseman, J. R.; Scalmani, G.; Barone, V.; Petersson, G. A.; Nakatsuji, H.; Li, X.; Caricato, M.; Marenich, A. V.; Bloino, J.; Janesko, B. G.; Gomperts, R.; Mennucci, B.; Hratchian, H. P.; Ortiz, J. V.; Izmaylov, A. F.; Sonnenberg, J. L.; Williams; Ding, F.; Lipparini, F.; Egidi, F.; Goings, J.; Peng, B.; Petrone, A.; Henderson, T.; Ranasinghe, D.; Zakrzewski, V. G.; Gao, J.; Rega, N.; Zheng, G.; Liang, W.; Hada, M.; Ehara, M.; Toyota, K.; Fukuda, R.; Hasegawa, J.; Ishida, M.; Nakajima, T.; Honda, Y.; Kitao, O.; Nakai, H.; Vreven, T.; Throssell, K.; Montgomery Jr., J. A.; Peralta, J. E.; Ogliaro, F.; Bearpark, M. J.; Heyd, J. J.; Brothers, E. N.; Kudin, K. N.; Staroverov, V. N.; Keith, T. A.; Kobayashi, R.; Normand, J.; Raghavachari, K.; Rendell, A. P.; Burant, J. C.; Iyengar, S. S.; Tomasi, J.; Cossi, M.; Millam, J. M.; Klene, M.; Adamo, C.; Cammi, R.; Ochterski, J. W.; Martin, R. L.; Morokuma, K.; Farkas, O.; Foresman, J. B.; Fox, D. J. Gaussian 16 Rev. C.01, **2016**.

Chapter IV: Developing CPPs as a Bioconjugation Handle

4.1 CPPs as Fluorophores for Multiplexed Imaging in Biological Systems

4.1.1 Contributions

This chapter discusses new CPP bioconjugation methods. We've made preliminary progress on two projects, one using norbornene modified CPPs for thiol-ene click chemistry and terminated meta-cycloparaphenylenes (**m[n]CPPs**) for azide mediated conjugation. Norbornene Cycloparaphenylenes (CPPs) for Thiol-ene Click Mediated Protein Bioconjugation is the focus of section 4.1, my contributions for this project include: project conception and design, synthesis, characterization, writing and editing. Alkyne multiplex systems being discussed briefly in future work. Both projects are a collaborative effort between the Jasti, DeRose, OHSU, and Hettiaratchi Labs. Synthesis and development of the alkyne terminated meta-CPPs was previously reported by the Jasti Lab.[1] This project furthers the previous research by expanding the colors available toward applications in multiplex imaging (using 3 or more colors simultaneously for better imaging resolution). This project is in collaboration with Katy Wyatt, Gabriela Bailey, Katelyn Alley, and Justin Svendsen; we've worked on synthesis and characterization of CPPs and bioconjugate products. Multiple aspects of these projects are ongoing.

4.1.2 Abstract

Fluorescent probes are widely employed in multiplexed imaging to resolve complex biological processes. By enabling the simultaneous detection of multiple signals, multiplexed imaging improves spatial and temporal resolution and facilitates identification of interactions among signaling components. Here, we functionalize norbornene-substituted cycloparaphenylenes (CPPs) as tunable fluorescent reporters via thiol–ene click chemistry. We demonstrate efficient conjugation to small molecules, peptides, and proteins – establishing a versatile platform for fluorescent labeling across diverse biological systems.

4.1.3 Introduction

Cycloparaphenylenes (CPPs) are a class of carbon nanomaterials consistent with a single slice of a carbon nananotube (CNT). CNTs have broad applications in optoelectronics due to their conductivity and mechanical properties. Typically, CNTs are synthesized through high energy means resulting in single to multi-walled products. Single walled CNTs (SWCNTs) have been explored for their fluorescent properties, however, their applications are limited with their low quantum yields (QY) (~1%) and difficult purification.[2–6] Multi-walled CNTs dissipate energy through non-radiative pathways, and while their intrinsic porosity can be useful for drug-delivery applications, there remains a need for brighter multi-purpose fluorophores toward new theranostics. CPPs are great candidates for multiplexed imaging fluorophores due to their bottom-up rational design leading to pure products with tunable optoelectronics. Their cyclic nature leads to radially oriented π-orbitals and unique optoelectronic properties with a shared absorption maximum (~330-340 nm). In addition, their quantum yields are high (typically >40%) with high molar absorptivity (scale of 10^5), and a large effective Stokes Shift (~120+ nm). Their shared absorption, large Stokes Shifts, and intrinsic porosity all hold promise as a novel thernanostic with applications in two-photon imaging, drug delivery, and multiplex imaging. To date, CPPs have only been studied for few biological imaging applications.[1,7,8] In 2021, Jasti and co-workers developed an azide-alkyne click mediated conjugation method to append solubilizing groups and cell targeting moieties. Some drawbacks to this approach are the need for PEG groups (which complicates purification of precursors) and the use of highly reactive azide linkers. Since they are cyclic hydrocarbons, they are difficult to dissolve in water; however, they are soluble in most organic solvents as their structure disrupts π-π stacking that typically renders linear paraphenylene chains insoluble. As research for CPPs toward biological applications is still in its infancy additional bioconjugation strategies are needed to help expand the CPP library to fully develop these small molecules as fluorescent probes for multiplexed imaging. Here we report a photoinitiated thiol-ene click methodology as a broad approach to bioconjugate norbornene CPPs directly to biological entities with available cysteine groups. Due to larger protein sizes and solubility of peptides, this method acts to additionally solubilize the CPPs

without the need for PEG linkers. To date, this is the first thiol-ene reaction developed for CPPs toward bioconjugate applications.

4.1.4 Results and Discussion

Synthesis of Norbornene CPPs Norbornene[10]CPP was synthesized according to reported literature procedures.[9] Norbornene has a double bond that is slightly strained, yet stable throughout CPP synthesis. We can use this alkene bond as a handle for diverse late-stage modifications. For this project we also aim to leverage CPPs shared absorption maxima for multiplexed imaging by introducing different functionalities that change the CPPs' emissive properties. One way to do this is by changing the size of the CPP, however, this method can also decrease the quantum yield of the CPP significantly. To avoid this, we've instead designed a CPP with an acceptor benzothiadiazole unit that red shifts emissions for the same ring size maintaining porosity as well as quantum yield (see future work for synthesis of compound **6**).[10]

Photoinitiated Thiol-ene Conjugation We showed using a small molecule model system, a facile method to append thiophenol to compound **2** using benzophenone as the photo initiator for the thiol-ene click reaction.[11–13] In this thiol-ene click reaction, light initiates a radical cascade with a ketyl radical on the benzophenone. Since the substrate is bulky, and the radical is stabilized by the C-O bond, the sulfenyl radical has specificity for addition into the norbornene double bond (**Scheme 4.5**). We've shown efficacy of this method at room temperature with a variety of solvent conditions (**Table 4.3**). This method improves upon past methods as it uses room temperature conditions and biocompatible solvent systems. We can vary the R-group on the thiolate broadly using any small peptide or protein with available cysteine groups. For proof of concept, we've used small peptides developed by the Hettiaratchi Lab for use in exogenous protein delivery. These peptides (**B4C1** and **G1C2**) are bone morphogenic protein-2 (BMP-2) binders, they bind at different strengths (Low and High binding respectively) and have terminal cysteine groups for conjugation specificity.[14] As we also wanted to test this method with proteins that aren't compatible with organic solvents, we used BSA as a test system that was dissolved in a 1X PBS buffer system, and organics dissolved in

DMSO. All conjugated systems showed blue fluorescence under UV light while in solution as well as protein present when subjected to a Bradford protein assay. Proton NMR demonstrates changes in proton shifts, and complex protein structure. Notably, the conjugates were able to be dissolved in water and continued to show emission.

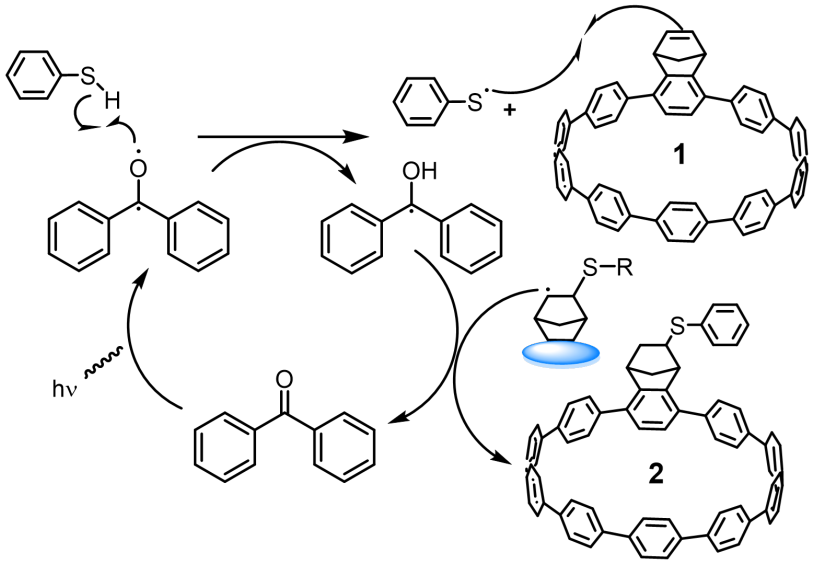

Scheme 4.5: Mechanistic example of model system using thiol-ene click photochemistry. Thiophenol small molecule example shown with the CPP. The thiol's R group is varied for different protein conjugates -see synthesis methods.

R-SH Substrate	Synthesis Conditions
Thiophenol	DMSO, BzPhen*, RT, UV, ¥
B4-C1 Affibody (low)	DMSO, BzPhen*, RT, UV, ¥
G1-C2 Affibody (high)	DMSO, BzPhen*, RT, UV, ¥
Bovine Serum Albumin (BSA)	BSA in 1X PBS, BzPhen*, Organics in DMSO, RT, UV, ¥

¥The reaction flask was irradiated with UV lamp (115 V 254/365 nm wavelength 4-Watt 60 Hz) for 12-18h
*BzPhen – Benzophenone radical source

Table 4.3: Synthetic conditions for different thiolate peptides.

Photophysical Characteristics of Bioconjugate CPPs The photophysical properties of the parent CPP compound **1**, were compared to the small molecule thiophenol conjugate. We see the photophysical properties are maintained with little shifting of the emission, confirmed by DFT modeling (see methods section for DFT comparisons of compound **2**). UV-Fluorescence on the BSA conjugated CPP reveals dominate absorption profile to be from the BSA unit. However, upon excitement

at 340 nm we see a clear CPP emission trace at the expected wavelengths (**Figure 4.18**).

4.1.5 Conclusion and Future Work

Here we report a thiol-ene click reaction to bioconjugate CPPs displaying bioconjugates with emissive properties, and water solubility without the need for PEG linkers under facile reaction conditions. This work is ongoing, exploring red-shifted Norbornene CPP analogues to additionally apply this idea toward multiplexed imaging *in-vivo* (**Figure 4.19**).

Another approach to modify CPPs for multiplexed imaging applications is through an azide-alkyne click reaction. This method had been developed in 2021 with the Jasti Lab, but has yet to be applied in antibody systems, or for multiplexed imaging. Future work on this project aims to use a series of meta-alkyne CPPs to click on antibody targeting systems (**Figure 4.20**). In collaboration with OHSU, we aim to test both conjugation methods for precise therapeutic imaging.

4.1.6 Bridge to Chapter V

This concludes the work specifically on CPP late-stage modifications. In my first two-years, I was part of the Hettiaratchi Lab, and Chapter V is the focus of the manuscript that came out of that research. I modified hyaluronic acid (HA) with norbornene to append peptides for controlled protein delivery through a thiol-ene photo-initiated reaction. This was the main inspiration for the development of the Norbornene CPP modification using a similar route. Chapter V dives deeper into how we used these HA scaffolds to successfully control protein delivery rate and how to modify them for optimized results.

4.1.7 Experimental Appendix: Supplementary Information

Commercially available materials were used without purification unless otherwise indicated. Moisture and oxygen sensitive reactions were carried out in flame-dried glassware and under an inert atmosphere of purified nitrogen using syringe/septa technique. Tetrahydrofuran (THF) and dimethylformamide (DMF) were dried by filtration through alumina according to the methods de-

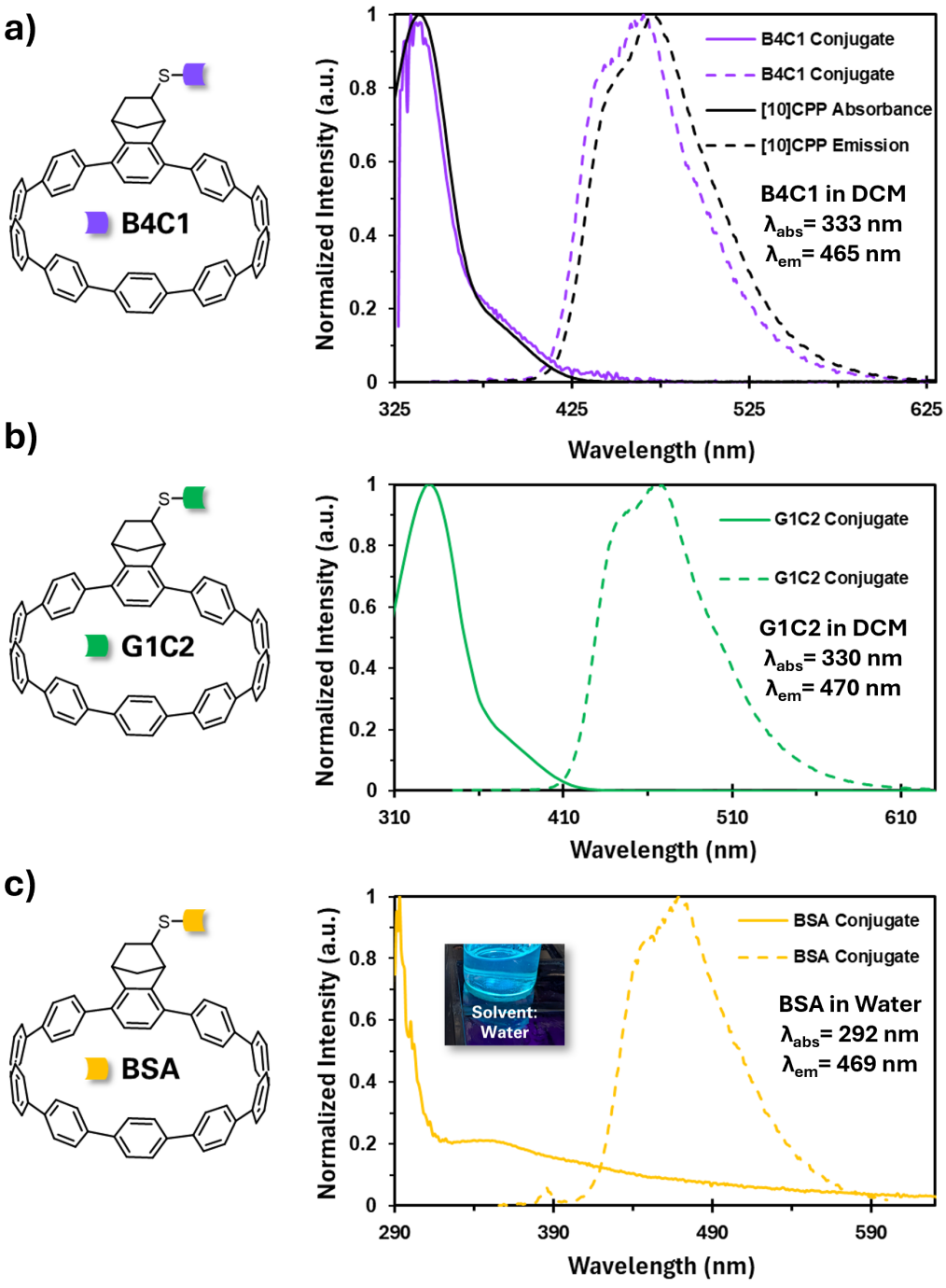

Figure 4.18: a) Overlay of B4C1 conjugate absorption and emission profiles from the standard H[10]CPP absorption/emission. b) Absorption and emission profiles of the G1C2 CPP conjugate. c) Absorption and emission profiles of BSA CPP Conjugate.

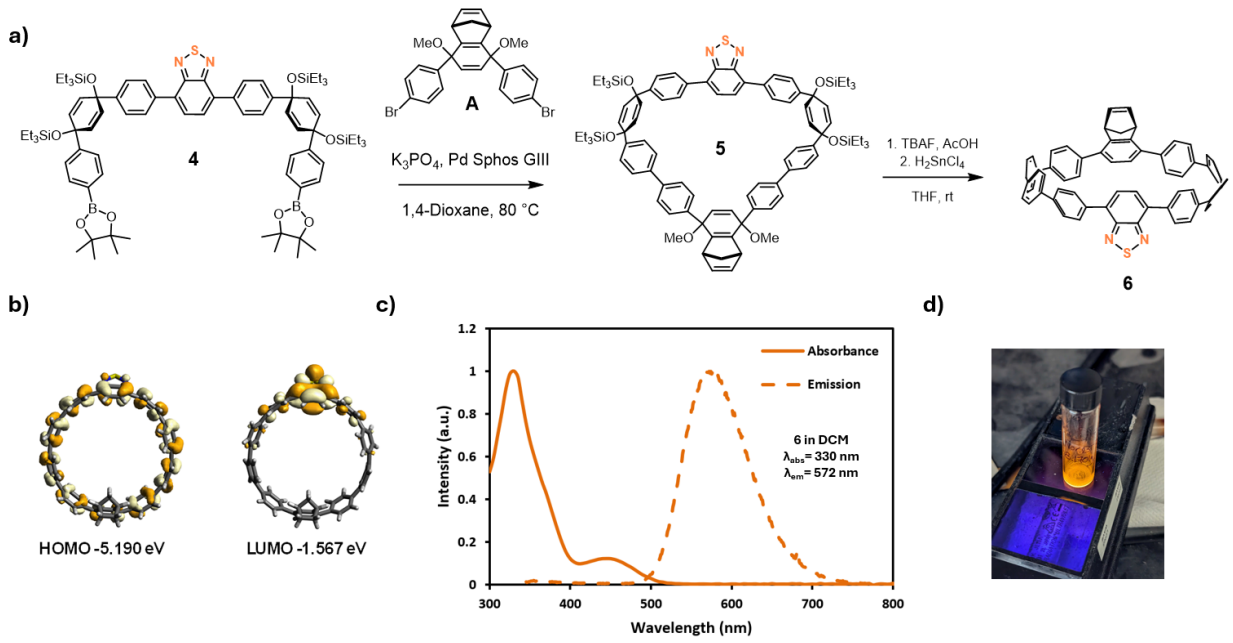

Figure 4.19: a) Synthesis of BT-Nor[10]CPP for use a bright red fluorophore conjugate. b) DFT orbital diagram showing donor-acceptor character of FMOs ran in *G09* using B3LYP/6-31(d,p) level of theory. c) Absorption and emission profiles of compound **6**. d) UV Irradiated sample showing bright orange emission.

scribed by Grubbs.[15] Alumina column chromatography was conducted with SorbTech basic alumina (pH 10), Act. II-III, 50-200 µm. 1H and 13C NMR spectra were recorded on a Bruker Avance III HD 500 (1H: 500 MHz, 13C: 126 MHz) NMR spectrometer. The chemical shifts (δ) were reported in parts per million (ppm) and were referenced to the solvent (CD2Cl2, 1H: δ = 5.32 ppm and 13C: δ = 53.84 ppm or CDCl3, 1H: δ = 7.26 ppm and 13C: δ = 77.801 ppm). Coupling constants (J) are given in Hz and the apparent resonance multiplicity is reported as s (singlet), d (doublet), t (triplet), q (quartet), dd (doublet of doublets) or m (multiplet). UV/Vis absorption and fluorescence spectra were recorded on an Agilant Cary 100 spectrophotometer and a Horiba Jobin Yvon Fluoromax-4 Fluorimeter, respectively. All measurements were carried out under ambient conditions in a Spectrocell RF-1010-T threaded top vacuum formed borosilicate fluorometer cell (10 mm light path). Mass spectroscopy HRMS measurements were performed on Bruker Daltonics UltrafleXtreme MALDI TOF/TOF by a third-party lab.

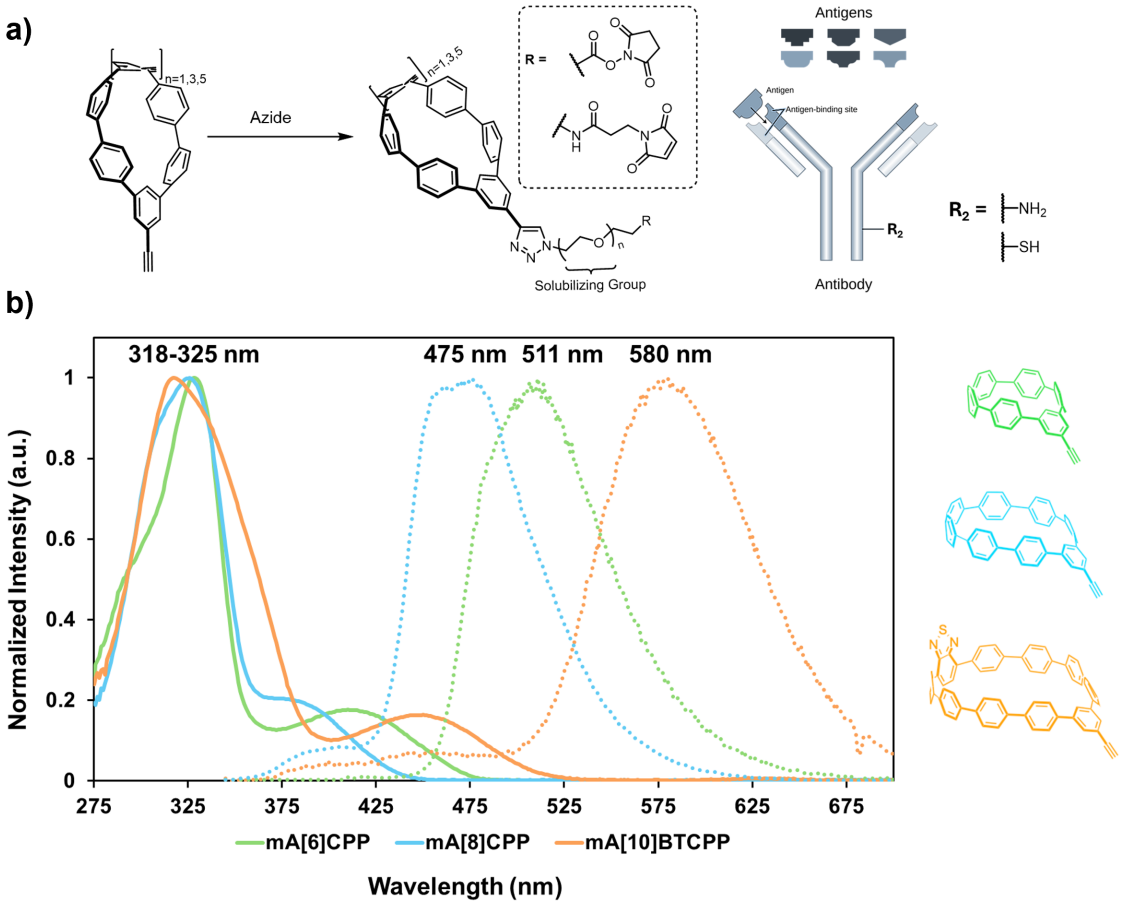

Figure 4.20: a) Example of alkyne CPP systems being conjugated to a model antibody. b) Photophysical profiles of meta-alkyne CPP library for multiplex imaging.

I. Synthesis

Compound 1 was synthesized according to literature procedures.[9]

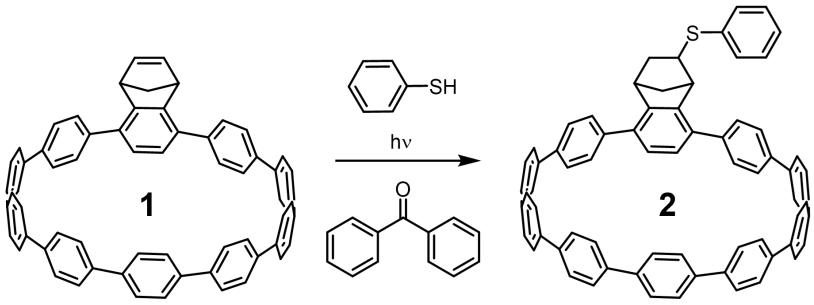

Compound 2. A mixture of compound 1 (1 mmol), benzophenone (10 mol%), thiophenol (1 mmol) and nitrile (3 mL) was stirred at r.t. under a nitrogen atmosphere and irradiated with visible light (18 W compact fluorescent lamp) for 12-18 h. After completion of reaction which was monitored by TLC, water (5 mL) was added, and the mixture was extracted with ethyl acetate (3 × 5 mL). The combined organic phase was dried over anhydrous Na2SO4, filtered and evaporated under reduced pressure. Brine was added to the aqueous emulsion (~20 mL) and it turned from yellow to clear/slightly cloudy. This was further extracted with ethyl acetate and these organic layers combined in a different flask. This layer showed emission after UV irradiation, so it was also dried and transferred to a round bottom flask to reduce and analyze via NMR which also had product. 1H NMR (500 MHz, d-CD2Cl2) δ 7.74 – 7.51 (m, 35H), 7.50 – 7.37 (m, 4H), 7.37 – 7.30 (m, 2H), 7.23 (d, J = 8.6 Hz, 1H), 6.80 (d, J = 0.9 Hz, 1H), 3.98 – 3.75 (m, 2H), 3.61 – 3.28 (m, 2H), 2.32 – 1.84 (m, 3H). HRMS (ESI, TOF), m/z calculated for C71H50S (M)+ Expected: 934.3633, Found: 934.3628.

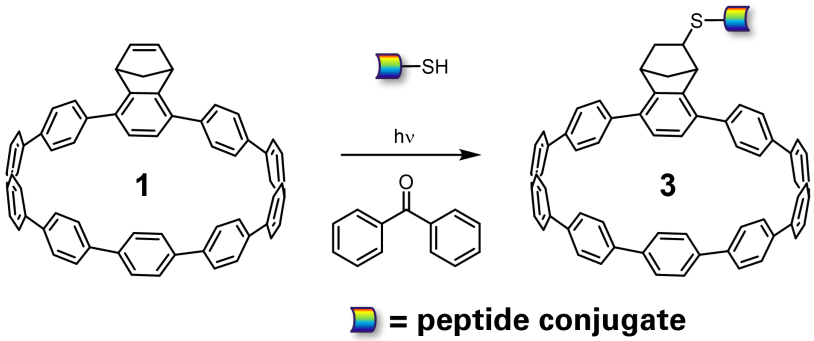

Compound 3. Peptide/Protein-SH(~8-9 mg) was dissolved in 1 mL DMSO in glass syn vial which dissolved pretty quickly. This was added to a small rbf flask that was flame dried and allowed to cool. Nor[10]CPP (6 mg) was dissolved in 5 mL of DMSO and added via syringe to the reaction flask followed by 0.2 mL of 4.3 mM benzophenone in DMSO. The reaction flask was irradiated with UV lamp (115 V 254/365 nm wavelength 4 Watt 60 Hz) for 12-18 hr. After completion of reaction (monitored by TLC), water (5 mL) was added and the mixture was extracted with ethyl acetate (3 × 5 mL). The combined organic phase was dried over anhydrous Na2SO4, filtered and evaporated under reduced pressure. Salt was added to the aqueous layer and further extracted causing a milky white emulsion to enter the EtOAc layer (F3). After 24 hr add ~ 10mL water and 5 mL EtOAc and let stir ~ 10 min Extracted with Ethyl Acetate (15 mL x2), aqueous layer looked like a yellow emulsion and still had a slight blue tinge to it. Brine was added to the aqueous emulsion (~20 mL) and it turned from yellow to clear/slightly cloudy. This was further extracted with ethyl acetate and these organic layer combined with the other organic layers. Organic ethyl acetate layers were washed with water (x10 mL) then dried with sodium sulfate then transferred to a round bottom and reduced under pressure then dried under high vac. H NMR was taken in d-dcm. Aqueous layer was transferred to a plastic tube and stored at 0C for lyophilization to check the NMR in d-D2O. Bradford assay was performed to determine protein present in sample and found positive for all protein conjugates.

II. Structural Characterization

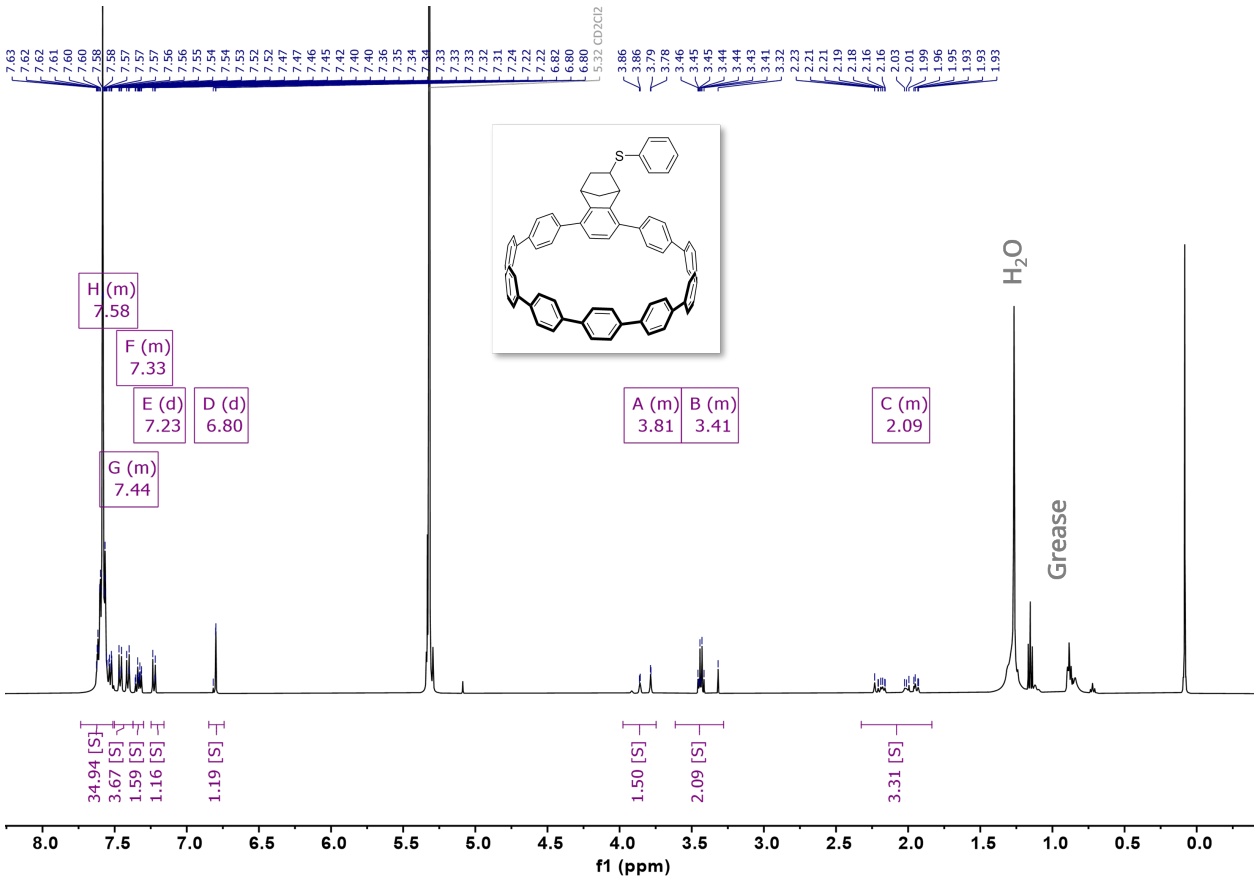

Figure S1. ^{1}H NMR of compound 2.

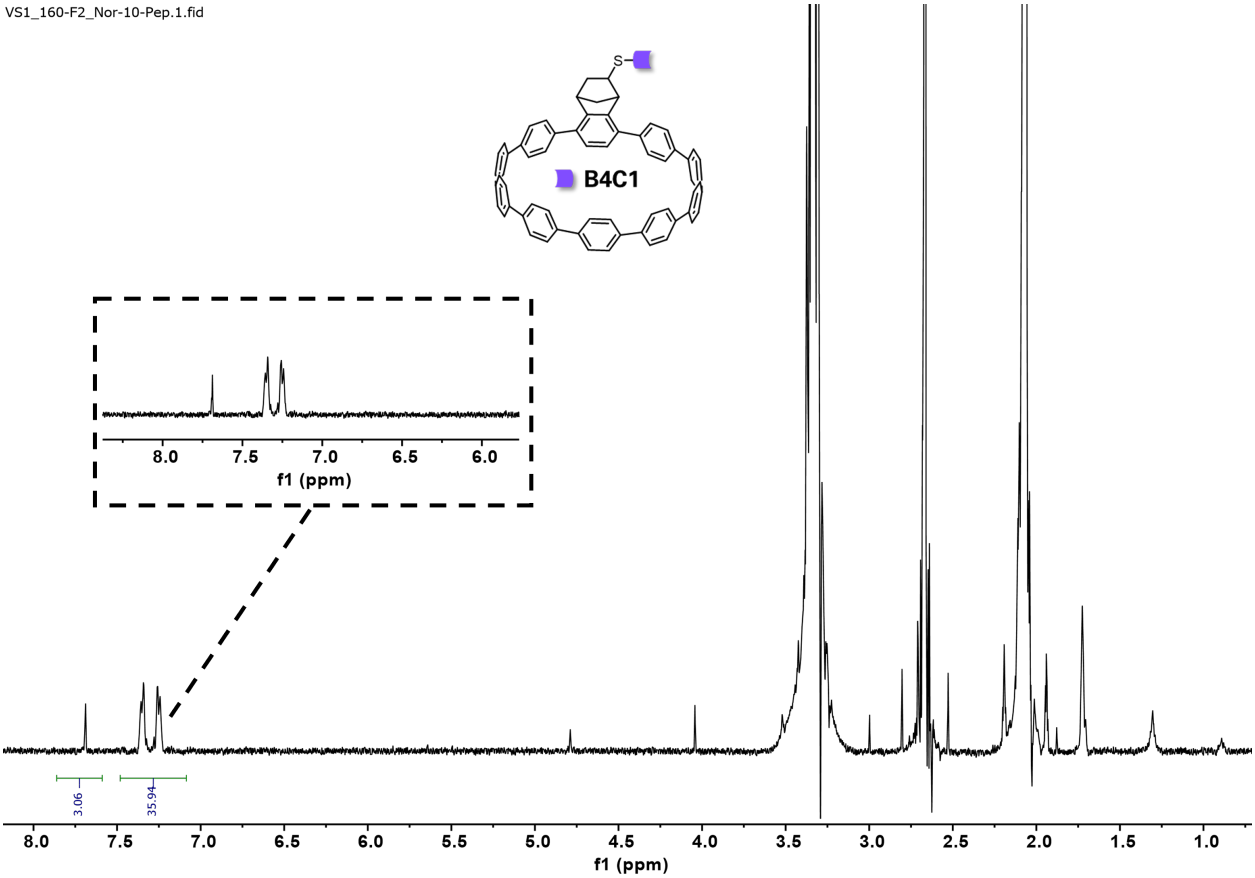

Figure S2. ^{1}H NMR of CPP B4C1 Conjugate.

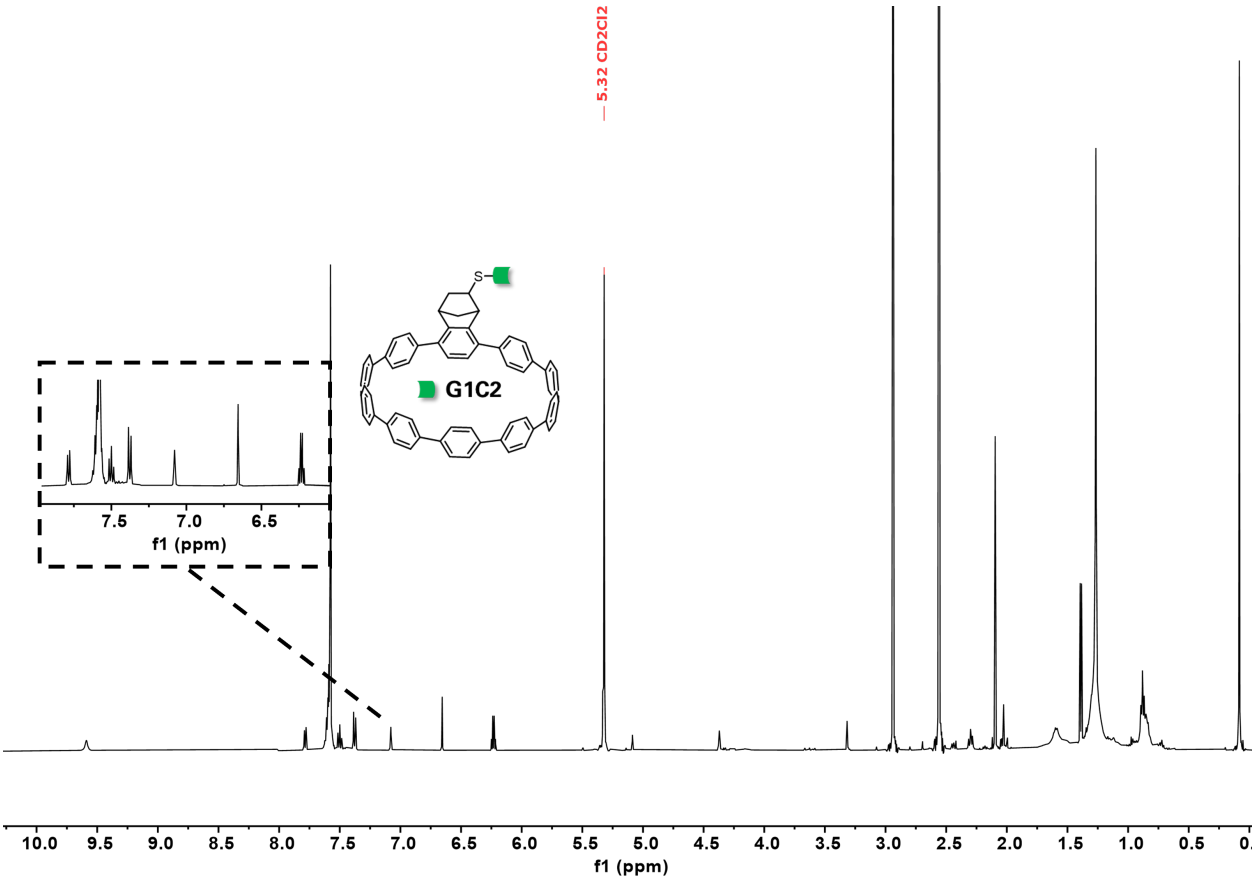

Figure S3. ^{1}H NMR of CPP G1C2 Conjugate.

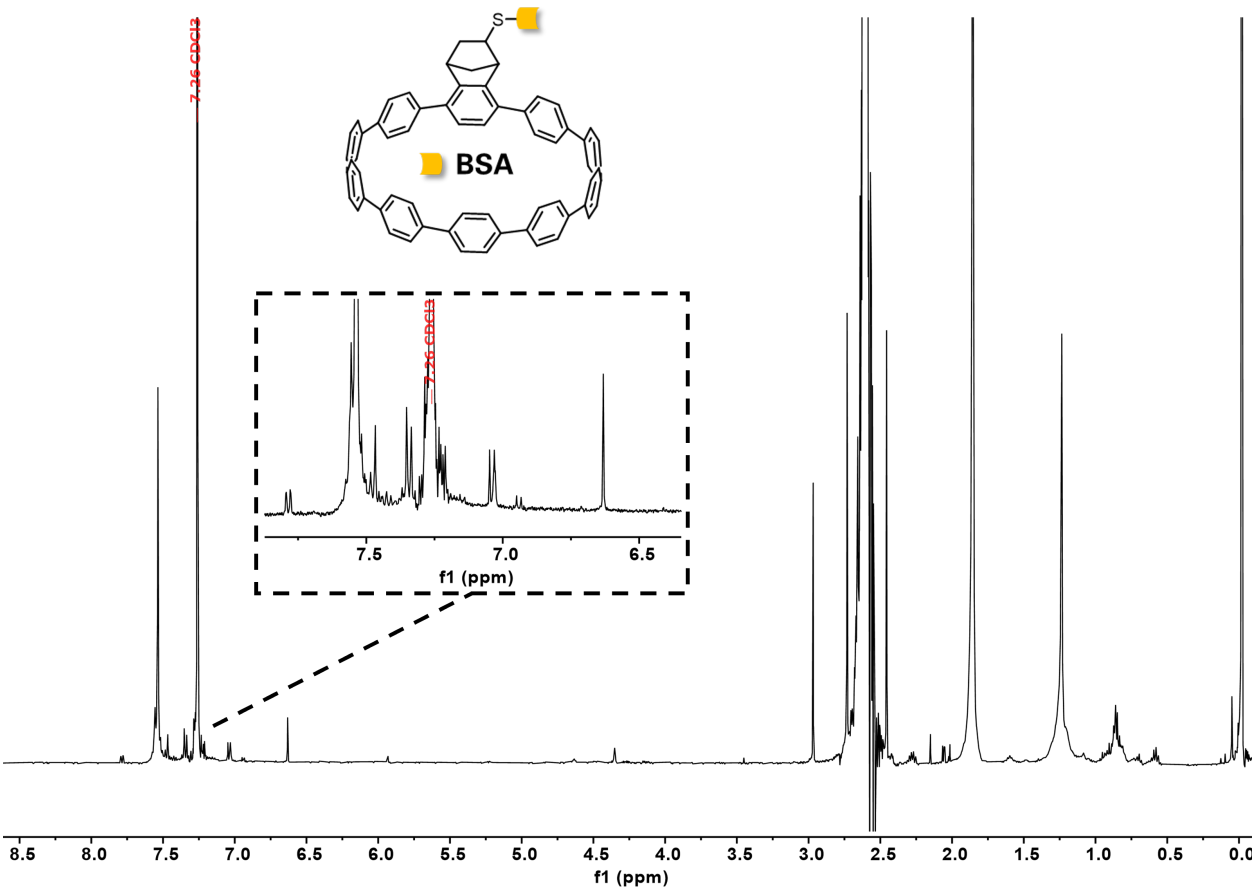

Figure S4. ^{1}H NMR of CPP BSA Conjugate.

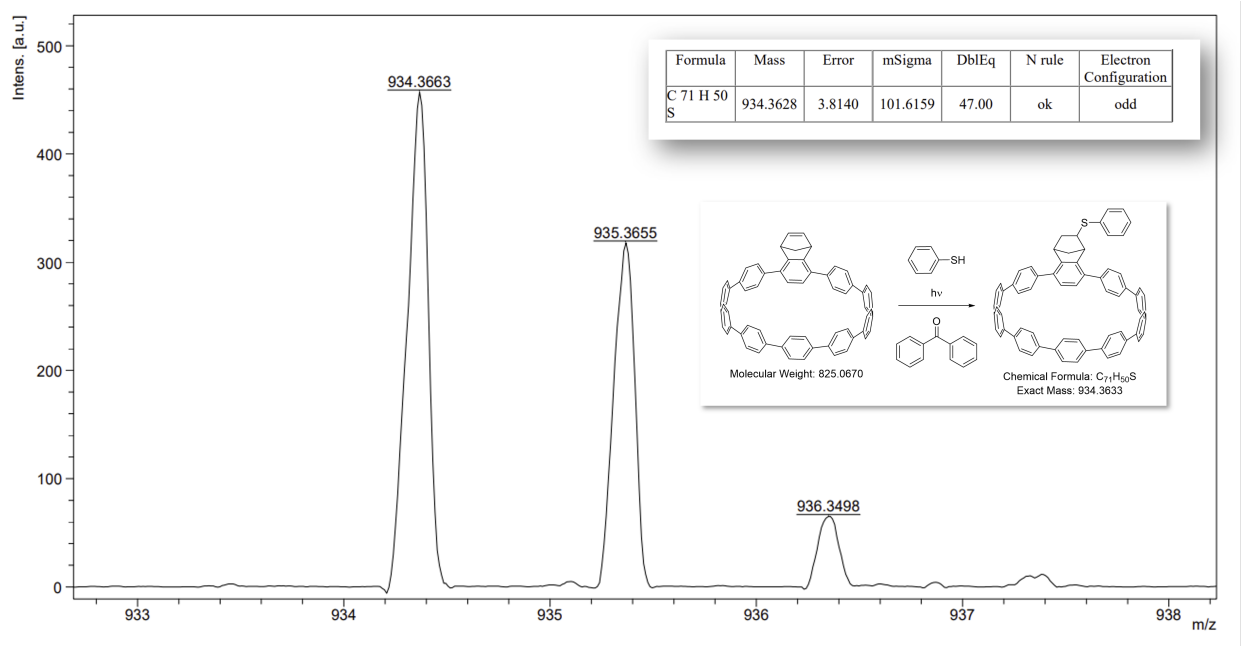

Figure S5. Mass Spectrum of compound 2.

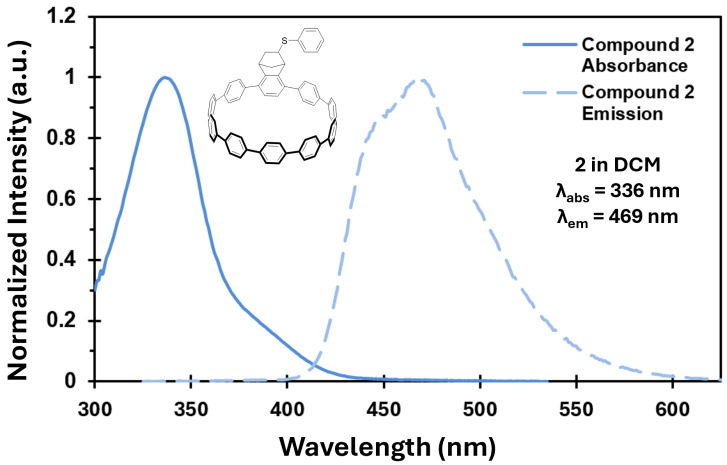

Figure S6. Photophysical characterization of compound 2.

4.1.8 Citations

(1) Lovell, T. C.; Bolton, S. G.; Kenison, J. P.; Shangguan, J.; Otteson, C. E.; Civitci, F.; Nan, X.; Pluth, M. D.; Jasti, R. Subcellular Targeted Nanohoop for One- and Two-Photon Live Cell Imaging. *ACS Nano* **2021**, 15 (9), 15285–15293. https://doi.org/10.1021/acsnano.1c06070.

(2) Anzar, N.; Hasan, R.; Tyagi, M.; Yadav, N.; Narang, J. Carbon Nanotube - A Review on Synthesis, Properties and Plethora of Applications in the Field of Biomedical Science. *Sens. Int.* **2020**, 1, 100003. https://doi.org/10.1016/j.sintl.2020.100003.

(3) Handbook of Carbon Nanotubes; Abraham, J., Thomas, S., Kalarikkal, N., Eds.; *Springer International Publishing: Cham*, **2022**. https://doi.org/10.1007/978-3-030-91346-5.

(4) Chen, J.; Wei, S.; Xie, H. A Brief Introduction of Carbon Nanotubes: History, Synthesis, and Properties. *J. Phys. Conf. Ser.* **2021**, 1948 (1), 012184. https://doi.org/10.1088/1742-6596/1948/1/012184.

(5) Al-Owaedi, O. A. Carbon Nanohoops: Multiple Molecular Templates for Exploring Spectroscopic, Electronic, and Thermoelectric Properties. *ACS Omega* **2024**, 9 (9), 10610–10620. https://doi.org/10.1021/acsomega.3c08944.

(6) Greene, M. K.; Scott, C. J. Carbon Nanotubes Activate Inflammatory Signalling through Binding to Siglec-14. *Nat. Nanotechnol*. **2023**, 1–2. https://doi.org/10.1038/s41565-023-01420-4.

(7) White, B. M.; Zhao, Y.; Kawashima, T. E.; Branchaud, B. P.; Pluth, M. D.; Jasti, R. Expanding the Chemical Space of Biocompatible Fluorophores: Nanohoops in Cells. *ACS Cent. Sci.* **2018**, 4 (9), 1173–1178. https://doi.org/10.1021/acscentsci.8b00346.

(8) Qiu, Z.; He, M.; Chu, K.; Tang, C.; Chen, X.; Zhu, L.; Zhang, L.; Sun, D.; Qian, J.; Tan, Y. Well-Defined Segment of Carbon Nanotube with Bright Red Emission for Three-Photon Fluorescence Cerebrovascular Imaging. *Adv. Opt. Mater.* **2021**, 9 (19), 2100482. https://doi.org/10.1002/adom.202100482.

(9) Maust, R. L.; Li, P.; Shao, B.; Zeitler, S. M.; Sun, P. B.; Reid, H. W.; Zakharov, L. N.; Golder, M. R.; Jasti, R. Controlled Polymerization of Norbornene Cycloparaphenylenes Expands Carbon Nanomaterials Design Space. *ACS Cent. Sci.* **2021**, 7 (6), 1056–1065. https://doi.org/10.1021/acscentsci.1c00345.

(10) Lovell, T. C.; Garrison, Z. R.; Jasti, R. Synthesis, Characterization, and Computational Investigation of Bright Orange-Emitting Benzothiadiazole [10]Cycloparaphenylene. *Angew. Chem. Int. Ed.* **2020**, 59 (34), 14363–14367. https://doi.org/10.1002/anie.202006350.

(11) Singh, M.; Yadav, A. K.; Yadav, L. D. S.; Singh, R. K. P. Visible Light Photocatalysis with Benzophenone for Radical Thiol-Ene Reactions. *Tetrahedron Lett.* **2017**, 58 (23), 2206–2208. https://doi.org/10.1016/j.tetlet.2017.04.060.

(12) Hoyle, C. E.; Bowman, C. N. Thiol–Ene Click Chemistry. *Angew. Chem. Int. Ed.* **2010**, 49 (9), 1540–1573. https://doi.org/10.1002/anie.200903924.

(13) Uygun, M.; Tasdelen, M. A.; Yagci, Y. Influence of Type of Initiation on Thiol–Ene "Click" Chemistry. *Macromol. Chem. Phys.* **2010**, 211 (1), 103–110. https://doi.org/10.1002/macp.200900442.

(14) Mozipo, E. A.; Galindo, A. N.; Khachatourian, J. D.; Harris, C. G.; Dorogin, J.; Spaulding, V. R.; Ford, M. R.; Singhal, M.; Fogg, K. C.; Hettiaratchi, M. H. Statistical Optimization of

Hydrazone-Crosslinked Hyaluronic Acid Hydrogels for Protein Delivery. *J. Mater. Chem. B* **2024**, 12 (10), 2523–2536. https://doi.org/10.1039/D3TB01588B.

(15) Pangborn, A. B.; Giardello, M. A.; Grubbs, R. H.; Rosen, R. K.; Timmers, F. J. Safe and Convenient Procedure for Solvent Purification. *Organometallics* **1996**, 15 (5), 1518–1520. https://doi.org/10.1021/om9503712.

Chapter V: Additional Work

5.1 Statistical Optimization of Hydrazone-Crosslinked Hyaluronic Acid Hydrogels for Protein Delivery

5.1.1 Contributions

In collaboration with the Hettiaratchi lab, I worked on modifying the natural polymer hyaluronic acid (HA) through a thiol-ene photoinitiated conjugation method. The goal for this work was to append a binding peptide to the polymer backbone to release exogenous protein with controlled kinetics that match the body's natural healing mechanisms for improved healing outcomes. My contribution to this work included project design, synthesis, and characterization of polymers and hydrogels as well as work in statistical analysis using design of experiments (DOE), cell imaging and analysis, writing and editing. Esther A. Mozipo, Alycia, N. Galindo, and Jenna D. Khatchatourian, contributed to synthesis, characterization, writing and editing. Jonathan Dorogin, Madeleine Ford, and Malvika Singhal contributed to affibody synthesis and purification. Dr. Kaitlin C. Fogg and Conor G. Harris contributed to DOE design, manuscript writing and editing, Dr. Marian H. Hettiaratchi contributed to project design and manuscript editing. This work was published in *J. Mater. Chem. B*, **2024**, 12, 2523. Citations for this paper immediately follow this section.

5.1.2 Introduction

Hydrazone-crosslinked hydrogels are attractive protein delivery vehicles for regenerative medicine. However, each regenerative medicine application requires unique hydrogel properties to achieve an ideal outcome. The properties of a hydrogel can be impacted by numerous factors involved in its fabrication. We used design of experiments (DoE) statistical modeling to efficiently optimize the physicochemical properties of a hyaluronic acid (HA) hydrazone-crosslinked hydrogel for protein delivery for bone regeneration. We modified HA with either adipic acid dihydrazide (HA-ADH) or aldehyde (HA-Ox) functional groups and used DoE to evaluate the interactions

of three input variables, the molecular weight of HA (40 or 100 kDa), the concentration of HA-ADH (1–3% w/v), and the concentration of HA-Ox (1–3% w/v), on three output responses, gelation time, compressive modulus, and hydrogel stability over time. We identified 100 kDa HA-$ADH_{3.00}$HA-$Ox_{2.33}$ as an optimal hydrogel that met all of our design criteria, including displaying a gelation time of 3.7 minutes, compressive modulus of 62.1 Pa, and minimal mass change over 28 days. For protein delivery, we conjugated affinity proteins called affibodies that were specific to the osteogenic protein bone morphogenetic protein-2 (BMP-2) to HA hydrogels and demonstrated that our platform could control the release of BMP-2 over 28 days. Ultimately, our approach demonstrates the utility of DoE for optimizing hydrazone-crosslinked HA hydrogels for protein delivery.

Recombinant protein delivery is a promising strategy for the repair of injured or damaged tissues including bone, muscle, nerves, vasculature, and skin.[1] Specifically in the case of bone repair, the delivery of bone morphogenetic protein-2 (BMP-2) has demonstrated success as a bone regeneration strategy in both animal models and human patients.[2] A wide variety of biomaterials have been investigated for protein delivery to the body, and their properties have been tuned to enable control over protein release rate, material degradation rate, material compressive modulus, and injectability. However, tuning all of these properties simultaneously to develop the ideal biomaterial for protein delivery is challenging. Furthermore, biomaterial delivery vehicles must be individually optimized for different clinical applications, as unique properties may be necessary to control the release of different proteins to different tissues. Hydrogels are chemically or physically crosslinked waterswollen polymer networks that can be effective vehicles for the delivery of a variety of cells, proteins, and drugs due to their ability to support cell viability, provide sustained release of cargo, and mimic the mechanical and biochemical properties of tissues.[1,3–5] The relative ease in which a variety of natural and synthetic polymers can be chemically modified with different functional groups has facilitated the fabrication of diverse hydrogels with a wide array of properties suitable for numerous applications. Varying individual input parameters to create a hydrogel, such as polymer concentration, crosslinking ratio, and molecular weight of the polymer, one at a time to

determine the combination of parameters that yields a hydrogel with the optimal properties can be time-intensive and expensive. While extensive prior work has been performed to determine the ideal physicochemical properties of hydrogels for a variety of biomedical applications, there has been limited investigation of the collective, combinatorial effects of varying multiple input parameters on the properties of hydrogels in the context of protein delivery.

To tackle this challenge, we used a statistical optimization technique known as design of experiments (DoE) to efficiently screen the effects of multiple input parameters on several hydrogel properties and create a mathematical model to predict the optimal and pessimal hydrogel formulations given a specific set of design criteria. Design of experiments (DoE) is a method of experimental design in which a combination of factors are varied simultaneously instead of the typical "one factor at a time' ' approach. The responses to each set of input parameters is mapped to generate a model for how the different input parameters collectively influence each hydrogel property (i.e., the output responses), known as the response surface methodology.[6,7] Mathematical models can then be used to define the response surface and predict expected outcomes. DoE was originally developed in the 1920s for agricultural pur- poses, but has since been used in a broad array of applications, including the development and optimization of biomaterials.[7-10] It lends itself particularly well to applications such as hydrogel design, in which it is highly likely that multiple input parameters will have interactive effects on hydrogel properties, which makes individually varying input parameters less infor- mative. We and others have used DoE to predict responses of hydrogels and cells within hydrogels in systems with multiple input variables.[8,11-14] This approach can be widely used in regenerative medicine applications such as scaffold design, cell culture optimization, and the development of in vitro model systems, accelerating the timeframe in which new platforms can be optimized.[15-17]

In this study, we were specifically interested in tuning the properties of hyaluronic acid hydrogels formed via hydrazone crosslinking. Hyaluronic acid (HA) is an abundant biopolymer found throughout the body. It is a critical extracellular matrix component of connective tissue, skin,

and the brain that functions by creating a hydrated polymer matrix for cells to migrate and proliferate.[18–20] HA also exists at a range of molecular weights, which can activate different cell signaling pathways.[21,22] Although HA itself is soluble in aqueous media, modifications can be made to the carboxylic acid, adjacent alcohol, and secondary alcohol groups on the HA backbone to form crosslinks throughout the polymer, resulting in a stable three-dimensional, water-swollen network. HA hydrogels have been used successfully in several biomedical applications, including protein and cell delivery and tissue regeneration.[23–25] While there are numerous criteria that may be considered important for the design of a hydrogel for protein delivery, we narrowed down our desired hydrogel properties to three essential criteria for optimization: compressive modulus, gelation time, and mass change over four weeks. Compressive modulus can have a profound effect on cell differentiation,[26,27] while the bulk stiffness of an implanted material must be matched to the target tissue to avoid eliciting mechanical irritation and subsequent inflammation. Hydrogel gelation time should allow for sufficient time to mix components (different polymers, proteins, cells) before gelation. Typically, hydrogel gelation times of less than 10 minutes are preferred.[28,29] Finally, the mass change of the hydrogel due to swelling or degradation of the crosslinked network can impact cellular responses over time, such cell spreading, cell-cycle progression, and differentiation.[30–32]

We formed HA hydrogels using dynamic covalent hydrazone crosslinks as this approach can yield a wide range of physicochemical properties, making them an attractive hydrogel platform for numerous regenerative medicine applications.[33–40] The properties of hydrazone-crosslinked HA hydrogels can be easily tuned by adjusting the ratios of the two dynamic covalent crosslinking polymers: oxidized HA (HA-Ox) and HA adipic acid dihydrazide (HA-ADH). Thus, we narrowed our input parameters to HA molecular weight, HA-Ox concentration, and HA-ADH concentration. We then used DoE to identify the contributions and combinatorial effects of the concentration of HA-ADH, the concentration of HA-Ox, and the molecular weight of HA on hydrogel compressive modulus, gelation time, and mass change over time. We then created a statistical model that predicted physicochemical properties as a function of input parameters. This model was validated by evaluating

the hydrogels predicted to be the optimal and pessimal delivery vehicles. Finally, as a proof-of-concept for protein delivery, we conjugated a protein-binding peptide known as an affibody to the HA hydrogels using thiol–ene click chemistry to enable affinity-controlled delivery of bone morphogenetic protein-2 (BMP-2), which is a potent osteogenic protein that is clinically used as a bone graft substitute. Overall, we developed a hydrogel platform and used DoE analysis to optimize the vast tunability of hydrazone-crosslinked HA hydrogels for protein delivery for tissue regeneration.

5.1.3 Experimental Appendix: Supplementary Information

Sodium hyaluronate (HA, 40 kDa and 100 kDa) was purchased from Lifecore Biomedical LLC (Chaska, MN). Adipic acid dihydrazide (ADH) was purchased from Spectrum Chemical (Gardena, CA). Hydroxybenzotriazole (HOBt) was purchased from Chem Impex (Wood Dale, IL). 1-Ethyl-3-(3-dimethylaminopropyl)carbodiimide (EDC) was purchased from G Biosciences (St. Louis, MO). Sodium Periodate, AmberLite MB Ion Exchange Resin, tetrabutylammonium hydroxide (TBA-OH), DMSO, 4-dimethylaminopyridine (DMAP), di-tert-butyl decarbonate (BoC2O) and 5-norbornene-2-carboxylic acid were purchased from Sigma Aldrich (St. Louis, MO). Irgacure 2959 was purchased from Advanced Biomatrix (Carlsbad, CA). Recombinant human bone morphogenetic protein-2 (BMP-2) and the human BMP-2 DuoSet enzyme-linked immunosorbent assay (ELISA) were purchased from R&D Systems (Minneapolis, MN).

I. Synthesis Synthesis of adipic acid dihydrazide HA (HA-ADH)

HA (200 mg, 0.527 mmol) was dissolved in 20 mL of diH_2O to form a 1% w/v solution. Adipic acid dihydrazide (183.75 mg, 1.05 mmol) and hydroxy-benzotriazole (142.53 mg, 1.05 mmol) were added to the HA solution and the pH was adjusted to 4.75. EDC was added (91.00 mg, 0.47 mmol) to the solution, and the pH was monitored and maintained at 4.75 for 4 hours using 1 M HCl and 1 M NaOH. The solution was stirred for 24 hours at room temperature and dialyzed against 0.1 M NaCl in diH_2O for 2 days followed by diH_2O for 2 days. The solution of HA functionalized with ADH (HA-ADH) was sterile filtered through a 0.22 mm filter, frozen at 80 °C, and lyophilized

using a VirTis BenchTop Prolyophilizer (SP Scientific, Warminster, PA).

Synthesis of oxidized HA (HA-Ox)

HA (200 mg, 0.561 mmol) was dissolved in 10 mL of diH_2O to form a 2% w/v solution. Sodium periodate (322.00 mg, 0.281 mmol) was added to the solution and stirred for 4 hours at room temperature protected from light. The reaction was quenched with 1 mL of propylene glycol and dialyzed against diH_2O for 3 days. The oxidized HA solution (HA-Ox) was sterile filtered through a 0.22 mm filter, frozen at 80 °C, and lyophilized.

Synthesis of HA norbornene (HA-Nor)

HA (1.01 g, 2.506 mmol) was dissolved in 50 mL diH_2O to form a 2% w/v solution. AmberLite MB Ion Exchange Resin (3.03 g) was added to the reaction and stirred at room temperature for 5 hours. The resin was vacuum-filtered, and the filtrate was titrated to pH of 7 with TBA-OH and dialyzed against diH_2O for 3 days. The HA-TBA solution was sterile filtered through a 0.22 mm filter, frozen at 80 °C, and lyophilized. HA-TBA (153 mg, 0.35 mmol) was dissolved in 0.75 mL DMSO to form a 2% w/v solution. The flask was purged with N_2 for 5 minutes, then 5-norbornene-2-carboxylic acid (145 mg, 1.05 mmol) and DMAP (145 mg, 1.049 mmol) was added to the reaction flask. Boc_2O was added via syringe (32 mL, 0.14 mmol). The solution was stirred at 45 °C for 20 hours, then quenched with cold diH_2O (10 mL) before being dialyzed against diH_2O for 3 days. Norbornene-functionalized HA (HA-Nor) was precipitated from the solution by adding NaCl and cold acetone (30 mL), then filtered and dialyzed against diH_2O for 3 days. The solution was sterile filtered through a 0.22 mm filter, frozen at -80 °C, and lyophilized.

Oxidization of HA norbornene (HA-Nor-Ox)

HA-Nor (91.75 mg, 0.18 mmol) was dissolved in diH_2O to form a 1% w/v solution. Sodium periodate (10.57 mg, 0.049 mmol) was dissolved in diH_2O to create a 0.5 M solution and added to the HA-Nor solution. The solution was stirred overnight at room temperature protected from light. The reaction was quenched with 1 mL of propylene glycol and dialyzed against diH_2O for 3 days. The oxidized HA-Nor solution (HA-Nor-Ox) was sterile filtered through a 0.22 mm filter, frozen

at -80 °C, and lyophilized.

Molecular weight analysis of modified HA

Gel permeation chromatography (GPC) was used to determine the molecular weight of unmodified and modified HA at both 40 kDa and 100 kDa. Lyophilized HA samples were sent to Polyanalytik, Inc. (London, ON, Canada) for analysis using a Viscotek TDA 305 and GPCmax (Malvern Panalytical Ltd, Malvern, United Kingdom) fitted with PAA-202 and PAA-206M aqueous columns. Samples were diluted to 1.00–2.50 mg mL^{-1} in a mobile phase of 8.5 g L^{-1} NaCl in ultrapure water, allowed to dissolve at room temperature for several hours, and then filtered through a 0.22 mm Nylon syringe filter prior to injection. Samples were run in triplicate at a flow rate of 0.7 mL min^{-1} and temperature of 30 °C.

Affibody bioconjugation

BMP-2-specific affibodies were expressed in E. coli and purified as previously described.[41] HA-Nor-Ox (14.5 mg) was dissolved in 1.5 mL of 0.71 mg mL^{-1} affibody in PBS (1.45 10^{-4} mmol) to create a solution with 1 : 1 ratio of affibody to HA-Nor-Ox. 15 mL of 10% w/v Irgacure 2595 in methanol was added to the reaction vial, stirred, and illuminated with 365 nm light for 10 minutes. The solution was dialyzed against HEPES buffer pH 7.0 for 1 day and diH_2O for 2 days. The affibody-conjugated solution of HA (HA-Nor-Ox-Affibody) was sterile filtered through a 0.22 mm filter, frozen at -80 °C, and lyophilized. The amount of affibody conjugated to the polymer was quantified by dis- solving 2–3 mg of HA-Nor-Ox-Affibody in PBS at 2% w/v and determining the protein concentration of the solution using a Pierce 660 Protein Assay Kit (Thermo Fisher Scientific).

II. Degree of modification (DOM) determination The degree of chemical modification of HA-ADH and HA-Nor was quantified using proton nuclear magnetic resonance spectroscopy (^{1}H NMR, 500 Hz, Bruker, USA). 2–5 mg of modi- fied polymer was dissolved in 600 mL of deuterium oxide (D_2O) for ^{1}H NMR (256 scans). To calculate the degree of modification for HA-ADH, the peaks from the aliphatic chain were integrated from 2.5–2.1 ppm and 1.7–1.44 ppm (8H) and

normalized to the *n*-acetyl methyl group peaks from 1.8–2 ppm (3H) (Fig. S1, ESI†).[42] The degree of modification for HA-Nor was calculated by integrat- ing the vinyl peaks from 5.7–6.3 ppm and normalizing to the n-acetyl methyl group from 1.8–2 ppm (3H) (Fig. S2, ESI†).[42] The degree of oxidation for HA-Ox was determined by hydroxylamine hydrochloride titration.[43,44] Briefly, 100 mg of oxidized polymer was dissolved in 0.25 N hydroxylamine hydro- chloride containing 0.05% w/v methyl orange reagent for 2 hours. The solution was then titrated with 0.1 M NaOH while monitoring the pH until the pH indicator changed from red to yellow at a pH of 4. The reaction of hydroxylamine hydrochloride with the aldehydes on oxidized HA is shown below.

$$HA-(CHO)_n + H_2N-OH \cdot HCl \rightarrow HA-(CH=N-OH)_n + H_2O + HCl$$

Eqn (1) was used to calculate the percent degree of modification (% DOM) or the percentage of HA disaccharide units that contain aldehydes.

$$\%DOM = \left(\frac{379.2\ g}{mol} HA \times 0.1M\ NaOH \times \left(\frac{V_f - V_0}{m_{HA-Ox}}\right)\right) \times 100 \qquad \textbf{(1)}$$

where 379.2 g mol $^{-1}$ is the monomeric molecular weight of HA, 0.1 M is the molarity of NaOH used to adjust the solution pH, V_f is the final volume of NaOH in the burette after titration recorded in liters, V_0 is the initial volume of NaOH in the burette before titration recorded in liters, and $m_{\text{HA-Ox}}$ is the mass in g of HA-Ox used in the titration.

III. Hydrogel Analysis Preparation of HA hydrogels

HA-ADH and oxidized HA (HA-Ox, HA-Nor-Ox, or HA-Nor-Ox- Affibody) were each reconsti- tuted at 1–3% w/v in PBS. Hydrogels were then prepared by mixing 50 mL of each polymer in 2 mL microcentrifuge tube or 8 mm diameter cylindrical silicone mold to create 100 mL hydrogels.

Physicochemical characterization of hydrogels Gelation time

Due to the rapid nature of hydrazone crosslinking between HA-Ox and HA-ADH, in which bonds form too rapidly to measure the gelation point using rheology, the gelation time of each hydrogel was determined using the inverted tube test, which measures the point at which the hydrogel reaches a fully gelled state.[45–47] 50 mL each of HA-ADH and HA-Ox were pipetted into 2 mL microcen-

trifuge tubes to create 100 mL hydrogels and inverted every minute until gelation occurred. The time at which there was no viscous flow was recorded as the gelation times.

Compressive modulus

Compressive moduli of the hydrogels were evaluated using a Discovery Hybrid Rheometer-2 (DHR-2) (TA Instruments, New Castle, DE). 100 mL hydrogels were formed in 8 mm cylindrical silicone molds. The hydrogels were cross- linked overnight at room temperature before being removed from the molds and placed on the rheometer. Hydrogels were com- pressed within an 8 mm parallel plate to 15% of their original height at 37 °C, and the slope of the linear stress versus strain curve was used to calculate the compressive modulus.[48]

Mass change over time

Hydrogels were formed overnight in pre-weighed 2 mL microcentrifuge tubes and incubated in 100 mL of 1 PBS. At 0 hours, 24 hours, 4, 7, 10, 14, 21, and 28 days, the supernatant was removed, hydrogels were blotted of excess PBS with a KimWipe, and the tube containing the hydrogel was weighed. The mass of the hydrogel was recorded, and fresh PBS was added to the tube. The percentage mass change was calculated using eqn (2).

$$\%Mass\ Change = \frac{m_t - m_0}{m_0} \times 100\% \qquad \textbf{(2)}$$

where m_t is the mass of the hydrogel at time t and m_0 is the initial mass of the hydrogel immediately after it was formed.

Release of BMP-2 from HA hydrogels

Release of BMP-2 was assessed from HA hydrogels with and without conjugated BMP-2-specific affibodies over 28 days. To load BMP-2 into the hydrogels, BMP-2 was added to the HA-Ox and HA-Nor-Ox- Affibody solutions and then crosslinked with HA-ADH. For hydrogels without affibodies, 200 ng of BMP-2 were added to a 50 mL solution of 2% w/v HA-Ox. For affibody-conjugated HA hydrogels, BMP-2 was added to a 50 mL solution of 2% w/v HA- Nor-Ox-Affibody, which resulted in 1000 molar excess of affibody to BMP-2. For each hydrogel, 50 mL of HA-ADH

were added to the HA-Nor-Ox or HA-Nor-Ox-Affibody solutions to create 100 mL HA hydrogels in 2 mL microcentrifuge tubes. 900 mL of 0.1% w/v BSA in PBS was added to each tube, and the hydrogels were incubated at 37 °C. 300 mL aliquots of supernatant were collected and replenished with fresh 0.1% w/v BSA in PBS at multiple time points over 28 days. BMP-2 in the supernatant was quantified using a BMP-2-specific ELISA. Cumulative BMP- 2 release was calculated by adding the total mass of BMP-2 in each collected aliquot. Cumulative fractional release versus the square root of time was plotted, and the data were fit to a short time approximation of one-dimensional diffusion from a thin sheet, and the slope of Fickian diffusion, *k*, was determined using eqn (3).[49,50]

$$\frac{M_t}{M_\infty} = kt^{\frac{1}{2}} \qquad \textbf{(3)}$$

where M_t is the mass of BMP-2 released at time t, M_∞ is the total mass of BMP-2 released at the end of the experiment, and *k* is the slope of Fickian diffusion.

IV. Design of Experiments Design of experiments (DoE) statistical optimization was used to investigate how the chemical composition of the hydrogels influenced their physicochemical properties. More specifically, D-optimal design was used to generate a design matrix of 15 hydrogel formulations with 1 centrally repeated condition (**Table 5.4**). We used a D-optimal design due to the constrained range of polymer concentrations from 1 to 3% w/v and the use of two distinct molecular weights of HA, either 40 kDa or 100 kDa, which resulted in a categorical variable in our model. The input variables for HA hydrogel composition were the concentration of HA-ADH (1–3% w/v), the concentration of HA-Ox (1–3% w/v), and the molecular weight of HA (40 kDa or 100 kDa) used to synthesize the hydrogel. The concentrations of HA-ADH and HA-Ox were continuous variables that were examined at equidistant low, medium, and high levels, whereas the molecular weight was a categorical variable that was examined at either 40 kDa or 100 kDa. The physicochemical properties quantified as response variables were gelation time, compressive modulus, and mass change at 1, 7, 14, 21, and 28 days after hydrogel fabrication.

HA-ADH (% w/v)	HA-Ox (% w/v)	Molecular weight (kDa)
1.00	1.00	40
1.00	3.00	40
1.67	1.00	40
2.00	2.00	40
3.00	1.00	40
3.00	3.00	40
1.00	1.00	100
1.00	3.00	100
1.00	1.67	100
1.67	3.00	100
2.00	**2.00**	**100**
2.00	**2.00**	**100**
2.00	**2.00**	**100**
2.33	1.00	100
3.00	1.00	100
3.00	3.00	100
3.00	2.33	100

Table 5.4: HA hydrogel formulations evaluated to generate D-optimal multilinear regression model. 15 Unique hydrogel formulations were evaluated in triplicate with a centrally repeating condition at 100 kDa HA-$ADH_{2.00}$HA-$Ox_{2.00}$ evaluated with 9 replicates to determine the system's variance. The centrally repeated condition is bolded.

MODDE-Pro 13.0 software (Sartorius, Fremont, CA) was used to generate the D-optimal experimental matrix of 15 hydrogel formulations and analyze the experimental data obtained. Experimental data were collected from each of the hydrogel formulations then used to fit a multiple linear regression model for each response variable as a function of the statisti- cally significant input variables. An input variable was consid- ered statistically significant if it had a p value of o 0.05 as determined by ANOVA. The model performance was further assessed using R^2, adjusted R^2, and Q^2. R^2 describes the varia- tion of the response explained by the model for every variable. Adjusted R^2 describes the variation of the response explained by the model only for the variables that affect the response. Q^2 describes the variation of the response predicted by the model for new data. R^2 and adjusted R^2 values close to 1.0 indicate a high correlation between observed and predicted values. Q^2 above 0.50 and a difference between R^2 and Q^2 values below 0.30 validate that the model works independently of the specific data used to train the model.[51,52] Residual plots, Box–Cox plots, and ANOVA tables were used to diagnose outliers, trends, or lack of fit. The model was then refined by removing any outliers and input variables that were not statistically significant to increase the validity of our model. Our overall engineering objective was to maximize the compressive modulus, set the gelation time to a value within 1–10 min, and set the mass change at all time points to 0%. Thus, to validate the predictive models, we generated hydrogels predicted to either fulfill these optimization parameters (optimal hydrogels) or fulfill reciprocal objectives (pessimal hydrogels). Specifically, the pessimal hydrogels were predicted to minimize the compressive modulus, maximize the gelation time, and either maximize or minimize the hydrogel mass change at all time points (i.e., induce hydrogel swelling or degradation). Hydrogel morphology. Scanning electron microscopy (SEM) was performed on the optimal hydrogel formulation, HA-$ADH_{3.00}$HA-$Ox_{2.33}$, using a ThermoFisher Apreo 2 SEM. A 100 mL hydrogel was formed in an 8 mm mold, frozen at -80 °C, and lyophilized for imaging. Images were taken at 100 times magnification at 0.80 nA and 10.00 kV.

5.1.4 Results and Discussion

Functionalization of HA polymers

HA was modified with either aldehyde (HA-Ox) or ADH func- tional groups (HA-ADH) for hydrazone crosslinking (**Fig. 5.21**). Because polymer molecular weight can influence crosslinking density and subsequent physicochemical properties of the hydrogel,[28] we functionalized both 40 kDa and 100 kDa HA for hydrogel fabrication and evaluation. To expose aldehyde groups on HA, we oxidized the polymer in the presence of sodium periodate ($NaIO_4$) for 4 h in the dark before quenching the reaction with propylene glycol. Using the same starting material, we added ADH to HA in the presence of EDC at a pH of 4.75 for 24 h to create HA-ADH. The degree of oxidization was characterized using titration with hydroxylamine hydrochloride and was found to be 27.5 5.9% and 41.4 12.8% of HA repeating disaccharide units for 40 kDa and 100 kDa HA-Ox, respectively. The degree of modification of the ADH functional groups on the polymer was 67.6 1.2% for 40 kDa HA-ADH and 50.6 10.1% for 100 kDa HA-ADH as characterized by ^{1}H NMR (Fig. S1, ESI†). The degrees of modification and yields of all modified polymers are summarized in Table S1 (ESI†). Degrees of oxidation between 27–82%[33,53] and degrees of modification with ADH between 30–49%[54,55] have been previously reported, which is consistent with our results. Gel permeation chromato- graphy was used to determine how the modifications to the HA polymer changed its molecular weight and polydispersity (Table S2, ESI†). Our results revealed a decrease in molecular weight during the oxidation reaction due to the ring break on HA; however, the size of the polymer backbone was not greatly affected by hydrolysis as observed in other HA oxidation reactions.[56] Furthermore, the polydisperity indices of the two oxidized HA polymers were similar to unmodified HA. Inter- estingly, the average molecular weights of both the 40 kDa and 100 kDa HA-ADH were much larger than expected at 366 16.8 kDa and 332 9.58 kDa, respectively, suggesting that ADH reacted with multiple HA polymer chains during synthesis, resulting in larger polymer chains. Similar results have been documented in a previous HA-ADH synthesis in the presence of EDC and a low molar excess of ADH due to the bifunctionality of ADH.[57] This finding was further supported by the higher polydispersity indices for both 40 kDa and 100 kDa HA-ADH

at 2.02 0.03 and 2.18 0.10, respectively, compared to un- modified HA, which indicate a larger distribution of polymer chain molecular weights. We then used these modified HA polymers to fabricate the 15 hydrogels in Table 1 and evaluated their gelation time, compressive moduli, and mass change over time to generate a predictive model for DoE analysis.

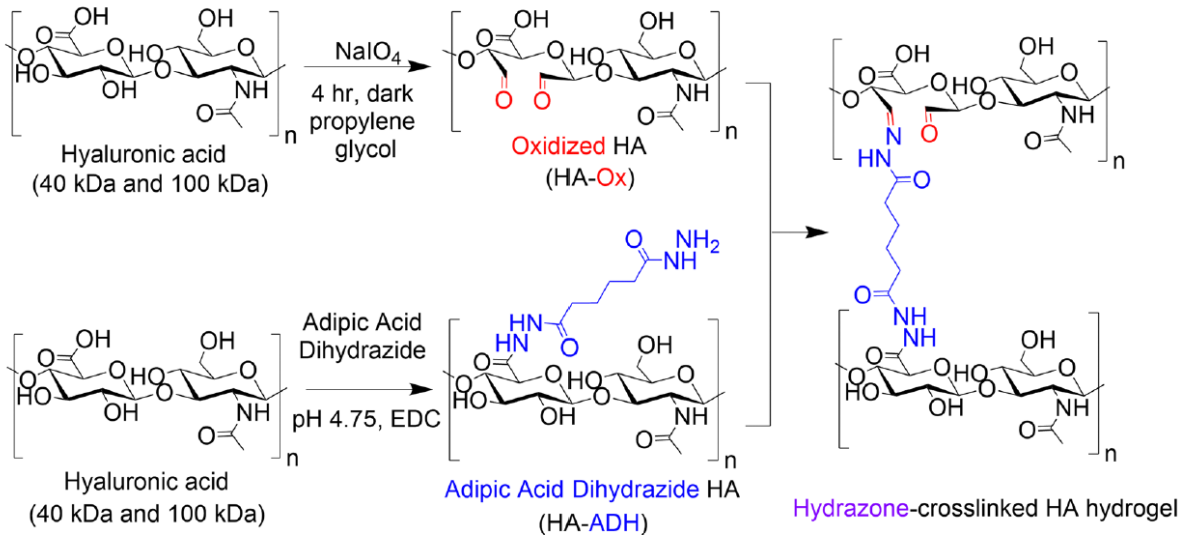

Figure 5.21: Functionalization of HA and hydrogel formation via hydrazone crosslinking. Hyaluronic acid (40 kDa or 100 kDa) was either stirred with sodium periodate in water for 4 h in the dark to oxidize the polymer and reveal aldehyde functional groups (HA-Ox) or mixed with adipic acid dihydrazide (ADH) and 1-ethyl-3-(3-dimethylaminopropyl)carbodiimide (EDC) in water and maintained at pH 4.75 for 24 h to create ADH-functionalized HA (HA-ADH). All polymers were dialyzed, filtered, and lyophilized before use. HA-Ox and HA-ADH were re-dissolved in phosphate buffered saline (PBS) and mixed at room temperature and pH 7.4 to form hydrazone-crosslinked HA hydrogels.

Hydrogel gelation time

HA hydrogels were fabricated by mixing 50 mL of HA-ADH and 50 mL of HA-Ox at different polymer concentrations and mole- cular weights. Inversion tests were used to quantify the gelation time of each of the HA hydrogel formulations. As expected, increasing the polymer content of the hydrogels increased the crosslinking density of the polymer network and subsequently decreased the gelation time (**Fig. 5.22A**). Changing the polymer concentrations of the 40 kDa hydrogels had a greater effect on gelation time compared to the 100 kDa hydrogels, such that the 40 kDa hydrogels had a larger range of average gelation times ranging from 4.5 to 292.7 min. Addition-

ally, increasing the HA-ADH content in the 40 kDa hydrogels decreased the gela- tion time of the hydrogels, except for the HA-ADH$_{1.00}$HA-Ox$_{3.00}$ hydrogel. The gelation times of the 100 kDa hydrogels all fell between 1.4 and 71.5 min. The 100 kDa HA hydrogels similarly exhibited decreasing gelation time in response to increasing HA-ADH content, except for the HA-ADH$_{1.67}$HA-Ox$_{3.00}$ and HA-ADH$_{1.00}$HA-Ox$_{3.00}$ hydrogels, which demonstrated faster gelation times than the HA-ADH$_{2.00}$HA-Ox$_{2.00}$ hydrogel. Excess HA-Ox content compared to HA-ADH content also resulted in shorter gelation times in both the 40 kDa and 100 kDa hydro- gels. Overall, the 100 kDa hydrogels gelled faster than 40 kDa hydrogels, potentially due to increased entanglement of the longer polymer chains.[58] Gelation time of the centrally repeated hydrogel condition (100 kDa HA-ADH$_{2.00}$HA-Ox$_{2.00}$) was evaluated using 50 mL, 100 mL, and 200 mL hydrogels to determine if the hydrogel size had an effect on the gelation time. As the hydrogel volume increased, gelation time also increased. This was likely due to the increased time required to establish more crosslinks to effect complete gelation of a larger hydrogel.

Hydrogel compressive modulus

The compressive moduli of the hydrogels ranged from 4.5 to 42.2 Pa (**Fig. 5.22B**). The compressive moduli of all the 100 kDa HA hydrogels fell within a narrow range of 20–40 Pa except for the HA-ADH$_{1.00}$HA-Ox$_{1.00}$ hydrogel, which exhibited an average compressive modulus of 13.6 Pa, which was significantly lower than HA-ADH$_{3.00}$HA-Ox$_{2.33}$ and HA-ADH$_{2.00}$HA-Ox$_{2.00}$ hydrogels and likely due to the lower polymer concentration. In contrast, the compressive moduli of all of the 40 kDa HA hydrogels fell within 4.5 to 20 Pa. Increasing the overall polymer content and HA-ADH content of the 40 kDa HA hydrogels resulted in higher compressive moduli, which was similar to the trends of increasing polymer concentration and HA-ADH content decreasing gelation time.

Hydrogel mass change over time

The hydrogels were incubated in PBS at room temperature for 28 days, and their masses were periodically measured to observe swelling and/or degradation over time. For the 40 kDa HA hydrogels, the HA-ADH$_{3.00}$HA-Ox$_{1.00}$ hydrogel exhibited the maximum swelling of 185% of its original

mass at 21 days (**Fig. 5.22C**). The HA-$ADH_{1.00}$HA-$Ox_{3.00}$ and HA-$ADH_{1.00}$HA-$Ox_{1.00}$ hydrogels demonstrated complete degradation (i.e., minimum mass change of 100%) at 14 days. For the 100 kDa HA hydrogels, the HA-$ADH_{1.00}$HA-$Ox_{3.00}$ hydrogel demonstrated the greatest degradation of 68% at 28 days, while the HA-$ADH_{2.33}$HA-$Ox_{1.00}$ hydrogel demonstrated the maximum swelling of 62% at 4 days (**Fig. 5.22D**). Overall, the 40 kDa HA hydrogels demonstrated larger changes in mass (swelling or degradation) than the 100 kDa HA hydrogels. This may be due to the lower degree of modification achieved for 40 kDa HA-Ox compared to 100 kDa HA-Ox, which may have resulted in lower crosslinking densities of the polymer network and less stable hydrogels. Hydrogels that contained either excess ADH or aldehyde content also demonstrated increased degradation or swelling, likely due to lower crosslinking density and a less stable crosslinked polymer network.

Our results corroborate the findings of other groups who have fabricated hydrazone-crosslinked HA hydrogels. Similar to the results of our study, others have demonstrated a large range of gelation times, an inverse relationship between gelation time of their HA hydrogels and concentration of ADH crosslinker, and less stable hydrogels with excess aldehydes.[34] In another study exploring hydrazone-crosslinked HA hydrogels for a vitreous substitute, the use of higher amounts of free ADH crosslinker stabilized the hydrogels;[33] however, we found that excess HA-ADH increased hydrogel swelling at early time points. A wide range of Young's moduli have been observed with hydrazone-crosslinked HA hydrogels with values ranging between 1–2000 Pa reported in the literature.[36] In comparison, our HA hydrogels exhibited relatively low compressive moduli within a narrow range of 4.5–42.2 Pa. Others have found that a higher degree of modification for HA-ADH led to stiffer hydrogels, which was similar to what we observed for the 40 kDa hydrogels.[35]

Ultimately, our method of fabricating hydrazone-crosslinked HA hydrogels yielded hydrogels with a wide range of physicochemical properties, including large ranges in hydrogel gelation time and mass change, with the capacity to swell, degrade, or maintain a relatively constant mass over 28 days depending on the molecular weight and concentrations of HA-ADH and HA-Ox used (**Table 5.5**).

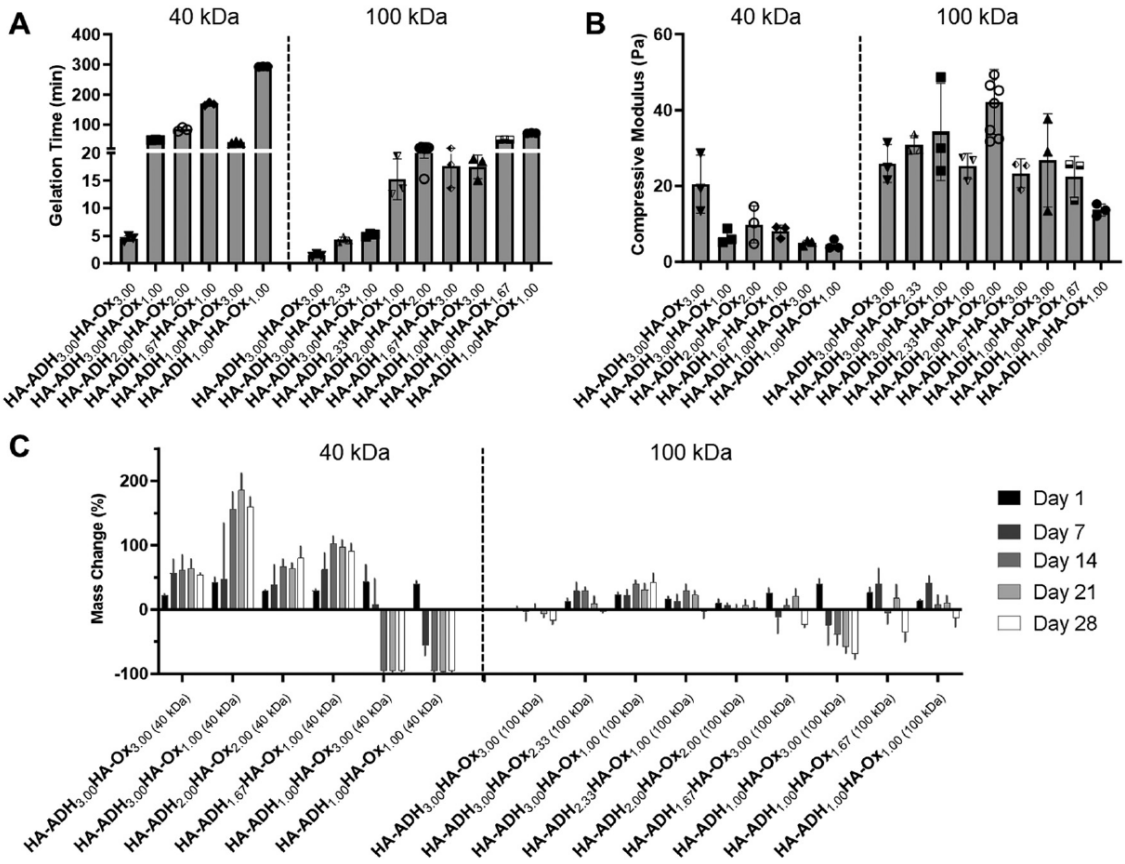

Figure 5.22: Physicochemical properties for each of the 15 hydrogel formulations for the D-optimal design. HA hydrogels were fabricated using 40 kDa or 100 kDa HA-Ox and HA-ADH at different polymer weight percentages. (A) Gelation time of HA hydrogels. (B) Compressive moduli of HA hydrogels. (C) Mass change of HA hydrogels incubated in phosphate-buffered saline at room temperature for 28 days. Data presented as mean SD with 3 replicates for all hydrogel formulations, except for the centrally repeated condition, HA-$ADH_{2.00}$HA-$Ox_{2.00}$ (100 kDa), which had 9 replicates. A summary of statistical significance for gelation time, compressive modulus, and mass change can be found in Tables S3–S5 (ESI), respectively.

Property	Range
Gelation time	1.4–292.7 min
Compressive modulus	4.5–42.2 Pa
Mass change day 1	1.0–43.1%
Mass change day 7	−56.3 to 62.2%
Mass change day 14	−100 to 156.9%
Mass change day 21	−100 to 185.3%
Mass change day 28	−100 to 160.7%

Table 5.5: Ranges of physicochemical properties exhibited by HA hydrogels.

Design of experiments analysis

After obtaining response data for our 15 hydrogel formulations, we used this data to generate a multivariate model for DoE analysis to better understand how HA-Ox concentration, HA-ADH concentration, and HA molecular weight interacted to produce a wide range of physicochemical properties demonstrated by our platform and to predict the hydrogel formulations that would yield responses that met our desired design criteria. We fit second order multiple linear regression models for each response (gelation time, compressive modulus, mass change at 1, 7, 14, 21, and 28 days) and eliminated the terms that were not statistically significant unless they contributed to square terms or interaction terms that were statistically significant (p<0.05) (**Table 5.6**). There was a significant effect of HA-ADH concentration on all responses except for mass change at day 7 and a significant effect of HA-Ox concentration on all responses except for mass change at day 1. The molecular weight of the HA had a significant effect on all responses. Notably, several squared and interaction terms also had significant effects on individual responses. We found that all of our models fit the success criteria of R^2 and adjusted R^2 values close to 1.0, Q^2 above 0.50, and the difference between R^2 and Q^2 values below 0.30. The models with the lowest R^2 and Q^2 values, indicating the poorest fit, were for mass change at days 1 and 7. This may be due to large variations in the initial swelling of the hydrogel network when incubated in PBS resulting in unpredictable short-term changes in mass compared to hydrogels that have swollen to a stable, more predictable equilibrium at later time points (days 14, 21, and 28).[54]

Three-dimensional response surface plots of gelation time for the 40 kDa HA hydrogels. demonstrated that higher polymer content resulted in faster gelation with the shortest gelation time occurring at HA-$ADH_{3.0}$HA-$Ox_{3.0}$ and longest gelation time occurring at HA-$ADH_{1.0}$HA-$Ox_{1.0}$ (**Fig. 5.23A**). This response surface was identical but smaller in magnitude for the 100 kDa HA hydrogels (**Fig. 5.23B**). These plots indicate that gelation time was dependent on the concentrations of both HA-ADH and HA-Ox. The response surfaces of compressive modulus for 40 kDa and 100 kDa HA hydrogels both depicted a negative quadratic dependance on the HA-Ox and HA-ADH concentrations with a maximum compressive modulus predicted to occur at HA-$ADH_{2.21}$HA-$Ox_{2.08}$.

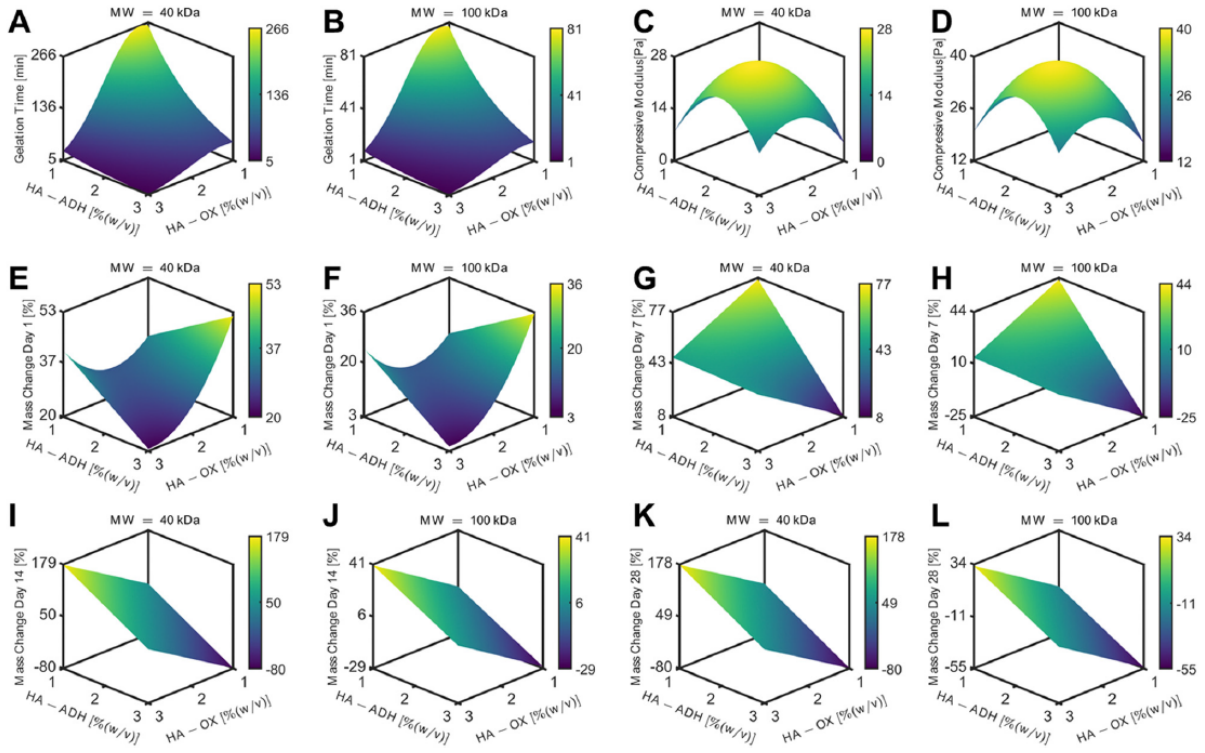

Figure 5.23: Three-dimensional response surfaces demonstrating the effect of input parameters on different output responses. Polymer weight percentages of HA-ADH and HA-Ox are on the x- and y-axes respectively, and output responses are on the z-axes. Responses for 40 kDa and 100 kDa HA hydrogels are plotted separately. The colored bars represent the magnitude of the response from low (blue) to high (yellow) for each response surface. Response surfaces for gelation time for (A) 40 kDa HA and (B) 100 kDa HA, compressive moduli for (C) 40 kDa HA and (D) 100 kDa HA, mass change at day 1 for (E) 40 kDa HA and (F) 100 kDa HA, mass change at day 7 for (G) 40 kDa HA and (H) 100 kDa HA, mass change at day 14 for (I) 40 kDa HA and (J) 100 kDa HA, and mass change at day 28 for, (K) 40 kDa HA and (L) 100 kDa HA.

For the 40 kDa HA hydrogels, this maximum compressive modulus was predicted to be 39.2 Pa (**Fig. 5.23C**), while, for the 100 kDa HA hydrogels, the maximum compressive modulus was predicted to be 27.3 Pa (**Fig. 5.23D**). The relationship between mass change and input parameters was different at different time points. Mass change at day 1 was dependant on interactions between HA-ADH and HA-Ox concentrations and demonstrated a positive quadratic dependance on HA-ADH. The minimal mass change for for both 40 kDa and 100 kDa hydrogels occurred at HA-$ADH_{3.0}$HA-$Ox_{3.0}$ and was found to be similar at 4.65% and 4.67%, respectively (**Fig. 5.23E, Fig. 5.23F)**. Mass change at day 7 demonstrated quadratic dependances on HA-ADH and HA-Ox as well as dependance on interactions between HA-ADH and HA-Ox. For both 40 kDa and 100 kDa hydrogels, the minimum mass change occurred at HA-$ADH_{1.0}$HA-$Ox_{3.0}$; however, the predicted minimum was 13.52% for 40 kDa hydrogels(**Fig. 5.23G**), and -20.22% for 100 kDa hydrogels (**Fig. 5.23H**). At day 14, the model predicted a maximum mass change of 164.4% at HA-$ADH_{3.0}$HA-$OX_{3.0}$ and a minimum mass change of -82.4% at HA-$ADH_{1.0}$HA-$OX_{3.0}$ for 40 kDa hydrogels (**Fig. 5.23I**). Minimum and maximum mass change occurred at the same polymer compositions for 100 kDa hydrogels on day 14 (**Fig. 5.23J**) and at 40 and 100 kDa for day 28 (**Fig. 5.23K, Fig. 5.23L**). Overall, the response surfaces and ANOVA table demonstrate that gelation time, compressive modulus, and mass change at day 1 were dependent on interactions between HA-ADH concentration and HA-Ox concentration, while no interactions of the input parameters were observed with mass change at the other time points.

Optimal and Pessimal Hydrogel Predictions

Our overall objective was to use DoE to optimize HA hydrogels for protein delivery for bone regeneration. We aimed to formulate a hydrogel that exhibited a gelation time between 1-10 minutes, minimal mass change (i.e., 0%) over 28 days, and the maximum possible compressive modulus. D-optimal design generated predictive models describing how HA-ADH polymer concentration, HA-Ox polymer concentration, and HA molecular weight influenced compressive modulus, gela-

Response	Gelation time	Compressive modulus	Mass change day 1	Mass change day 7	Mass change day 14	Mass change day 21	Mass change day 28
p-Values							
[HA-ADH]	<0.0001	0.0258	0.0136	0.612	<0.0001	<0.0001	<0.0001
[HA-Ox]	<0.0001	0.173	0.725	0.000539	<0.0001	<0.0001	<0.0001
Molecular weight (MW)	<0.0001	0.00122	0.000702	0.000222	0.000494	0.00107	0.000234
$[HA\text{-}ADH]^2$	0.000985	0.00375	0.0399	—	—	—	—
$[HA\text{-}Ox]^2$	—	0.000782	—	—	—	—	—
MW^2	—	—	—	—	—	—	—
[HA-ADH]* [HA-Ox]	—	—	0.00213	0.00237	—	—	—
[HA-ADH]* MW	—	—	—	—	0.00166	0.000823	0.0125
[HA-Ox]* MW	—	—	—	—	0.000964	0.00304	0.00763
Lack of fit	0.177	0.363	0.948	0.213	0.410	0.472	0.548
Total sample size (N)	17	13	17	16	16	16	16
Degrees of freedom (DF)	12	7	11	11	10	10	10
R^2	0.964	0.970	0.828	0.852	0.950	0.937	0.936
R^2-Adjusted	0.952	0.903	0.750	0.799	0.926	0.905	0.904
Q^2	0.918	0.949	0.601	0.683	0.710	0.840	0.792

Table 5.6: ANOVA assessment of regression models. Excluded non-significant values are indicated with a dash (–).

tion time, and mass change.

To validate this model, we generated a hydrogel formulation that was predicted to optimize our target parameters (Optimal) as well as two hydrogels that were optimized with opposite objectives (Pessimal 1 and 2) (**Table 5.7**). More specifically, Pessimal 1 was set to degrade over 28 days, while Pessimal 2 was set to swell over 28 days. Our optimal formulation had a molecular weight of 100 kDa while both pessimal formulations had a molecular weight of 40 kDa. This may be due to the longer gelation times, softer compressive moduli, and larger mass changes over time that were observed in our 40 kDa hydrogels. The optimal formulation, HA-$ADH_{3.0}$HA-$OX_{2.33}$, met our targeted responses with a gelation time of 3.7 min (**Fig. 5.24A**), compressive modulus of 62.1 Pa (**Fig. 5.24B**), and minimal mass change from -22.2 to 5.5% over 28 days (**Fig. 5.24C**). Conversely, our Pessimal 1 formulation, HA-$ADH_{1.17}$HA-$OX_{1.02}$, displayed a gelation time of 262.2 min, compressive modulus of 23.1 Pa, and swelling up to 85.3% of its initial mass on day 4, followed by fully degradation by day 21. The Pessimal 2 formulation, HA-$ADH_{1.70}$HA-$OX_{1.80}$ displayed a gelation time of 100 min, a compressive modulus of 70.6 Pa, and swelling up to 172.3% by day 28 with no degradation.

The gelation time of the optimal formulation was significantly lower than that of the pessimal formulations. Mass change for the optimal formulation was closer to the 0% target mass change at all timepoints, while both pessimal formulations exhibited initial swelling before either degrading

	HA-ADH (%w/v)	HA-Ox (%w/v)	Molecular weight (kDa)
Optimal	3.00	2.33	100
Pessimal 1	1.17	1.02	40
Pessimal 2	1.70	1.80	40

Table 5.7: Formulations for optimal and pessimal hydrogels.

completely or continuing to swell excessively. However, there were no significant differences between the compressive moduli of the optimal formulation and the two pessimal formulations. Thus, trying to independently target each of our desired physicochemical properties with our hydrogel formulation would have been successful, highlighting the importance of using DoE to simultaneously optimize multiple output responses. Scanning electron microscopy of the optimal hydrogel formulation revealed interconnected pores of different sizes (Fig. S5, ESI†). This porous morphology resembles the morphology observed in other HA hydrogels.[60]

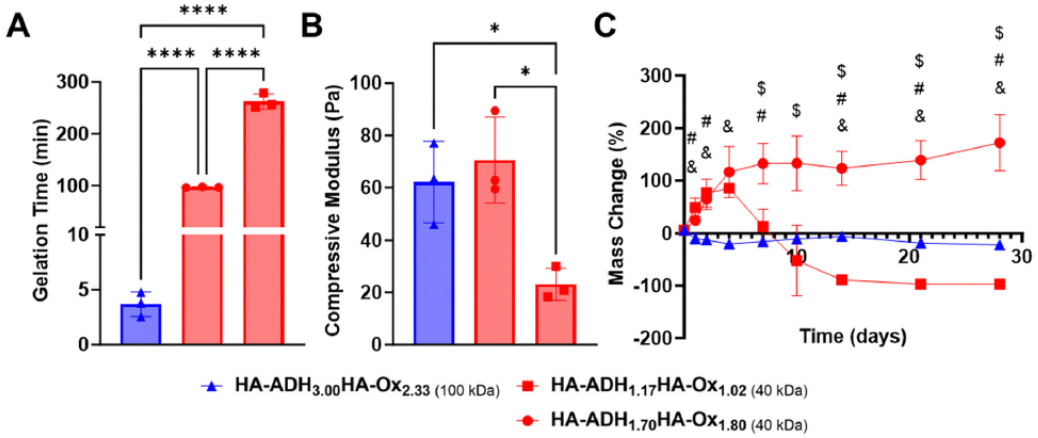

Figure 5.24: Validation of predictive models to optimize HA hydrogels. (A) Gelation time of optimal (blue) and pessimal (red) hydrogels. One-way ANOVA, *post hoc* Tukey's multiple comparisons. n = 3; ** $p < 0.01$, **** $p < 0.0001$. (B) Compressive modulus of optimal and pessimal hydrogels. One-way ANOVA, *post hoc* Tukey's multiple comparisons. n = 3; * $p < 0.05$. (C) Mass change over 28 days of optimal and pessimal hydrogels. Two-way ANOVA, *post hoc* Tukey's multiple comparisons. n = 3; & $p < 0.05$ HA-ADH3.00HA-Ox2.33 (100 kDa) vs. HA-ADH1.17HA-Ox1.02 (40 kDa), # $p < 0.05$ HA-ADH3.00HA-Ox2.33 (100 kDa) vs. HA-ADH1.70HA-Ox1.80 (40 kDa), and $ $p < 0.05$ HA-ADH1.17HA-Ox1.02 (40 kDa) vs. HA-ADH1.70HA-Ox1.80 (40 kDa).

BMP-2 release from affibody-containing hydrogels

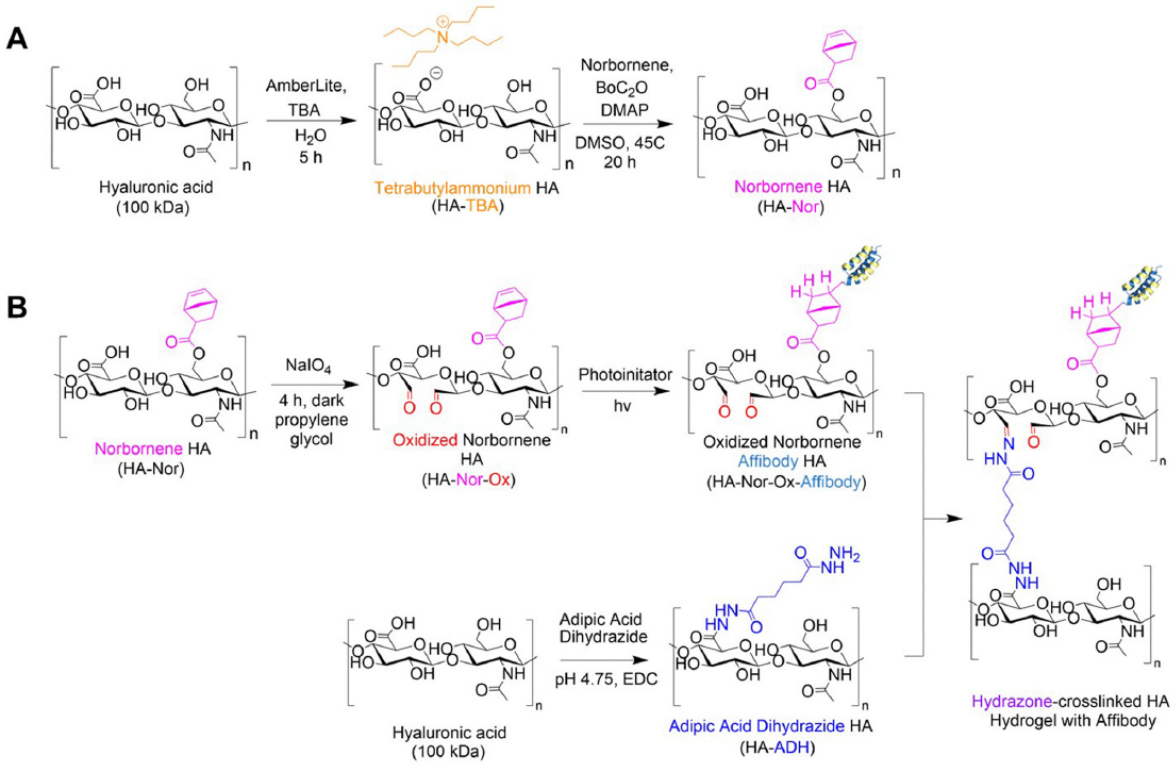

Figure 5.25: Synthesis of HA-Nor, HA-Nor-Ox, and HA-Nor-Ox-Affibody. (A) HA was functionalized with a norbornene group through BoC_2O activated coupling prior to oxidation resulting in HA-Nor-Ox. (B) HA-Nor-Ox was then used to bioconjugate our BMP-2 affibody to the norbornene group through a photoinitiated reaction and thiol–ene click chemistry. The product was then crosslinked with HA-ADH to form a hydrazone-crosslinked hydrogel containing affibodies.

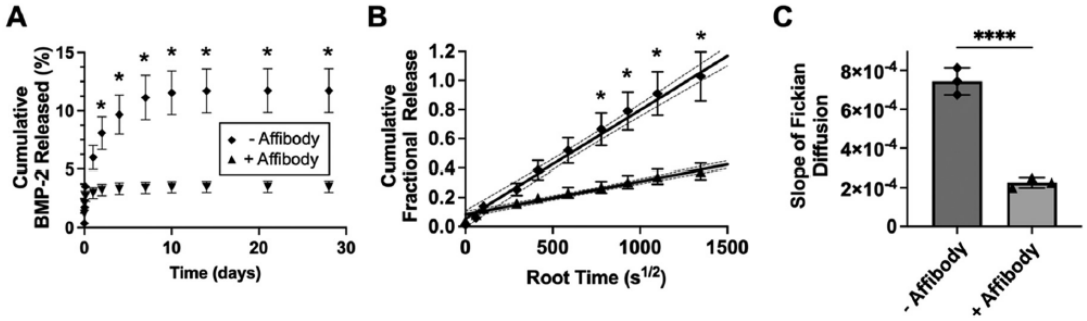

Figure 5.26: Release of BMP-2 from HA hydrogel. (A) Cumulative release of BMP-2 from HA hydrogel without affibody (diamond) and with affibody (triangle). Two-way ANOVA,*post hoc* Dunnett's T3 multiple comparisons. n = 3; * $p < 0.05$. (B) Linearized release of BMP-2 affibody from hydrogels with and without affibody. Two-way ANOVA, *post hoc* Dunnett's T3 multiple comparisons. n = 3; * $p < 0.05$. (C) Slope of linearized release of BMP-2 from HA hydrogels. One-way ANOVA, *post hoc* Dunnett's T3 multiple comparisons. n = 3; * $p < 0.05$, **** $p < 0.0001$.

As proof-of-concept of affinity-controlled protein delivery from our HA hydrogels, we modified HA-Ox to contain a norbornene functional group for bioconjugation of a previously discovered BMP-2-specific affibody with high affinity for BMP-2 (dissocia- tion constant, KD = 10.7 nM).[41] Affibodies are small proteins with 58 amino acids folded into a bundle of three a-helices.[61,62] Affibodies can be engineered to bind to different proteins with a range of affinities and can be used to release proteins at various rates by tuning the strength of the affinity interac- tions.[41,63,64] HA was functionalized with norbornene through BoC_2O activated coupling (**Fig. 5.25A**). The resulting product was then modified a second time by the previously described oxidation reaction, resulting in oxidized, norbornene- functionalized HA (HA-Nor-Ox; **Fig. 5.25B**). Two times molar excess affibody to HA was then added to HA-Nor-Ox in the presence of a photoinitiator and exposed to light at 365 nm to create affibody-conjugated HA-Nor-Ox (HA-Nor-Ox-Affibody). The average concentration of affibody conjugated to HA-Nor-Ox was 2.80 1.95 nmol mg^{-1} HA polymer (Fig. S6, ESI†). This modified polymer was crosslinked with HA-ADH to form a hydrazone-crosslinked, affibody-containing HA hydrogel. Release of BMP-2 was evaluated over 28 days from unmodified HA hydrogels or hydrogels conjugated with affibodies with high affinity and specificity for BMP-2 (dissociation constant, K_D = 10.7 nM).[41] Hydrogels were formed with BMP-2 and incubated in 1% w/v BSA in PBS. Aliquots were taken from the supernatant over 28 days to evaluate a release profile of BMP-2 from the HA hydrogel. The HA hydrogel with BMP-2 affibody reduced the release of BMP-2 compared to a HA hydrogel without affibody (**Fig. 5.26A**). After 28 days, 11.7% of BMP-2 was released from the hydrogel without the affibodies, whereas 3.5% of BMP-2 was released from the hydrogel with the BMP-2-specific affibodies. Fig. 6B depicts the cumulative fraction release at each time point (M_t/M_∞) as a function of the square root of time of the linear region of the BMP-2 release profile. The diffusivity (i.e., release rate) or the Fickian diffusion slope, k, was calculated using the slope of the cumulative fractional release (eqn (3)), demonstrating that the release rate of BMP-2 was significantly slower in the affibody-containing hydrogel compared to the hydrogel without affibodies (**Fig. 5.26C**). Our goal was to use BMP-2-specific affibodies

to increase BMP-2 retention within the HA hydrogel for future applications in bone regeneration, since increased BMP-2 reten- tion has been shown to stimulate localized bone formation within an injury site.[65] In other work, we have demonstrated that BMP-2 release from polyethylene glycol (PEG) hydrogels can be tuned over a range of release rates and amounts by changing the affinity between the affibodies and BMP-2.[41] In the future, we plan to further explore how changes to the HA hydrogel formulation, affibody amount, and affibody affinity strength can influence BMP-2 release to enhance bone regeneration.

5.1.5 Conclusion

Although hydrazone chemistry is similar in many applications, each hydrogel requires distinct properties for a specific use. Designing an appropriate hydrogel for a biomedical application requires the consideration of many design criteria, such as gelation time, compressive modulus, and stability over time, that can be affected by many factors, including polymer molecular weight and concentration. In this work, we optimized hydrazone-crosslinked HA hydrogels for protein delivery for bone regeneration using DoE to better understand how various input parameters interacted to affect physicochemical properties, while reducing the number of experiments required to obtain this information. We generated models to describe how HA-ADH concentration, HA-Ox concentration, and HA molecular weight affected hydrogel compressive modulus, gelation time, and mass change over time. We identified an optimized hydrogel formulation that simultaneously maximized compres- sive modulus (62.1 Pa), achieved a target gelation time between 1–10 minutes (3.7 minutes), and was stable over 28 days with minimal mass change. We confirmed the validity of our model by evaluating two pessimal hydrogel formulations that were predicted to provide responses opposite to our optimal formulation. We also demonstrated that protein release from hydrazone-crosslinked HA hydrogels could be sustained over 28 days by conjugated BMP-2-specific affibodies to the hydrogels to control the release of BMP-2. Ultimately, hydrazone crosslinked HA hydrogels are a promising platform for protein delivery and DoE is a valuable tool to optimize hydrogels for this application.

5.1.6 Citations

(1) J. Dorogin, J. M. Townsend and M. H. Hettiaratchi, Biomaterials for protein delivery for complex tissue healing responses, *Biomater. Sci.*, **2021**, 9(7), 2339–2361.

(2) A. W. James, G. LaChaud, J. Shen, G. Asatrian, V. Nguyen and X. Zhang, et al., A Review of the Clinical Side Effects of Bone Morphogenetic Protein-2, *Tissue Eng., Part B*, **2016**, 22(4), 284–297.

(3) M. Bartnikowski, R. M. Wellard, M. Woodruff and T. Klein, Tailoring Hydrogel Viscoelasticity with Physical and Chemical Crosslinking, *Polymers*, **2015**, 7(12), 2650–2669.

(4) T. Vermonden, R. Censi and W. E. Hennink, Hydrogels for Protein Delivery, Chem. Rev., 2012, 112(5), 2853–2888.

(5) S. Naahidi, M. Jafari, M. Logan, Y. Wang, Y. Yuan and H. Bae, et al., Biocompatibility of hydrogel-based scaffolds for tissue engineering applications, *Biotechnol. Adv.*, **2017**, 35(5), 530–544.

(6) M. Darnell and D. J. Mooney, Leveraging advances in biology to design biomaterials, *Nat. Mater.*, **2017**, 16(12), 1178–1185.

(7) J. Telford. A Brief Introduction to Design of Experiments. *Johns Hopkins APL Technical Digest*, **2007**, 27 (3).

(8) J. Lam, S. T. Carmichael, W. E. Lowry and T. Segura, Hydrogel Design of Experiments Methodology to Optimize Hydrogel for iPSC-NPC Culture, *Adv. Healthcare Mater.*, **2015**, 4(4), 534–539.

(9) A. S. H. Ahmed, U. K. Mandal, M. Taher, D. Susanti and J. M. D. Jaffri, PVA-PEG physically cross-linked hydrogel film as a wound dressing: experimental design and optimization, *Pharm. Dev. Technol.*, **2018**, 23(8), 751–760.

(10) L. R. Nih, P. Moshayedi, I. L. Llorente, A. R. Berg, J. Cinkornpumin and W. E. Lowry, et al., Engineered HA hydrogel for stem cell transplantation in the brain: biocompatibility data using a design of experiment approach, *Data Brief.*, **2017**, 10, 202–209.

(11) I. A. Cadena, M. R. Buchanan, C. G. Harris, M. A. Jenne, W. E. Rochefort and D. Nelson,

et al., Engineering high throughput screening platforms of cervical cancer, *J. Biomed. Mater. Res., Part A*, **2023**, 111(6), 747–764.

(12) M. G. Arafa and B. M. Ayoub, DOE Optimization of Nanobased Carrier of Pregabalin as Hydrogel: New Therapeutic & Chemometric Approaches for Controlled Drug Delivery Systems, *Sci. Rep.*, **2017**, 7(1), 41503.

(13) A. Nastruzzi, G. Pitingolo, G. Luca and C. Nastruzzi, DoE Analysis of Approaches for Hydrogel Microbeads' Preparation by Millifluidic Methods, *Micromachines*, **2020**, 11(11), 1007.

(14) M. M. Pakulska, K. Vulic, R. Y. Tam and M. S. Shoichet, Hybrid Crosslinked Methylcellulose Hydrogel: A Predictable and Tunable Platform for Local Drug Delivery, *Adv. Mater.*, **2015**, 27(34), 5002–5008.

(15) A. M. Yousefi, J. Liu, R. Sheppard, S. Koo, J. Silverstein and J. Zhang, et al., I-Optimal Design of Hierarchical 3D Scaffolds Produced by Combining Additive Manufacturing and Thermally Induced Phase Separation, *ACS Appl. Bio Mater.*, **2019**, 2(2), 685–696.

(16) M. Asadi-Eydivand, M. Solati-Hashjin, A. Fathi, M. Padashi and N. A. Abu Osman, Optimal design of a 3D-printed scaffold using intelligent evolutionary algorithms, *Appl. Soft Comput.*, **2016**, 39, 36–47.

(17) M. Kuterbekov, P. Machillot, F. Baillet, A. M. Jonas, K. Glinel and C. Picart, Design of experiments to assess the effect of culture parameters on the osteogenic differentiation of human adipose stromal cells, *Stem Cell Res. Ther.*, **2019**, 10(1), 256.

(18) M. F. P. Graça, S. P. Miguel, C. S. D. Cabral and I. J. Correia, Hyaluronic acid-Based wound dressings: a review, *Carbohydr. Polym.*, **2020**, 241, 116364.

(19) J. Necas, L. Bartosikova, P. Brauner and J. Kolar, Hyaluronic acid (hyaluronan): a review, *Veterina´rnı´ Med.*, **2008**, 53(8), 397–411.

(20) M. Dovedytis, Z. J. Liu and S. Bartlett, Hyaluronic acid and its biomedical applications: a review, *Eng. Regener.*, **2020**, 1, 102–113.

(21) M. K. Cowman, H. G. Lee, K. L. Schwertfeger, J. B. McCarthy and E. A. Turley, The Content and Size of Hyaluronan in Biological Fluids and Tissues, *Front. Immunol.*, **2015**, 6, DOI:

10.3389/fimmu.2015.00261.

(22) A. G. Tavianatou, I. Caon, M. Franchi, Z. Piperigkou, D. Galesso and N. K. Karamanos, Hyaluronan: molecular size-dependent signaling and biological functions in inflammation and cancer, *FEBS J.*, **2019**, 286(15), 2883–2908.

(23) J. Yang, C. C. Hsu, T. T. Cao, H. Ye, J. Chen and Y. Q. Li, A hyaluronic acid granular hydrogel nerve guidance conduit promotes regeneration and functional recovery of injured sciatic nerves in rats, *Neural Regener. Res.*, **2023**, 18(3), 657.

(24) M. Halperin-Sternfeld, A. Pokhojaev, M. Ghosh, D. Rachmiel, R. Kannan and I. Grinberg, et al., Immunomodulatory fibrous hyaluronic acid-Fmoc-diphenylalanine-based hydrogel induces bone regeneration, *J. Clin. Periodontol.*, **2023**, 50(2), 200–219.

(25) S. J. Yoon, Y. H. Fang, C. H. Lim, B. S. Kim, H. S. Son and Y. Park, et al., Regeneration of ischemic heart using hyaluronic acid-based injectable hydrogel, *J. Biomed. Mater. Res., Part B*, **2009**, 91B(1), 163–171.

(26) A. J. Engler, S. Sen, H. L. Sweeney and D. E. Discher, Matrix Elasticity Directs Stem Cell Lineage Specification, *Cell*, **2006**, 126(4), 677–689.

(27) D. A. Young, Y. S. Choi, A. J. Engler and K. L. Christman, Stimulation of adipogenesis of adult adipose-derived stem cells using substrates that mimic the stiffness of adipose tissue, *Biomaterials*, **2013**, 34(34), 8581–8588.

(28) X. Xue, K. Liang, W. Huang, H. Yang, L. Jiang and Q. Jiang, et al., Molecular Engineering of Injectable, Fast SelfRepairing Hydrogels with Tunable Gelation Time: Characterization by Diffusing Wave Spectroscopy, *Macromolecules*, **2022**, 55(15), 6474–6486.

(29) V. Delplace, P. E. B. Nickerson, A. Ortin-Martinez, A. E. G. Baker, V. A. Wallace and M. S. Shoichet, Nonswelling, Ultralow Content Inverse Electron-Demand Diels–Alder Hyaluronan Hydrogels with Tunable Gelation Time: Synthesis and In Vitro Evaluation, *Adv. Funct. Mater.*, **2020**, 30(14), 1903978. (30) H. Park, X. Guo, J. S. Temenoff, Y. Tabata, A. I. Caplan and F. K. Kasper, et al., Effect of Swelling Ratio of Injectable Hydrogel Composites on Chondrogenic Differentiation of Encapsulated Rabbit Marrow Mesenchymal Stem Cells In

Vitro, *Biomacromolecules*, **2009**, 10(3), 541–546.

(30) W. Mubarok, K. C. M. L. Elvitigala, M. Nakahata, M. Kojima and S. Sakai, Modulation of Cell-Cycle Progression by Hydrogen Peroxide-Mediated Cross-Linking and Degradation of Cell-Adhesive Hydrogels, *Cells*, **2022**, 11(5), 881.

(31) C. Wang, X. Tong, X. Jiang and F. Yang, Effect of Matrix Metalloproteinase-Mediated Matrix Degradation on Glioblastoma Cell Behavior in 3D PEG-based Hydrogels, *J. Biomed. Mater. Res., Part A*, **2017**, 105(3), 770–778.

(32) W. Y. Su, K. H. Chen, Y. C. Chen, Y. H. Lee, C. L. Tseng and F. H. Lin, An Injectable Oxidated Hyaluronic Acid/Adipic Acid Dihydrazide Hydrogel as a Vitreous Substitute, *J. Biomater. Sci., Polym. Ed.*, **2011**, 22(13), 1777–1797.

(33) C. G. França, D. P. Sacomani, D. G. Villalva, V. F. Nascimento, J. L. Da´vila and M. H. A. Santana, Structural changes and crosslinking modulated functional properties of oxi-HA/ADH hydrogels useful for regenerative purposes, *Eur. Polym. J.*, **2019**, 121, 109288.

(34) L. Vı´tkov´a, L. Musilova´, E. Achbergerova´, R. Kolarˇı´k, M. Mrlı´k and K. Korpasova´, et al., Formulation of MagnetoResponsive Hydrogels from Dually Cross-Linked Polysaccharides: Synthesis, Tuning and Evaluation of Rheological Properties, *Int. J. Mol. Sci.*, **2022**, 23(17), 9633.

(35) C. G. França, D. G. Villalva and M. H. A. Santana, Oxi-HA/ ADH Hydrogels: A Novel Approach in Tissue Engineering and Regenerative Medicine, *Polysaccharides*, **2021**, 2(2), 477–496.

(36) Department of Orthopaedics, National Taiwan University College of Medicine and National Taiwan University Hospital, No. 1, Sec. 1, JenAi Road, Taipei 100, Taiwan, M. Hu, K. Yang, Y. Sun, Y. Chen and S. Yang, et al., In situ forming oxidised hyaluronic acid/adipic acid dihydrazide hydrogel for prevention of epidural fibrosis after laminectomy, *eCM.*, **2017**, 307–320.

(37) X. Jia, G. Colombo, R. Padera, R. Langer and D. S. Kohane, Prolongation of sciatic nerve blockade by in situ crosslinked hyaluronic acid, *Biomaterials*, **2004**, 25(19), 4797–4804.

(38) Y. Yeo, C. B. Highley, E. Bellas, T. Ito, R. Marini and R. Langer, et al., In situ cross-linkable hyaluronic acid hydrogels prevent post-operative abdominal adhesions in a rabbit model, *Biomaterials*, **2006**, 27(27), 4698–4705.

(39) N. de Paiva Narciso, R. S. Navarro, A. E. Gilchrist, M. L. M. Trigo, G. Aviles Rodriguez and S. C. Heilshorn, Design Parameters for Injectable Biopolymeric Hydrogels with Dynamic Covalent Chemistry Crosslinks, *Adv. Healthcare Mater.*, **2023**, 2301265.

(40) J. Dorogin, H. B. Hochstatter, S. O. Shepherd, J. E. Svendsen, M. A. Benz and A. C. Powers, et al., Moderate-Affinity Affibodies Modulate the Delivery and Bioactivity of Bone Morphogenetic Protein-2, *Adv. Healthcare Mater.*, **2023**, 2300793.

(41) M. D. Davidson, E. Ban, A. C. M. Schoonen, M. H. Lee, M. D'Este and V. B. Shenoy, et al., Mechanochemical Adhesion and Plasticity in Multifiber Hydrogel Networks, *Adv. Mater.*, **2020**, 32(8), 1905719.

(42) H. Zhao and N. D. Heindel, Determination of Degree of Substitution of Formyl Groups in Polyaldehyde Dextran by the Hydroxylamine Hydrochloride Method, *Pharm. Res.*, **1991**, 8(3), 400–402.

(43) Q. Wang, Z. Wang, D. Zhang, J. Gu, Y. Ma and Y. Zhang, et al., Circular Patterns of Dynamic Covalent Hydrogels with Gradient Stiffness for Screening of the Stem Cell Microenvironment, *ACS Appl. Mater. Interfaces*, **2022**, 14(42), 47461–47471.

(44) J. M. Alonso, J. Andrade Del Olmo, R. Perez Gonzalez and V. Saez-Martinez, Injectable Hydrogels: From Laboratory to Industrialization, *Polymers (Basel)*, **2021**, 13(4), 650.

(45) N. R. Raia, B. P. Partlow, M. McGill, E. P. Kimmerling, C. E. Ghezzi and D. L. Kaplan, Enzymatically Crosslinked SilkHyaluronic Acid Hydrogels, *Biomaterials*, **2017**, 131, 58–67.

(46) P. Rosaming, J. Jirayupapong, S. Thamnium, Y. Y. Win, V. Limprasutr and R. Rodsiri, et al., Interpenetrating LowMolecular Weight Hyaluronic Acid in Hyaluronic AcidBased In Situ Hydrogel Scaffold for Periodontal and Oral Wound Applications, *Polymers*, **2022**, 14(22), 4986.

(47) V. G. Muir, S. Weintraub, A. P. Dhand, H. Fallahi, L. Han and J. A. Burdick, Influence of Microgel and Interstitial Matrix Compositions on Granular Hydrogel Composite Properties, *Adv. Sci.*, **2023**, 10(10), 2206117.

(48) P. L. Ritger and N. A. Peppas, A simple equation for description of solute release I. Fickian and non-fickian release from non-swellable devices in the form of slabs, spheres, cylinders or discs, *J. Controlled Release*, **1987**, 5(1), 23–36.

(49) M. M. Pakulska, K. Vulic and M. S. Shoichet, Affinity-based release of chondroitinase ABC from a modified methylcellulose hydrogel, *J. Controlled Release*, **2013**, 171(1), 11–16.

(50) R. E. Bruns, I. S. Scarminio and B. B. de Neto, Statistical Design – Chemometrics, Elsevier Science, Amsterdam; Boston, **2006**. 1st edn, p. 422.

(51) MODDEs 12 User Guide. June 21, **2017**. Sartorius Stedim Data Analytics AB.

(52) C. G. França, D. P. Sacomani, D. G. Villalva, V. F. Nascimento, J. L. Da´vila and M. H. A. Santana, Structural changes and crosslinking modulated functional properties of oxi-HA/ADH hydrogels useful for regenerative purposes, *Eur. Polym. J.*, **2019**, 121, 109288.

(53) S. Uman, L. L. Wang, S. L. Thorn, Z. Liu, J. S. Duncan and A. J. Sinusas, et al., Imaging of injectable hydrogels delivered into myocardium with SPECT/CT, *Adv. Healthcare Mater.*, **2020**, 9(14), e2000294.

(54) Y. Wang, Y. Chen, J. Zheng, L. Liu and Q. Zhang, ThreeDimensional Printing Self-Healing Dynamic/Photocrosslinking Gelatin-Hyaluronic Acid Double-Network Hydrogel for Tissue Engineering, *ACS Omega*, **2022**, 7(14), 12076–12088.)

(55) L. L. Wang, C. B. Highley, Y. C. Yeh, J. H. Galarraga, S. Uman and J. A. Burdick, 3D extrusion bioprinting of single- and double-network hydrogels containing dynamic covalent crosslinks, *J. Biomed. Mater. Res., Part A*, **2018**, 106(4), 865–875.

(56) S. Kadi, D. Cui, E. Bayma, T. Boudou, C. Nicolas and K. Glinel, et al., Alkylamino Hydrazide Derivatives of Hyaluronic Acid: Synthesis, Characterization in Semidilute Aqueous Solutions, and Assembly into Thin Multilayer Films, *Biomacromolecules*, **2009**, 10(10), 2875–2884.

(57) N. Lagneau, P. Tournier, B. Halgand, F. Loll, Y. Maugars and J. Guicheux, et al., Click and bioorthogonal hyaluronic acid hydrogels as an ultra-tunable platform for the investigation of cell-material interactions, *Bioact. Mater.*, **2023**, 24, 438–449.

(58) N. R. Richbourg, M. Wancura, A. E. Gilchrist, S. Toubbeh, B. A. C. Harley and E. Cosgriff-Hernandez, et al., Precise control of synthetic hydrogel network structure via linear, independent synthesis-swelling relationships, *Sci. Adv.*, **2021**, 7(7), eabe3245.

(59) J. M. Alonso, J. Andrade Del Olmo, R. Perez Gonzalez and V. Saez-Martinez, Injectable Hydrogels: From Laboratory to Industrialization, *Polymers*, **2021**, 13(4), 650.

(60) J. Lo ̈fblom, J. Feldwisch, V. Tolmachev, J. Carlsson, S. Ståhl and F. Y. Frejd, Affibody molecules: engineered proteins for therapeutic, diagnostic and biotechnological applications, *FEBS Lett.*, **2010**, 584(12), 2670–2680.

(61) S. Ståhl, T. Gra ̈slund, A. Eriksson Karlstr ̈om, F. Y. Frejd, P. Å. Nygren and J. Lo ̈fblom, Affibody Molecules in Biotechnological and Medical Applications, *Trends Biotechnol.*, **2017**, 35(8), 691–712.

(62) C. J. Teal, M. H. Hettiaratchi, M. T. Ho, A. Ortin-Martinez, A. N. Ganesh and A. J. Pickering, et al., Directed Evolution Enables Simultaneous Controlled Release of Multiple Therapeutic Proteins from Biopolymer-Based Hydrogels, *Adv. Mater.*, **2022**, 34(34), 2202612.

(63) C. Bostock, C. J. Teal, M. Dang, A. W. Golinski, B. J. Hackel and M. S. Shoichet, Affibody-mediated controlled release of fibroblast growth factor 2, *J. Controlled Release*, **2022**, 350, 815–828.

(64) M. H. Hettiaratchi, L. Krishnan, T. Rouse, C. Chou, T. C. McDevitt and R. E. Guldberg, Heparin-mediated delivery of bone morphogenetic protein-2 improves spatial localization of bone regeneration, *Sci. Adv.*, **2020**, 6(1), eaay1240.

Chapter VI: Summary

6.1 Concluding Remarks

Overall, this work expands the accessibility of new CPP properties through the development of high-yielding, late-stage synthetic methodologies without de novo synthesis. We demonstrated multiple modifications using S_NAr chemistry, enabling tunable binding affinity to C_{60} and showing reversible redox properties. We further showed that the cyclic CPP framework preferentially undergoes S_NAr compared to linear analogues, likely due to strain-induced effects. We expanded the CPP synthetic toolkit by demonstrating the first Diels–Alder reaction on alkyne-containing CPPs and achieve photophysical tuning with an observed increase in the Stokes shift. In this system, we also observed size-dependent reactivity, showing smaller alkyne CPPs react at lower temperatures. To expand CPP applications in bio-materials, we explored thiol–ene photochemistry as a facile, room-temperature method to append proteins and small peptides to norbornene-functionalized CPPs. Collectively, this dissertation provides a framework for the rational modification of strained π-systems, establishing design principles that extend beyond CPPs to broader classes of curved and conjugated nanomaterials.

6.2 Acknowledgements

6.2.1 Redox-Active Multi-Thianthrene-Containing Cycloparaphenylenes

T.D.C., V.R.S., and R. J. were supported by generous funds from the National Science Foundation (CHE-2400147). The electrochemistry measurements are supported by the National Science Foundation (CHE-2439936). C.K.B acknowledges the Research Corporation for Science Advancement (Cottrell Award).

6.2.2 Statistical Optimization of Hydrazone-Crosslinked Hyaluronic Acid Hydrogels for Protein Delivery

We are grateful for funding from the Collins Medical Trust, National Institutes of Health (R21-EB032112), and Wu Tsai Human Performance Alliance. JD is supported by a doctoral level post-graduate scholarship (PGS-D) from the Natural Sciences and Engineering Research Council of Canada (NSERC). EAM and JK were supported by the Knight Campus Undergraduate Scholars Program. MF was supported by the University of Oregon's Summer Program in Undergraduate Research (SPUR) and Vice President for Research and Innovation (VPRI) Fellowship. We would like to thank Dr. Casey Check and Professor Willie (Skip) Rochefort for their guidance on rheology, Patrick Hall for his guidance on scanning electron microscopy, and Professor Danielle Benoit for her guidance on gel permeation chromatography. We would also like to thank Chandler Asnes and Payton Jefferis for their thoughtful feedback on this work.